Toward the Discovery of Small Molecules that Target Adenosine 5'-Phosphosulfate Reductase

by

Jiyoung A. Hong

A dissertation submitted in partial fulfillment
Of the requirements for the degree of
Doctor of Philosophy
(Chemistry)
In The University of Michigan
2012

Doctoral Committee:

      Professor Kate S. Carroll, co-Chair
      Professor John Montgomery, co-Chair
      Professor Heather A. Carlson
      Professor Katrin Karbstein
      Professor Hollis D. Showalter

Jiyoung A. Hong

2012

This thesis is dedicated to my parents who gave me unconditional support and love.

Acknowledgements

Foremost, I would like to thank my mentor, Dr. Kate Carroll, for all of her guidance, patience and instruction since day one. None of this work would have been possible without her academic, financial and moral support. I would like to acknowledge and thank all of the former and current Carroll lab members who made the lab a convivial place to work as one team. They helped me through the best and worst research times and became a boundless scientific resource. My special appreciation goes out to my fellow graduate students, Devayani Bhave, Steve Leonard, Candie Paulsen, Thu Ha Truong, and Francisco Garcia for their friendship, encouragement and numerous fruitful discussions. My thanks also goes to Karbstein lab for the help they provide and the fun we share. I would like to thank Dr. John Montgomery, Dr. Hollis Showalter, Dr. Heather Carlson and Dr. Katrin Karbstein for serving as my thesis committee. They have attended my meetings, given me valuable input on my research and provided valuable advice for determining my future directions. I would also like to thank Dr. Sandro Cosconati, Dr. David Goodsell and Dr. Arthur Olson for their collaborative work on the virtual ligand screening project.

I am very fortunate to have been blessed with loving and supportive family and friends. My parents, Seokmin Hong and Younghee Lee provided me with unlimited love throughout my entire life and my brother, Junyoung Hong was always there for me.

Thanks to my aunts and godmother for praying for me. I must also acknowledge my amazing friends, without whose love I would not have finished my journey through graduate school specially Younji Kim, Anna Kang and Soojeong Kim. Finally, my heartfelt appreciation goes to Taehoon Kang, who stood by me when I needed it the most. You are my love, inspiration and compass in life.

Preface

This thesis is a compilation of published and unpublished work investigating the mechanism of sulfonucleotide reductases (SRs) and the identification of SR inhibitors. Sulfur catalysis by metabolic pathways are essential for the *de novo* biosynthesis of cysteine in human pathogens, including *Mycobacterium tuberculosis*. SRs catalyze the first committed step in the generation of reduced sulfur for cysteine and are a validated target for the development of antitubercular agents, particularly for the treatment of latent infection.

In Chapter 1, we discuss the urgent need to discover new antibacterial targets for multidrug resistant and latent tuberculosis infection. I explore different methods of identifying small-molecule inhibitors against the SR known as, adenosine-5'-phosphosulfate (APS) reductase (APR), which is an essential enzyme for mycobacterial survival.

In Chapter 2, we identify the first non-phosphate-based inhibitors of APR using virtual ligand screening and experimental validation of in silico hits. This work has been published as Cosconati, S.*, Hong, J.A.*, Novellino, E., Carroll, K.S., Goodsell, D.S. and Olson, A.J., "Structure-based virtual ligand screening and biological evaluation of

Mycobacterium tuberculosis adenosine 5'-phosphosulfate reductase inhibitors," J. Med. Chem. (2008) Oct;51(21):6627-30. * Co-first authors.

In Chapter 3, we investigate the molecular determinants that underlie substrate binding and, specificity of APR. This study presents the structural and functional features required for APR-ligand interaction of APR and provides the pharmacological roadmap for future rational inhibitor design. These data are published as Hong, J.A., Bhave, D.P. and Carroll, K.S., "Identification of critical ligand binding determinants in *Mycobacterium tuberculosis* adenosine-5'-phosphosulfate reductase," J. Med. Chem. (2009) Aug;52(17):5485-95.

Chapter 4 details the role of a conserved active site residue, His252, in APR catalysis. Our biochemical and biophysical data demonstrate that His252 enhances substrate affinity *via* interaction with the substrate α-phosphate and endoxyclic ribose oxygen. This work has been published as Hong, J.A. and Carroll, K.S., "Deciphering the role of His252 in mycobacterial APS reductase catalysis," J. Biol. Chem. (2011) Aug;286(32):28567-73.

In Chapter 5, we probe the role of the iron-sulfur cluster cofactor in APR through EPR and kinetic studies. We identify Lys144 as a "bridge" linking the iron-sulfur cluster and substrate and that this network ultimately tends to transition state stabilization. The citation for this article is Bhave, D.B., Hong, J.A., Lee, M., Jiang, W., Krebs, C., and Carroll, K.S., "Spectroscopic studies on the [4Fe-4S] cluster in adenosine 5'-phosphate

reductase from *Mycobacterium tuberculosis*," J. Biol. Chem. (2011) Jan;286(2):1216-26.

Chapter 6 demonstrates that protein redesign is a powerful tool to examine substrate discrimination in family of SRs. Although it has been proposed that SR substrate specificity is dictated by an active site phosphate-binding loop, our studies reveal that the iron sulfur cluster in APR is the major determinant of substrate specificity, thereby extending the known functions of protein-bound iron sulfur clusters. This work has been accepted as Bhave D.B., Hong, J.A., Keller, R., Krebs, C., and Carroll, K.S., "Iron-sulfur cluster engineering provides insight into the evolution of substrate specificity among the family of sulfonucleotide reductases," ACS Chem. Biol. (2011).

Finally, Chapter 7 is a discussion of future directions toward the development and evaluation of APR inhibitors.

Table of Contents

3. Identification of critical ligand binding determinants in *Mycobacterium tuberculosis* adenosine-5'-phosphosulfate reductase

List of Figures

List of Schemes

List of Tables

List of Abbreviations

TB	Tuberculosis
APS	Adenosine 5'-phosphosulfate
APR	Adenosine 5'-phosphosulfate reductase
WHO	World Health Organization
MDR	Multi-drug resistant
XDR	Extensively-drug resistant
MSH	Mycothiol
CoA	Coenzyme A
PAPS	3'-Phosphoadenosine 5'-phosphosulfate
PAPR	3'-Phosphoadenosine 5'-phosphosulfate reductase
AMP	Adenosine 5'-phosphate
Trx	Thioredoxin
ATP	Adenosine 5'-triphosphate
SR	Sulfonucleotide reductase
HTS	High throughput screening
VLS	Virtual ligand screening
PaAPR	*Pseudomonas aeruginosa* APR
MtAPR	*Mycobacterium tuberculosis* APR
EcPAPR	*Escheri coli* PAPR
ScPAPR	*Saccharomyces cerevisiae* PAPR
SAR	Structure activity relationship

[4Fe-4S]	Four iron, four sulfur
AD4	Autodock4
NCI	National Cancer Institute
PAP	3'-Phosphoadenosine 5'-phosphate
ADP	Adenosine 5'-diphosphate
ADPβS	Adenosine 5'-O-β-thiodiphosphate
ADPβF	Adenosine 5'-O-β-fluorodiphosphate
AMPCF$_2$P	Adenosine 5'-O-α,β-difluoromethylenediphosphate
AMPCP	Adenosine 5'-O-α,β-methylenediphosphate
AMPNP	Adenosine 5'- O-α,β-imidodiphosphate
AMPPN	Adenosine 5'- O-β -amidodiphosphate
APSβM	Adenosine 5'-O-α,β-methylenephosphosulfate
AMPS	Adenosine 5'-O-thiophosphate
AMPN	Adenosine 5'-O-amidophosphate
Cys-Sγ–SO$_3^-$	S-sulfocysteine
ITC	Isothermal titration calorimetry
E	Enzyme
L	Ligand
ε	Extinction coefficient
DTT	Dithiothreitol
HPLC	High-performance liquid chromatography
MANT	(2′)3′-O-(N-Methylanthraniloyl).

MES	(*N*-morpholino)ethanesulfonic acid
WT	Wild type
CAPS	*N*-cyclohexyl-3-aminopropanesulfonic acid
PpAPR-B	*Physcomitrella patens* APR
EPR	Electron paramagnetic resonance
FAD	Flavin adenine dinucleotide
IPTG	Isopropyl-*β-D*-thio-galactoside
PMSF	Phenylmethanesulfonylfluoride
Da	Daltons
ESI-FT-ICR MS	Electrospray ionization Fourier transform ion cyclotron mass spectrometry
ESEEM	Electron spin echo envelope modulation
ENDOR	Electron nuclear double resonance
P-loop	Phosphate-binding loop
BsAPR	*Bacillus subtilis* APR
NADP	Nicotinamide adenine dinucleotide phosphate
NAD	Nicotinamide adenine dinucleotide
EcPAPR4cys	*Escheri coli* PAPR with 4 cysteine
ICP	Inductively coupled plasma
ATP PPase	ATP pyrophosphatase
DmsA	Dimethyl-sulfoxide reductase
MBI	Mechanism based inhibitor

ABSTRACT

Toward the Discovery of Small Molecules that Target Adenosine 5'-Phosphosulfate Reductase

by

Jiyoung A. Hong

Co-chairs: Kate S. Carroll and John Montgomery

Adenosine-5'-phosphosulfate reductase (APR) is an iron-sulfur protein that catalyzes the first committed step in the *de novo* biosynthesis of cysteine in mycobacteria. APR is a validated target for the development of new antitubercular agents, particularly for the treatment of latent infection. The goal of this research is to develop small-molecule inhibitors of APR that serve as tools for biological discovery or as leads for drug discovery. Toward this end, we have combined virtual ligand screening (VLS), rational structure-based design, and enzyme mechanism analysis. Through VLS and experimental testing, we have identified the first nonphosphate-based inhibitors of APR and discovered an additional ligand-binding site, which could be exploited for the design of bifunctional small-molecules. To facilitate the development of potent and specific inhibitors of APR, we have also probed the molecular determinants that underlie binding and specificity *via* a series of substrate and product analogs. Our findings reveal a critical role for the α-phosphate group and provide evidence for ligand-specific conformational states within the C-terminal domain. In addition, we demonstrate that a conserved histidine within the flexible segment plays an essential role in substrate

binding and in closure of the active site lid. Subsequently, a structure-based approach was utilized in the design and synthesis of an irreversible cysteine-targeted inhibitor of APR, which locks the enzyme in its closed, inactive state. Finally, we have investigated the function of the iron-sulfur cluster in APR and provide kinetic evidence that the cofactor plays an essential role in substrate specificity of sulfonucleotide reductases. Collectively, these data further our understanding of the APR reaction mechanism and pave the way for development of new inhibitors to target this therapeutically important class of enzymes.

Chapter 1

Strategies for discovering inhibitors against adenosine 5'-phosphosulfate reductase

1.1 Abstract

Even today tuberculosis remains a deadly infectious disease. The current chemotherapy is resulting in poor patient compliance and the emergence of drug resistance strains. In addition to toxic side effects, the TB drugs target biological processes required for bacterial growth and are less effective against latent tuberculosis infection. With new advances in mycobacterial genomic and metabolic studies, new drug targets have been identified. Adenosine 5'-phosphosulfate reductase (APR), an enzyme involved in mycobacterial sulfate assimilation is one of the validated drug targets against latent tuberculosis. Herein, we outline a combination of computational and rational design strategies to identify small molecule inhibitors of APR that may represent new leads for drug development.

1.2 The current TB epidemic and chemotherapy

The history of Tuberculosis (TB) reveals that the disease has been a great threat to human health since ancient times. Definite signs of TB were identified as early as 2400 BC, in the spinal column of Egyptian mummies. Physicians in ancient Greece called this disease "phthisis" (consumption) to reflect its wasting nature and considered it as the most widespread and fatal disease of their time. This trend continued during the 17th and 18th centuries, when 25% of all deaths in Europe were related to TB (*1*). It was in

1720 that a physician, Benjamin Marten, first suggested in his "A Theory of Consumption" that TB might be caused by small living creatures that are transmitted through the air to other patients. Then, in 1882, Robert Koch discovered *Mycobacterium tuberculosis* as the bacterium that causes TB (*2, 3*). However, it was almost a century later, in 1944 when Selman Waksman introduced Streptomycin purified from *Streptomyces griseus* as the first effective antibiotic against TB. Following this breakthrough in drug discovery, a cocktail of four drugs, including isoniazid, rifampin, pyrazinamide and ethambutol were discovered during the 1950s and '60s and are still in use today (*4, 5*).

Today, Tuberculosis remains one of the deadliest infectious diseases and major challenges in global health. More than one-third of the world population is infected with TB, and one in every ten of these individuals develop TB at some point in their lifetime. In fact, in 2009, 1.7 million people died of TB including 380,000 people with HIV, a number equal to 4,700 deaths a day (*6*). Most casualties are in developing countries including Southeast Asia, Africa and Western pacific regions where TB is still endemic and sufficient treatment is not available (*7-9*). In 1993, the World Health Organization (WHO) declared TB as a global emergency and developed a strategy to control TB globally (*10*). Following proper treatment, most cases of TB were curable. However, the typical treatment regime for TB takes 6-9 months with 4-5 different antibiotics. The requirements of extensive chemotherapy have resulted in poor compliance leading to the emergence of drug resistant strains of TB. Currently, 50 million people are estimated to be infected with multi-drug resistant (MDR) stains of *M. tuberculosis*, only 50-70 % of which are curable. In addition, extensively-drug resistant (XDR) strains are emerging with very high mortality rates (*11*). In addition to the toxic side effects of the aggressive antibiotic therapy, most of the current drugs target only biological processes

required for bacterial growth such as cell wall biosynthesis, protein and DNA/RNA synthesis (*5*) However less active subpopulations of TB also exist in a dormant or persistent phase and are not effectively killed by the current treatment. Taken together, the problem of MDR-TB and the lack of effective treatment against persistent bacteria, stress the urgent need for identification of novel antibacterial targets. In 2006, WHO launched a new 'Stop TB' strategy which called for immediate attention to identify new chemical scaffolds for possible drug candidates against TB, supported by an increase in research funds (*12*). This significant step toward TB eradication promise to accelerate the understanding of the fundamental aspects of mycobacterial metabolism, pathogenesis and the discovery of potential drugs.

1.3 Life cycle of TB infection

M. tuberculosis infection is a complex process that initiates with aerosol inhalation to the host lung (*13, 14*). Therein, the mycobacteria are engulfed by host immune cells known as macrophages. By a complex mechanism that is not fully understood, the bacteria prevent maturation of the phagosome and its fusion with lysosomes. In response to the infection, macrophages produce pro-inflammatory signals – cytokines and chemokines – that recruit additional host immune cells (T-cells and neutrophils) to the infected tissue (*14, 15*). These immune cells enclose the infected macrophage and segregate it from the surrounding tissue in a structure called the granuloma, which is the defining pathological feature of this disease. By unknown mechanisms, the infection can be reactivated after many years or decades to produce active, infectious TB. This event is often associated with a reduction in immune function due to co-infection with HIV, drug use, or aging. Reactivated granuloma cracks and spills thousands of viable, infectious bacilli into the airway, resulting in lung tissue damage. Coughing is induced by this damage and provides an exit strategy for the bacteria to spread to another host (*9*).

1.4 Survival strategy of *M. tuberculosis*

M. tuberculosis has to survive within the hostile environment of the macrophage, where superoxide and nitric oxide are generated in response to infection. Once the granuloma is formed, mycobacteria enter a persistent or "latent" state characterized by lack of cell division and induction of metabolism. These latent mycobacteria are difficult to eradicate since they are not reliant on machinery targeted by conventional antibiotics. A better understanding of bacterial survival within the granuloma and/or the seeking of efficacy against latent *M. tuberculosis* is required for effective treatment (*16*).

Recently, bacterial genes involved in sulfur metabolism have been shown to be up-regulated in response to the oxidatively hostile environment (*17, 18*). Sulfur is an essential element for life (*9, 19*), is used mainly in cysteine biosynthesis. Cysteine is one of amino acids, and also serves as a building block for the biosynthesis of reduced sulfur containing metabolites such as methionine and mycothiol (*9*). These reduced sulfur-containing biomolecules are known to be involved in antioxidant defense. For instance, mycothiol (MSH) is the major low-molecular mass thiol in most action-mycetes, including mycobacteria. MSH is the equivalent of glutathione in mycobacteria and is associated with the protection of *M. tuberculosis* from toxic oxidants and antibiotics. Another reduced sulfur-containing metabolite, coenzyme A (CoA), is utilized for lipid metabolism, which plays an important role in the unique cell wall structure and virulence of bacteria by inducing cytokine mediated events (*20*). Moreover, the sulfuryl moiety can be transferred to proteins, polysaccharides and lipids for regulating cell-to-cell communication (*21*). Hence, the pathway used for the production of reduced sulfur, known as the sulfate assimilation pathway, is paramount to mycobacterial virulence and survival.

1.5 Sulfate assimilation pathway in mycobacteria

Sulfate assimilation begins with the active transport of inorganic sulfate (SO_4^{2-}) across the mycobacterial cell membrane (Figure 1.1). Imported sulfate is activated by adenylation to form adenosine 5'-phosphosulfate (APS) using ATP sulfurylase. APS lies at a metabolic hub where in one pathway it can be phosphorylated at the 3'-hydroxy position on the ribose ring by APS kinase and ATP to form 3'-phosphoadenosine 5'-phosphosulfate (PAPS). PAPS can later transport the sulfate to hydroxyl or amide moieties of metabolites involved in cell-cell communication (*21*). In the other reductive pathway, the terminal sulfate group of APS is reduced to sulfite (SO_3^{2-}) by APS reductase (APR). In this reaction, APS is reduced to SO_3^{2-} and adenosine 5'-phosphate (AMP). Thioredoxin (Trx), a 12.7 kDa protein with a redox active disulfide bond, serves as a cofactor and supplies the reducing potential necessary for this two electron reduction. The sulfite is further reduced to sulfide, which is used for the biosynthesis of reduced sulfur-containing metabolites such as cysteine, methionine, CoA, iron-sulfur clusters and MSH (Figure 1.1). Interestingly, not all microorganisms that assimilate sulfate use APS as the source of sulfite. Instead, some organisms such as *E. coli* and *S. cerevisiae* reduce the related metabolite PAPS, using PAPS reductase (PAPR). Both enzymes, APR and PAPR belong to the family of sulfonucleotide reductases (SR) and share the structural and sequence homology, and a conserved reaction mechanism. SRs are highly significant with respect to primary metabolism in prokaryotes, have enormous antimicrobial potential and carry out an unusual chemical reaction (*22*). Furthermore, SRs can be studied in order to elucidate mechanistic details and fundamental evolutionary relationships. The strategies to develop the small molecule inhibitors shed light into the mechanism, targeting and therapeutic potential of APR.

Figure1.1. The sulfate assimilation pathway in mycobacteria (*9*)
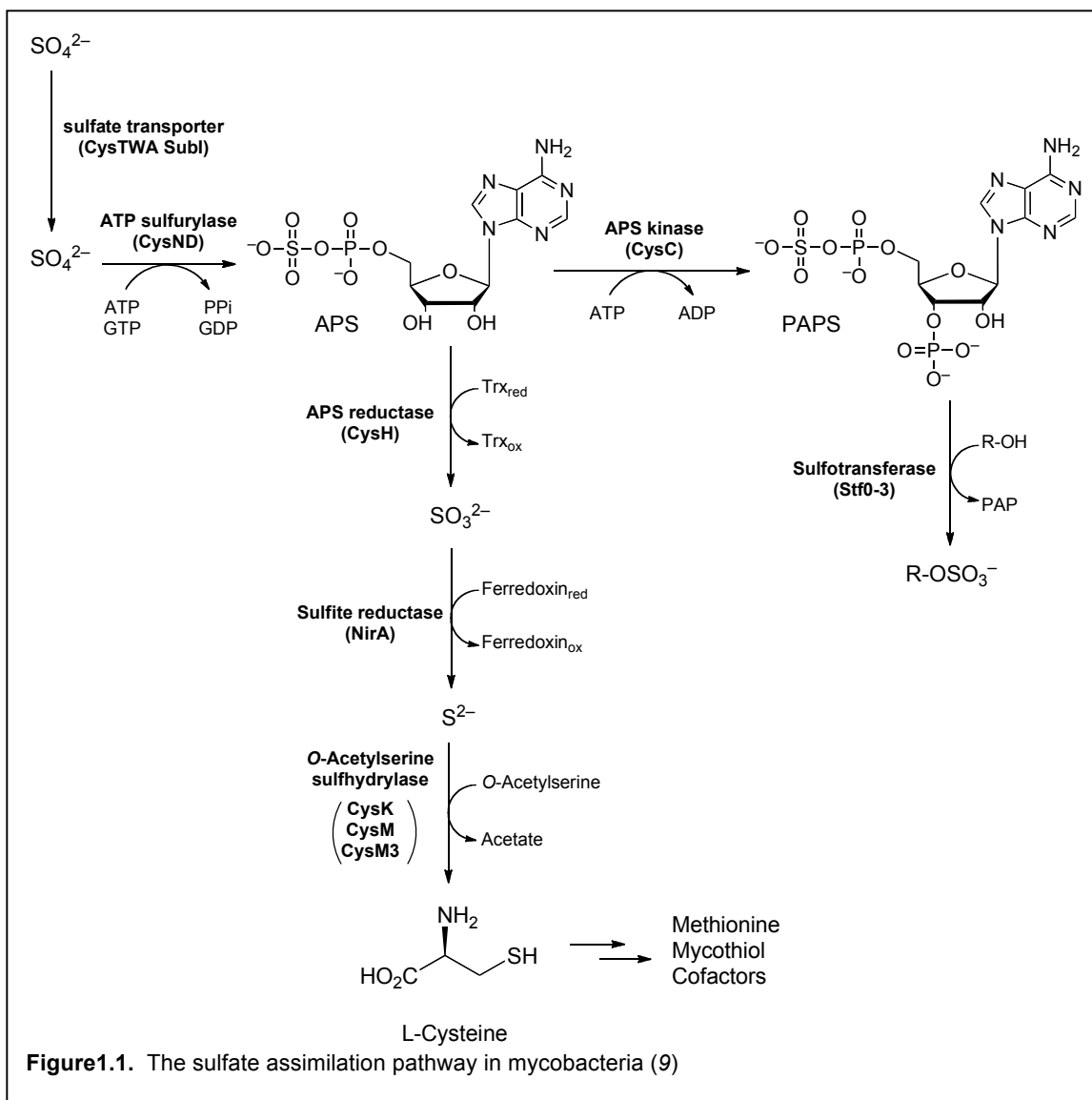
1.6 Strategies to identify small molecule inhibitors of APR

In this study we present an overview of the process of drug discovery and highlight the combination of strategies that we have employed towards identifying potential small molecule inhibitors of APR. In general, drug discovery is a challenging process that can take decades and consume over a billion dollars in resources (*23-25*). Figure 1.2 outlines the workflow of the process of drug discovery. The process of drug discovery involves the identification of candidates, characterization, screening and assays for therapeutic efficacy. After the identification and validation of a biological target protein,

Figure1.2. The process of drug discovery phase with various methods.
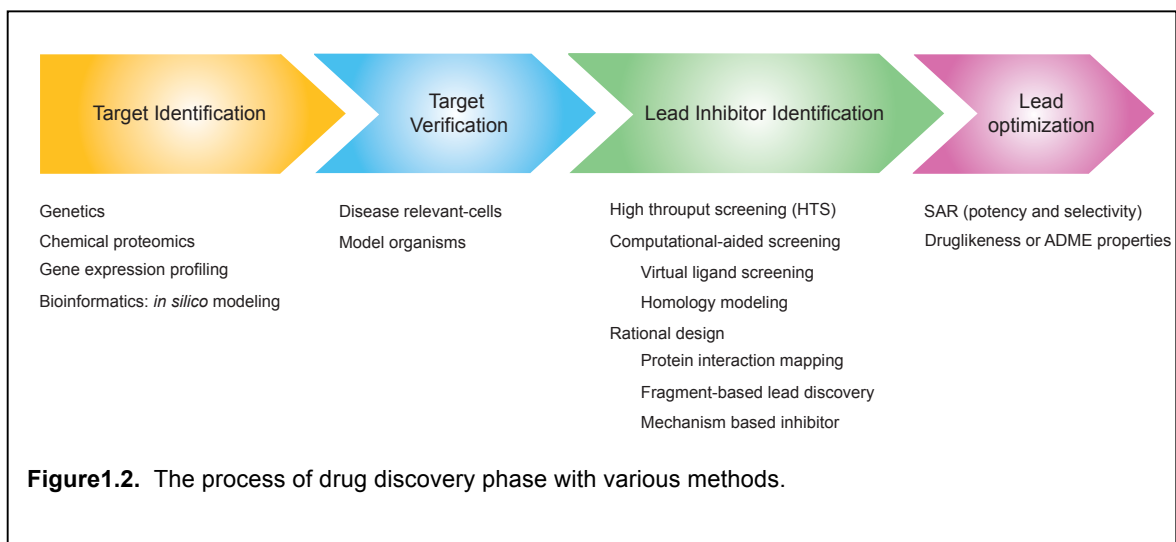
the process of finding a new inhibitors against the target, usually involves high throughput screening (HTS) using large libraries of chemical compounds. Recently, computational-aided screening is used to dock virtual libraries to a target. Another method for drug discovery is drug design, whereby the biochemical and biophysical properties of the target are studied and prediction is made to fit into active site. Once a lead compound is identified the compound is optimized for its selectivity and pharmacokinetic properties. Even though the process was shown as a linear workflow in Figure 1.2, it is actually an iterative process. Herein, we focus on developing strategies to discover small molecule inhibitors, which can eventually become lead candidates for drug design (*26*).

1.6.1 Target identification

The complete genome sequence of *M. tuberculosis (27)* and functional studies provide an opportunity to identify novel drug targets. Molecular profiling using genomic knowledge has been recognized as a well-established strategy for identifying drug targets. This technique correlates changes in gene (genomics) and protein (proteomics) expression in response to varying environmental conditions. An obvious example is mRNA expression profiling using DNA microarrays for large-scale analysis of cellular

transcripts by comparing expression levels of mRNAs (*28*). Using microarray technology in a transposon site hybridization (TraSH) assay, Sassetti and coworkers identified the compete set of genes required for the growth of mycobacteria under different conditions (*17, 29*). From this assay, APR was identified in a screen for essential virus genes in *M. bovis* (*29*), consistent with its important metabolic role. Moreover, the gene encoding APR was actively expressed during the dormant phase of *M. tuberculosis* in the environment of the macrophage (*9*). Although these techniques identify large numbers of targets including APR, the correlative nature of the data they generate means that it is not possible to determine whether changes in gene protein expression are a cause or effect of the disease and it is necessary to validate the functional role of potential targets in the disease phenotype (*28*).

1.6.2 Target validation

Once a protein target has been identified, it has to undergo a validation process wherein its role in the disease is clearly defined. Target validation is required when the target is expressed in the disease-relevant cells and target modulation in model organisms improves the disease phenotype (*30*). Genetically modified transgenic or knockout animals are extremely useful in the target validation. Recently, Senaratne and coworkers demonstrated the attenuation of an APR mutant in a murine model of *M. tuberculosis* infection (*31*). Moreover, the authors established that APR plays a central role in protecting *M. tuberculosis* against the effects of reactive nitrogen species and is critical for bacterial survival during the adaptive phase of the immune response of TB infection (*31*). Notably, APR is not found in humans and therefore represents an attractive therapeutic target.

1.6.3 Lead inhibitor identification

Traditional methods for drug discovery have mainly relied on trial-and-error *via* high throughput screening (HTS) of large chemical compound libraries. Since the technology was introduced in 1984, the field of HTS has evolved the process of lead drug discovery (*32*). Even though there has been an increase in the library of available screening compounds and the time for screening has been shortened by automation of technology, a disadvantage of HTS remains and the number of newly discovered drugs *via* HTS has been relatively low (*33*). To apply HTS for the discovery of inhibitors to APR, we need to develop a robust, efficient and economical biochemical assay. In the past, several assays, including a coupled enzyme assay and sulfite detection methods, have been proposed, but selectivity and the high cost of reagents have limited the use of these assays for HTS. Our lab has undertaken the development of a fluorophore to detect the release of sulfite by APR. This represents a promising approach toward the development of assays for HTS and is currently under way. As discussed above, For the HTS method, serendipity plays an important role in finding new drugs. However, current trends in drug discovery have shifted from discovery to design, which means that understanding the biochemistry of the proteins that cause the disease is necessary prior to designing compounds that are capable of modulating the role of these proteins (*34*). Furthermore, the advances in new technologies have fueled the development of new methods for drug design such as computer-aided screening and rational design (*35-38*).

1.6.3.1 Virtual ligand screening

Computer-aided drug design has become an essential technique used in the pharmaceutical industry, and capitalizes on the availability of structural information of the target protein. For instance, a well-developed strategy known as Virtual ligand screening (VLS) involves *in silico* screening of the chemical compound databases to identify small molecules inhibitors of enzyme targets (*39, 40*). In order to employ VLS

9

for the discovery of inhibitors for APR, we have exploited Autodock, one of the most widely used docking programs that has been used to identify inhibitors (*41*). Autodock uses a fast conformational search method based on genetic algorithms, along with an empirical free energy force field calibrated against a large set of diverse ligand-receptor complexes. This combination allows Autodock to find an optimal docked conformation with modest computational effort, while predicting free energies of binding leads to VLS (*42*). Molecular docking is performed with the crystal structure of the target and the

Figure 1.3. Strategies to develop the small molecular inhibitors against APR, A. Virtual ligand screening (VLS) and B Rational design.
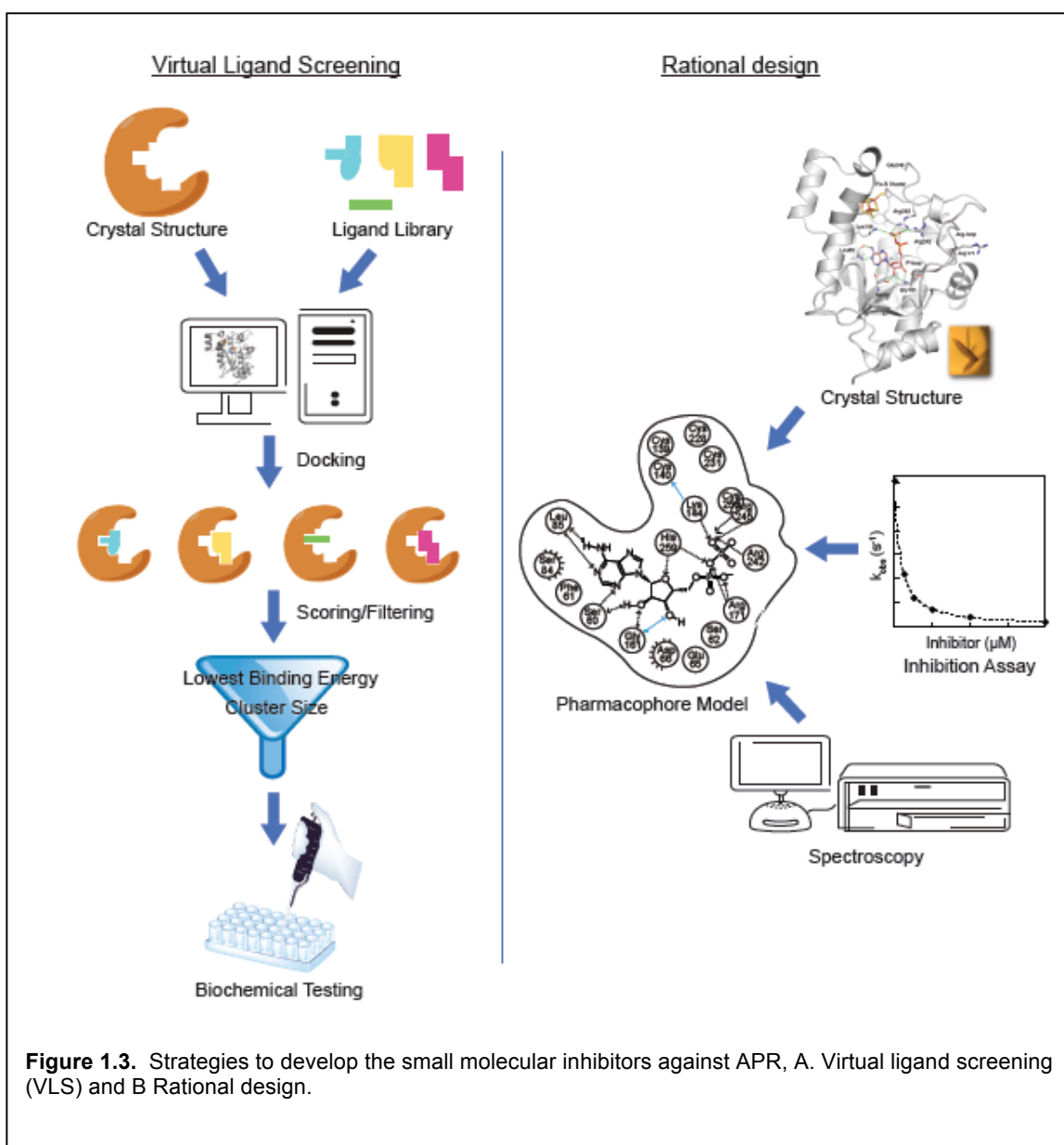
virtual ligand library as shown in Figure 1.3A. Using the x-ray crystal structure of

Pseudomonas aeruginosa APR (PaAPR), we have initiated small scale screening of the

NCI (National Cancer Institute) diversity set library. The results are filtered based on the

docking score, which consists of the lowest free binding energy and cluster size as well

as compounds identified from the screen and investigated experimentally for their

potency. These lead compounds will serve as a starting point for structure activity

relationship (SAR) studies and provide scaffolds for the construction of potent inhibitors

(*41, 43*). There are several advantages of the application of VLS for our study. First,

VLS does not require small molecule compound collections, synthesized ligand libraries

or a purified target receptor. Second, this process is fast, economical and does not rely

on the availability of chemical compounds. Finally, VLS avoids the need to consider

influences that could possibly interfere with experimentally applied assay conditions

such as limited solubility, aggregate formation and side interactions (*33*).

1.6.3.2 Rational drug design

Rational drug design is based on the lock and key analogy first postulated in 1894 by

Emil Fischer (*44*). This analogy helps explain the specific interaction between an

enzyme and its substrate if we consider the enzyme as the lock and its substrate as the

key. It has also been observed that enzymes are rather flexible structures, in which the

active site amino acid residues position themselves to make optimum contacts with the

substrate. Extending the idea that the enzyme and the substrate possess specific

complementary geometric shapes that fit exactly into one another, an induced fit model

has been proposed for rational drug design wherein small molecules are designed such

that they complementary in shape and charge to the active site of the enzyme. This

powerful technique that has now come to dominate the drug discovery process. In fact,

the discovery of drugs for HIV infection and AIDS was performed entirely *via* a rational

11

drug design approach targeting HIV protease binding sites (*45, 46*).

For our study, the crystal structure of PaAPR bound to APS serves as a starting point to identify functional groups on the substrate that are likely to contribute favorably to ligand binding (Figure 1.3B). The protein monomer has a Rossmann-like fold with a central six-stranded β-sheet interleaved with seven α-helices that create a deep active site pocket. The enzyme coordinates a [4Fe-4S] cluster via four cysteine residues. The substrate APS extends across the C-terminal ends of the β strands such that its phosphosulfate moiety is positioned toward the [4Fe-4S] cluster (*47*). Using chemically synthesized substrate/product analogs of APR, we can perform functional experiments to investigate the contacts between APR and its substrate. Analyses of the energetic contribution of individual portions of APS to the enzyme-binding interaction will offer valuable insights into substrate recognition of APR. Furthermore, the mapping of interactions (electrostatic, hydrogen bonding, hydrophobic and charged) in the active site will provide a pharmacology roadmap for future inhibitor design. Active site interactions are defined by the residues where the substrate binds. In the case of APR, it involves positively charged Lys and Arg residues, which make contacts with the phosphosulfate moiety and the phosphate-binding loop, which interacts with the ribose sugar of APS. In addition, there are two dynamic elements, the C-terminal peptide that bears the catalytically essential cysteine residue and the Arg-loop. These dynamic features of the enzyme suggest that APR can undergo conformational rearrangement at the catalytic step and adopt either an 'open' or a 'closed' conformation depending on the position of the C-terminal peptide over or out of the active site, respectively (*47*). Exploring the dynamics of the C-terminal peptide would provide clues for designing effective inhibitors that trap certain conformations and deactivate the enzyme. Additionally, the exact role of the

[4Fe-4S] cluster in catalysis and the binding determinants for the interaction of SRs with Trx need to be elucidated to understand the mechanistic details of SRs. These investigations would facilitate the design of inhibitors that target the iron-sulfur cluster or disrupt protein-protein interactions.

One of the probable reasons for why most experimental compounds entering clinical trials fail is a lack of mechanistic knowledge of the biological target (*25*). Rational design approach can help bridge this gap as it not only helps to understand the molecular interactions between ligands and enzymes, but also facilitates elucidation of the enzyme mechanisms using biochemical and biophysical analysis. Our understanding of biological ligand-receptor systems leads the way to applications in the drug discovery process and the successful design of efficient, specific, and non-toxic small-molecule therapeutics. Other chapters in this thesis describe our efforts towards the identification of APR inhibitors, leading to new fundamental insights in bacterial sulfur metabolism that could have a major impact on human health.

1.7 References

1.   Daniel, T. M. (2006) The history of tuberculosis, *Respir. Med. 100*, 1862-1870.

2.   Doetsch, R. N. (1978) Benjamin Marten and his "New Theory of Consumptions", *Microbiol. Rev. 42*, 521-528.

3.   Kaufmann, S. H. (2000) Is the development of a new tuberculosis vaccine possible?, *Nat. Med. 6*, 955-960.

4.   Check, E. (2007) Unlikely partners tackle TB funding woes, *Nat. Med. 13*, 265.

5.   Zhang, Y. (2005) The magic bullets and tuberculosis drug targets, *Annu. Rev. Pharmacol. Toxicol. 45*, 529-564.

6.   World Health Organization, *Global Tuberculosis Control 2010*, http://www.who.int/tb/publications/global_report/2010/en/index.html.

7.   Dye, C., and Williams, B. G. (2010) The population dynamics and control of tuberculosis, *Science 328*, 856-861.

8.   Corbett, E. L., Watt, C. J., Walker, N., Maher, D., Williams, B. G., Raviglione, M. C., and Dye, C. (2003) The growing burden of tuberculosis: global trends and interactions with the HIV epidemic, *Arch. Intern. Med. 163*, 1009-1021.

9.   Bhave, D. P., Muse, W. B., 3rd, and Carroll, K. S. (2007) Drug targets in mycobacterial sulfur metabolism, *Infect. Disord. Drug Targets 7*, 140-158.

10.   Murray, C. J., and Salomon, J. A. (1998) Modeling the impact of global tuberculosis control strategies, *Proc. Natl. Acad. Sci. U S A 95*, 13881-13886.

11.   Chan, E. D., and Iseman, M. D. (2008) Multidrug-resistant and extensively drug-resistant tuberculosis: a review, *Curr. Opin. Infect. Dis. 21*, 587-595.

12.   Raviglione, M. C., and Uplekar, M. W. (2006) WHO's new Stop TB Strategy, *Lancet 367*, 952-955.

13.   Flynn, J. L., and Chan, J. (2001) Immunology of tuberculosis, *Annu. Rev. Immunol. 19*, 93-129.

14.   Houben, E. N., Nguyen, L., and Pieters, J. (2006) Interaction of pathogenic mycobacteria with the host immune system, *Curr. Opin. Microbiol. 9*, 76-85.

15.   Vergne, I., Chua, J., Lee, H. H., Lucas, M., Belisle, J., and Deretic, V. (2005) Mechanism of phagolysosome biogenesis block by viable *Mycobacterium tuberculosis*, *Proc. Natl. Acad. Sci. U S A 102*, 4033-4038.

16.   Chao, M. C., and Rubin, E. J. (2010) Letting sleeping dos lie: does dormancy play a role in tuberculosis?, *Annu. Rev. Microbiol. 64*, 293-311.

17.   Sassetti, C. M., and Rubin, E. J. (2003) Genetic requirements for mycobacterial survival during infection, *Proc. Natl. Acad. Sci. U S A 100*, 12989-12994.

18.   Rengarajan, J., Bloom, B. R., and Rubin, E. J. (2005) Genome-wide requirements for *Mycobacterium tuberculosis* adaptation and survival in macrophages, *Proc. Natl. Acad. Sci. U S A 102*, 8327-8332.

19.   Schelle, M. W., and Bertozzi, C. R. (2006) Sulfate metabolism in mycobacteria, *Chembiochem 7*, 1516-1524.

20. Takayama, K., Wang, C., and Besra, G. S. (2005) Pathway to synthesis and processing of mycolic acids in *Mycobacterium tuberculosis*, *Clin. Microbiol. Rev. 18*, 81-101.

21. Mougous, J. D., Green, R. E., Williams, S. J., Brenner, S. E., and Bertozzi, C. R. (2002) Sulfotransferases and sulfatases in mycobacteria, *Chem. Biol. 9*, 767-776.

22. Carroll, K. S., Gao, H., Chen, H., Stout, C. D., Leary, J. A., and Bertozzi, C. R. (2005) A conserved mechanism for sulfonucleotide reduction, *PLoS Biol. 3*, e250.

23. Lesko, L. J., and Woodcock, J. (2004) Translation of pharmacogenomics and pharmacogenetics: a regulatory perspective, *Nat. Rev. Drug Discov. 3*, 763-769.

24. DiMasi, J. A., Hansen, R. W., and Grabowski, H. G. (2003) The price of innovation: new estimates of drug development costs, *J. Health. Econ. 22*, 151-185.

25. Chan, J. N., Nislow, C., and Emili, A. (2010) Recent advances and method development for drug target identification, *Trends Pharmacol. Sci. 31*, 82-88.

26. Alonso, H., Bliznyuk, A. A., and Gready, J. E. (2006) Combining docking and molecular dynamic simulations in drug design, *Med. Res. Rev. 26*, 531-568.

27. Cole, S. T., Brosch, R., Parkhill, J., Garnier, T., Churcher, C., Harris, D., Gordon, S. V., Eiglmeier, K., Gas, S., Barry, C. E., 3rd, Tekaia, F., Badcock, K., Basham, D., Brown, D., Chillingworth, T., Connor, R., Davies, R., Devlin, K., Feltwell, T., Gentles, S., Hamlin, N., Holroyd, S., Hornsby, T., Jagels, K., Krogh, A., McLean, J., Moule, S., Murphy, L., Oliver, K., Osborne, J., Quail, M. A., Rajandream, M. A., Rogers, J., Rutter, S., Seeger, K., Skelton, J., Squares, R., Squares, S., Sulston, J. E., Taylor, K., Whitehead, S., and Barrell, B. G. (1998) Deciphering the biology of *Mycobacterium tuberculosis* from the complete genome sequence, *Nature 393*, 537-544.

28. Lindsay, M. A. (2003) Target discovery, *Nat. Rev. Drug Discov. 2*, 831-838.

29. Sassetti, C. M., Boyd, D. H., and Rubin, E. J. (2001) Comprehensive identification of conditionally essential genes in mycobacteria, *Proc. Natl. Acad. Sci. U S A 98*, 12712-12717.

30. Zuccato, C., Tartari, M., Goffredo, D., Cattaneo, E., and Rigamonti, D. (2005) From target identification to drug screening assays for neurodegenerative diseases, *Pharmacol. Res. 52*, 245-251.

31. Senaratne, R. H., De Silva, A. D., Williams, S. J., Mougous, J. D., Reader, J. R., Zhang, T., Chan, S., Sidders, B., Lee, D. H., Chan, J., Bertozzi, C. R., and Riley, L. W. (2006) 5'-Adenosinephosphosulphate reductase (CysH) protects *Mycobacterium tuberculosis* against free radicals during chronic infection phase in mice, *Mol. Microbiol. 59*, 1744-1753.

32. Pereira, D. A., and Williams, J. A. (2007) Origin and evolution of high throughput screening, *Br. J. Pharmacol. 152*, 53-61.

33. Klebe, G. (2006) Virtual ligand screening: strategies, perspectives and limitations, *Drug Discov. Today 11*, 580-594.

34. Morphy, R., and Rankovic, Z. (2007) Fragments, network biology and designing multiple ligands, *Drug Discov. Today 12*, 156-160.

35. Wlodawer, A. (2002) Rational approach to AIDS drug design through structural biology, *Annu. Rev. Med. 53*, 595-614.

36. Schneider, G., and Fechner, U. (2005) Computer-based de novo design of drug-like molecules, *Nat. Rev. Drug Discov. 4*, 649-663.

37. Jorgensen, W. L. (2004) The many roles of computation in drug discovery, *Science 303*, 1813-1818.

38. Verlinde, C. L., and Hol, W. G. (1994) Structure-based drug design: progress, results and challenges, *Structure 2*, 577-587.

39. Koh, J. T. (2003) Making virtual screening a reality, *Proc. Natl. Acad. Sci. U S A 100*, 6902-6903.

40. Koppen, H. (2009) Virtual screening - what does it give us?, *Curr. Opin. Drug Discov. Devel. 12*, 397-407.

41. Cosconati, S., Hong, J. A., Novellino, E., Carroll, K. S., Goodsell, D. S., and Olson, A. J. (2008) Structure-based virtual screening and biological evaluation of *Mycobacterium tuberculosis* adenosine 5'-phosphosulfate reductase inhibitors, *J. Med. Chem. 51*, 6627-6630.

42. Huey, R., Morris, G. M., Olson, A. J., and Goodsell, D. S. (2007) A semiempirical free energy force field with charge-based desolvation, *J. Comput. Chem. 28*, 1145-1152.

43. Chang, M. W., Belew, R. K., Carroll, K. S., Olson, A. J., and Goodsell, D. S. (2008) Empirical entropic contributions in computational docking: evaluation in APS reductase complexes, *J. Comput. Chem. 29*, 1753-1761.

44. Lichtenthaler, F. W. (1995) 100 Years Schlussel-Schloss-Prinzip - What Made Fischer,Emil Use This Analogy, *Angew. Chem. Int. Edit. 33*, 2364-2374.

45. Mastrolorenzo, A., Rusconi, S., Scozzafava, A., Barbaro, G., and Supuran, C. T. (2007) Inhibitors of HIV-1 protease: current state of the art 10 years after their introduction. From antiretroviral drugs to antifungal, antibacterial and antitumor agents based on aspartic protease inhibitors, *Curr. Med. Chem. 14*, 2734-2748.

46. Congreve, M., Murray, C. W., and Blundell, T. L. (2005) Structural biology and drug discovery, *Drug Discov. Today 10*, 895-907.

47. Chartron, J., Carroll, K. S., Shiau, C., Gao, H., Leary, J. A., Bertozzi, C. R., and Stout, C. D. (2006) Substrate recognition, protein dynamics, and iron-sulfur cluster in *Pseudomonas aeruginosa* adenosine 5'-phosphosulfate reductase, *J. Mol. Biol. 364*, 152-169.

Chapter 2

Structure-based virtual ligand screening and biological evaluation of

***Mycobacterium tuberculosis* Adenosine 5'-phosphosulfate reductase inhibitors**

This work has been published as "Structure-based virtual ligand screening and biological evaluation of *Mycobacterium tuberculosis* adenosine 5'-phosphosulfate reductase inhibitors." *J. Med. Chem.* **2008**, 51, 6627-6630. I performed all biological testing of hits identified from the virtual ligand screen.

2.1 Abstract

Tuberculosis is among the world's deadliest infectious diseases. Adenosine 5'-phosphosulfate reductase (APR) catalyzes the first committed step in bacterial sulfate reduction and is a validated drug target against latent tuberculosis infection. We performed a virtual screening to identify APR inhibitors. These inhibitors represent the first non-phosphate-based molecules to inhibit APR. Common chemical features lay the foundation for the development of agents that could shorten the duration of chemotherapy by targeting the latent stage of TB infection.

2.2. Introduction

Despite advances in chemotherapy and the *Bacillus* Calmette-Guérin (BCG) vaccine, tuberculosis (TB) remains a leading infectious killer worldwide (*1, 2*). Although drugs exist to treat TB, they are not effective against bacilli that persist in a dormant or latent state within host lesions (*3, 4*). As a result, current treatments for TB require a cocktail

of three to five drugs for at least 6 months, a regime that many patients are unable or unwilling to follow (*5*). The lengthy and complex therapy also contributes to the development of drug-resistant TB, which is even more difficult and expensive to treat. Of the 9 million known cases of TB worldwide, as many as 2% could be extensively drug-resistant (*6*). This statistic raises the specter of virtually untreatable strains of TB and represents a severe public health problem. For these reasons, there is an urgent need for drugs that target the latent phase of TB infection.

To this end, microbial sulfate metabolism represents a promising new area for TB therapy (*7*). Reduction of inorganic sulfate is the means by which bacteria produce sulfide, the oxidation state of sulfur required for the synthesis of essential biomolecules including amino acids, proteins, and metabolites (*7-10*). Adenosine 5'-phosphosulfate reductase (APR, encoded by *cysH*) catalyzes the first committed step in bacterial sulfate reduction. In this reaction adenosine 5′-phosphosulfate (APS) is reduced to sulfite and adenosine 5′-phosphate (AMP) (*11*). Consistent with its important metabolic role APR was identified in a screen for essential genes in *M. bovis* BCG and *cysH* is actively expressed during the dormant phase of *M. tuberculosis* and in the environment of the host macrophage (*7*). Most recently, Senaratne *et al.* demonstrated that APR is required for survival in the latent phase of TB infection (*12*). APR is not found in humans and thus represents a unique target for antibacterial therapy. Recognizing its value as novel antibiotic target, in 2006 Chartron *et al.* reported the three-dimensional (3D) crystal structure of *Pseudomonas aeruginosa* APR in complex with APS substrate (*13*). *P. aeruginosa* and *M. tuberculosis* APR are related by high sequence homology (27.2% of sequence identity and 41.4% of sequence similarity), particularly in residues that line the active site (Appendix 3.7.2). In this structure, APS is situated in a deep active site cavity with the phosphosulfate extending toward the protein surface.

Conserved and semiconserved residues participate in four main-chain hydrogen bonds with adenine and the ribose O2′hydroxyl (Figure 2.1). Interaction between the phosphosulfate and APR occurs *via* strictly conserved residues Lys144, Arg242, and Arg245 (Figure 2.1). The phosphosulfate is also positioned opposite an [4Fe-4S] cofactor and Cys140. However, the substrate is not in direct contact with the [4Fe-4S] cluster; the sulfate oxygens are 7 Å from the closest iron atom and 6 Å from the closest cysteine sulfur atom.

Figure 2.1. Experimental binding conformations of APS in APR structure. Substrate is displayed with carbon atoms in green, and key binding site residues are labelled. Hydrogen bonds are represented with dashed yellow lines.
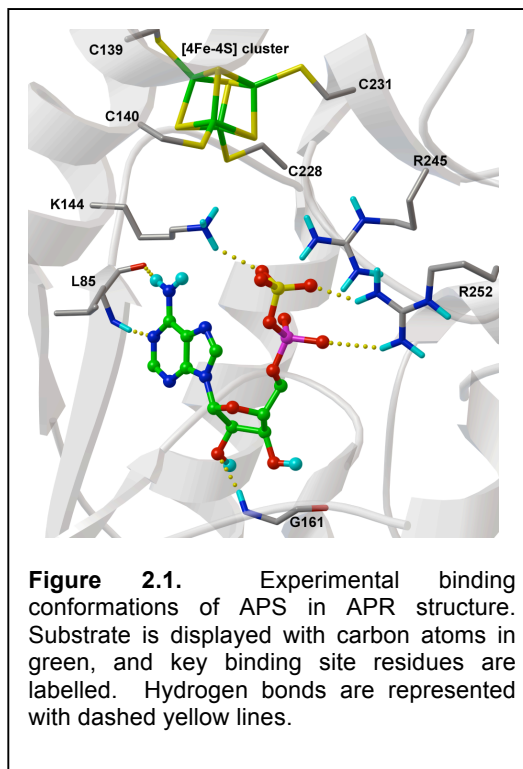
To date, only nucleotide-based inhibitors have been reported for APR, and these are expected to have limited bioavailability (*14*). Solution of the *P. aeruginosa* APR structure in complex with substrate affords a new opportunity for the discovery of inhibitors, particularly in the application of high-throughput docking of molecular databases to identify lead compounds. To this end, we have taken an approach that combines computational docking methods with biochemical evaluation.

2.3 Results and Discussion

2.3.1 Virtual ligand screening of NCI diversity set

The new version of AutoDock (AD4) (*15*) was used to conduct virtual ligand screening (VLS) of the National Cancer Institute (NCI) Diversity Set (*16*) against the *P. aeruginosa* APR crystal structure (PDB code 2GOY). Initial docking calculations were performed using APS substrate to evaluate APR as a structural model for VLS. The docked conformation determined by AD4 with the lowest predicted binding energy (-9.46 kcal/mol, ΔG_{AD4}) was in excellent agreement with the bound conformation observed for APS in the crystal structure (rmsd 0.7 Å); the calculated positions of the adenine ring, ribose sugar, and phosphosulfate group were almost identical to those found in the crystal structure. On the basis of these encouraging results, VLS calculations were performed with the APR crystal structure using the database of compounds in the NCI Diversity Set. The VLS results were sorted on the basis of their predicted binding free energies (ΔG_{AD4}), which ranged from -3.16 to -13.76 kcal/mol, and according to the cluster size for each docking conformation. Solutions with a predicted binding free energy greater than -8.0 kcal/mol and a cluster size lower than 20 out of 100 individuals were discarded.
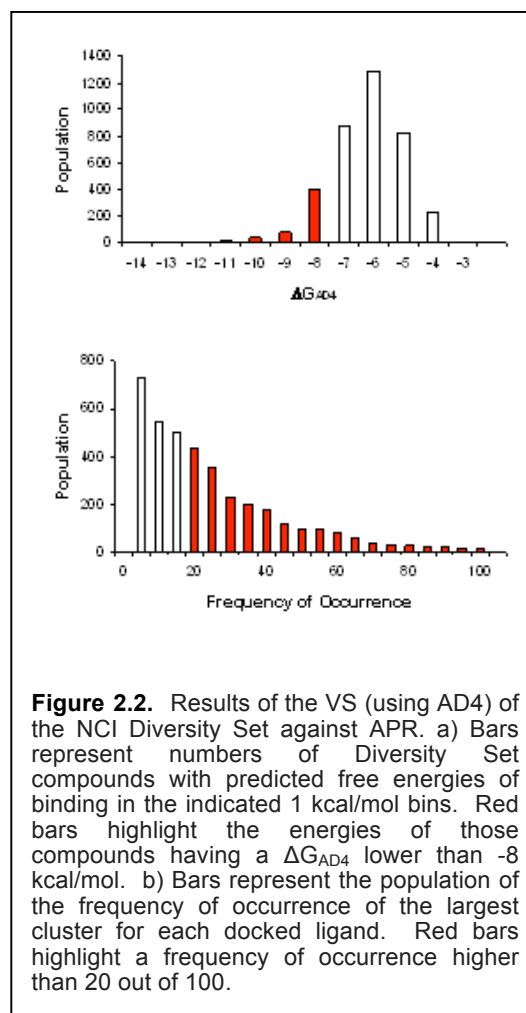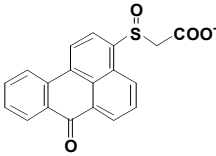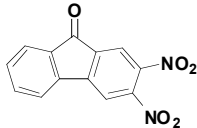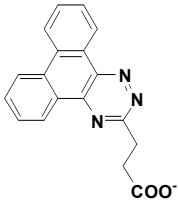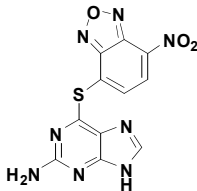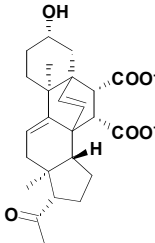
Figure 2.2. Results of the VS (using AD4) of the NCI Diversity Set against APR. a) Bars represent numbers of Diversity Set compounds with predicted free energies of binding in the indicated 1 kcal/mol bins. Red bars highlight the energies of those compounds having a ΔG_{AD4} lower than -8 kcal/mol. b) Bars represent the population of the frequency of occurrence of the largest cluster for each docked ligand. Red bars highlight a frequency of occurrence higher than 20 out of 100.

Cluster size is included in these criteria as an empirical measure of the configurational entropy, as shown in previous work (*14*). On the basis of these criteria, 14.8% of the solutions had energies lower than -8.0 kcal/mol, 43.3% had a cluster population higher than 20 individuals, and 10.0% (192 compounds) met both these criteria (Figure 2.2). The predicted binding conformations for these 192 solutions were visually inspected. Compounds that were not predicted to interact with important residues such as Lys144, Arg242, or Arg245 were removed from consideration. After this final step, 42 compounds corresponding to 2% of the original NCI Diversity Set were selected for further analysis. When ordered from NCI (The NCI/DTP Open Chemical Repository), three of these

Table 2.1. Structures, AutoDock Binding Energies and Activities of APR First Generation Inhibitor Compounds.

Chemical Structure	NSC Number	ΔG_{AD4} (kcal/mol)	K_d (μM)
	16211	-8.72	180.35
	133896	-8.75	37.11
	327704	-8.21	46.85
	348401	-9.63	15.19
	9746	-9.34	127.19

compounds were not available, so 39 compounds were obtained for biochemical testing. Assessment of the 39 top-ranked compounds from the VLS as potential inhibitors of APR was performed using a standard radioactive assay, measuring APR reduction of ^{35}S-labeled APS substrate. The compounds that exhibited significant inhibitory activity (more than 50% inhibition) are listed in Table 1, along with the AD4 binding energies and

measured activities. Three compounds from this set, tested at 100 μM, inhibited APR activity by more than 50%: 133896, 327704, and 348401 (Table 2.1). In particular, 348401 resulted in more than 90% inhibition (Table 2.1). Compounds listed in Table 1 were predicted to have the similar affinities for APR (see Table 1, ΔG_{AD4}); however, the experimental binding constants span a range of 6.81-48.11 μM. This is not unexpected, since the computed binding energies in calibration experiments typically have errors in the range of 2 kcal/mol, which corresponds roughly to a 30-fold difference in predicted binding constants. The above-mentioned compounds, representing the most potent inhibitors from our screen, were investigated further and were found to produce concentration-dependent inhibition of APR activity without promiscuous inhibition. Data were fit to a competitive inhibition model ($R^2 \geq 0.98$), and the inhibition constant (K_i) was determined for each compound in Table 2.1. Under the conditions employed for these assays the K_i was equal to the dissociation constant (K_d) of each compound. Dissociation constants for the most potent inhibitors in Table 1 ranged from 15 to 50 μM.

2.3.2 Virtual ligand screening of NCI similarity database
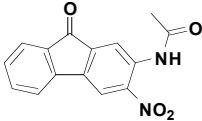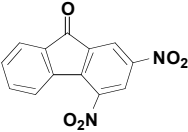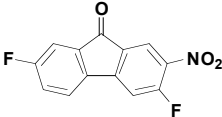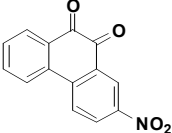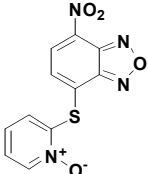
Second-generation lead compounds were identified by docking and assaying compounds from similarity searches, based on chemical structures and substructures of the Diversity Set leads. This search was performed using the Enhanced NCI Database Browser, a Web-based graphical user interface with a large number of possible query types and output formats. The 890 out of 250 000 compounds were identified in the Open NCI database with at least 80% Tanimoto similarity and docked. The 40 highest-scoring solutions, ranked according to the criteria outlined above, were experimentally evaluated using our biochemical assay.   Five compounds were identified with dissociation constants less than 50 μM, with four similar to primary lead 133896 (60826, 55545, 57476, and 23180) and one similar to primary lead 348401 (228155).

The similarity search based on the parent compound 133896 identified three new leads (60826, 55545, and 57476) with a 9-fluorenone core structure and activity against APR and the 9-fluorenone core structure (Table 2.2). The dihydrophenanthrendione 23180 was the most potent inhibitor identified in this study, with a dissociation constant of less than 10 μM. Visual inspection of the predicted binding pose for 23180 (Figure 2.3a) reveals that the aromatic polycyclic scaffold inserts into a profound gorge (referred to as L1) and makes favorable hydrophobic contacts with the side chains of residues Leu90 and Ile98. Additional interactions include the nitro functional group in proximity to positively charged active site residues Lys144 and Arg245 (referred to as P1) as well as hydrogen bonding from the carbonyl oxygens in the aromatic moiety to the backbone amide of Leu85 and side chain of Ser62.

Table 2.2. Structures, AutoDock Binding Energies and Activities of APR Second Generation Inhibitor Compounds.

Chemical Structure	NSC Number	ΔG_{AD4} (kcal/mol)	K_d (μM)
	60826	-8.46	31.79
	55545	-8.23	48.11
	57476	-8.60	44.59
	23180	-8.94	6.81
	228155	-8.7	19.51

Similar binding poses and interactions are predicted for compounds 133896, 60826, 55545, and 57476. However, these molecules have one less carbonyl oxygen in the aromatic moiety relative to the dihydrophenanthrendione chemical scaffold.

23

As a result, the 9-fluorenone-derived compounds are not predicted to form a hydrogen bond with Ser62 and could account for the difference in potency between the two structural cores. We also note that neither 9-fluorenone nor 2-nitro-9-fluorenone, which are closely related to 133896, exhibited significant activity against APR. Rather, our data indicate that a H-bond acceptor group is required at position 3 or 4 of the 9-fluoronone scaffold to acquire inhibitor potency (Table 2.2 and Figure 2.3).

Previous studies show that compound 23180 can inactivate the tyrosine phosphatase CD45 via a catalytic and oxygen-dependent reaction ($K_{inactivation}$ 4300 $M^{-1}s^{-1}$) (17). Although the precise mechanism remains unknown, inactivation of CD45 by 23180 is correlated with oxidation of a catalytic cysteine residue to sulfinic and sulfonic acid. To test whether 23180 inhibited APR in a

Figure 2.3. Docked conformations of NSC23180 (a) and NSC348401 (b) in APSR structure. Ligands are displayed as in Figure 2.1. Hydrogen bonds are represented with dashed yellow lines.

similar fashion, control experiments were performed. Unlike CD45, preincubation of APR with 23180 did not result in enzyme inactivation and Cys256 was not covalently modified.

Compound 327704 is structurally unrelated to other inhibitor cores identified by these studies. Nonetheless, this compound is also predicted to interact with the L1 pocket via
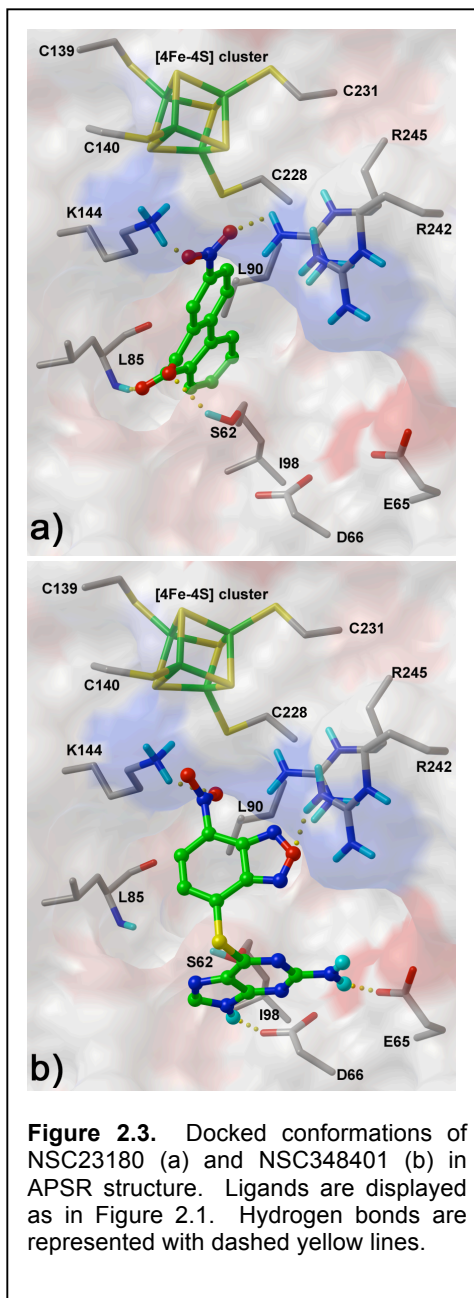
its polycyclic aromatic ring and the P1 region through the polar carboxylate group.

Compounds 348401 and 228155 contain a benzoxadiazole moiety. This functional group adopts the same binding pose in both compounds and is oriented in a way that maximizes electrostatic interactions with Arg242 and Lys144 (Figure 2.3b). Each benzoxadiazole is distinguished by a pendent thioaryl group, which is embedded in a hydrophilic cleft (referred as L2) and forms two hydrogen bonds to the side chains of Asp66 and Glu65. The low micromolar activity of 348401 and 228155, combined with the ability to chemically derivatize the purine scaffold, suggests that this compound class may be a promising lead.

Interestingly, though compounds 23180 and 348401 contain a polycyclic aromatic ring, they are not predicted to adopt the same binding position and interact with similar residues (Figure 2.4). Rather, 23180 is positioned deep inside the L1 cavity, flanked by the [4Fe-4S] cluster while 34801 occupies the shallower and more polar L2 region of the active site, which is consistent with the more polar nature of the ring in this

Figure 2.4. Binding pose of both NSC23180 and NSC348401 in the APSR binding site. Ligands and residues belonging to the P_1 site and are depicted in capped sticks colored by atom types. Residues belonging to the L_1 and L_2 sites are depicted as MSMS surface colored with ΔG colors, the protein secondary structure (white ribbon) is also depicted.
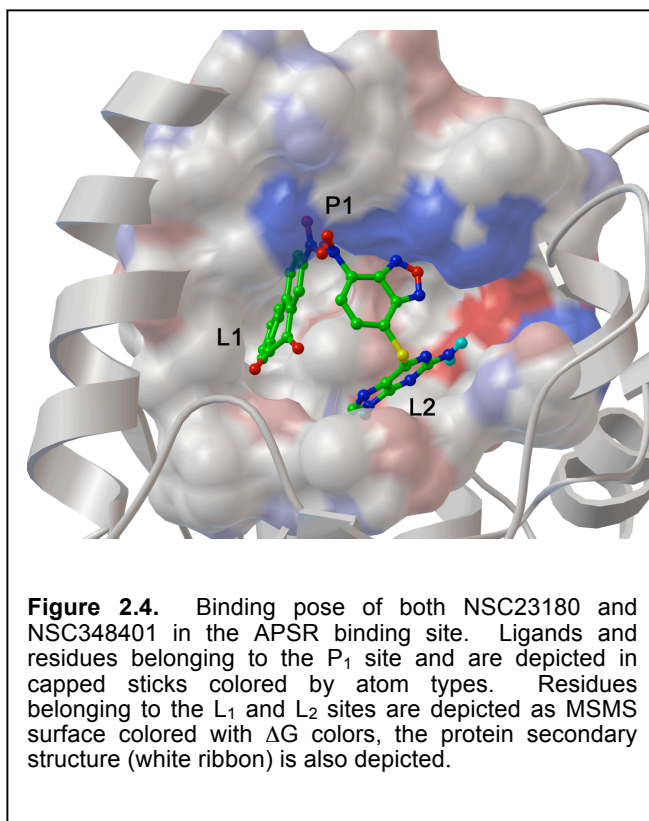
compound. Nevertheless, both classes of inhibitors are predicted to interact with the conserved positively charged residues that border both clefts in the P1 site. These

observations suggest that a ligand, which can occupy both L1/L2 clefts and bears polar hydrogen bond accepting groups to interact with the P1 site, may exhibit higher activity against APR. We are currently testing this model, and the results of these studies will be reported in due course.

2.4 Conclusion

In conclusion, we have applied virtual ligand screening of compounds from the NCI database to identify low micromolar inhibitors of *M. tuberculosis* APR, a validated target against latent TB infection. The molecules described here are the first non-phosphate-based inhibitors of this enzyme and may form the basis for development of an APR inhibitor pharmacophore. Further studies on the inhibitors identified here should also shed light into the mechanism, targeting, and therapeutic potential of this enzyme.

2.5 Experimental Procedure

2.5.1 Virtual Screening Calculations

The AutoDock 4.0 (AD4) (*15, 18*) software package, as implemented through the graphical user interface called AutoDockTools (ADT) (*19*), was used to dock small molecules to APR. The enzyme file was prepared using published coordinates (PDB 2GOY) (*13*). The terminal residues were modified to charged quaternary amine and carboxylate forms. The [4Fe-4S] cluster was retained with the protein structure. Charges of this group were manually assigned. In our case, the cluster is believed to have two ferric (+3) and two ferrous (+2) irons (*20*). Since the eight sulfur atoms (four belonging to the cluster

Table 2.3. Calculated Charges for $[Fe_4S_4(SCH_3)_4]^{2-}$

Atom	ESP Charges
Fe_{ox}	+0.642 (×2)
Fe_{red}	+0.635 (×2)
S^*_{ox}	-0.584 (×2)
S^*_{red}	-0.580 (×2)
S_{ox}	-0.574 (×2)
S_{red}	-0.571 (×2)

and four belonging to the four cysteines) have a net charge of -1, the total net charge of

the system should be of -2. Noodleman and co-workers calculated the ESP charges for models of the cluster in this oxidation state (*21*). These charges were added to APR iron-sulfur cluster atoms and to the four sulfur of the coordinating cysteines (Table 2.3).

All other atom values were generated automatically by ADT. The docking area was assigned visually around the enzyme active site. A grid of 80 Å x 80 Å x 80 Å with 0.375 Å spacing was calculated around the docking area for 13 ligand atom types using AutoGrid4. These atom types were sufficient to describe all atoms in the NCI database. For VS, compound structures of the NCI Diversity Set and the ones derived from the similarity search were prepared using the ZINC database server (http://zinc.docking.org/uploads.html) (*22*) to take into account the different protomeric and tautomeric states of each compound. All the ligands were then converted in the AutoDock format file (.pdbqt). For each ligand, 100 separate docking calculations were performed. Each docking calculation consisted of 10 million energy evaluations using the Lamarckian genetic algorithm local search (GALS) method. The GALS method evaluates a population of possible docking solutions and propagates the most successful individuals from each generation into the subsequent generation of possible solutions. A low-frequency local search according to the method of Solis and Wets is applied to docking trials to ensure that the final solution represents a local minimum. All dockings described in this paper were performed with a population size of 150, and 300 rounds of Solis and Wets local search were applied with a probability of 0.06. A mutation rate of 0.02 and a crossover rate of 0.8 were used to generate new docking trials for subsequent generations, and the best individual from each generation was propagated to the next generation. The docking results from each of the eight calculations were clustered on the basis of rootmeansquare deviation (rmsd) between the Cartesian coordinates of the atoms and were ranked on the basis of free energy of

binding. The top-ranked compounds were visually inspected for good chemical geometry. Pictures of the modeled ligand/enzyme complexes were rendered with PMV (*19*).

2.5.2 Preparation of NCI Compounds

Compounds determined by AD4 to have low binding energies to APR were requested in groups of 40 and received from the Drug Synthesis and Chemistry Branch, Developmental Therapeutics Program, Division of Cancer Treatment and Diagnosis, National Cancer Insititute (http://dtp.nci.nih.gov/branches/dscb/repo_request.html). Chemical compounds were dissolved in DMSO to 10 mM final concentration and stored at room temperature.

2.5.3 Enzyme Purification

Purification of APR was carried out as previously described (*13*).

2.5.4 APS Reductase Activity Assay

APR activity was assayed using a modification of an assay for monitoring $^{35}SO_4^{2-}$ release from ATP-sulfurylase as follows (*20*). Reactions were performed in a final volume of 100 μl. At various time points, a 10 μl aliquot was removed from the reaction and added to 0.5 ml of a 2% (w/v) charcoal solution containing 20 mM Na_2SO_3. The suspension was vortexed, clarified by centrifugation and a 400 μl aliquot of the supernatant solution, containing the radiolabeled sulfite product, was counted in 10 ml of scintillation fluid. ^{35}S-labeled APS was synthesized and purified as previously described (*23*) with the inclusion of an additional anion exchange purification step (5 ml Fast Flow Q column (GE Healthcare) eluting with a linear gradient of ammonium bicarbonate, pH 8.0, from 0.005 to 0.7 M.

2.5.5 General Kinetic Methods.

Unless otherwise specified, the reaction buffer was 100 mM Bis-Tris pH 7.5, 5 mM DTT, and the temperature was 30 °C. The auxillary protein reductant, thioredoxin was added at 10 μM. With the exception of slow reactions, the enzymatic reactions were monitored to completion ($\geq$ 3 half lives) and rate constants were obtained by nonlinear least-squares fit to a single exponential (Kaleidagraph). To ensure single-turnover reactions, the concentration of APR was kept in excess of the concentration of labeled APS (~1 nM). Two or three concentrations of APR were chosen that were at least 10-fold below the K_M value. Under these conditions, the observed rate constant was linearly dependent on enzyme concentration. Thus, reactions were first order in APS and APR in all cases. Under subsaturing conditions, with [APS] << K_M, the Michaelis-Menton equation (eq 1) simplifies to equation 2 (*24*). The reaction progress curve was plotted as a function of time and the fractional extent of reaction, and fit by a single-exponential function (eq 3) to yield k_{obs}, which is the product of enzyme concentration and the apparent second-order rate constant (eq 4). Kinetic data were measured in at least two independent experiments and the standard error was typically less than 15%.

$$V_{obs} = [E][S]k_{cat}/(K_m + [S]) \qquad (1)$$

$$V_{obs} = (k_{cat}/K_m)[E][S] \qquad (2)$$

$$\text{fraction product} = 1 - e^{-k_{obs}t} \qquad (3)$$

$$k_{obs} = (k_{cat}/K_m)[E] \qquad (4)$$

2.5.6 Inhibitor Screening.

For initial screening, compounds were tested in kinetic assays at 100 μM final concentration. Compounds that inhibited more than 50% at this concentration were analyzed further as described below.

29

2.5.7 Analog Dissociation Constants.

The standard assays and conditions described above were used to monitor the k_{cat}/K_m for reduction of APS in the presence and absence of inhibitor. Values of K_i were determined from the dependence of the observed rate constant (k_{obs}) on inhibitor concentration. With subsaturating APS, the inhibition constant is equal to the dissociation constant ($K_i = K_d$). Except in cases where solubility was a limiting factor, a range of inhibitor concentrations was employed from at least 5-fold below to 10-fold above the inhibition constant. Nonlinear least-squares fits of the equation for competitive inhibition (eq 5) gave excellent fits in all cases, and the standard error was typically less than 15%.

$$(k_{cat}/K_m)_{obs} = (k_{cat}/K_m)/(1 + [I]/K_i) \qquad (5)$$

2.5.8 Catalytic inactivation of APR by 2-nitro-9,10-phenanthrenedione. APR (9 μM) was incubated with compound 23180 (0.9 μM) or DMSO and enzyme activity was measured at 1, 15 and 30 min. No statistical difference was observed in the activity of the enzyme in these experiments indicating that compound 23180 did not catalytically inactivate APR.

2.5.9 Thiol Quantification.

Labeling of APR by the thiol-reactive probe NBDCl was carried out using a modification of a following the published procedure (17). Briefly, APR (10 μM) was incubated, at room temperature, in a final volume of 1 ml of buffer containing 50 mM BisTris (pH=7.5), 1 mM EDTA, and 1 mM DTT with (a) DMSO or (b) 10 μM compound 23180. NBDCl (50 μM) was added to each of the resulting solutions and incubated for 30 minutes at room temperature. Excess NBDCl was removed from the labeled APR by ultracentrifugation

prior to the UV-vis scan. No loss in APR thiol labeling was observed in the presence of inhibitor.

2.5.10 Promiscuous Inhibition.

At the suggestion of one reviewer, we tested members of each structural class of inhibitor for promiscuous inhibition. Assays were carried out as described above in the presence of 0.01% Triton, and showed no significant difference in K_d with the assay without detergent. We also performed a gel shift assay of trypsin activity acting on APR in the presence of inhibitors. By this gel assay, none of the inhibitors at concentrations of 50 μM changed the proteolysis pattern of trypsin and qualitatively indicates that the compounds are not inhibiting trypsin.

2.6 Appendices

Figure 2.6.1 Structure based sequence alignment of 17 APR from prokaryotes.

The ClustalW Multiple Sequence Alignment program was used. Strictly conserved residues are outlined in red, red letters indicate conserved residues and conserved regions are boxed in blue. Alignment pictures were rendered with the server ESPript 2.2 (http://espript.ibcp.fr)

```
                          1                                             .         .         .         .         .         .
Mycobacterium_tuberc      1   ......MSGETTRLTEPQLRELAARGAAELDGATATDMLRWTDETFGDIGGAGGG..VSGHRGWTTCNY
Corynebacterium_glut      1   MSFQLVNALKNTGSVKDPEISPEGPRTTTPLSPEVAKHNEELVEKHAAALYDASAQEILEWTAEHAPGAI
Corynebacterium_effi      1   MSFVTVNALKNAGPTQDPEVSPEGPRTTAPLPEEVAHRNEELVDKHADELYHADAATILEWAAEHVPGRV
Bacillus_subtilis         1   .....................MLTYDNWEEPTITFPEDDPYKGALSVLKWAYGHYGDQL
Pseudomonas_aerugino      1   ........MLPFATIPATERNSAAQHQDPSPMSQPFDLPALASSLADKSPQDILKAAFE..HFGDE
Azotobacter_vineland      1   ..................MKQAVNTAELAAACIGKSPQDILQIAFD..HFGDD
Pseudomonas_syringae      1   .................MSQPFDVAELATTYATKSAQDILKLAFE..HFGDD
Pseudomonas_putida        1   .................MSQPFDVAALAATYANKSPQDILKIAFE..HFGDD
Methylococcus_capsul      1   .........MTQT.EIDTLQAELAGRSPRTILETALS..RF.QR
Pyrobaculum_aerophil      1   ............MRREWTDLEVEELSLRFENSTAEELLSWALNEFYP.NI
Desulfitobacterium_h      1   ............MNRSELDLELDEINQAFAGEDPRKLLAYVVEKIGPARI
Clostridium_thermoce      1   ............MVQLDLEKLNKEYSDKSPEDIVRFVVENIGIEKV
Rhizobium_meliloti        1   .........MTTQSLKAEAVALEADVMALDAEAKALNDKLESLDLAGRLALIAGLEGRA
Bordetella_parapertu      1   ...............MMAARPLAA...IAGLTAAAARWHDLQSRLAIIARQYPDA
Ralstonia_eutropha        1   ......MSTVLSEIAVVDAGAASAMRPPALWVAPEYTGSIAALEQKERELGERLAGIAGRFFRA
Dechloromonas_aromat      1   ..........MTPSLLNITPELTASVAV...KTKTVKALLADIATNWSSA
Wolinella_succinogen      1   .........MRDATKESLERLCEVK...GLI
consensus>50                  ..................e.......q.....a.........d.

                          .         .         .         .         .         .         .         .         .
Mycobacterium_tuberc     62   VVASN..MADAVLVDLAAKVRP....GVPVIFLDTGYHFVETIGTRDAIESVY.DVRVLNVTPEHTVAEQ
Corynebacterium_glut     71   AVTLS..MENTVLAELAARHLP....EADFLFLDTGYHFKETLEVARQVDERY.SQKLVTALPILKRTEQ
Corynebacterium_effi     71   AVTLS..MENTVLAELAARHLP....QADFLFLDTGYHFEETLEVARKVDERY.SQTLVTALPILTRAEQ
Bacillus_subtilis        39   VYACSFGIEGIVLIDLIYKVKK....DAEIVFLDTGLHFKETYETIERVKERYPGLNIILKKPDLTLEEQ
Pseudomonas_aerugino     57   LWISFSGAEDVVLVDMAWKLNR....NVKVFSLDTGRLHPETYRFIDQVREHYGIAIDVLSPDPRLLEPL
Azotobacter_vineland     34   LWISFSGAEDVVLLDMAWKLNK....NVKVFSLDTGRLHPETYRFIEQVREHYGLAIEVLSPDARLLEPL
Pseudomonas_syringae     34   LWISFSGAEDVVLVDMAWKLNK....NVKVFSLDTGRLHAQTYRFIEQVREHYKIEIEIVSPDHSKLEPF
Pseudomonas_putida       34   LWISFSGAEDVVLVDMAWKLNK....QVKVFSLDTGRLHPETYRFIDQVREQYNLPIEILSPDRAKLDPF
Methylococcus_capsul     32   IAVSFSGAEDVVLVEMAARLRP....GIEVFTLDTGRLHPETYRFIEEVREFAVRLDVLSPDAAELEAM
Pyrobaculum_aerophil     38   ALAFSGQAEDVVVLDIMHKVAPD....KIRVFMLDTGRLPEEIYELVDKVREHYGVEIEIYYPDTKEIEEF
Desulfitobacterium_h     39   ALASSLSIEDQVLTQMLLKVDA....RARIFFIDTGRNFQQTYDLMEETMGRYKFHYEVYAPENSELEPF
Clostridium_thermoce     35   ALASSLSIEDQVLTDILLKINP....KVRVFFLDTGRHFQQTYDLMEETMHRYGFHYEVYAPESKELEQA
Rhizobium_meliloti       51   VFTTSLGIEDQVITAAIGSNR....LDIEVATLKTGRLFNETVALIDQTEETYDILIKRYYPEKADIDAY
Bordetella_parapertu     39   ALASSLAAEDMVLTHAIYAGG....LDLEVFTLDTGRLHTETLGVLDAVATRYGRAITVYRPDAAAVQAH
Ralstonia_eutropha       59   RFASSLAAEDMVLTDAILRGTEAVRAGIRVFTLQTGRLHAETLAVLDKVQAHYGYSIEQFTPDAEAVENY
Dechloromonas_aromat     38   AFANSLGAEDMVLTDLIVKAK....LPIEIFSLDTGRLPLETYDLIAAVDKHYGLKLKLYFPQAEEVESY
Wolinella_succinogen     20   TLAFSHQAEDVVVLDLLLKHYP...RSFEVFTLETGKLFTQTLAFHEEVERFFNLTIQKYHPSPKALLEL
consensus>50                  ..ass..aed.Vl.dl..k......dv.vf.ldTGrl..#ty..idqv.e.%...iev..pd...le..

                          .         .         .         .         .         .         .         .         .
Mycobacterium_tuberc    125   DELLGKDLFARN...PHECCRLRKVVPLGKTLRGYSAWVTGLRRVDAP.TRANAPLVSFDETF.....KL
Corynebacterium_glut    134   DSIYGLNLYRSN...PAACCRMRKVEPLAASISPYAGWITGLRRADGP.TRAQAPALSLDATG.....RL
Corynebacterium_effi    134   DSLYGKNLYRSN...PTACCRMRKVEPLAASISPYAGWITGLRRSDGP.TRAQAPALSLDATG.....RL
Bacillus_subtilis       105   AEEHGDKLWERE...PNQCCYLRKVVPLKRKIAGVRAWATGQRRDQSPGTRSQAVLEIDGAFSTPEKPL
Pseudomonas_aerugino    123   VKEKGLFSFYRDG..HGECCGIRKIEPLKRKIAGVRAWATGQRRDQSPGTRSQAVLEIDGAFSTPEKPL
Azotobacter_vineland    100   VREKGLFSFYRDG..HGECCGIRKIEPLKRKIATVSAWATGQRRDQSPGTRSQVAEFEVDGAFSTPDRPL
Pseudomonas_syringae    100   VKEKGLFSFYRDG..HGECCGIRKIEPLRRKISGVSAWATGQRRDQSPGTRSAVAAVEIDSAFSTAERTL
Pseudomonas_putida      100   VKEKGLFSFYRDG..HGECCGIRKIEPLRRKIATVSAWATGQRRDQSPGTRSQVAALEIDSAFSTPERTL
Methylococcus_capsul     98   VREKGLFSFYRDG..HQECCGIRKVRPLRRKIATLDAWITGQRRDQNP.TRQAVPEVEALPAFATGHHPL
Pyrobaculum_aerophil    105   VKRYGINPFYRDVELRHLCCKIRKVNPLLRAISGLDAWITGLRRDQFP.TRATTRKIQIDHD....HYGI
Desulfitobacterium_h    105   LAEYGPNAFYDKVELRQKCCELRKVRPLQRVISAVDGWICGLRREQSP.TRQEIGLLEWDSH....H.AI
Clostridium_thermoce    101   VSKYGPNFFYESVELRKKCCEIRKVNPLKRVISTVDAWICGLRREQSL.TRQELNIFEWDGL....H.SI
Rhizobium_meliloti      117   VAQYGMNGFYESVEARHACCGVRKLKPLARALDGASYWITGLRRGQSG.NRATTPFAEADVE....R.GL
Bordetella_parapertu    105   VDAHGMHAFYESVELRQKCCEIRKVEPLRRALAGRGAWITGQRRAQSA.TRGELPDEERDPV....F.GL
Ralstonia_eutropha      129   LKKHGLNAFYDSVELRKECCGIRKVEPLNRAISHADAWLTGQRREQAV.TRAELPFEEQDEA....R.GI
Dechloromonas_aromat    104   VRNHGINAFYESVTLRKACCYRKAIAGKRAWITGMRAEQAA.TRGNLAIREYDEG.....N.GL
Wolinella_succinogen     87   ERELGEWGMRESLENRHRCCGRVRKIEPLKEALKGKSAWVTGLRAEQSI.TRAELKSVEFDETF.....DL
consensus>50                  v.e.Gln.fy.d......CC.iRKvePL.r.L.g...aWitGlRrd#sp.tR.q.....e.D.........l

                          .         .         .         .         .         .         .         .
Mycobacterium_tuberc    186   VKVNPLAAWTDQDVQEYIADNDVLVNPLVREGYPSIGCAPCTAKP......AEGADPRSGRW..QGLAKT
Corynebacterium_glut    195   .KISPIITWSLEETNEFIADNNLIDHPLTHQGYPSIGCETCTLPV......AEGQDPRAGRW..AGNAKT
Corynebacterium_effi    195   .KISPIITWSLEETNRFITDNNLIDHPLTHQGYPSIGCATCTLPV......AEGQDPRAGRW..AGNAKT
Bacillus_subtilis       166   VKVCPLIHWTWKDIWRYTSRNELDYNPLHDQGYPSIGCAPCTSPA......FTAEDLRSGRW..NGMAKT
Pseudomonas_aerugino    191   YKFNPLSSMTSEEVWGYIRMLELPYNSLHERGYISIGCEPCTRPV......LPNQHEREGRWWWEEATHK
Azotobacter_vineland    168   YKFNPLAQMSSEEIWGYIRMLEIPYNSLHERGYISIGCEPCTRPV......LPNQHEREGRWWWEEATHK
Pseudomonas_syringae    168   YKFNPLAQMSSEEIWGYIRMLELPYNSLHERGFISIGCEPCTRPV......LPNQHEREGRWWWEEATQK
Pseudomonas_putida      168   YKFNPLAQMSSEEVWGYIRMLELPYNSLHERGFISIGCEPCTRPV......LPNQHEREGRWWWEESTQK
Methylococcus_capsul    165   VKFNPLAAWTSAQVWDYITACEIPFNALHLKGYVSIGCEPCTRPV......RPGQHEREGRWWWEDALKK
Pyrobaculum_aerophil    170   LKISPICDWTWDEVWGYIKKYNLPYCKLYDRGYTSIGCEPCTRPTFVSLGDVTGEELKGRWWWEKNAPK
Desulfitobacterium_h    169   YKVNPLAAWSEEQVWAYIRRENIPYSSLYNKGFRSIGCQPCTRAV......APGADVRSGRWWWEDPSKK
Clostridium_thermoce    165   YKINPIVFWSEDRVWEYIKNYNSLYSKGFRSIGCQPCTRAV......RPGEDVRSGRWWWEDPDKK
Rhizobium_meliloti      181   IKINPLADWGIETIQAHVAAEGIPVNPLHSRGYPSIGCEPCTRAI......KPGEPERAGRWWWENDEKR
Bordetella_parapertu    169   YKFNPLAAWNEADVWSVIRALGIPYNPLHDQGYPSIGCEPCTRAV......RPGEDVRAGRWWWESSDSK
Ralstonia_eutropha      193   PKFNPLADWSEEYWATYIKNHNVPVNDLHAKGYPSIGCEPCTRAV......RAGEDVRAGRWWWESKDSK
Dechloromonas_aromat    168   EKFNPLSDWTEKEVWTYIKQNAVPYNALHDKFYPSIGCAPCTRAI......SPGEDIRAGRWWWENPESK
Wolinella_succinogen    151   LKFNPLSTWSETEVFEYIKEHALPLHPLYTEGYRSIGCSPCTRAI......EAGEELRAGRWWWENPEHK
consensus>50                  .KfnPla.ws.eevw.yi...nipyn.Lhd.g%.SIGCepCTrpv.......pged.R.GRWwwee...k

Mycobacterium_tuberc    248   ECGLHAS.....................
Corynebacterium_glut    256   ECGLHS......................
Corynebacterium_effi    256   ECGLHS......................
Bacillus_subtilis       228   ECGLHE......................
Pseudomonas_aerugino    255   ECGLHAGNLISKA...............
Azotobacter_vineland    232   ECGLHAGNLIGKS...............
Pseudomonas_syringae    232   ECGLHAGNLIVRD...............
Pseudomonas_putida      232   ECGLHAGNLISKA...............
Methylococcus_capsul    229   ECGLHIGDASRV................
Pyrobaculum_aerophil    240   ECGIHCSLEAGSFERHMETVFKLKIKIK
Desulfitobacterium_h    233   ECGLHPSLNPPAKEEEKR..........
Clostridium_thermoce    229   ECGLHARVGQV.................
Rhizobium_meliloti      245   ECGLHVPEAASSIIPNASNAA.......
Bordetella_parapertu    233   ECGLHAGNRVIQIAARPA..........
Ralstonia_eutropha      257   ECGLHEQNIKH.................
Dechloromonas_aromat    232   ECGLHVKG....................
Wolinella_succinogen    215   ECGLHLKGAQWTS...............
consensus>50                  ECGlH.......................
```

Figure 2.6.2 Structure based sequence alignment of PaAPR and MtAPR.

The ClustalW Multiple Sequence Alignment program was used. Strictly conserved residues are outlined in red, red letters indicate conserved residues and conserved regions are boxed in blue. Residues flanking the active site are outlined in green.

2.7 Reference

1.   Corbett, E. L., Watt, C. J., Walker, N., Maher, D., Williams, B. G., Raviglione, M. C., and Dye, C. (2003) The growing burden of tuberculosis: global trends and interactions with the HIV epidemic, *Arch. Intern. Med. 163*, 1009-1021.

2.   Dye, C., Scheele, S., Dolin, P., Pathania, V., and Raviglione, M. C. (1999) Consensus statement. Global burden of tuberculosis: estimated incidence, prevalence, and mortality by country. WHO Global Surveillance and Monitoring Project, *JAMA 282*, 677-686.

3.   Flynn, J. L., and Chan, J. (2001) Tuberculosis: latency and reactivation, *Infect. Immun. 69*, 4195-4201.

4.   Zhang, Y. (2004) Persistent and dormant tubercle bacilli and latent tuberculosis, *Front. Biosci. 9*, 1136-1156.

5.   Espinal, M. A. (2003) The global situation of MDR-TB, *Tuberculosis (Edinb) 83*, 44-51.

6.   World Health Organization. http://www.who.int/gtb/, 2003.

7.   Bhave, D. P., Muse, W. B., 3rd, and Carroll, K. S. (2007) Drug targets in mycobacterial sulfur metabolism, *Infect. Disord. Drug Targets 7*, 140-158.

8.   Mougous, J. D., Green, R. E., Williams, S. J., Brenner, S. E., and Bertozzi, C. R. (2002) Sulfotransferases and sulfatases in mycobacteria, *Chem. Biol. 9*, 767-776.

9.   Schelle, M. W., and Bertozzi, C. R. (2006) Sulfate metabolism in mycobacteria, *Chembiochem 7*, 1516-1524.

10.   Williams, S. J., Senaratne, R. H., Mougous, J. D., Riley, L. W., and Bertozzi, C. R. (2002) 5'-adenosinephosphosulfate lies at a metabolic branch point in mycobacteria, *J. Biol. Chem. 277*, 32606-32615.

11.   Carroll, K. S., Gao, H., Chen, H., Leary, J. A., and Bertozzi, C. R. (2005) Investigation of the iron-sulfur cluster in *Mycobacterium tuberculosis* APS reductase: implications for substrate binding and catalysis, *Biochemistry 44*, 14647-14657.

12.   Senaratne, R. H., De Silva, A. D., Williams, S. J., Mougous, J. D., Reader, J. R., Zhang, T., Chan, S., Sidders, B., Lee, D. H., Chan, J., Bertozzi, C. R., and Riley, L. W. (2006) 5'-Adenosinephosphosulphate reductase (CysH) protects *Mycobacterium tuberculosis* against free radicals during chronic infection phase in mice, *Mol. Microbiol. 59*, 1744-1753.

13.   Chartron, J., Carroll, K. S., Shiau, C., Gao, H., Leary, J. A., Bertozzi, C. R., and Stout, C. D. (2006) Substrate recognition, protein dynamics, and iron-sulfur cluster in *Pseudomonas aeruginosa* adenosine 5'-phosphosulfate reductase, *J. Mol. Biol. 364*, 152-169.

14.   Chang, M. W., Belew, R. K., Carroll, K. S., Olson, A. J., and Goodsell, D. S. (2008) Empirical entropic contributions in computational docking: evaluation in APS reductase complexes, *J. Comput. Chem. 29*, 1753-1761.

15. Huey, R., Morris, G. M., Olson, A. J., and Goodsell, D. S. (2007) A semiempirical free energy force field with charge-based desolvation, *J. Comput. Chem. 28*, 1145-1152.

16. http://dtp.nci.nih.gov/branches/dscb/diversity_explanation.html.

17. Wang, Q., Dube, D., Friesen, R. W., LeRiche, T. G., Bateman, K. P., Trimble, L., Sanghara, J., Pollex, R., Ramachandran, C., Gresser, M. J., and Huang, Z. (2004) Catalytic inactivation of protein tyrosine phosphatase CD45 and protein tyrosine phosphatase 1B by polyaromatic quinones, *Biochemistry 43*, 4294-4303.

18. Morris, G. M., Goodsell, D. S., Halliday, R. S., Huey, R., Hart, W. E., Belew, R. K., and Olson, A. J. (1998) Automated docking using a Lamarckian genetic algorithm and an empirical binding free energy function, *J. Comput. Chem. 19*, 1639-1662.

19. Sanner, M. F. (1999) Python: a programming language for software integration and development, *J. Mol. Graph. Model 17*, 57-61.

20. Gao, H., Leary, J., Carroll, K. S., Bertozzi, C. R., and Chen, H. (2007) Noncovalent complexes of APS reductase from *M. tuberculosis*: delineating a mechanistic model using ESI-FTICR MS, *J. Am. Soc. Mass. Spectrom. 18*, 167-178.

21. Torres, R. A., Lovell, T., Noodleman, L., and Case, D. A. (2003) Density functional and reduction potential calculations of Fe4S4 clusters, *J. Am. Chem. Soc. 125*, 1923-1936.

22. Irwin, J. J., and Shoichet, B. K. (2005) ZINC--a free database of commercially available compounds for virtual screening, *J. Chem. Inf. Model 45*, 177-182.

23. Carroll, K. S., Gao, H., Chen, H., Stout, C. D., Leary, J. A., and Bertozzi, C. R. (2005) A conserved mechanism for sulfonucleotide reduction, *PLoS Biol. 3*, e250.

24. Segel, I. H., Renosto, F., and Seubert, P. A. (1987) Sulfate-activating enzymes, *Methods Enzymol. 143*, 334-349.

Chapter 3

Identification of critical ligand binding determinants in *Mycobacterium tuberculosis* adenosine-5'-phosphosulfate reductase

This work has been published as "Identification of critical ligand binding determinants in *Mycobacterium tuberculosis* adenosine-5'-phosphosulfate reductase" *J. Med. Chem.* **2009**, 52, 5485-5495. I purified the enzyme required for these experiments and conducted all subsequent kinetic and thermodynamic analyses. I synthesized all analogs, with the exception of thio-APS, β-fluoro ADP, and compounds in Figure 3.6.

3.1 Abstract

Mycobacterium tuberculosis adenosine-5'-phosphosulfate (APS) reductase is an iron-sulfur protein and a validated target to develop new antitubercular agents, particularly for the treatment of latent infection. To facilitate the development of potent and specific inhibitors of APS reductase (APR), we have probed the molecular determinants that underlie binding and specificity through a series of substrate and product analogues. Our study highlights the importance of specific substituent groups for substrate binding and provides functional evidence for ligand-specific conformational states. An active site model has been developed for *M. tuberculosis* APR that is in accord with the results presented here as well as prior structural data reported for *Pseudomonas aeruginosa* APR and related enzymes. This model illustrates the functional features required for the interaction of APR with a ligand and provides a pharmacological roadmap for the rational design of small molecules as potential inhibitors of APR present in human pathogens,

including *M. tuberculosis*.

3.2 Introduction

Reduced sulfur appears in organic compounds essential to all organisms as constituents of proteins, coenzymes, and cellular metabolites (*1-3*). In the amino acid cysteine, the thiol functional group plays important biological roles in redox chemistry, metal binding, protein structure, and catalysis (*4*). In many human pathogens such as *Mycobacterium tuberculosis* and *Pseudomonas aeruginosa*, activation of inorganic sulfur for the biosynthesis of cysteine proceeds *via* adenosine 5′-phosphosulfate (APS) (*5, 6*). This high-energy intermediate is produced by the action of ATP sulfurylase, which condenses sulfate and adenosine 5'-triphosphate (ATP) to form APS. The iron-sulfur protein, APS reductase (APR) catalyzes the first committed step in sulfate reduction and is a validated target to develop new anti-tubercular agents, particularly for the treatment of latent infection (*7-9*).
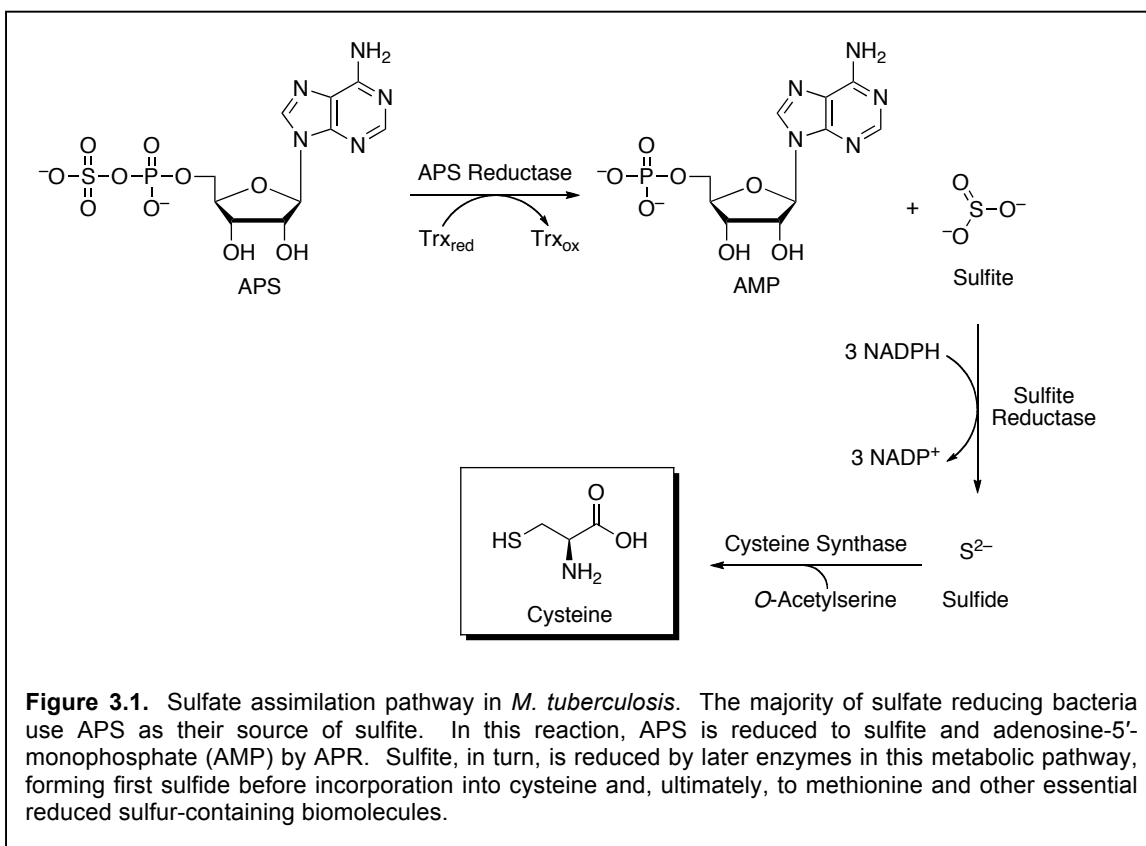
Figure 3.1. Sulfate assimilation pathway in *M. tuberculosis*. The majority of sulfate reducing bacteria use APS as their source of sulfite. In this reaction, APS is reduced to sulfite and adenosine-5′-monophosphate (AMP) by APR. Sulfite, in turn, is reduced by later enzymes in this metabolic pathway, forming first sulfide before incorporation into cysteine and, ultimately, to methionine and other essential reduced sulfur-containing biomolecules.

Figure 3.2. Mechanism of sulfonucleotide reduction.
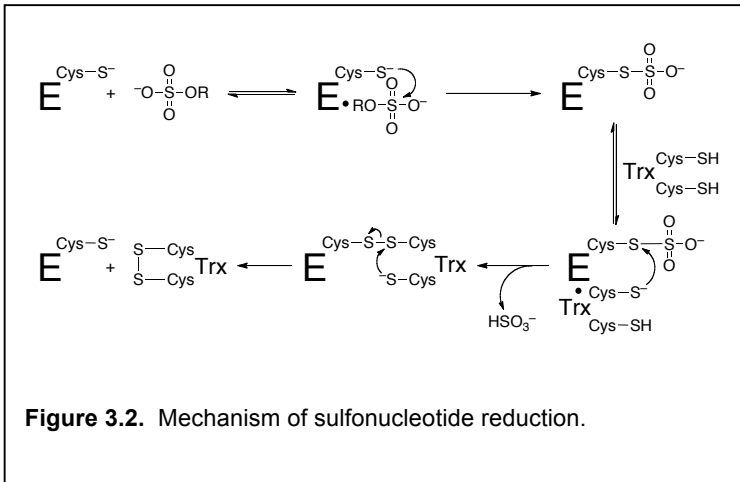
APR catalyzes the reduction of APS to sulfite (HSO_3^-) and adenosine 5'-monophosphate (AMP) using reduction potential supplied by the protein cofactor, thioredoxin as shown in Figure 3.1. Functional and structural studies have been used to investigate the mechanism of APR from sulfate-assimilating bacteria (*10-12*). The proposed mechanism in Figure 3.2 involves nucleophilic attack by cysteine 256 (Residue numbers throughout this chapter correspond to the APR sequence from *P. aeruginosa* (Appendix 3.6.1) on the sulfur atom in APS to form an enzyme *S*-sulfocysteine intermediate, E-Cys-Sγ–SO$_3^-$, which is then reduced through intermolecular thiol-disulfide exchange with thioredoxin. The iron-sulfur cluster in APR is essential for activity; however, it is not involved in redox chemistry and its exact role remains unknown (*6, 10*).

Crystal structure determination at 2.7 Å of *P. aeruginosa* APR (PaAPR) in complex with APS provided the first insight into the molecular basis for substrate recognition (Figure 3.3) (*12*). *M. tuberculosis* APR (MtAPR) and PaAPR are related by high sequence homology (27.2% of sequence identity and 41.4% of sequence similarity), particularly in the residues that line the active site. The protein monomer folds as a single domain with a central six-stranded β sheet, interleaved with seven α-helices (Figure 3.3). Opposite the nucleotide at one end of the active site is the [4Fe-4S] cluster. Three additional

38

elements define the active site: the P-loop (residues 60-66), the LDTG motif (residues 85-88) and the Arg-loop (residues 162-173). APS fits into the active site cavity with the phosphosulfate moiety extending toward the protein surface and ten residues interact directly, *via* hydrogen bonding or hydrophobic interactions with the substrate. The C-terminal segment of residues 250-267, which carries the catalytically essential Cys256, is disordered in this structure, but would be positioned above the active site cleft.

Figure 3.3. The structure of *P. aeruginosa* APS reductase in complex with substrate, APS (PDB 2GOY). The C-terminal segment of residues starting at Glu249 carries the catalytically essential Cys256 and is disordered.
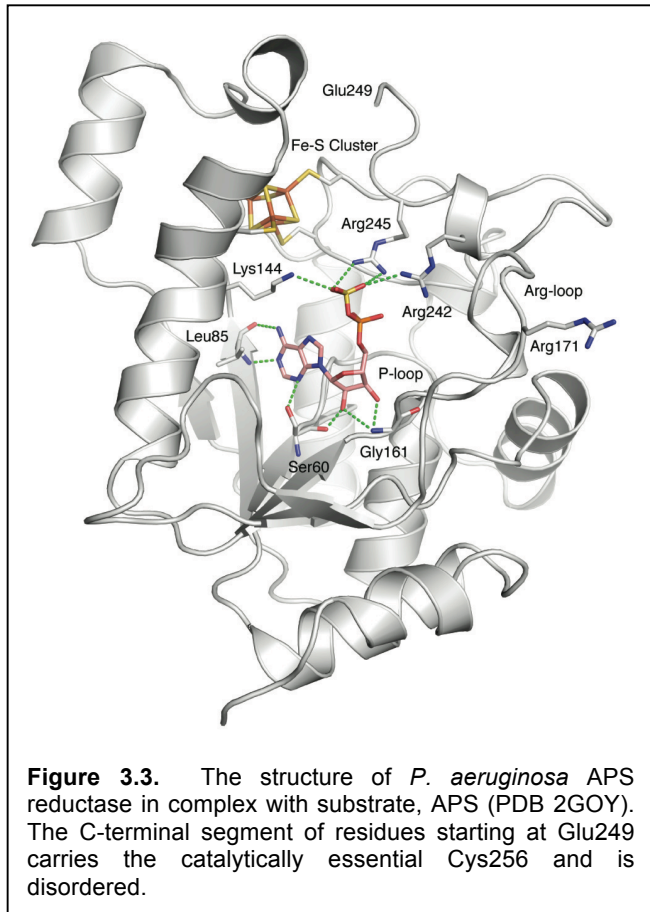
Not all organisms that assimilate sulfate reduce APS as the source of sulfite. Through divergent evolution, some organisms, such as *Escherichia coli* and *Saccharomyces cerevisiae* reduce the related metabolite 3'-phosphoadenosine-5'-phosphosulfate (PAPS) (*11*), which is produced by APS kinase from ATP and APS (*13*). PAPS reductases (PAPR) lack the iron-sulfur cofactor, but utilize the same two-step mechanism shown in Figure 3.2 (*10, 11*). *S. cerevisiae* PAPR (ScPAPR), crystallized in the presence of the product, 3'-phosphoadenosine 5'-phosphate (PAP) (*14*) has a fold similar to APR (1.6-Å rms deviation over 117 residues). In the structure of yeast PAPR, the Arg-loop and C-terminal segment are folded over the active site and this

conformation reveals additional enzyme-ligand contacts, which may also form between APR and its substrate, APS.

Even though *M. tuberculosis* has plagued humans for millennia, the antibiotic regime is complex and effective drugs that specifically target latent TB infection are yet to be developed (*15*). Novel targets (*16, 17*) and treatment strategies (*18, 19*) are emerging, but new avenues for therapeutic intervention must continue to be explored in order to combat multidrug-resistant strains of TB, which pose a significant threat to global human health (*20*). To this end, APR represents an attractive target for therapeutic intervention because it is essential for mycobacterial survival in the latent phase of TB infection (*9*) and humans do not possess an analogous metabolic pathway. Recently, we have discovered small-molecule inhibitors of APR through virtual ligand screening (*21*). However, the development of more specific and potent inhibitors will be greatly aided through knowledge of the functional importance of interactions between the substrate and enzyme at the active site, which have not yet been experimentally addressed.

Herein, we probe binding determinants of the MtAPR active site using synthetic ligand analogs. These studies define chemical groups that are essential for molecular recognition and reveal a network of electrostatic interactions, which play an important role in substrate discrimination. An active site model has been developed for MtAPR that is in accord with the results presented here as well as prior structural data reported for PaAPR and related enzymes. This model illustrates the functional features required for the interaction of APR with a ligand and provides a pharmacological road map for the rational design of small-molecules as potential inhibitors of APR present in human pathogens, including *M. tuberculosis*.

3.3 Results and Discussion

The substrate and fragments studied and results obtained in these experiments are summarized in Tables 3.1-3 and Figures 3.4-9.

3.3.1 Substrate Affinity
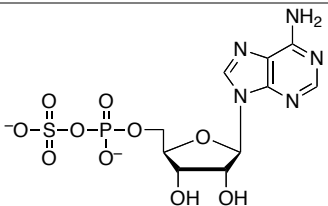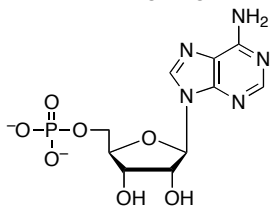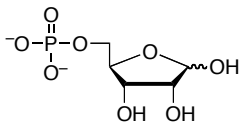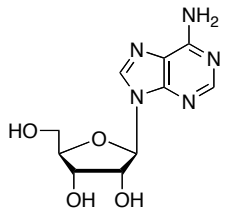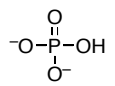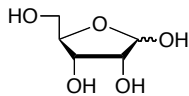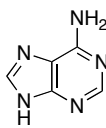
As a starting point to explore the molecular recognition properties of APR, we determined the K_d value of substrate APS for MtAPR from the dependence of the observed rate constant for S-sulfocysteine formation (Appendix 3.6.2), as described in Experimental procedures. The substrate APS binds to APR with a K_d value of 0.2 μM (Table 3.1), which is ~3-fold lower than the value of the reported substrate K_m (22).

3.3.2 Affinity of Substrate Fragments

To gain further insight into substrate recognition of MtAPR, we analyzed the energetic contribution of individual portions of APS to the enzyme-binding interaction. The results obtained in these experiments are summarized in Table 1. The product AMP differs chemically from the natural substrate, APS, by the absence of the sulfate moiety. The loss of sulfate from APS reduced binding to APR about 30-fold (2 kcal/mol), demonstrating that the AMP moiety makes a substantial contribution (7.3 kcal/mol) to the overall binding affinity (9.3 kcal/mol) of APS. Deletion of the adenine or phosphate group from AMP decreased binding to APR by ~170-fold (3.1 kcal/mol) and ~550-fold (3.8 kcal/mol), respectively. Fragments of adenosine – D-ribose and adenine – exhibited weak binding activity toward APR (0.2 and ≤1.5 kcal/mol). The respective free energy of binding to sulfate and phosphate dianions was ≤0.7 and 1.6 kcal/mol. Figure 3.4 summarizes the binding properties of the substrate, APS and product, AMP for MtAPR as compared with those of the fragments obtained by cutting these ligands at several positions, including the glycosidic bond, and at α- or β-positions within the diester moiety.

In all cases, the K_d value of APS or AMP was lower than those of its pieces. However, the free energies (ΔG_{conn}) associated with these connectivity effects for APR are modest (≤ 2.2 kcal/mol), as compared to values that have been determined for adenosine (*30*) and cytidine deaminases (*31*) (~10 kcal/mol).

Table 3.1. Ligand dissociation constants for substrate-fragments with APR.

Ligand	Structure	K_d [μM][c]	$\Delta\Delta G$ [kcal/mol][d]	pKa
APS[a]		0.20	N/A	~2 (O)[e]
AMP		5.4	2.0	6.8 (O) (*23*)
5'-Phosphoribose		93	5.1	~6.8 (O)[f]
Adenosine		3000	5.8	3.6 (N1), 12.4 (O) (*24*)
Phosphate		66000	7.7	1.97 (O), 6.82 (O), 12.5 (O) (*25*)
Ribose		680000	9.1	12.22 (O) (*26*)
Adenine[b]		≥ 90000	≥ 7.3	4.15 (N1), 9.80 (N9) (*26*)

42

Sulfate[b]	$^-O-\overset{\overset{O}{\|\|}}{\underset{\underset{O}{\|\|}}{S}}-O^-$	≥ 310000	≥ 8.6	-3 (O), 1.89 (O) (*27*)

[a] The K_d of APS was measured under single turnover conditions, in the absence of thioredoxin, as described in the methods section. [b] Due to the limits of solubility or solution ideality the reported values are lower limits. [c] For substrate-fragments in this table values of K_i were determined under single turnover conditions from the dependence of the observed rate constant at a given inhibitor concentration under conditions of subsaturating APS, such that K_i is equal to the K_d. Each value reflects the average of at least two independent experiments, and the standard deviation was less than 15% of the value of the mean. Kinetic data were nonlinear-least squares fit to a model of competitive inhibition. [d] Energetic difference in affinity of APS relative to inhibitor, $\Delta\Delta G = -RT\ln(K_d^{APS}/K_d^{Fragment})$. [e] p$K$a estimated from value measured for 2'-deoxy-5'-phosphoribose (*28*). [f] pKa estimated from value measured for 3'-phospho-5'-adenosinephosphosulfate (*29*).

3.3.3 Affinity of Substrate Analogs

3.3.3.1 β-Nucleotide Substitution
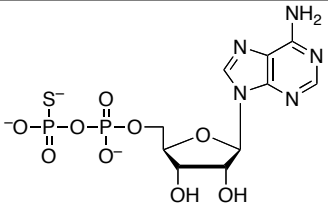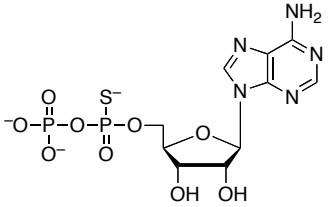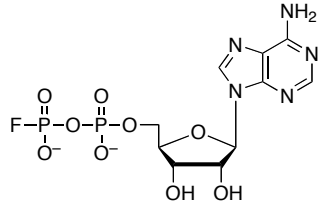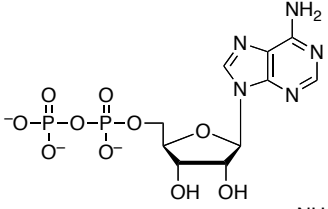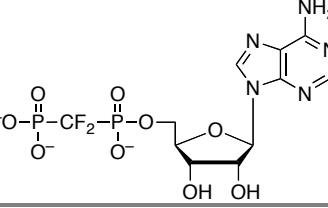
The results above suggest that the β-sulfate group plays a modest role (≤2.0 kcal/mol) in molecular recognition of APS. To probe this observation in further detail, we investigated binding affinities for a panel of nucleotide analogs containing systematic modifications at the β-position (Table 3.2 and Figure 3.5). A phosphate oxyanion has nearly the same size and shape as a sulfate oxyanion, four atoms arranged tetrahedrally around a sulfur instead of a phosphorous (*32, 33*). However, the overall charge of these analogs differs since the β-sulfate is monoanionic, whereas the β-phosphate is dianionic. Replacement of the β-sulfate moiety with β-phosphate, as in adenosine 5'-diphosphate (ADP), diminished binding to APR about 20-fold (1.8 kcal/mol). To determine whether this decrease in binding affinity is due to additional negative charge at the β-position of ADP, relative to APS, we examined sulfur (ADPβS), fluorine (ADPβF), or amine (AMPPN) substitution of the β-phosphate nonbridging oxygen atom in ADP (Table 3.2 and Figure 3.5). Sulfur substitution is considered to be a good mimic of the phosphate moiety since it is isosteric, pseudoisoelectronic, and has a similar charge distribution and similar net charge at physiological pH (*34, 35*). Fluorine substitution replaces

Figure 3.4. Effects of cutting the substrate, APS and the product, AMP into fragments on ligand K_d values. The energetic effect that results from connectivity was calculated based on the affinity of the parent ligand 'XY', compared with the affinities of its pieces, 'X' and 'Y': $\Delta G_{conn} = -RT\ln(K_{XY}/K_X K_Y)$, as previously reported (*23*).
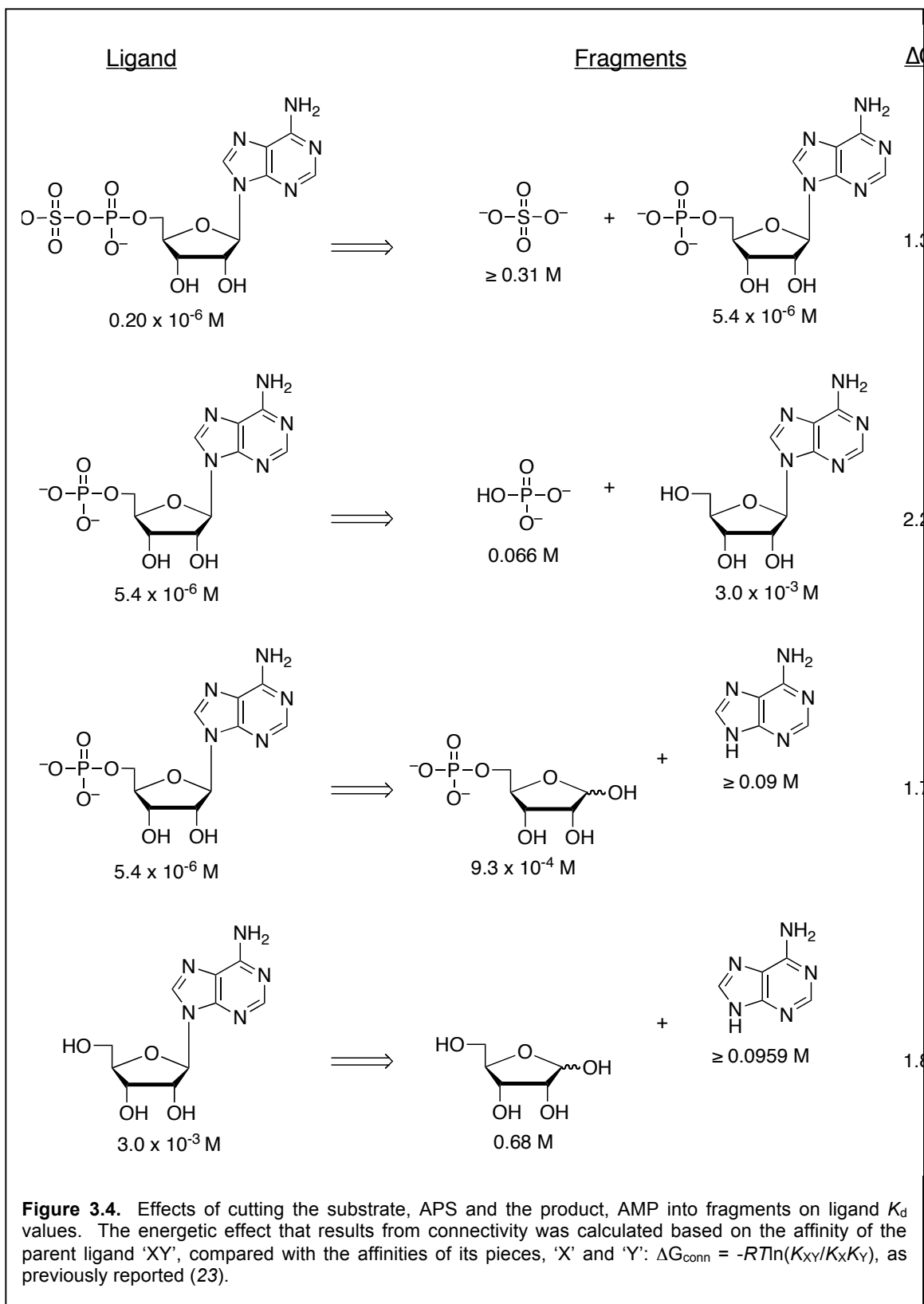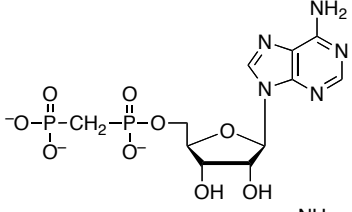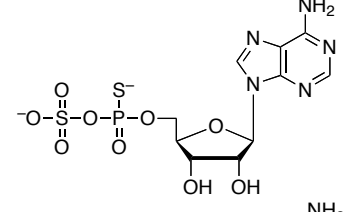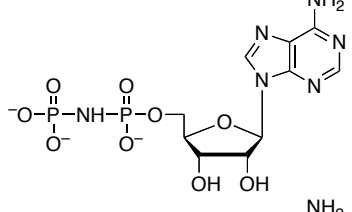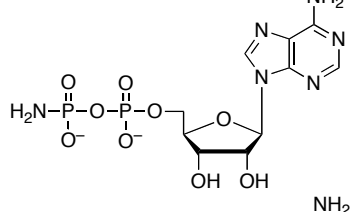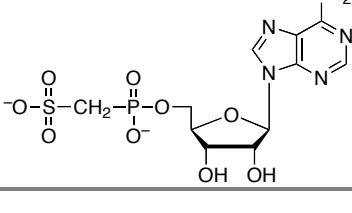
an ionizable hydroxyl group, thereby mimicking the protonated nucleotide species in net

charge at all pH values (*36*) and, at neutral pH, amine substitution neutralizes the -1 charge at the β-position. Compared to ADP, substitution by sulfur increased binding affinity by 2.0 kcal/mol, fluorine increased binding by less than two-fold (0.3 kcal/mol), and introduction of the amine group decreased the free energy of binding for APR by 2.8 kcal/mol.

Table 3.2. Ligand dissociation constants for substrate analogs with APR.

Ligand	Structure	K_d [μM][a]	$\Delta\Delta G$ [kcal/mol][b]	pKa
ADPβS		0.15	-0.17	5.2 (O) (*34*)
ADPαS[c]		0.80	0.83	6.8 (O) (*37*)
ADPβF		2.5	1.5	N/A
ADP		4.3	1.8	6.4 (O) (*37*)
AMPCF$_2$P		13	2.5	~5.7 (O)[d]

Compound	Structure			
AMPCP		27	2.9	8.1 (O) (*38*)
APSαS[c]		43	3.2	~1.6 (O)[e]
AMPNP		260	4.3	7.7 (O), 8.25 (N) (*39*)
AMPPN		410	4.6	3.0 (O), 8.15 (N)[f]
APSβM		700	4.9	~3.7 (O)[g]

[a] For substrate analogs in this table values of K_i were determined under single turnover conditions from the dependence of the observed rate constant at a given inhibitor concentration under conditions of subsaturating APS, such that K_i is equal to the K_d. Each value reflects the average of at least two independent experiments, and the standard deviation was less than 15% of the value of the mean. Kinetic data were nonlinear-least squares fit to a model of competitive inhibition. [b] Energetic difference in affinity of APS relative to inhibitor, $\Delta\Delta G = -RT\ln(K_d^{APS}/K_d^{Analog})$. [c] K_d value for the diastereoisomeric mixture of R_p and S_p isomers. [d] pK_a estimated from value for mono- and difluoro-substituted benzylphosphonic acid (*40*). [e] pK_a estimated from effect of thio-substitution on ADPαS (*37*). [f] pK_a estimated from value measured for phosphoramidic acid (*41*). [g] pK_a estimated from effect of β-methylene-substitution on AMPCP (*38*).

Taken together, the above data suggest that a net charge of -2 correlates with potent enzyme-ligand interactions. The negative charge can be localized entirely to the α-position, as in AMP, or it can be distributed across the diester, as in ADPβF. The similarity of K_d values for AMP and ADP could reflect different modes of nucleotide binding. For example, the α-phosphate of AMP could occupy the same position as the

β-phosphate in ADP, thereby establishing key electrostatic interactions with Lys144, Arg242, and Arg245 (Figure 3.3). However, an upward shift in the position of AMP would likely weaken important enzyme-binding contacts with the adenine ring and ribose sugar of AMP (Figure 3.3). An alternative possibility is that the C-terminus and Arg-loop of APR could adopt different conformations, depending on whether ADP or AMP is bound at the active site. In other words, binding energy gained through additional charge-charge interactions between the β-phosphate moiety of ADP, Lys144, Arg242 and Arg245 could be cancelled by a decrease in favorable interactions with residues in the C-terminus and the Arg-loop. Evidence in support for the latter proposal is provided in Section 3.3.5 below.

Interestingly, oxyanion substitution of the fluorine group slightly decreased binding affinity, whereas thiolate substitution increased binding potency by almost 30-fold. The larger size and polarizability of the sulfur atom could enhance binding affinity by: (i) shortening the distance to residues that directly contact the ligand, and/or (ii) enabling additional electrostatic or stacking interactions with APR (*42*). Finally, we note that neutralizing the -1 charge of the β-phosphate, as in AMPPN, is clearly unfavorable. This significant energetic penalty likely results from repulsive electrostatic interactions between the amine group, which is protonated at physiological pH (Figure 3.5), and adjacent positively charged residues (Figure 3.3). In line with this hypothesis, the

| APS | ADP Dianion | ADPβS | ADPβF | ADP Monoanion | AMPPN |

Figure 3.5. Electrostatic potential surfaces of substrate, APS and related nucleotide analogs. Color gradient: red corresponds to most negative and blue corresponds to most positive.
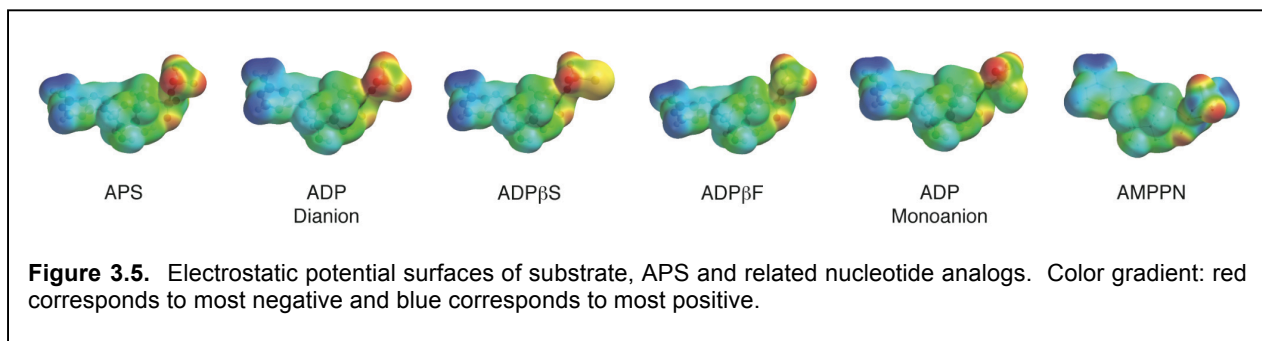
binding affinity of AMPPN for APS reductase increased at elevated pH (Appendix 3.6.5).

3.3.3.2 α-β Bridging Oxygen Substitution

Interactions between the 5'-phosphate and two highly conserved residues – Arg171 and His259 – are observed in the structure of ScPAPR bound to PAP (*14*). However, owing to the mobility of the Arg-loop and C-terminal residues, no direct contacts to the α-phosphate are observed in the structure of APR (*12*) (Figure 3.3). To gain insight into the functional importance of these contacts for MtAPR we examined the contribution of the α-β bridging oxygen to binding affinity (Table 3.2). Replacing the Pα-O-Sβ bridging oxygen in APS with a methylene group (Pα-CH$_2$-Sβ) significantly decreased binding affinity by ~3,500-fold (4.9 kcal/mol). Comparison of ADP with AMPNP (Pα-NH–Pβ), AMPCF$_2$P (Pα-CF$_2$-Pβ), and AMPCP (Pα-CH$_2$-Pβ) shows that imino, difluoromethylene, or methylene substitutions reduced binding potency by approximately 60-fold (2.5 kcal/mol), 3-fold (0.7 kcal/mol), and 6-fold (1.1 kcal/mol), respectively.

The above findings demonstrate that the α-β bridging oxygen does contribute to ligand recognition. Nonetheless, these data pose several questions: Why is the methylene substitution more detrimental for APS binding, relative to the energetic penalty paid for analogs modification of ADP? And, why does AMPNP bind more weakly to APR compared to AMPCF$_2$P? Replacing the bridging oxygen with a methylene group decreases the S/P–X–P bond angle, increases S/P–X bond length, increases the negative charge density on nonbridging oxygens, but makes the phosphate and sulfate groups less acidic (*43, 44*). It is possible that methylene subsitution of ADP is less detrimental to binding because (i) the phosphonate moiety has more torsional freedom, allowing the nucleotide to adopt an alternative favorable binding mode, and/or (ii) conformational differences in the C-terminal and Arg-loop segments minimize

unfavorable contacts to the α-β bridging position of AMPCP. NMR studies show that AMPPNP and PNP exist in solution primarily as the imido tautomers (*39*). Thus, the observed decrease in binding affinity could be due to restricted rotation about the Pα-NH–Pβ bonds.

3.3.3.3 α-Nucleotide Substitution.

Next, we examined the effect of sulfur substitution at the α-nonbridging oxygen atom using the analogs, APSαS and ADPαS (Table 2). (In principle, APSαS could be utilized as a substrate by APR. However, under saturating conditions, no evidence for formation of the *S*-sulfocysteine intermediate has been obtained (data not shown). At present, it is not understand why APR does not effectively reduce APSαS. One possible explanation is that the α-sulfur substitution disrupts contact with residues that could be important for stabilizing charge development in the transition state, such as Arg171 and His259.) Comparison of APS and APSαS shows that sulfur substitution for oxygen decreased binding by more than 200-fold (3.2 kcal/mol). However, compared to ADP, the binding potency of ADPαS increased by approximately 5-fold (1 kcal/mol). The larger energetic penalty for α-sulfur substitution of APS could result from ligand-related differences in enzyme conformation, analogous to the scenario presented in the subsection above.

3.3.4. Affinity of Product AMP Analogs
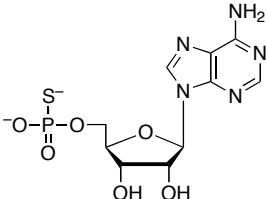
3.3.4.1 α-Nucleotide Substitution
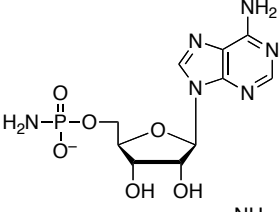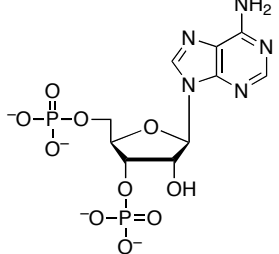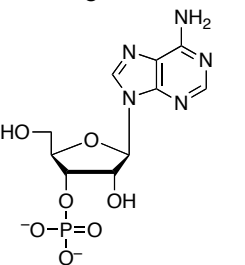
To probe the molecular binding determinants of APR at the α-position in greater detail, we compared the K_d value for the product, AMP to values measured for related analogs (Table 3). The respective effects of substitution at the α-oxygen by sulfur (AMPS) or amine (AMPN) are -0.3 and +1.8 kcal/mol, compared to AMP. The modest increase in

binding energy that results from sulfur modification is similar to the effect observed with ADPαS. The reduction in binding affinity of AMPN also parallels the decrease in observed for AMPPN.

In PAPR, residues in the P-loop interact with the 3'-phosphate of PAP (*14, 46*). However, in APR the acidic residue, Asp66, interacts with amide groups of the P-loop and thus, appears to mimic the interaction of the negatively charged 3'-phosphate group. To investigate the role of the 3'-hydroxyl group in ligand discrimination (see also Section 3.3.4.2 below) we determined the binding affinity for 3'-AMP, which reverses the position of the 5'-phosphate and 3'-hydroxyl groups (Table 3). Switching the position of the phosphate moiety decreased binding by ~600-fold (3.8 kcal/mol) indicating that, while the analog binds poorly, the 3'-phosphate does not impact binding to APR, as compared to adenosine. By contrast, addition of a 3'-phosphate group to AMP, as in PAP, decreased binding affinity by 3.0 kcal/mol. The energetic penalty for 3'-phosphate in PAP, but not 3'-AMP, likely reflects additional binding interactions to the 5'-phosphate, which could decrease conformational freedom and increase unfavorable protein-ligand contacts.

Table 3. Ligand dissociation constants for product AMP analogs with APR.

Ligand	Structure	K_d [μM][a]	$\Delta\Delta G$ [kcal/mol][b]	pKa
5'-AMPS		3.3	-0.30	5.3 (O) (*34*)

Compound	Structure	K_i	$\Delta\Delta G$	pK_a
5'-AMPN		100	1.8	~3.0 (N), ~8.15 (O)[c]
3',5'-ADP		770	3.0	2.49 (O), 8.61(O) (45)
3'-AMP		3200	3.8	5.92 (O) (23)

[a] For analogs in this table values of K_i were determined under single turnover conditions from the dependence of the observed rate constant at a given inhibitor concentration under conditions of subsaturating APS, such that K_i is equal to the K_d. Each value reflects the average of at least two independent experiments, and the standard deviation was less than 15% of the value of the mean. Kinetic data were nonlinear-least squares fit to a model of competitive inhibition. [b] Energetic difference in affinity of AMP relative to inhibitor, $\Delta\Delta G = -RT\ln(K_d^{AMP}/K_d^{Analog})$. [c] p$K_a$ estimate from value measured for phosphoramidic acid (41).

3.3.4.2 Purine and Ribose Substitution

Next, we analyzed the relative energetic contributions of individual purine and ribose substituents to the enzyme-binding interaction. Owing to the relative difficulties traditionally associated with the preparation of ADP analogs and the weak binding of adenosine, we determined affinities for a series of compounds derived from the AMP scaffold. As shown in Figure 3.6, energetic penalties for individual substitutions ranged from 0.6 to 4.7 kcal/mol. First, we probed interactions between the N6 amine and N1 of adenine and Leu85 (Figure 3.3), the first residue in the conserved LDTG motif. Loss of the N6 amine from AMP reduced the free energy of binding to APR by 1.8 kcal/mol. Replacing hydrogen atoms with methyl groups at the N6 position of adenine decreased

binding affinity by 35-fold (2.1 kcal/mol) per substitution. Inverting the hydrogen bond donor and acceptor, as in inosine 5'-monophosphate, was also disfavoured (4.7 kcal/mol), presumably due to electrostatic repulsion between the O6-keto and the Leu85 carbonyl, and the N1 by the Leu85 amine. Likewise, introduction of an N1 amine markedly reduced the affinity of this analog for APR (4.7 kcal/mol). In subsequent experiments, we determined

Figure 3.6. Free energy of binding for purine and ribose-modified analogs of product, AMP. Numbers represent the energetic effect of a given substitution in kcal/mol, relative to AMP ($\Delta\Delta G = -RT\ln(K_d^{Analog}/K_d^{AMP})$). Positive $\Delta\Delta G$'s indicate a penalty for substitution.
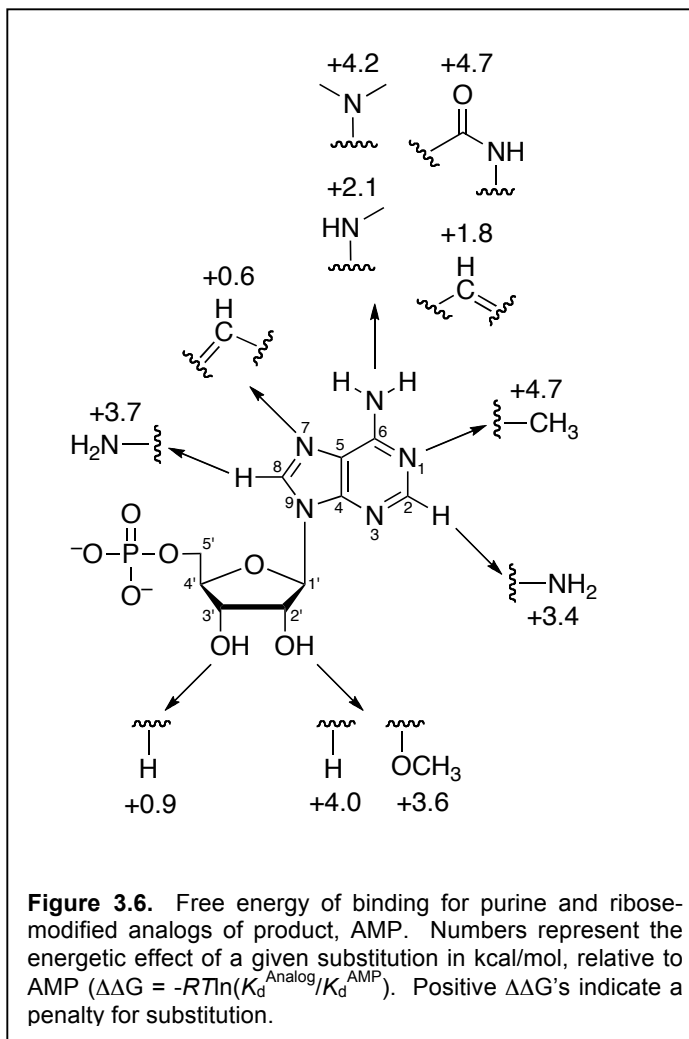
the binding potency of AMP analogs with substitutions at the 2, 7 and 8-positions of the purine ring. Methylation at N2 had a detrimental effect on binding (3.4 kcal/mol), likely due to steric clashes with the surrounding adenine-binding pocket (Figure 3.3). The structure of APR bound to APS shows that C8-H group is directed toward the 5'-phosphosulfate moiety (Figure 3.3). Not surprisingly then, amine substitution at this position decreased the free energy of binding by 3.7 kcal/mol. No contacts are formed between N7 and APR (Figure 3.3). Consistent with this observation, replacing N7 with a carbon atom had a relatively minor effect on binding affinity (0.6 kcal/mol). Finally, we investigated the influence of modification at the 2' and 3'-hydroxyl groups of the ribose sugar. 2'-deoxy and methoxy group substitutions reduced the free energy of binding by

a respective 4.0 and 3.6 kcal/mol, whereas 3'-deoxy substitution had only a modest effect on binding affinity (0.9 kcal/mol). This indicates that hydrogen bonds between the 2'-hydroxy group and Ser60 and Gly161 residues (Figure 3.3) play a vital role in substrate recognition.

3.3.5 pH Dependence of Ligand Binding

The pH dependence for ligand binding provides information about the relative affinities of the different nucleotide ionization states, and thus provides information about the active site environment. Initially, we investigated the pH dependence for APS binding. However, the substantial increase in reaction rate at higher pH precludes measurement by conventional kinetic methods (data not shown). As an alternative, we determined the affinities of APR for the substrate analog, ADP, and product, AMP, as a function of pH to investigate whether ionizations at α and β-positions are important for binding affinity (Figure 3.7). The pH dependence for ADP binding is best fit by a pK_a of 6.4 ± 0.2, which could reflect ionizations of the free enzyme and ligand (Figure 3.7A). The most likely candidate for this ionization is the ligand, as the second pK_a values of phosphate esters fall in this region (37). If this were true, the pH profile would be expected to shift to lower pH for an ADP analog with lower pK_a values. To test this, we determined the pH dependence for ADPβS, which differs in its respective pK_a value by approximately one pH unit (34). The pH dependence for ADPβS binding is best fit by a pK_a of 5.8 ± 0.2 (Appendix 3.6.4A). The dependence of the pK_a upon the identity of the ligand suggests that deprotonation of the ligand is responsible for the increase in binding at higher pH.

The pH dependence for AMP binding is best to best fit by a pK_a of 8.1 ± 0.1 (Figure 6.7B), which could reflect ionizations of the free enzyme and ligand, as described above. The simplest model to explain the weaker binding of AMP below pH 8 is that the dianion binds more tightly than the monoanion. However, the apparent pKa for AMP differs from the expected pK_a of 6.8 by more than one unit. The discrepancy between the experimental data and the simplest model is most likely due to concurrent ionization of the enzyme that affects ligand binding, leading to shift in the apparent pK_a of AMP. One model that could account for this upward deviation is that an enzymatic group with a pKa of ~6 contributes slightly (~5-fold)

Figure 3.7. pH dependence for ADP (A) and AMP (B) binding. The association equilibrium constant, ($K_a = 1/K_d$) is plotted as a function of pH. Values of K_d were determined by inhibition of APS reductase (pH 6.0-9.5). Buffers were as follows: MES (pH 6.0-6.5), BisTris (pH 6.5-7.5), TrisHCl (pH 7.5-9.5), CAPS (pH 9-9.5). See Experimental procedures for additional details. (A) The pH dependence for ADP binding. Nonlinear-least-squares fit of the data to a model for a single ionization gave pKa values of 6.4 ± 0.2. (B) The pH dependence for AMP binding. The dashed line represents the best fit of a model for a single ionization and yields a pKa of 7.9 ± 0.1.
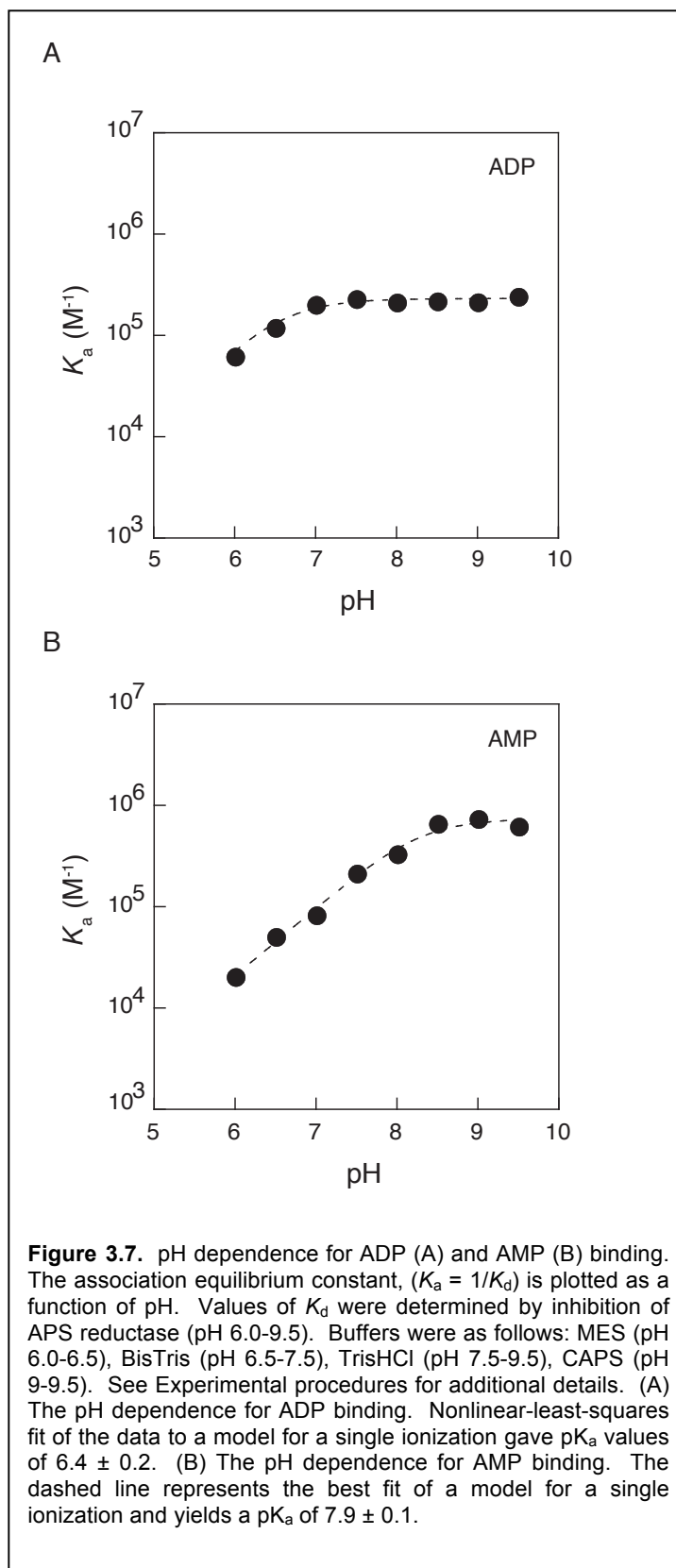
to AMP binding when protonated. The most likely residue to exert such an effect on

ligand binding is His259, which interacts with the 5'-phosphate of PAP in the structure of *S. cerevisiae* PAPR (*14*). Since a stimulatory effect is not observed for ADP binding, the C-terminal segment containing His259, and possibly the Arg-loop, may adopt different conformations depending on whether ADP or AMP is bound at the active site. To further confirm that the apparent pK_a measured for AMP depends upon the identity of the ligand, we measured the pH dependence for AMPS binding (Appendix 3.6.4B). The resulting data are best fit by a pK_a of 7.7 ± 0.1. The downward shift in apparent pK_a suggests that deprotonation of the ligand is responsible for the increase in binding at higher pH.

The observed pH dependence for ADP and AMP binding indicates that the dianion binds more tightly to APR than the monoanion. These data seemingly contradict our earlier comparison between ADP and ADPβF, whose net charges differ by one unit, but bind to APR with similar affinity (Table 3.2 and Figure 3.5). Indeed, fluorine modification is often used to determine whether binding of mono- or dianionic phosphate is favored (*40*). However, hydroxyl and fluorine groups are distinguished by unique chemical properties. For example, the high electron density of fluorine gives rise to the ability to act as an acceptor in hydrogen bonds (*47*). By contrast, the hydroxyl group is a strong dipole, with spatially separated partial positive and negative charges that can donate as well as accept hydrogen bonds (Figure 3.5). Hence, the weaker binding observed for the monoanion may not reflect a loss of charge-charge interactions, but rather an energetic penalty that results from unfavorable charge-dipole interactions with the hydroxyl group.

3.3.6 Effect of Mg^{2+} on Ligand Affinity

In the absence of metal ions, APS binds ~20-tighter to APR, compared to ADP and AMP. However, the cellular concentrations of these nucleotides are higher than APS (*48*) and thus, raise an important question: How does APS compete against binding of ADP or

AMP to the active site of APR in the cell? For the majority of biochemical reactions using ATP and, related nucleotides, the active species is the Mg^{2+} complex rather than the free nucleotide (*49*). To gain insight into ligand discrimination by APR *in vivo*, we measured the K_d values for APS, ADP and AMP in the presence of Mg^{2+}. These studies show that the K_d value of APS was independent of Mg^{2+} concentration (data not shown). This observation is consistent with weak formation constants of APS with Mg^{2+} (*50*) and the general observation that other sulfonucleotide binding enzymes, such sulfokinases and sulfotransferases also do not require Mg^{2+} as a cofactor (*10*). However, Mg•ADP and Mg•AMP complexes bind approximately 5-6 times weaker to APR, as compared to the free nucleotide (Appendix 3.6.6). The observed reduction in binding energy is most likely due to repelling interactions with multiple positively charged amino acids in the enzyme active site, such as Lys144, Arg242 and Arg245 (Figure 3.3). Together, these findings indicate that APR discriminates against noncognate adenosine nucleotides through favourable interactions with the sulfate moiety of APS and by disfavouring the binding of Mg^{2+}-nucleotide complexes.

3.4 Conclusion: Implications for Rational Inhibitor Design

Given that APR is essential for mycobacterial survival during persistent infection (*51*), small-molecule inhibitors of APR might be a source for new drugs to treat latent tuberculosis infection. The increasing number of antibiotic-resistant strains suggests that the availability of such compounds could play an important role in treating the disease and minimizing the negative impact on human health. By defining chemical groups that are essential for molecular recognition, the work described here sets the stage for the development of such drugs. Figure 3.8 summarizes the network of interactions predicted to occur between APR active site residues and substrate, APS. The structural model was constructed by homology to ScPAPR (*14*) and systematically

56
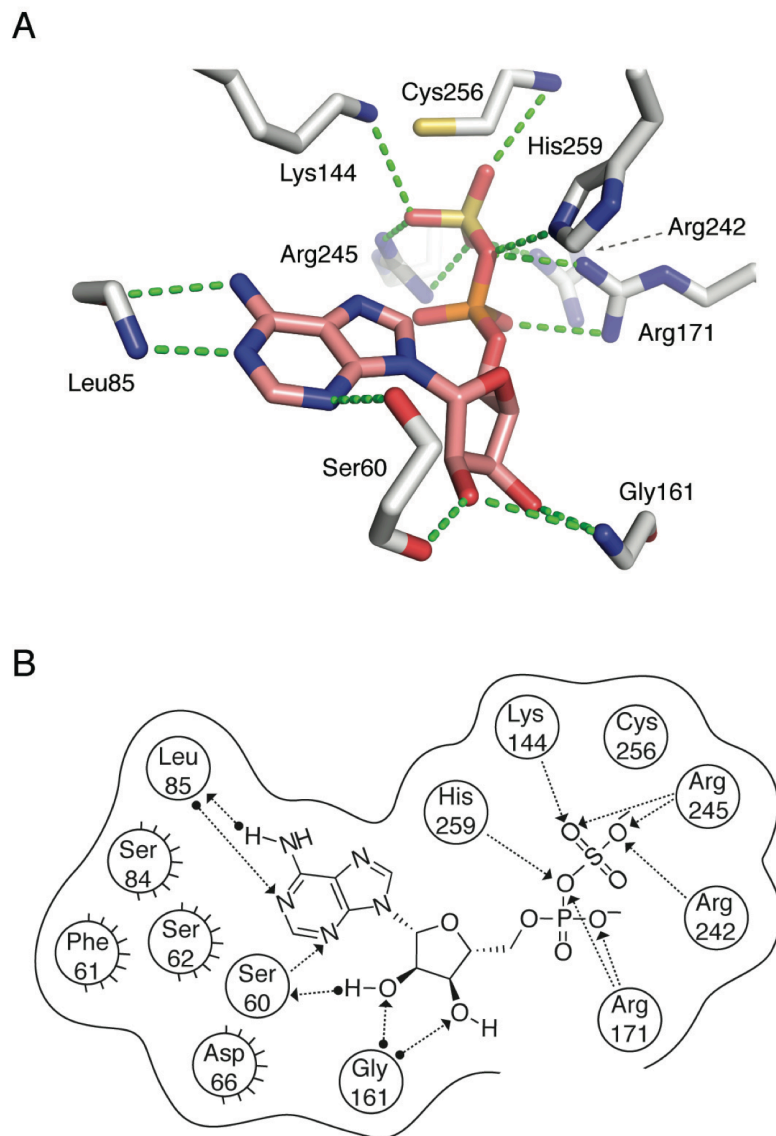
Figure 3.8. APS reductase interactions with substrate, APS inferred from *P. aeruginosa* APS reductase (PDB deposition 2GOY) and *S. cerevisiae* PAPS reductase (PDB deposition 2OQ2) structures and functional data obtained in the present study. (A) Summary of proposed active site contacts to APS. (B) Summary of proposed active site contacts to APS, plotted in two dimensions. A total of nine protein residues are shown in proximity around the ligand, with hydrogen bonding interactions shown where detected. Hydrogen bonds are draw as dotted lines with arrows denoting the direction of the bond. Interactions from substrate or the residue backbones of the enzyme are distinguished from the interactions with residue side chains by a solid dot at the end of the interaction line. Active site residues between *P. aeruginosa* and *M. tuberculosis* APS reductase are largely conserved, with the exception of residues implicated in hydrophobic interactions (Ser62 to Met67, Ser84 to Phe87, Phe61 to Asn66). The corresponding numbers for residues conserved between *M. tuberculosis* and *P. aeruginosa* APS reductase are: Ser65 (Ser60), Leu88 (Leu85), Lys145 (Lys144), Gly162 (Gly161), Arg171 (Arg171), Arg237 (Arg242), Arg240 (Arg245) Cys249 (Cys256), and His252 (His259). See also Appendix 3.6.1.

tested in the present study, from the perspective of the ligand. The total binding energy

of APS resulting from these collective interactions is 9.3 kcal/mol and our data indicate several features that are essential for optimized substrate and inhibitor binding. The hydrophobic adenine-binding pocket, pyrimidine ring, 2'-hydroxyl and the α-position are the main determinants for strong target affinity (Figure 3.9). The significant losses of binding affinity that are found to result from apparently minor structural modifications of ligands at these key positions have encouraging implications for inhibitor design and suggests that, in some cases, the potency of a weak inhibitor might be greatly enhanced by one or two simple modifications. Our studies also suggest that small-molecules that target dynamic elements within the active site – particularly Arg171, Cys256 and His259 – may lead to inhibitors with improved binding affinity. Alternatively, molecules that trap an inactive, "open" conformational state of APR may also represent new opportunities for inhibitor design (*16*).

Figure 3.9. Pharmacophore model of substrate, APS. Chemical structure of APS highlighting key hydrogen bond accepting (HBA) and donating (HBD) interactions, ionic interactions, and van der Waals interaction, based on functional data obtained in the present study.
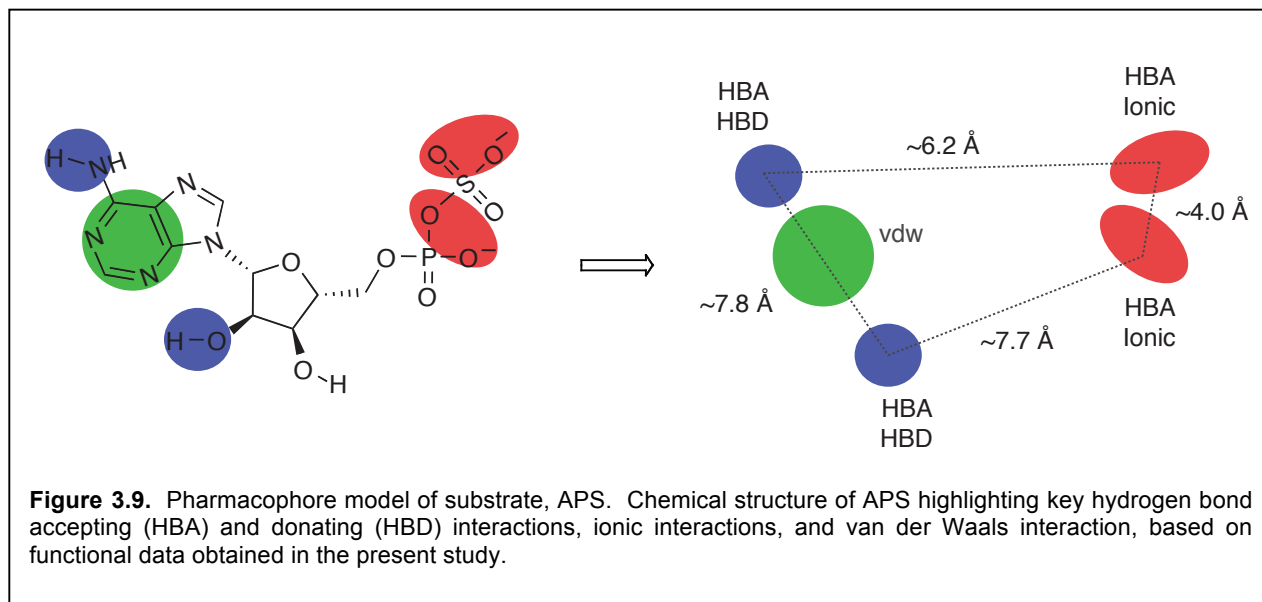
3.5 Experimental Procedures

3.5.1 Materials

Inosine, adenosine, 2-aminoadenosine, 3'-deoxyadenosine, 2'-deoxyadenosine and 1-methyladenosine were purchased from Sigma. 5'-Phosphoribose, 3'-phosphoadenosine,

3'5'-diphosphoadenosine, adenine and ribose were also purchased from Sigma. 7-Deazaadenosine-5-*O*-monophosphate and purine riboside-5'-*O*-monophosphate were from Biology Life Science Institute. Nucleosides and other analogs were of the highest purity available, typically ≥ 98%. Additional reagents and solvents were purchased from Sigma or other commercial sources and were used without further purification.

3.5.2 General Synthetic Methods

Reactions that were moisture sensitive or using anhydrous solvents were performed under a nitrogen or argon atmosphere. Analytical thin layer chromatography (TLC) was performed on pre-coated silica plates obtained from Analtech. Visualization was accomplished with UV light or by staining with ethanolic H_2SO_4 or ceric ammonium molybdate. Nucleosides were purified by flash chromatography using Merck silica gel (60-200 mesh).

3.5.3 Preparation of Nucleoside and Nucleotide Analogs

N^6, N^6-Dimethyl-5'-phosphoadenosine was prepared from inosine by the procedure described by Veliz and Beal (*52*) and purified by flash chromatography developed in 60:40 ethyl acetate:hexanes. N^6-Methyl-5'-phosphoadenosine was prepared via reaction of 6-bromoinosine with methylamine as previously described (*53*). 8-Amino-5'-phosphoadenosine was prepared by selective bromination of adenosine at the C8 position, exchange of bromine for azide, followed by reductive hydrogenation to afford the amine, as previously described (*54*). 2'-Methoxy-5'-phosphoadenosine was prepared from adenosine, by reaction with methyl iodide under alkaline conditions as previously described (*55*). Adenosine 5'-O-α,β,-imidodiphosphate (AMPNP) was synthesized by reaction of 5'-tosyladenosine (*56*) with imidodiphosphate salt (*56, 57*). Adenosine 5'-O-α,β-difluoromethylenediphosphate (ADPβF) was prepared by coupling

5'-tosyladenosine to difluoro substituted methylenediphosphonic acid, as previously reported (*56, 58*). Adenosine 5'-O-thiophosphosulfate (APSαS) was synthesized by reacting pyridine-N-sulfonic acid with adenosine 5'-O-thiopshophate (AMPS), as previously described (*59*).

3.5.4 Nucleoside Phosphorylation

Nucleotide analogs were synthesized by chemical phosphorylation of the corresponding adenosine analog, followed by purification via reversed phase HPLC. Nucleosides were phosphorylated by reaction of nucleoside with $POCl_3$ as described (*60*). The nucleoside (0.15 mmole) was suspended in triethylphosphate at 0 °C (0.65 ml). Water (1 equiv) was added to the reaction. Subsequently, $POCl_3$ (3-5 equivalents) were added over a period of 30 min with constant stirring. The suspension was kept stirring for an additional 1.5 h, when the white suspension became a clear solution. Water (1 ml) was added to hydrolyze the phosphoryl chloride and terminate the reaction. The pH was neutralized to ~7 by dropwise addition of NH_4OH. The reaction was passed over a C18 SPE column (Fisher) to remove the majority of the triethylphosphate. Nucleotides were purified by reversed phase HPLC employing isocratic separation in 20 mM ammonium acetate, pH 7 on a semi-preparative C18 column. The physical and spectral data for these analogs (confirmed by ^1H, ^{13}C and ^{31}P NMR and mass spectrometry) were consistent with those previously reported for these compounds. The concentrations nucleotide analogs was determined by absorbance at 260 nm, assuming ε_{260} = 15,300 M^{-1} cm^{-1} (*23*).

3.5.5 Enzyme purification.

Purification of APR was carried out as previously described (*61*).

3.5.6 General Kinetic Methods.

[35]S-labeled APS was synthesized and purified as previously described (*61*) with the inclusion of an additional anion exchange purification step on a 5-ml FFQ column (GE Healthcare) eluting with a linear gradient of ammonium bicarbonate, pH 8.0. The reduction of APS to sulfite and AMP was measured in a ^{35}S-based assay as previously described (*62*). Reactions were quenched by the addition of charcoal solution (2% w/v) containing Na_2SO_3 (20 mM). The suspension was vortexed, clarified by centrifugation and an aliquot of the supernatant containing the radiolabeled sulfite product was counted in scintillation fluid. APR activity was measured in single turnover reactions, with trace amounts of ^{35}S-APS (~1 nM) and excess protein. These reactions can typically be followed to ≥90% completion (Appendix 3.6.5), and the reaction time courses fit well to eq 1, in which Frac P is the fraction product, *k* is the observed rate constant, and *t* is time:

$$Frac\ P = 1 - \exp^{-k_{obs}t} \qquad (1)$$

Unless otherwise specified, the standard reactions conditions were 30 °C with 100 mM bis-tris propane at pH 7.5, DTT (5 mM), and thioredoxin (10 μM). Kinetic data were measured in at least two independent experiments and the standard error was typically less than 15%.

The affinity of APR (E) for APS was determined from the dependence of the observed rate constant for *S*-sulfocysteine formation on protein concentration according to eq 2:

$$K_{obs} = K_{max} \times \left(\frac{[E]}{K_{1/2} + [E]} \right) \qquad (2)$$

In this equation, k_{obs} is the observed rate constant at a particular protein concentration, k_{max} is the maximal rate constant with saturating protein, and $K_{1/2}$ is the protein concentration that provides half the maximal rate. To ensure that the chemical step was rate-determining, reactions were performed in NaMes (10 mM) at pH 5.5 and control experiments demonstrate that the enzyme is stable under these assay conditions (data not shown). Because the chemical step is rate-determining for *S*-sulfocysteine formation ($k_{st} <$, k_{max} is equal to the rate constant for the reaction of the E•APS complex, and $K_{1/2}$ is equal to the dissociation constant (K_d) of APS for APR. The concentration of active protein was determined by direct titration with a high concentration of APS (*i.e.* [APS] >> K_d). In theory, the binding affinity of APS could increase at physiological pH. However, several lines of evidence argue against this possibility. First, the pK_a of the β-sulfate moiety is less than 2 and thus, at pH 5.5, the sulfonucleotide is completely ionized. Second, the pH dependence of ADP binding (see below) reflects the pK_a of this nucleotide in solution. Finally, the K_d measured at pH 5.5 is in line with the apparent K_m value measured at pH 8.0 (*22*).

The affinity of various ligands for APR was determined by inhibition methods. The observed rate constant of the reaction: E + ^{35}S-APS → products (k_{obs}) was determined at varying inhibitor (I) concentrations (Appendix 3.6.4B), and the [I]-dependence was fit to a simple model for competitive inhibition (eq 3). In eq 3, k_o is the rate of the reaction in the absence of analog, and K_i is the inhibition constant of the analog. With subsaturating APR, K_i is equal to the equilibrium dissociation constant (K_d) of the ligand.

$$k_{obs} = k_o \times \left(\frac{K_i}{[I] + K_i} \right) \qquad (3)$$

3.5.7 pH Dependence of Inhibitor Binding.

Values of K_i were determined by inhibition of APS reduction (pH 6-9) with [^{35}S-APS] <<

$K_{1/2}$, such that K_i is expected to be the K_d. The following buffers were used for the

indicated pH ranges: NaMES (6.0-7.0), Bis-Tris (6.5-7.5), Tris (7.5-9.0) and CAPS (9.0-

9.5). Reactions were typically carried out with 100 mM buffer and the standard assays

and conditions described above were used to monitor k_{cat}/K_m for reduction of ^{35}S-APS in

the presence and absence of inhibitor. The rate constants at each pH value for multiple

reactions were averaged, and the standard deviations were ≤15% of the average. pK_a

values were determined using eq 4, derived from a model where the binding of the

ligand depends on a single ionizable group.

$$K_{d,app} = K_d^{HA} \times \frac{K_a}{K_a + [H^+]} + K_d^{A-} \times \frac{[H^+]}{K_a + [H^+]} \qquad (4)$$

3.5.8 Energetic Contribution of Ligand Substituents to Binding.

The energetic contributions of individual ligand substitutents to APR binding were

expressed as $\Delta\Delta G = -RT\ln(K_d1/K_d2)$ in which R is the gas constant, T is the temperature

(303 K), and K_d is the equilibrium dissociation constant. A negative value of $\Delta\Delta G$

indicates that a given substitutent contributes to ligand binding by APR.

3.5.9 Electrostatic Surface Potentials.

The electrostatic surface potential was calculated using PM3 semi-empirical molecular

orbital calculations implemented in SPARTAN software (Wavefunction, Inc) for the fully

optimized structure.

3.6 Appendices

Figure 3.6.1 Structure based sequence alignment of APR from *Pseudomonas aeruginosa, Mycobacterium tuberculosis* and *Saccharomyces cerevisiae*.

The ClustalW Multiple Sequence Alignment program was used. Strictly conserved residues are outlined in red, red letters indicate conserved residues and conserved regions are boxed in blue. Alignment picture was rendered with the server ESPript 2.2 (http://espript.ibcp.fr).

```
                                                          α1                α2              β1
Pseudomonas_aeruginosa                                 ℓℓℓℓℓℓℓℓ      ℓℓℓℓℓℓℓℓℓℓ        ←        ℓ
Pseudomonas_aeruginosa      1 ...MLPFATIPATERNSAAQHQDPSPMSQPFDLPALASSLADKSPQDILKAAFEHFGDELWISFSGAEDV
Mycobacterium_tuberculosis  1 MSGETTRLTEPQLRELAARGAAELDGATATDMLRWTDETFGDIGGAGGGVSGHRGWTTCNYVVASNMADA
Saccharomyces_cerevisiae    1 ...............MKTYHLNNDIIVTQEQLDHWNEQLIKLETPQEIIAWSIVTFPHLFQTTAFGLTGL

                                 α3             β2          α4                 β3        α5
Pseudomonas_aeruginosa       ℓℓℓℓℓℓℓℓℓ       ←        ℓℓℓℓℓℓℓℓℓℓℓℓ          ←      ℓℓℓℓℓℓℓℓℓ   ℓ
Pseudomonas_aeruginosa     68 VLVDMAWKLNRN...VKVFSLDTGRLHPETYRFIDQVREHYG....IAIDVLSPDPRLLEPLVKEKGLFS
Mycobacterium_tuberculosis 71 VLVDLAAKVRPG...VPVIFLDTGYHFVETIGTRDAIESVYD....VRVLNVTPEHTVAE.QDELLGKDL
Saccharomyces_cerevisiae   56 VTIDMLSKLSEKYYMPELLFIDTLHHFPQTLTLKNEIEKKYYQPKNQTIHVYKPDGCESEADFASKYGDF

                                 α6       α7         α8        β4     η1        β5           β6
Pseudomonas_aeruginosa       ℓℓℓℓ   ℓℓℓℓℓℓℓ   ℓℓℓℓℓℓℓ     ←     ℓℓℓ      ←   TTT        ←
Pseudomonas_aeruginosa    131 FYRDGHGECCGIRKIEPLKRKLAGVRAWATGQ.RRDQSPGTRSQVAVLEIDGAFSTPEKPLYKFNPLSSM
Mycobacterium_tuberculosis 133 FARNPH.ECCRLRKVVPLGKTLRGYSAWVTGL.RRVDAP.TRANAPLVSFDETFK.....LVKVNPLAAW
Saccharomyces_cerevisiae   126 LWEKDDDKYDYLAKVEPAHRAYKELHISAVFTGRRKSQGSARSQLSIIEIDELNG.....ILKINPLINW

                                 α9          η2          η3      TT   η4     TT
Pseudomonas_aeruginosa       ℓℓℓℓℓℓℓℓℓℓ      ℓℓℓℓℓ      ℓℓℓ        ℓℓℓℓ
Pseudomonas_aeruginosa    200 TSEEVWGYIRMLELPYNSLHERGYISIGCEPCTRPVLPNQHEREGRWWWEEATHKECGLHAGNLISKA..
Mycobacterium_tuberculosis 195 TDQDVQEYIADNDVLVNPLVREGYPSIGCAPCTAKPAEGADPRSGRWQGLAKT..ECGLHASLE......
Saccharomyces_cerevisiae   191 TFEQVKQYIDANNVPYNELLDLGYRSIGDYHSTQPVKEGEDERAGRWKGKAKT..ECGIHEASRFAQFLK

Pseudomonas_aeruginosa

Pseudomonas_aeruginosa          ...
Mycobacterium_tuberculosis      ...
Saccharomyces_cerevisiae    259 QDA
```

64

Figure 3.6.2 The apparent affinity, $K_{1/2}$, of APR in single turnover experiment.

The affinity of APR (E) for APS was determined from the dependence of the observed rate constant for *S*-sulfocysteine formation on protein concentration according to:

$$K_{obs} = K_{max} \times \left(\frac{[E]}{K_{1/2} + [E]} \right)$$

In this equation, k_{obs} is the observed rate constant at a particular protein concentration, k_{max} is the maximal rate constant with saturating protein, and $K_{1/2}$ is the protein concentration that provides half the maximal rate. Because the chemical step is rate-determining for *S*-sulfocysteine formation, k_{max} is equal to the rate constant for the reaction of the E•APS complex, and $K_{1/2}$ is equal to the dissociation constant (K_d) of APS for APR. The concentration of active protein was determined by direct titration with a high concentration of APS (*i.e.* [APS] >> K_d).
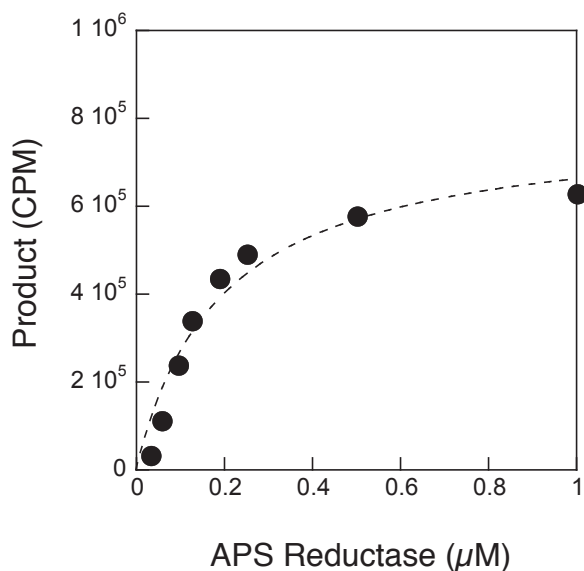
Figure 3.6.3 pH dependence for ADPβS (A) and AMPS (B) binding.

The association equilibrium constant, ($K_a = 1/K_d$) is plotted as a function of pH. Values of K_d were determined by inhibition of APS reduction (pH 6.0-9.5). See methods for details. (A) The pH dependence for ADPbS binding. Nonlinear-least-squares fit of the data to a model for a single ionization gave pK_a values of 5.8 ± 0.15. The pK_a of AD Implications for rational inhibition design PbS in solution is 5.2 (*34*). (B) The pH dependence for AMPS binding. The dashed line represents the best fit of a model for a single ionization and yields a pK_a of 7.7 ± 0.15. The pKa of AMPS in solution is 5.3 (*34*).

A

B

67
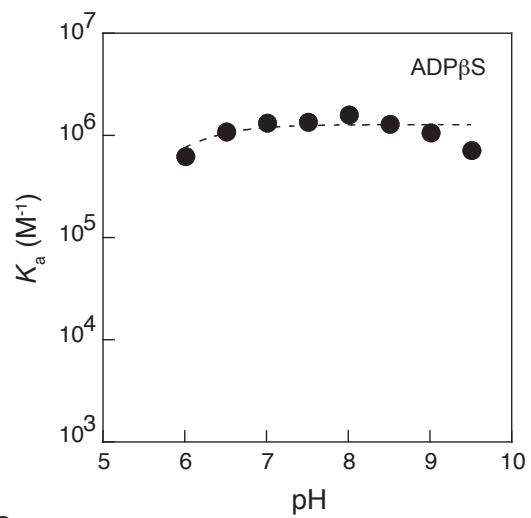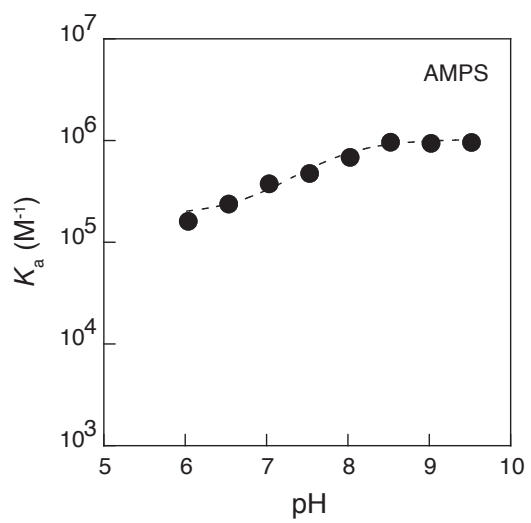
Figure 3.6.4 The radioactive assay for APR.

(A) The reaction progress curve for APR. Under the subsaturating concentration of substrate, the reaction is described by the apparent second-order rate constant, k_{cat}/K_m, which under the conditions of this assay is ~2×10^6 M^{-1}s^{-1}. (B) AMP inhibits APR activity. Nonlinear least squares fit to a model of competitive inhibition gives a K_d value of 5.4 μM.

A
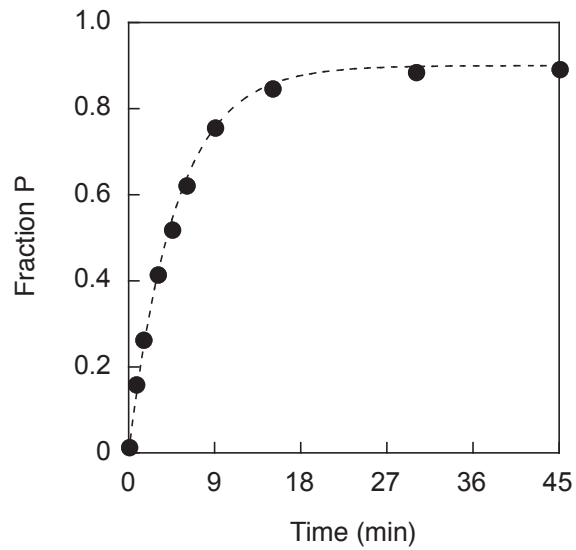
B
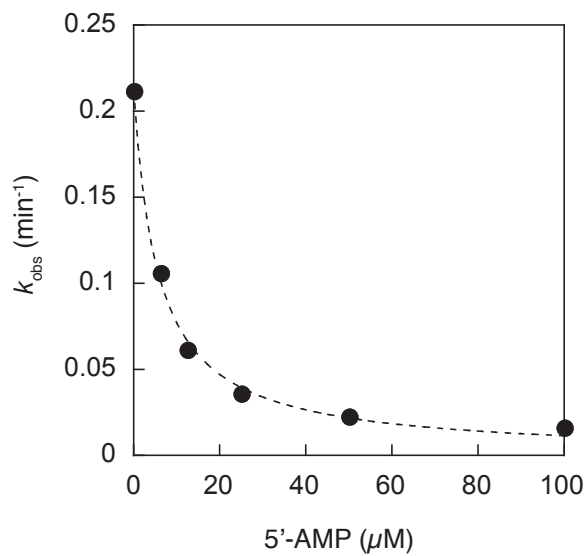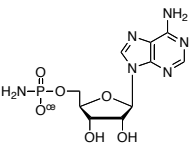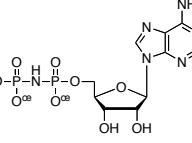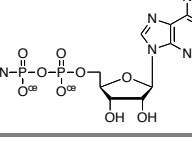
Table 3.6.5 Ligand dissociation constants for nitrogen-containing ligands at pH 7.5 and pH 9.0 with APR.[a]

Ligand	Structure	K_d pH 7.5 [μM]	K_d pH 9.0 [μM]	$\Delta\Delta G$ [kcal/mol][b]	pKa
5'-AMPN		100	82	-0.16	3.0 (O), 8.15 (N)[c]
AMPNP		257	110	-0.53	7.7 (O), 8.25 (N) (*39*)
AMPPN		410	56.8	-1.2	3.0 (O), 8.15 (N)[c]

[a] For ligands in this table values of K_i were determined at pH 7.5 or 9.0 under single turnover conditions from the dependence of the observed rate constant at a given inhibitor concentration under conditions of subsaturating APS, such that K_i is equal to the K_d. Each value reflects the average of at least two independent experiments, and the standard deviation was less than 15% of the value of the mean. Kinetic data were nonlinear-least squares fit to a model of competitive inhibition. [b] Energetic difference in affinity of ligand at pH 9.0 relative to pH 7.5, $\Delta\Delta G$ = $-RT\ln(K_d^{9.0}/K_d^{7.5})$. [c] p$K_a$ estimate approximated from value for phosphoramidic acid (*41*).

Table 3.6.6 Ligand dissociation constants for AMP and ADP with APR in the presence and absence of MgCl$_2$. [a]

Ligand	MgCl$_2$ [mM]	K_d [μM]	$\Delta\Delta$G [kcal/mol][b]
AMP	0	5.4	N/A
	0.5	21	0.82
	2.0	31	1.0
ADP	0	4.3	N/A
	0.5	7.3	0.32
	2.0	20	0.93

[a] For ligands in this table values of K_i were determined at pH 7.5 and the concentration of MgCl$_2$ indicated under single turnover conditions from the dependence of the observed rate constant at a given inhibitor concentration under conditions of subsaturating APS, such that K_i is equal to the K_d. Each value reflects the average of at least two independent experiments, and the standard deviation was less than 15% of the value of the mean. Kinetic data were nonlinear-least squares fit to a model of competitive inhibition. [b] Energetic difference in affinity for ligand with magnesium relative to without metal ion, $\Delta\Delta$G = $-RT$ln($K_d^{+MgCl_2}/K_d^{-MgCl_2}$).

3.7 Reference

1.   Schelle, M. W., and Bertozzi, C. R. (2006) Sulfate metabolism in mycobacteria, *Chembiochem 7*, 1516-1524.

2.   Michell, S. (1996) Biological interractions of sulfur compounds, In *Biology of sulfur* (Michell, S., Ed.), pp 20-41, CRC Press, New York.

3.   Kredich, N. M. (1996) *Escherichia coli* and *Samonella*: Cellular and Molecular Biology, In *Biosynthesis of cysteine* (Niedhardt, F. C., and Curtiss, R., Eds.) 2nd ed., pp 514-527, ASM Press, Washington, D. C. .

4.   Giles, N. M., Watts, A. B., Giles, G. I., Fry, F. H., Littlechild, J. A., and Jacob, C. (2003) Metal and redox modulation of cysteine protein function, *Chem. Biol. 10*, 677-693.

5.   Williams, S. J., Senaratne, R. H., Mougous, J. D., Riley, L. W., and Bertozzi, C. R. (2002) 5'-adenosinephosphosulfate lies at a metabolic branch point in mycobacteria, *J. Biol. Chem. 277*, 32606-32615.

6.   Kopriva, S., Buchert, T., Fritz, G., Suter, M., Benda, R., Schunemann, V., Koprivova, A., Schurmann, P., Trautwein, A. X., Kroneck, P. M., and Brunold, C. (2002) The presence of an iron-sulfur cluster in adenosine 5'-phosphosulfate reductase separates organisms utilizing adenosine 5'-phosphosulfate and phosphoadenosine 5'-phosphosulfate for sulfate assimilation, *J. Biol. Chem. 277*, 21786-21791.

7.   Bhave, D. P., Muse, W. B., 3rd, and Carroll, K. S. (2007) Drug targets in mycobacterial sulfur metabolism, *Infect. Disord. Drug Targets 7*, 140-158.

8.   Mdluli, K., and Spigelman, M. (2006) Novel targets for tuberculosis drug discovery, *Curr. Opin. Pharmacol. 6*, 459-467.

9.   Senaratne, R. H., De Silva, A. D., Williams, S. J., Mougous, J. D., Reader, J. R., Zhang, T., Chan, S., Sidders, B., Lee, D. H., Chan, J., Bertozzi, C. R., and Riley, L. W. (2006) 5'-Adenosinephosphosulphate reductase (CysH) protects *Mycobacterium tuberculosis* against free radicals during chronic infection phase in mice, *Mol. Microbiol. 59*, 1744-1753.

10.   Carroll, K. S., Gao, H., Chen, H., Leary, J. A., and Bertozzi, C. R. (2005) Investigation of the iron-sulfur cluster in *Mycobacterium tuberculosis* APS reductase: implications for substrate binding and catalysis, *Biochemistry 44*, 14647-14657.

11.   Carroll, K. S., Gao, H., Chen, H., Stout, C. D., Leary, J. A., and Bertozzi, C. R. (2005) A conserved mechanism for sulfonucleotide reduction, *PLoS Biol. 3*, e250.

12.   Chartron, J., Carroll, K. S., Shiau, C., Gao, H., Leary, J. A., Bertozzi, C. R., and Stout, C. D. (2006) Substrate recognition, protein dynamics, and iron-sulfur cluster in *Pseudomonas aeruginosa* adenosine 5'-phosphosulfate reductase, *J. Mol. Biol. 364*, 152-169.

13.   Chapman, E., Best, M. D., Hanson, S. R., and Wong, C. H. (2004) Sulfotransferases: structure, mechanism, biological activity, inhibition, and synthetic utility, *Angew. Chem. Int. Ed. Engl. 43*, 3526-3548.

14. Yu, Z., Lemongello, D., Segel, I. H., and Fisher, A. J. (2008) Crystal structure of *Saccharomyces cerevisiae* 3'-phosphoadenosine-5'-phosphosulfate reductase complexed with adenosine 3',5'-bisphosphate, *Biochemistry 47*, 12777-12786.

15. Young, D. B., Gideon, H. P., and Wilkinson, R. J. (2009) Eliminating latent tuberculosis, *Trends Microbiol. 17*, 183-188.

16. Lee, G. M., and Craik, C. S. (2009) Trapping moving targets with small molecules, *Science 324*, 213-215.

17. Liu, Y., and Gray, N. S. (2006) Rational design of inhibitors that bind to inactive kinase conformations, *Nat. Chem. Biol. 2*, 358-364.

18. Palomino, J. C., Ramos, D. F., and da Silva, P. A. (2009) New anti-tuberculosis drugs: strategies, sources and new molecules, *Curr. Med. Chem. 16*, 1898-1904.

19. Hugonnet, J. E., Tremblay, L. W., Boshoff, H. I., Barry, C. E., 3rd, and Blanchard, J. S. (2009) Meropenem-clavulanate is effective against extensively drug-resistant *Mycobacterium tuberculosis*, *Science 323*, 1215-1218.

20. Nguyen, L., and Pieters, J. (2009) Mycobacterial subversion of chemotherapeutic reagents and host defense tactics: challenges in tuberculosis drug development, *Annu. Rev. Pharmacol. Toxicol. 49*, 427-453.

21. Cosconati, S., Hong, J. A., Novellino, E., Carroll, K. S., Goodsell, D. S., and Olson, A. J. (2008) Structure-based virtual screening and biological evaluation of *Mycobacterium tuberculosis* adenosine 5'-phosphosulfate reductase inhibitors, *J. Med. Chem. 51*, 6627-6630.

22. Sun, M., and Leyh, T. S. (2006) Channeling in sulfate activating complexes, *Biochemistry 45*, 11304-11311.

23. Dawson, R. M. C., Elliott, D. C., Elliott, W. H., and Jones, K. M. (1989) *Data for Biochemical Research*, 3 ed., Oxford University Press, Oxford.

24. Chargaff, E., and Davidson, J. N. (1955) *The Nucleic Acids I*, Academic Press New York.

25. Kumler, W. D., and Eiler, J. J. (1943) The acid strength of mono and diesters of phosphoric acid. The n-alkyl esters from methyl to butyl, the esters of biological importance, and the natural guanidine phosphoric acids, *J. Am. Chem. Soc. 65*, 2355-2361.

26. Isbell, H. S. (1973) *Carbohydrate in Solution*, American Chemical Society, Wachington, DC.

27. Chang, R. (2005) Acids and bases, In *General Chemistry* 8 ed., McGraw-Hill.Inc, New York.

28. Hirota, K., Inoue, Y., and Chujo, R. (1984) Effect of the base stacking association on the phosphate ionization of 2'-deoxyguanosine 5'-monophosphate, *Bull. Chem. Soc. Jpn. 57*, 247-250.

29. Falany, C. N. (1997) Enzymology of human cytosolic sulfotransferases, *Faseb. J. 11*, 206-216.

30. Dzingeleski, G. D., and Wolfenden, R. (1993) Hypersensitivity of an enzyme reaction to solvent water, *Biochemistry 32*, 9143-9147.

31. Carlow, D., and Wolfenden, R. (1998) Substrate connectivity effects in the transition state for cytidine deaminase, *Biochemistry 37*, 11873-11878.

32. Nikolic-Hughes, I., Rees, D. C., and Herschlag, D. (2004) Do electrostatic interactions with positively charged active site groups tighten the transition state for enzymatic phosphoryl transfer?, *J. Am. Chem. Soc. 126*, 11814-11819.

33. (1994-1995) *CRC Handbook of Chemistry and Physics*, 75 ed., CRC Press, Boca Raton, FL.

34. Jaffe, E. K., and Cohn, M. (1978) ^{31}P nuclear magnetic resonance spectra of the thiophosphate analogues of adenine nucleotides; effects of pH and Mg^{2+} binding, *Biochemistry 17*, 652-657.

35. Frey, P. A., and Sammons, R. D. (1985) Bond order and charge localization in nucleoside phosphorothioates, *Science 228*, 541-545.

36. Satishchandran, C., Myers, C. B., and Markham, G. D. (1992) Adenosine-5'-O-(2-fluorodiphosphate) (ADP-β-F), an analog of adenosine-5'-phosphosulfate, *Bioorganic Chem. 20*, 107-114.

37. Cullis, P. M., Maxwell, A., and Weiner, D. P. (1992) Energy coupling in DNA gyrase: a thermodynamic limit to the extent of DNA supercoiling, *Biochemistry 31*, 9642-9646.

38. Vogel, H. J., and Bridger, W. A. (1982) Phosphorus-31 nuclear magnetic resonance studies of the methylene and fluoro analogues of adenine nucleotides. Effects of pH and magnesium ion binding, *Biochemistry 21*, 394-401.

39. Reynolds, M. A., Gerlt, J. A., Demou, P. C., Oppenheimer, N. J., and Kenyon, G. L. (1983) N-15 and O-17 NMR-Studies of the Proton Binding-Sites in Imidodiphosphate, Tetraethyl Imidodiphosphate, and Adenylyl Imidodiphosphate, *J. Am. Chem. Soc. 105*, 6475-6481.

40. Rye, C. S., and Baell, J. B. (2005) Phosphate isosteres in medicinal chemistry, *Curr. Med. Chem. 12*, 3127-3141.

41. Chanley, J. D., and Feageson, E. (1963) A study of hydrolysis of phosphoramides .2. Solvolysis of phosphoramidic acid and comparison with phosphate esters, *J. Am. Chem. Soc. 85*, 1181-1190.

42. Gregoret, L. M., Rader, S. D., Fletterick, R. J., and Cohen, F. E. (1991) Hydrogen bonds involving sulfur atoms in proteins, *Proteins 9*, 99-107.

43. Yount, R. G., Babcock, D., Ballantyne, W., and Ojala, D. (1971) Adenylyl imidodiphosphate, an adenosine triphosphate analog containing a P--N--P linkage, *Biochemistry 10*, 2484-2489.

44. Larsen, M., Willett, R., and Yount, R. G. (1969) Imidodiphosphate and pyrophosphate: possible biological significance of similar structures, *Science 166*, 1510-1511.

45. Singer, B. (1989) Nucleosides, nucleotides, and nucleic acids, In *Practical Handbook of Biochemistry and Molecular Biology* (Fasman, G. D., Ed.) 2 ed., pp 392-393, CRC Press, Cleveland.

46. Savage, H., Montoya, G., Svensson, C., Schwenn, J. D., and Sinning, I. (1997) Crystal structure of phosphoadenylyl sulphate (PAPS) reductase: a new family of adenine nucleotide alpha hydrolases, *Structure 5*, 895-906.

47. O'Hagan, D. (2008) Understanding organofluorine chemistry. An introduction to the C-F bond, *Chem. Soc. Rev. 37*, 308-319.

48. Harris, D. A. (1996) Cell chemistry and physiology: part II, In *Principles of Medical Biology* (Bittar, E. E., and Bittar, N., Eds.), p 27, Elsevier, Conneticut.

49. Storer, A. C., and Cornish-Bowden, A. (1976) Concentration of MgATP^{2-} and other ions in solution. Calculation of the true concentrations of species present in mixtures of associating ions, *Biochem. J. 159*, 1-5.

50. Yount, R. G., Simchuck, S., Yu, I., and Kottke, M. (1966) Adenosine-5'-sulfatopyrophosphate, an analogue of adenosine triphosphate. I. Preparation, properties, and mode of cleavage by snake venoms, *Arch. Biochem. Biophys. 113*, 288-295.

51. Senaratne, R. H., De Silva, A. D., Williams, S. J., Mougous, J. D., Reader, J. R., Zhang, T., Chan, S., Sidders, B., Lee, D. H., Chan, J., Bertozzi, C. R., and Riley, L. W. (2006) 5'-Adenosinephosphosulphate reductase (CysH) protects *Mycobacterium tuberculosis* against free radicals during chronic infection phase in mice, *Mol. Microbiol. 59*, 1744-1753.

52. Veliz, E. A., and Beal, P. A. (2000) C6 substitution of inosine using hexamethylphosphorous triamide in conjunction with carbon tetrahalide or *N*-halosuccinimide, *Tet. Lett. 41*, 1695-1697.

53. Veliz, E. A., and Beal, P. A. (2001) 6-bromopurine nucleosides as reagents for nucleoside analogue synthesis, *J. Org. Chem. 66*, 8592-8598.

54. Townsend, L. B., and Tipson, R. S. (1978) *Nucleic Acid Chemistry:Improved and New Synthetic Procedures, Methods, and Techniques*, Vol. II, Wiley, New York.

55. Yano, J., Kan, L. S., and Ts'o, P. O. P. (1980) A simple method for the preparation of adenosine with methyl iodide in anhydrous alkaline medium, *Biochim. Biophys. Acta. 629*, 178-183.

56. Davisson, V. J., Davis, D. R., Dixit, V. M., and Poulter, C. D. (1987) Synthesis of Nucleotide 5'-Diphosphates from 5'-O-Tosyl Nucleosides, *J. Org. Chem. 52*, 1794-1801.

57. Ma, Q., Babbitt, P. C., and Kenyon, G. L. (1988) Adenosine 5'-[α,β-imido]triphosphate, a substrate for T7 RNA-polymerase and rabbit muscle creatine-kinase, *J. Am. Chem. Soc. 110*, 4060-4061.

58. Mohamady, S., and Jakeman, D. L. (2005) An improved method for the synthesis of nucleoside triphosphate analogues, *J. Org. Chem. 70*, 10588-10591.

59. Zhang, H. P., and Leyh, T. S. (1999) alpha-Thio-APS: A stereomechanistic probe of activated sulfate synthesis, *J. Am. Chem. Soc. 121*, 8692-8697.

60. Yoshikawa, M., Kato, T., and Takenishi, T. (1967) A novel method for phosphorylation of nucleosides to 5'-nucleotides, *Tet. Lett. 50*, 5065-5068.

61. Carroll, K. S., Gao, H., Chen, H., Stout, C. D., Leary, J. A., and Bertozzi, C. R. (2005) A conserved mechanism for sulfonucleotide reduction, *PLoS Biol. 3*, e250.

62. Gao, H., Leary, J., Carroll, K. S., Bertozzi, C. R., and Chen, H. Y. (2007) Noncovalent complexes of APS reductase from M-tuberculosis: Delineating a mechanistic model using ESI-FTICR MS, *J. Am. Soc. Mass Spectrom. 18*, 167-178.

Chapter 4

Deciphering the role of histidine 252 in mycobacterial adenosine 5'-phosphosulfate reductase catalysis

4.1 Abstract

Mycobacterium tuberculosis adenosine 5'-phosphosulfate reductase (APR) catalyzes the first committed step in sulfate reduction for the biosynthesis of cysteine and is essential for survival in the latent phase of TB infection. The reaction catalyzed by APR involves the nucleophilic attack by a conserved cysteine residue, Cys249 on adenosine 5'-phosphosulfate (APS), resulting in a covalent *S*-sulfocysteine intermediate that is reduced in subsequent steps by thioredoxin to yield the sulfite product. Cys249 resides on a mobile active site lid at the C-terminus, within a ECG(L/I)H motif. Owing to its strict conservation among sulfonucleotide reductases and its proximity to the active site cysteine, it has been suggested that His252 plays a key role in APR catalysis, specifically as a general base to deprotonate Cys249. Using site-directed mutagenesis we have changed His252 to an alanine residue and analyzed the effect of this mutation on the kinetic parameters, pH-rate profile and ionization of Cys249 of APR. These

75

findings were further supported by isothermal titration calorimetry (ITC) to provide a thermodynamic profile of ligand-protein interactions. Interestingly, our data demonstrate that His252 does not perturb the pK_a of Cys249 or play a direct role in rate-limiting chemical steps of the reaction. Rather, we show that His252 enhances substrate affinity *via* interaction with the α-phosphate and the endocyclic ribose oxygen. From an applied standpoint, this study suggests that small-molecules targeting dynamic elements within the active site, particularly His252, may lead to inhibitors with improved binding affinity.

4.2 Introduction

Tuberculosis (TB) remains a serious threat to public health, and new drugs are needed to simply and shorten treatment, and fight multi-drug resistant TB. Toward this end, the inhibition of cysteine biosynthesis and, by extension, associated downstream metabolites represents fertile ground for the development of novel antibiotics (*1, 2*). In mycobacteria, the enzyme adenosine 5′-phosphosulfate reductase (APR) catalyzes the committed step in the biosynthesis of cysteine (Scheme 4.1) and is a validated target to develop new anti-TB agents, particularly for the treatment of latent infection (*3, 4*). APR lacks a human homolog, but is highly conserved across a wide range of bacterial species (*5*), raising the possibility that APR may also represent an attractive target for the discovery or rational design of broad-spectrum antibiotics. Moreover, APR is also present in plants and is recognized as a potential target for herbicide development (6-8).

Scheme 4.1. Reaction catalyzed by APR.

76
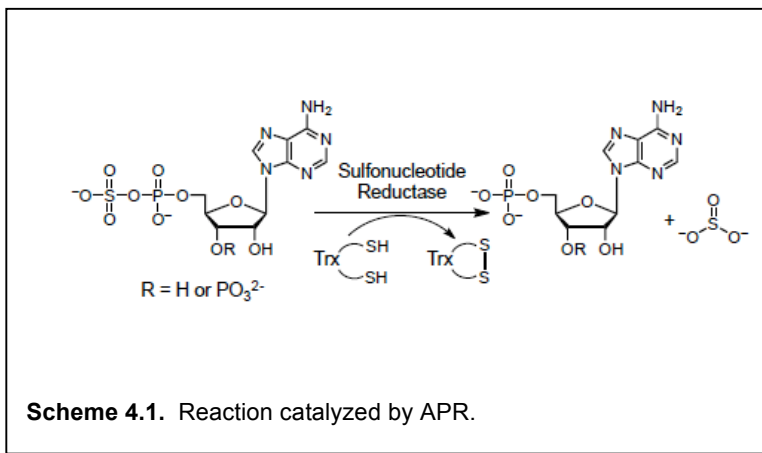
The importance of APR for microbial and plant survival has motivated investigations into its catalytic mechanism (9-12). These studies provide support for the two-step mechanism shown in Scheme 4.2, which involves nucleophilic attack by conserved Cys249[1] on adenosine 5′-phosphosulfate (APS) leading to the formation of a covalent enzyme S-sulfocysteine intermediate, E-Cys-Sγ–SO$_3^-$ bound to adenosine 5′-monophosphate (AMP). The sulfite product is then released *via* thiol-disulfide exchange with free thioredoxin in bacterial APR or via the action of the C-terminal thioredoxin-like protein domain in plant APR. In addition, APR contains a [4Fe-4S] cluster (iron-sulfur cluster) [2] that is essential for catalytic activity (*6, 13-15*). However, it is not involved in redox chemistry and its role remains an active area of investigation (*16, 17*).

Scheme 4.2. Proposed mechanism of sulfonucleotide reduction.
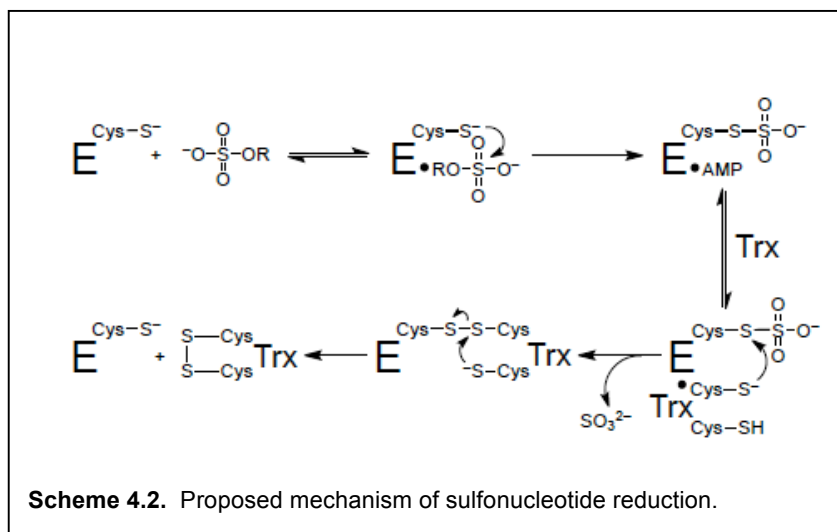
In 2006, the crystal structure of *Pseudomonas aeruginosa* APR (PaAPR) was solved in complex with APS, providing direct insight into substrate recognition (18). PaAPR and *Mycobacterium tuberculosis* APR (MtAPR) are homologous proteins sharing 27% identity and 41% similarity (Appendix 4.6.1), particularly in residues that line the active

---

[1] Residue numbers in this manuscript correspond to the APR sequence from *M. tuberculosis* (Figure 4.6, Appendix 4.6.1).

[2] The only known exception is the enzyme from *Physcomitrella Patens*, which lacks the [4Fe-4S] cluster, but retains APR activity (16).

site (84% identity and 92% similarity). PaAPR and MtAPR have comparable reaction kinetics and ligand binding affinity (*10, 19*). Likewise, the structure of PaAPR has been successfully employed in virtual ligand screening to identify low-micromolar chemical inhibitors of MtAPR (*20*).

The structure of PaAPR shows that APS binds in a deep active site cavity with the phosphosulfate extending toward the protein surface (Figure 4.1A). Conserved and semiconserved residues participate in four main-chain hydrogen bonds with adenine and the ribose O2′ hydroxyl. Interaction between the phosphosulfate and APR occurs *via* strictly conserved residues Lys145, Arg237, and Arg240. The phosphosulfate is also positioned opposite the [4Fe-4S] cluster[3]. The C-terminal 18 residues, carrying the

Figure 4.1. (A) Structure of PaAPR in complex with substrate, APS (PDB 2GOY). The C-terminal segment carries the catalytically essential cysteine is disordered. (B) Structure superposition of PaAPR bound to APS (gold, PDB 2GOY) and ScPAPR bound to PAP (orange, PDB 2OQ2). Overall structures show the proteins adopt a Rossman-like nucleotide binding fold with a central six stranded b-sheet and the substrates (APS and PAP) bind to active site in similar manner. Shown is the [4Fe-4S] cluster present only in PaAPR but absent in ScPAPR. The ScPAPR structure (orange) shows the complete intact C-terminal tail containing the strictly conserved active site ECG(I/L)H motif bound over the active site pocket. (C) A homology model of MtAPR was constructed using the Swiss Model server. The models were based upon ScPAPR (PDB 2OQ2) and the multiple sequence alignment from the sequence analysis step. The C-terminal segment of MtAPR shows direct interactions between the substrate (APS) and His252. The His252 is also 4.2 Å (magenta) from the Sg of Cys249 for plausible role in catalysis.

---

[3] APS is not in direct contact with the [4Fe-4S] cluster; the sulfate oxygens are 7 Å from the closest iron atom and 6 Å from the closest cysteine sulfur atom.

catalytically essential Cys249, were disordered in the structure of PaAPR. The lack of electron density information, coupled with limited proteolysis studies, led to the proposal that Cys249 resides on a flexible "lid peptide" that closes over the active site pocket upon ligand binding (18).

This hypothesis was later confirmed when Fisher and colleagues reported the crystal structure of the related enzyme, 3′-phosphoadenosine-5′-phosphosulfate (PAPS) reductase from *Saccharomyces cerevisiae* (ScPAPR) in complex with adenosine 3′,5′-diphosphate (PAP) (21). Although APS and PAPS differ by a 3′-phosphate and PAPR lacks the [4Fe-4S] cluster[4], structural and functional studies show that the two-step mechanism for sulfite production in Scheme 2 is conserved among this family of enzymes, known collectively as sulfonucleotide reductases (SRs) (*10, 18, 22, 23*). SRs share ~25% overall amino acid identity, including two highly conserved domains, the sulfonucleotide-binding pocket and C-terminal segment containing the K(R/T)ECG(L/I)H catalytic motif (Appendix 4.6.1; see also Ref. 18 for an alignment of 38 APR and 34 PAPR amino acid sequences). Likewise, SRs have virtually identical three-dimensional structures (superposition of 140 Cα backbone atoms from PaAPR and ScPAPR yields an r.m.s. deviation of 0.98 Å; Figure 4.1B). Significantly, the crystal structure of ScPAPR shows the flexible C-terminal segment folded over the active site pocket. In this conformation, a strictly conserved histidine residue His252 within the K(R/T)ECG(L/I)H motif is in proximity to the active site ligand and Cys249 (Figure 4.1B). These three-dimensional relationships are recapitulated in the homology model of MtAPR, generated on the basis of sequence alignment and ScPAPR template structures (r.m.s. deviation of 0.06 Å for Cα backbone atoms; Figure 4.1C).

---

[4] The only known exception is the enzyme from *Bacillus subtilis*, which possess an [4Fe-4S] cluster, but can utilize both substrates (13).

On the basis of conservation and juxtaposition to the catalytic cysteine, it was recently proposed that His252 acts as a general base in SRs to deprotonate the Cys249 nucleophile (21). However, this hypothesis has not yet been directly tested and thus, the precise function of this active site residue remains unknown. Herein, we have used site-directed mutagenesis to change His252 in MtAPR to an alanine residue and analyzed the effect of this mutation on the kinetic parameters, pH-rate profile and ionization of Cys249 of APR. These studies were further supported by isothermal titration calorimetry (ITC) to provide a thermodynamic profile of ligand-protein interactions. Collectively, these data indicate that His252 does not perturb the pK_a of Cys249 or play a direct role during chemical steps that lead to S-sulfocysteine formation. Instead, we show that interactions with His252 increase substrate affinity, which might be used in further inhibitor design to trap the enzyme in a closed, inactive conformation.

4.3 Results and Discussion

4.3.1 Kinetic characterization of WT and His252Ala MtAPR

To advance our understanding of the molecular recognition and catalytic mechanism of MtAPR, we used site-directed mutagenesis to change His252 to an alanine residue, and characterized single turnover kinetic parameters for wild-type and His252Ala. Mutation of His252 to Ala reduced k_{cat}/K_m by 230-fold (Table 4.1), indicating that this residue contributes to catalytic efficiency by enhancing substrate affinity and/or stabilizing the catalytic transition state. To gain further insight into the role of the conserved active-site histidine residue we compared the saturating single-turnover rate constant (k_{max}), the K_m and the substrate dissociation constant (K_d) for wild-type and His252Ala MtAPR (Table 1; see also Appendix 4.6.2-5 for representative data). The results show that alanine substitution of His252 decreased the value of k_{max} by only two-fold, whereas K_m and K_d

were both weakened by more than two orders of magnitude. Additional control experiments showed that there was no difference in iron incorporation or [4Fe-4S] cluster stability between the wild-type and variant MtAPR (Appendix 4.6.6), consistent with the approximate distance (~10 Å) between His252 and the metallocenter.

Table 4.1: Single-Turnover Rate and Equilibrium Constants for Wild-Type and His252Ala MtAPR[a]

Enzyme	k_{cat}/K_m (M^{-1} min^{-1})[b]	$(k_{cat}/K_m)_{rel}$	k_{max} (min^{-1})[c]	$(k_{max})_{rel}$	K_m (µM)[d]	$(K_m)_{rel}$	K_d (µM)[e]	$(K_d)_{rel}$
Wild-type	3.0×10^6	230	2.8	2.0	0.2[f]	>250	0.2	450
H252A	1.5×10^4	(1)	1.4	(1)	>50[g]	(1)	90	(1)

[a]Measurements are the average of ≥3 independent determinations and the S.D. was ≤15% of the value in all cases. Unless otherwise stated, reaction conditions are 100 mM Bis-Tris propane, pH 6.5, 5 mM dithiothreitol, and 10 µM thioredoxin at 30 °C (see Materials and Methods). Values in parenthesis are references values (*i.e.,* other values normalized to this rate). [b]k_{cat}/K_m values were measured as described in Materials and Methods. [c]Single-turnover rate constants with saturating wild-type or His252Ala MtAPR. [d]K_m values for *S*-sulfocysteine formation were measured in the absence of thioredoxin by varying the concentration of wild-type or His252Ala MtAPR (see Materials and Methods). [e]Dissociation constants were measured using ultrafiltration at 30 °C (100 mM Bis-Tris propane, pH 6.5) as described in Materials and Methods. [f]From Ref. (27). [g]In Bis-Tris propane at pH 7.5. Due to technical limitations of the TLC-based assay only a lower limit could be obtained.

4.3.2 pH dependence on catalysis of WT and His252Ala MtAPR

To examine the role of His252 in greater detail and provide additional insight into the overall catalytic mechanism of APR, we measured the pH dependence of k_{cat}/K_m for the wild-type enzyme and the His252Ala mutant. Figure 4.2 illustrates that the acidic limb for reaction of APS with wild-type or His252Ala has a first-order dependence on the proton concentration, consistent with a single inactivating protonation at acidic pH. For k_{cat}/K_m, these kinetic pK_a values could represent ionization of either free enzyme or substrate. The data described below support the model with ionization of the Cys249 nucleophile.

The acidic limb of the pH dependence for the APR-catalyzed reduction of APS is best fit by a pK_a of 6.1 ± 0.1 and 6.3 ± 0.1 for wild-type and His252Ala MtAPR, respectively (Figure 4.2). The most likely candidate for this ionization is the enzyme – specifically of catalytic cysteine – since the substrate pK_a falls significantly below this region. To test this proposal, we determined the pK_a of Cys249 by measuring the change in absorbance of ultraviolet (UV) light at

Figure 4.2. pH dependence for k_{cat}/K_m with APS substrate. The dashed lines represent the best fit with a single rate-controlling ionization (eq 5). (A) The pH dependence for reduction of APS yields a pK_a value of 6.1 ± 0.1 for wild-type (●) and 6.3 ± 0.1 for His252Ala (■) MtAPR. The average of three independent determinations is shown, and the error bars indicate the standard deviations.
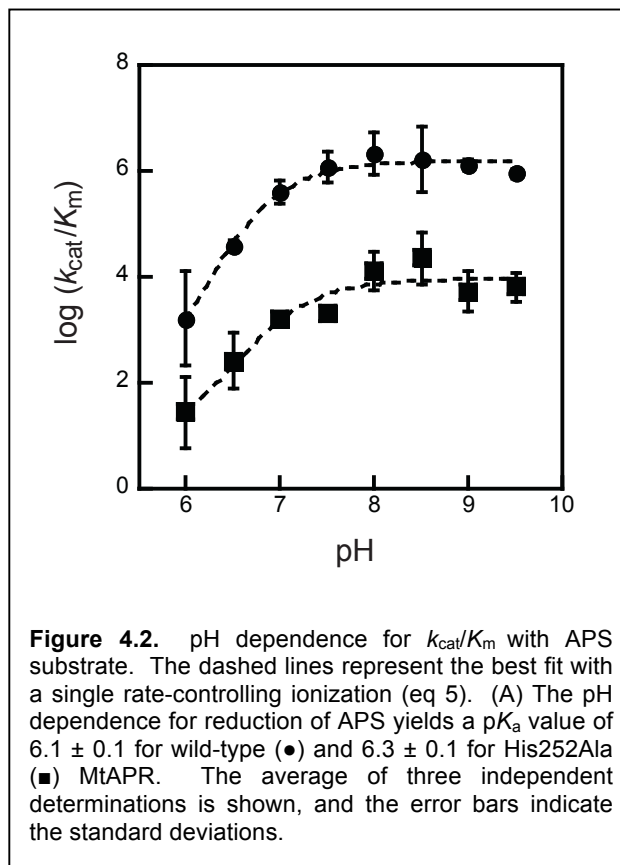
240 nm resulting from formation of the thiolate anion, as previously described (*23, 28, 29*). For these studies, we utilized Cys59Ala MtAPR, which has identical kinetic properties to the native enzyme (*10, 15*), but eliminates a non-conserved cysteine that could confound the analysis.

The pH dependence of the molar extinction coefficient of Cys59Ala MtAPR at 240 (ε_{240}) displays a transition with a pK_a of 6.2 ± 0.1 (Figure 4.3A). The change in ε_{240} is most likely due to ionization of Cys249, as indicated by the absence of a pH-dependent transition for Cys59Ala Cys249Ala MtAPR (Figure 4.3A). The pH dependence of the molar extinction coefficient of Cys59Ala His252Ala MtAPR at 240 (ε_{240}) shows a transition with a pK_a of 6.0 ± 0.1 (Figure 4.3B). For comparison, we evaluated the pK_a of

Cys249 within a synthetic peptide derived from the last 10 C-terminal residues of MtAPR (Appendix 4.6.5B). The pK_a of the thiol in the peptide segment was determined as 8.3, consistent with the pK_a value of free cysteine solution (*30*). Interestingly, our experiments indicate that thiolate formation at Cys249 correlates with decrease in signal at ε_{240}, as opposed to the increase that is normally observed. Therefore, the ionization constant of Cys249 was verified by an independent method using the thiol-specific reagent, monobromobimane (mBBr) (24). In this assay, the pK_a value of Cys249 for Cys59Ala MtAPR was determined to be 6.0 ± 0.1 (Appendix 4.6.5A), which is within error of the UV-based method. The similarity of the kinetic pK_a and the pK_a value for Cys249 deprotonation strongly suggest that the observed inflection in k_{cat}/K_m corresponds to the ionization of the active site cysteine to form the thiolate anion.

To further investigate the molecular recognition properties for wild-type and His252Ala MtAPR, we compared the pH dependence for binding of the nucleotide product, AMP. As shown in Figure 4.4, the logarithm of the association constant (K_a = 1/K_d) shows a first-order dependence on the proton concentration. The acidic limb for wild-type MtAPR binding to AMP has a pK_a of 8.1 ± 0.1, as previously reported (19). The pK_a values observed in product affinity could reflect ionizations in either, or both, the ligand and the enzyme, analogous to the pH dependence for k_{cat}/K_m discussed above. A likely explanation for the weaker binding of AMP below pH 8 is that the dianion binds more tightly than the monoanion. However, the apparent pK_a differs from the pK_a of AMP in solution (~6.8) by more than one unit. The discrepancy between the experimental data and this model is most likely due to concurrent ionization of the enzyme that affects ligand binding, leading to shift in the apparent pK_a of AMP. One model that could account for this upward deviation is that an enzymatic group with a pK_a of ~6 contributes slightly (~5-fold) to AMP binding when protonated. Given its proximity to the α-

Figure 4.3. Determination of the pK_a for MtAPR Cys249. The pK_a of Cys249 was determined by monitoring the change in the extinction coefficient at 240 nm ($\Delta\varepsilon_{240}$) as a function of pH, which monitors formation of the thiolate anion. (A) Cys59Ala MtAPR (●) exhibits a $\Delta\varepsilon_{240}$ transition corresponding to a pK_a of 6.2 ± 0.1, where mean data and associated standard deviations for triplicate measurements are shown. The dashed line shows the nonlinear regression fit of eq 9 to the measured data. Cys59Ala Cys249Ala MtAPR (■) shows no transition, indicating that the ionization of Cys249 is solely responsible for the observed transition in APR. (B) Cys59Ala His252Ala MtAPR exhibits a $\Delta\varepsilon_{240}$ transition corresponding to a pK_a of 6.0 ± 0.1, where mean data and associated standard deviations for triplicate measurements are shown. The dashed line shows the nonlinear regression fit of eq 9 to the measured data.

phosphate, the most likely residue to exert such an effect on ligand binding is His252. Consistent with this proposal, the acidic limb for His252Ala MtAPR binding to AMP displays a pK_a of 6.4 ± 0.1 (Figure 4.4). An additional observation from these data is that binding of the nucleotide product to His252Ala is weaker at physiological pH and above, as compared to wild-type MtAPR. For example, at pH 7.5 wild-type and His252Ala MtAPR bind to AMP with respective K_d values of 5.4 ± 0.2 μM and 50.5 ± 3 μM.

4.3.3 Binding interaction between His252 and substrate

The crystal structure of scPAPR (21) and the model of MtAPR shown in Figure 4.1 indicate that the side chain of His252 is positioned within hydrogen bonding distance of the α-phosphate and the endocyclic ribose oxygen of the active site ligand. Previous studies have demonstrated

the relative importance of the α-phosphate group for AMP binding to MtAPR (~3 kcal/mol) (19); however, the contribution of oxygen O4 in the ribose sugar has not been investigated. To examine the importance of the hydrogen bond contact between His252 and the endocyclic ribose oxygen, we synthesized 5'-phosphoaristeromycin, which replaces O4 in AMP with a methylene unit. Binding studies indicate that at pH 7.5 this analog binds to MtAPR with a K_d value of 25 ± 2.5 μM (Figure 4.5) or 5-fold more weakly than AMP. These data indicate that the interaction of His252 with the ribose O4 makes a modest contribution to ligand recognition (~1 kcal/mol).

To substantiate the role of His252 in substrate binding we performed additional biophysical experiments. In initial experiments, we attempted to
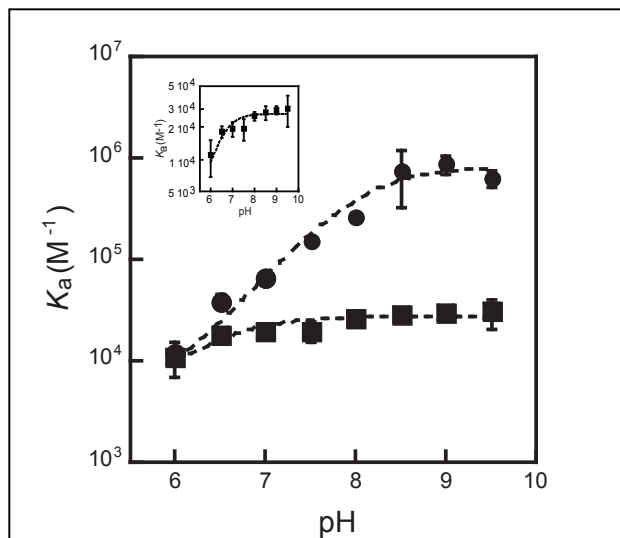
Figure 4.4. The pH dependence for AMP binding. The association equilibrium constant (K_a = 1/K_d) is plotted as a function of pH. Values of K_i were determined by inhibition of APS reduction with [S] < K_M, such that K_i is expected to be K_d. The average of three independent determinations is shown, and the error bars indicate the standard deviations. Nonlinear-least-squares fit of the data to a model for a single ionization (eq 6) gave pK_a values of 8.1 ± 0.1 for wild-type MtAPR (●) and 6.4 ± 0.1 for His252Ala MtAPR
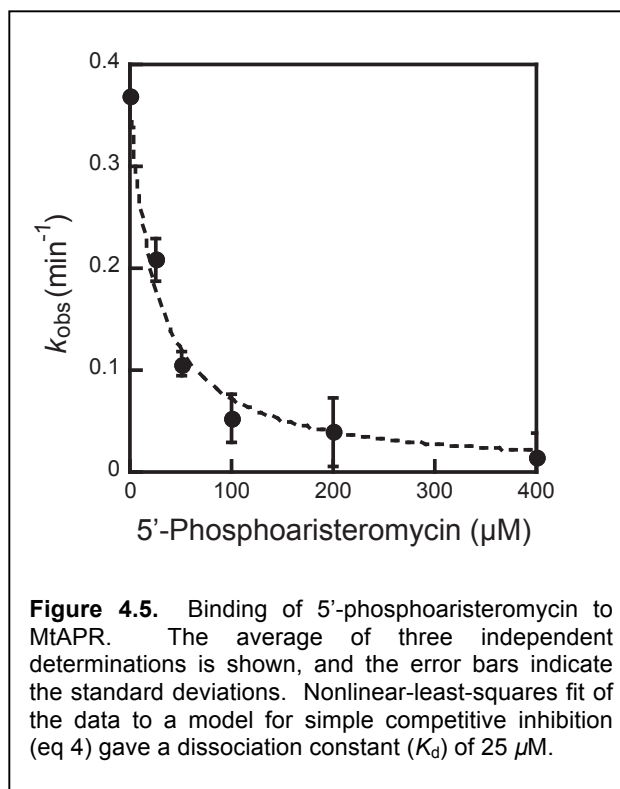
Figure 4.5. Binding of 5'-phosphoaristeromycin to MtAPR. The average of three independent determinations is shown, and the error bars indicate the standard deviations. Nonlinear-least-squares fit of the data to a model for simple competitive inhibition (eq 4) gave a dissociation constant (K_d) of 25 μM.

monitor the spectral perturbation of non-catalytic 2'(3')-O-(N-Methylanthraniloyl) (MANT) and N^6-etheno substrate analogs. However, the affinity of these ligands for wild-type MtAPR was extremely weak (K_d >1 mM) and associated signal changes were unreliably small (not shown).   As an alternative approach, we employed isothermal titration calorimetry (ITC) to measure affinities for wild-type and His252Ala MtAPR for substrate, APS and product, AMP (Appendix 4.6.7).   ITC offers a direct and complete characterization of the thermodynamic interaction whereby the ligand is titrated into the protein (*31, 32*). This analysis indicates that APS binds to wild-type MtAPR with a K_d of 0.6 ± 0.3 μM as compared to 42 ± 6.2 μM for His252Ala. Furthermore, AMP binds to wild-type MtAPR with a K_d of 7.5 ± 1.4 μM compared to 67 ± 8.4 μM for His252Ala. These data are in excellent agreement with the other kinetic and thermodynamic values obtained from our radiolabeled biochemical assay (*i.e.,* Table 4.1 and Figure 4.4).

4.4 Conclusion

Collectively, the data presented herein provide strong support for the existence of a direct interaction between His252 in the C-terminus with ligands including APS and nucleotide product, AMP. The flexible C-terminal segment must fold over the active site upon substrate binding to bring Cys249 in proximity to the β-sulfate group.   In this context, our studies do not support a role for His252 as a general base that deprotonates the catalytic cysteine since: i) wild-type and His252Ala exhibit similar pK_a values for both k_{cat}/K_m and Cys249 deprotonation, and ii) alanine substitution of His252 has an extremely modest affect on k_{max}. Rather, our data show that His252 plays an important role in ligand binding and likely facilitates docking of the C-terminal residues. These studies also reveal that the pK_a value of the cysteine nucleophile is perturbed downward by more than two units (i.e., 6.2) relative to the value we obtained for this residue within a peptide (i.e., 8.3). The low pK_a value of Cys249 in MtAPR is consistent with the

essential catalytic function of this residue. Positively charged amino acids in the active site, including Lys145, Arg242, and Arg245, are likely candidates for stabilization of the thiolate.

A critical motivating factor for these studies is that APR is essential for mycobacterial survival during persistent infection (4). This key discovery has led to the proposal that small-molecule inhibitors of APR might be a source for new drugs to treat latent tuberculosis infection (1, 33). The increasing number of antibiotic-resistant strains suggests that the availability of such compounds could play an important role in treating the disease and minimizing the impact on human health. Defining active site residues that are essential for molecular recognition in MtAPR sets the stage for the development of such drugs. Toward this end, targeting dynamic elements within the active site, particularly Cys249 and His252, may increase the potency of APR inhibitors.

4.5 Experimental Procedures

4.5.1 Materials

All chemicals, unless stated otherwise, were purchased from the Sigma Chemical Company and were of the highest purity available. The C-terminal peptide (AKTECGLHASW) was synthesized by solid-phase peptide synthesis using Fmoc-based chemistry and HPLC purified to >98%. The molecular weight of the peptide was confirmed by mass spectrometry (1202.4 Da). Aristeromycin was synthesized from dimethyl-3-cyclopentene-1,1-dicarboxylate as previously described (24). 5'-Phosphoaristeromycin was prepared by chemical phosphorylation of aristeromycin using established methods (25). The physical and spectral data for 5'-phosphoaristeromycin were consistent with values reported in the literature for this nucleotide (25).

4.5.2. Mutagenesis and Protein Expression

The construction of the expression vector encoding wild-type MtAPR cloned into the vector pET24b (Novagen) has been previously described (*26*). The His252Ala mutant plasmid was prepared using Quik-change site-directed mutagenesis (Stratagene). Wild-type and mutant MtAPR were overexpressed and purified to homogeneity according to published procedures using Ni-affinity and gel filtration column chromatography (*17*).

4.5.3 General APS Reductase Assay

APR assays were performed as described previously (*17, 19*). All assays were conducted at 30 °C. Unless otherwise indicated, the reaction conditions included 100 mM Bis-Tris propane (pH 6.5), supplemented with 5 mM dithiothreitol (DTT), and 10 µM *Escherichia coli* thioredoxin. Production of $^{35}SO_3^{2-}$ from ^{35}S-APS was monitored using charcoal-based separation and scintillation counting as previously reported (19). For each time point, the fraction product was calculated according to eq 1.

$$F = P/(P+S) \quad (1)$$

where *F* is the fraction converted to product, *P* is product, and *S* is intact substrate]. Reactions progress curves were analyzed using Kalediagraph (Synergy Software), as described below.

4.5.4 Single-Turnover Kinetics

Single-turnover APR assays were performed in the standard reaction buffer, as described above. To ensure single-turnover reactions, the concentration enzyme was kept in excess over the concentration of ^{35}S-APS (typically 2.5 nM). Reactions were followed to completion (≥ 5 half-lives) except for very slow reactions. The reaction progress curve was plotted as the fraction of product versus time and was fit by a single

exponential using Kaleidagraph (eq 2) where F is the fraction product, A is the fraction of substrate converted to product at completion, k_{obs} the observed rate constant, and t time.

$$F = A[1 - exp(-k_{obs}t)] \quad (2)$$

$$k_{obs} = k_{max}[E]/(K_{1/2} + [E]) \quad (3)$$

Under single-turnover conditions, the concentration dependence of the enzyme is hyperbolic (eq 3). The maximal observed rate constant (k_{max}) corresponds to the rate of reaction at a saturating enzyme concentration, and the $K_{1/2}$ value indicates the concentration at which half of the substrate is bound. For $K_{1/2}$ determinations, the APR concentration was varied over a wide range and reactions were carried out in the absence of thioredoxin, as described previously (19). Although we refer to the $K_{1/2}$ value for maximal activity as K_m, the value could differ from the K_m value for multiple turnover because the latter can be affected by product release. At least two or more enzyme concentrations were averaged to obtain the k_{cat}/K_m value ($k_{cat}/K_m = k_{obs}/[E]$ for conditions in which $[E] << K_{1/2}$). Under these conditions, the observed rate constant is linearly dependent upon enzyme concentration, and independent of substrate across a concentration range of at least 4-fold, which demonstrated that substrate was not saturating. The reported k_{cat}/K_m values are for single-turnover conditions, but are equivalent to steady-state k_{cat}/K_m (17).

The single-turnover rate constant (k_{max}) was determined at saturating concentration of APR, and this was confirmed by the observation of the same rate constant at two different concentrations of APR. Under these conditions, the observed rate constant is equal to the maximal single-turnover rate constant ($k_{obs} = k_{max}$) and monitors steps after binding up to and including the chemical step (eq 3). The inhibition constant (K_i) was measured for various ligands by inhibiting the APR reaction under k_{cat}/K_m conditions with

varying concentration of inhibitor (I). The data were fit to a simple model for competitive inhibition (eq 4) and, with subsaturating APR, the K_i is equal to the equilibrium dissociation constant (K_d) of the inhibitor.

$$(k_{cat}/K_m)^{obs} = (k_{cat}/K_m)/(1+ [I]/K_i) \qquad (4)$$

4.5.5 pH Dependence for k_{cat}/K_m

The following buffers were used for the indicated pH range: NaMES (6.0-7.0), Bis-Tris Propane (6.5-7.5), Tris-HCl (7.5-9.0), and NaCAPS (9.0-9.5). Reactions were carried out with 100 mM buffer. The rate constants obtained at each pH value for multiple reactions were averaged, and the standard deviations were ≤ 25% of the average. The data was fit to a model for a single rate-controlling ionization as described by eq 5.

$$(k_{cat}/K_m) = (k_{cat}/K_m)^{max}/(1+ [H^+]/K_a) \qquad (5)$$

4.5.6 pH Dependence of Inhibitor Binding

The following buffers were used for the indicated pH range: NaMES (6.0-7.0), Bis-Tris Propane (6.5-7.5), Tris-HCl (7.5-9.0), and NaCAPS (9.0-9.5). Reactions were carried out with 100 mM buffer. The conditions described above were used to monitor k_{cat}/K_m for reduction of ^{35}S-APS in the presence and absence of inhibitor. The rate constants at each pH value for multiple reactions were averaged, and the standard deviations were ≤ 25% of the average. K_a values were determined using eq 6, derived from a model where the binding of the ligand depends on a single ionizable group.

$$K_d^{app} = K_d/(1+ [H^+]/K_a) \qquad (6)$$

4.5.7 Determination of Substrate Affinity

The K_d for ^{35}S-APS from wild-type and His252Ala MtAPR-ligand complexes was measured using an ultrafiltration binding assay reported by Hernick and Fierke (27). In

brief, the concentration of substrate was kept low (*i.e.,* below the K_d) and constant, and the concentration of the enzyme was varied from 0 to 50 μM (wild-type) or 0 to 400 μM (His252Ala). The enzyme was added to reaction buffer containing 100 mM Bis-Tris Propane, pH 6.5 with 5 nM APS at 30 °C and then transferred into ultrafiltration devices (Microcon 30 kDa cutoff, Millipore), and the free and bound ligand separated by centrifuging the samples at 3,000 rpm for 2.5 min. Equal volumes of the filtrate and retentate were removed and quantified using scintillation counting. The ratio of EL/L_{total} was determined as a function of $[E]_{total}$, and the K_d value was obtained by fitting eq 7 to these data.

$$\frac{EL}{L_{total}} = \frac{\left(EL/L_{total}\right)_{Endpt}}{\left(1 + \frac{K_d}{E_{total}}\right)} + \left(\frac{EL}{L_{total}}\right)_{Background}$$

(7)

4.5.8 Spectrophotometric pKa Determination of Cys249

Buffer exchange of APR was performed using a PD-10 column (GE Healthcare) that had been pre-equilibrated with degassed water. Ionization of Cys249 was monitored by absorption of the thiolate anion at 240 nm (23) using a Cary 50 UV-visible spectrometer (Varian) and a 1 cm path length quartz cuvette. APR was diluted to a final concentration of 20 μM in 10 mM MES buffers of various pH (5.0-8.0), and the absorption of the sample was monitored at 240 and 280 nm after correction for the absorption of the MES buffer alone. The extinction coefficient at 240 nm (ε_{240}) was calculated using the ratio of absorbance at 280 and 240 nm (eq 8).

$$\varepsilon_{240} = \varepsilon_{280} \times (A_{240}/A_{280})$$

(8)

A_{240}/A_{280} is the ratio of the absorbance of the protein at 240 and 280 nm, ε_{280} is the known extinction coefficient of APR at 280 nm (36815 M^{-1}cm^{-1}), and ε_{240} is the extinction

coefficient at 240 nm (23). The data were plotted as a function of pH, and the pK_a was determined by fitting a version of the Henderson–Hasselbalch equation to the data (eq 9).

$$\varepsilon_{240}^{O}(\text{pH}) = \varepsilon_{240}^{SH} + (\varepsilon_{240}^{S-} - \varepsilon_{240}^{SH})/(1 + 10^{pKa-pH}) \quad (9)$$

4.5.9 Isothermal Titration Calorimetry (ITC)

Wild-type and His252Ala MtAPR were exchanged into 100 mM BisTris propane buffer, pH 7.5. ITC experiments were performed using an iTC200 calorimeter from MicroCal (Northhampton, MA). Experiments were carried out by titrating wild-type MtAPR (50 μM) with APS or AMP (250 μM) and His252Ala MtAPR (50 μM) with APS or AMP (1 mM) at 30 °C. A total of 20 injections were performed with a spacing of 180 s and a reference power of 5 μcal/s. Control experiments to determine the heat of dilution for each injection were performed by injecting the same volume of APS or AMP into the sample cell containing only buffer. The heat of dilution generated by the compounds was subtracted, and the binding isotherms were plotted and fit (eq 10) to a single-site binding model using Origin ITC software.

$$q = v \times \Delta H \times [E] \times \left(\frac{K_a[L]_i^n}{1 + K_a[L]_i^n} - \frac{K_a[L]_{i-1}^n}{1 + K_a[L]_{i-1}^n} \right) \quad (10)$$

where q is the directly measured amount of heat released during each injection, v is the volume of the reaction, L_i is the ligand concentration at the ith injection. The K_d was calculated as the inverse of the K_a.

4.6 Appendices

Figure 4.6.1 Sequence alignment of APR from *Pseudomonas aeruginosa*, *Mycobacterium tuberculosis* and PAPR from *Saccharomyces cerevisiae*

Sequence alignment of APR from *Pseudomonas aeruginosa*, *Mycobacterium tuberculosis* and PAPR from *Saccharomyces cerevisiae* generated by ClustalW (1) and rendered by ESPript 2.2 (http://espript.ibcp.fr). Strictly conserved residues are boxed in red, similar residues are represented by red letters indicate conserved residues, and conserved regions are boxed in blue. Residues flanking the active site are boxed in green.
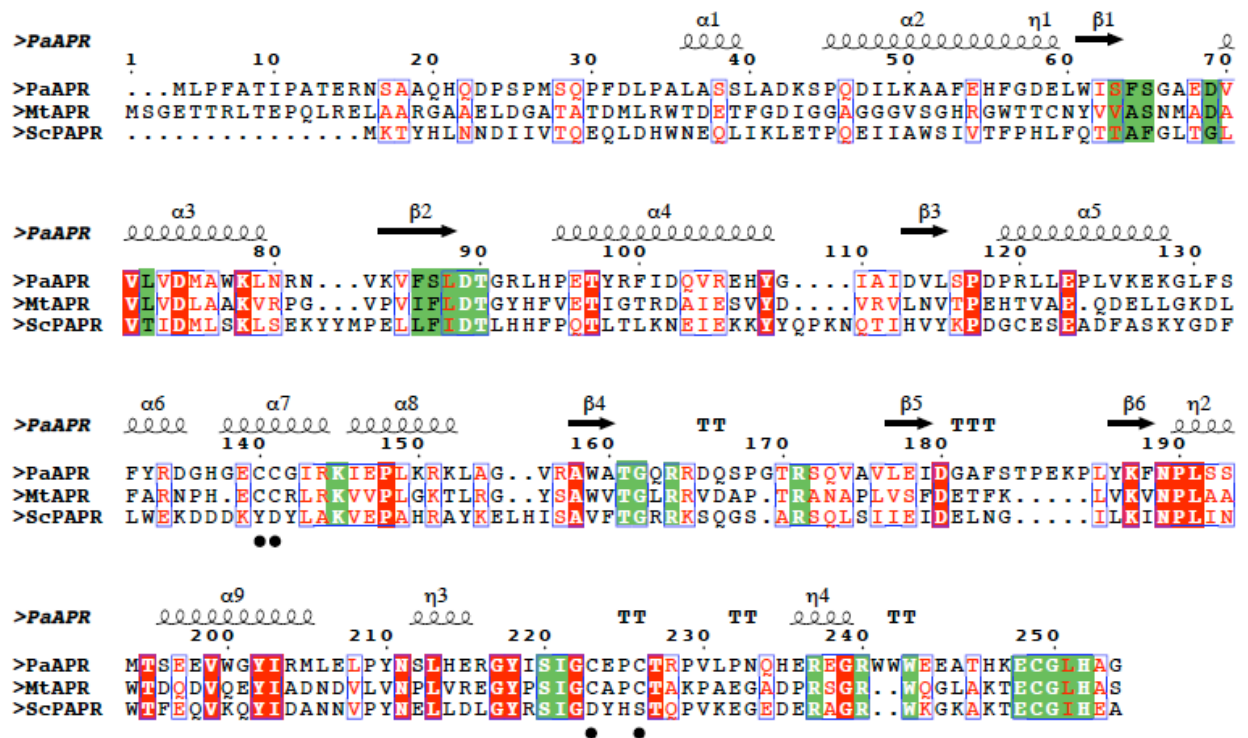
Figure 4.6.2 Wild-type MtAPR (A) and His252Ala MtAPR (B) binding to substrate (APS) as measured by ultrafiltration assay.

The lines indicate the best fit of eq 7 to the data and yield 0.2 mM for wild-type APR (pH 6.5) and 90 mM for His252Ala APR (pH 6.5).
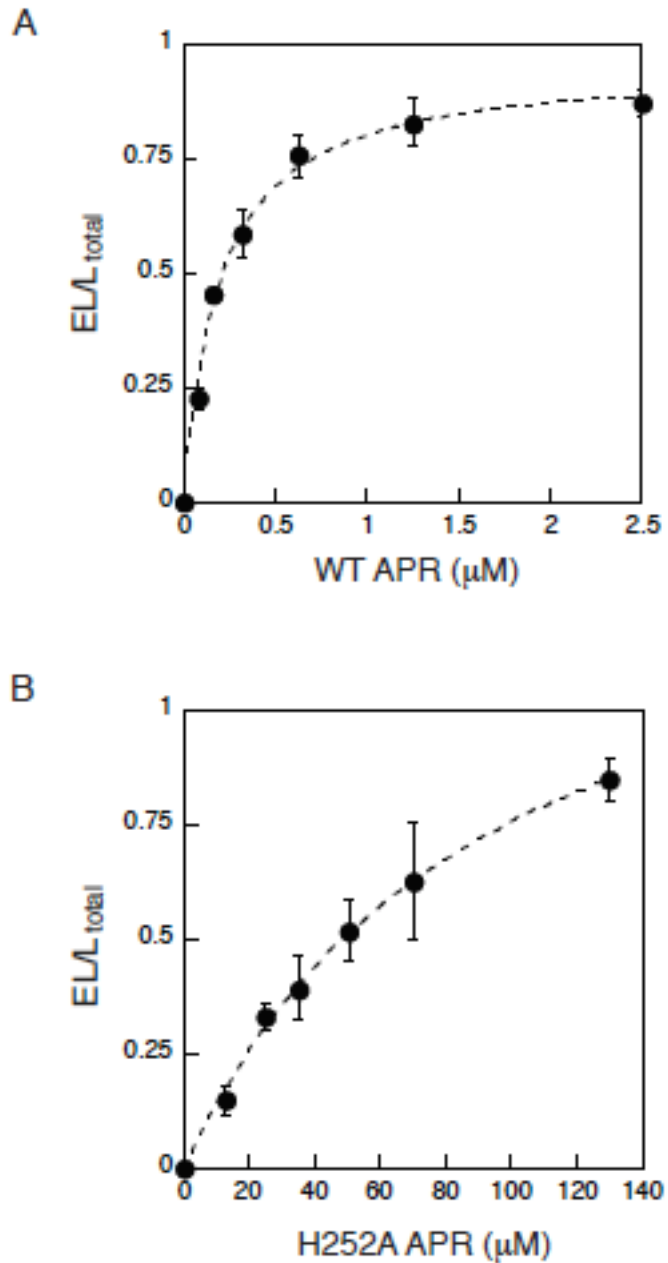
Figure 4.6.3 The C-terminal residue histidine 252 does not play a role in chemical catalysis.

(A) The k_{max} for wild-type MtAPR measured under single turnover conditions was 2.8 min^{-1}. (B) The k_{max} for the His252Ala variant measured under single turnover condition was 1.4 min^{-1}.
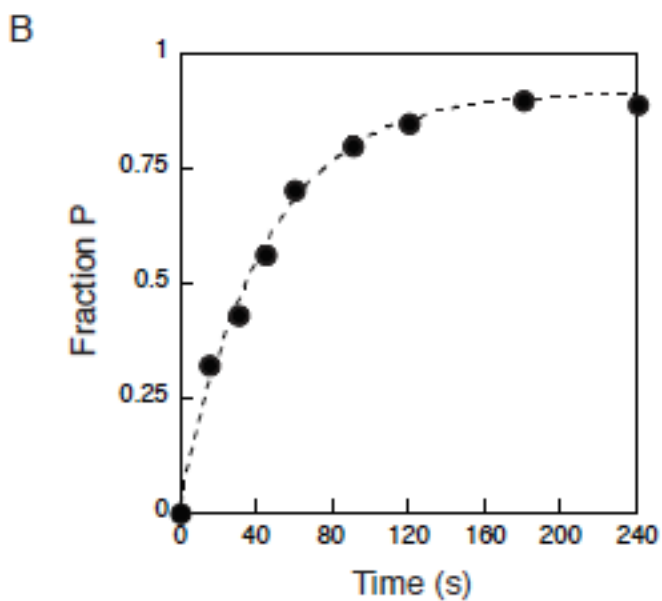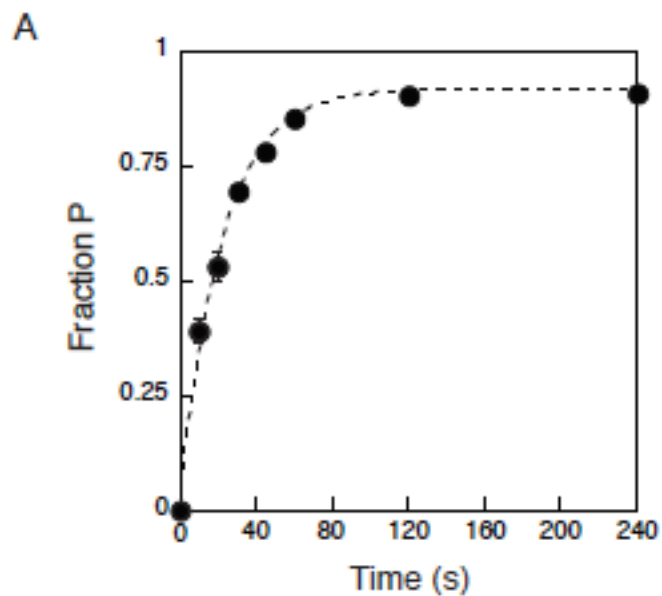
Figure 4.6.4 The K_m for S-sulfocysteine formation for wild-type (A) and His252Ala MtAPR (B) measured under single turnover conditions.

Representative data are shown for reactions that were conducted in duplicate, and the error bars indicated the standard deviation (in many cases, the standard deviation is smaller than the symbol).
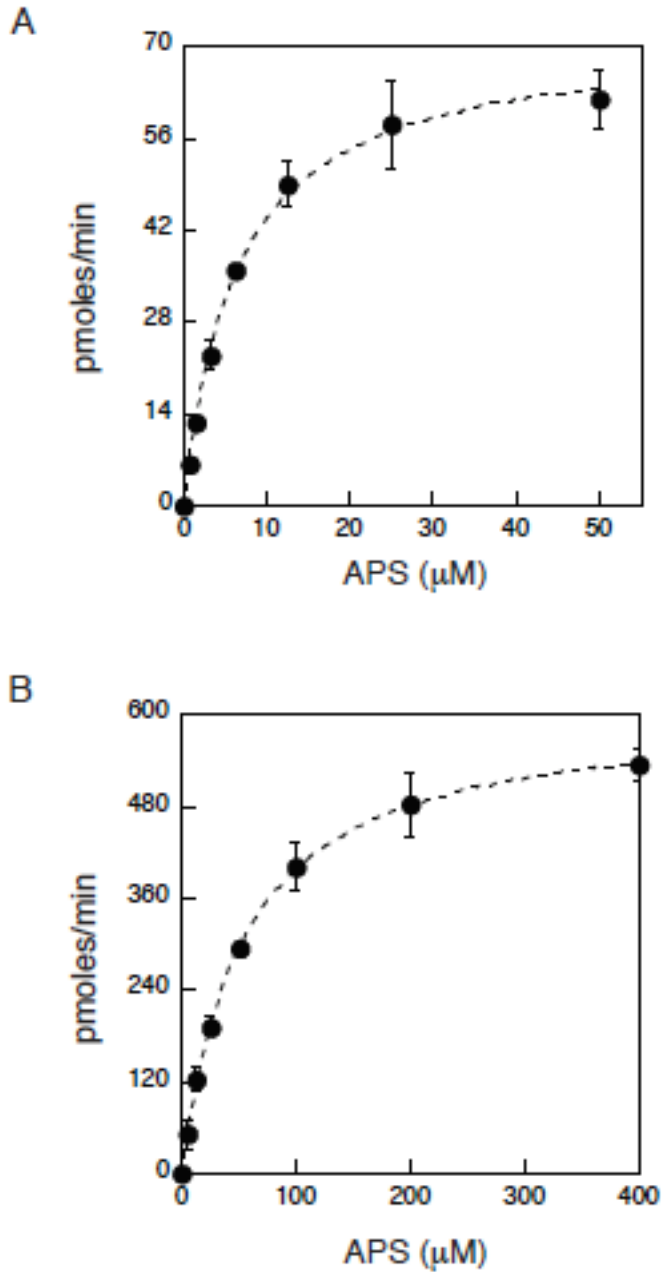
Figure 4.6.5 Determination of the pK_a value for the Cys249 nucleophile in MtAPR.

(A) The pK_a of Cys249 as determined by monobromobimane (mBBr) labeling. The fluorescent reaction product of mBBr and Cys249 was measured by incubating Cys59Ala MtAPR (200 µM) with mBBr (0.2 mM). Nonlinear-least-squares fit of the data to eq 9 gave a pK_a value of 6.0 ± 0.1. (B) The pK_a of cysteine in the C-terminal peptide was determined to be 8.3 ± 0.1.
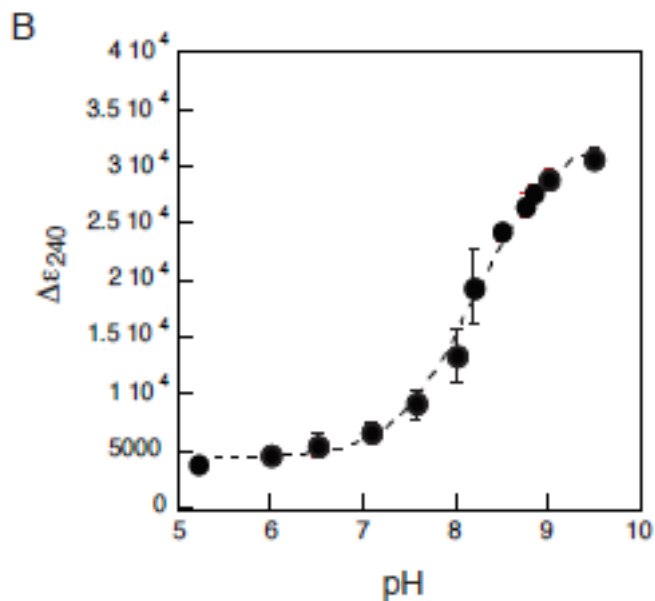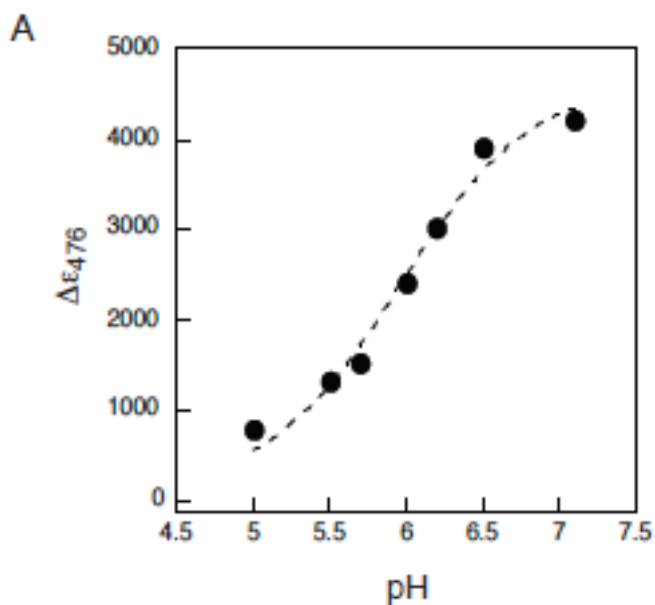
Figure 4.6.6 Relative stability of the [4Fe-4S] cluster in wild-type (●) and His252Ala MtAPR (■).

Proteins (10 μM) were stored under aerobic conditions at 4 ˚C for 2 days. Enzyme activity and molar extinction coefficient (see inset for representative data at 0 (red circles) and 48 hours (black circles) were monitored during this period.
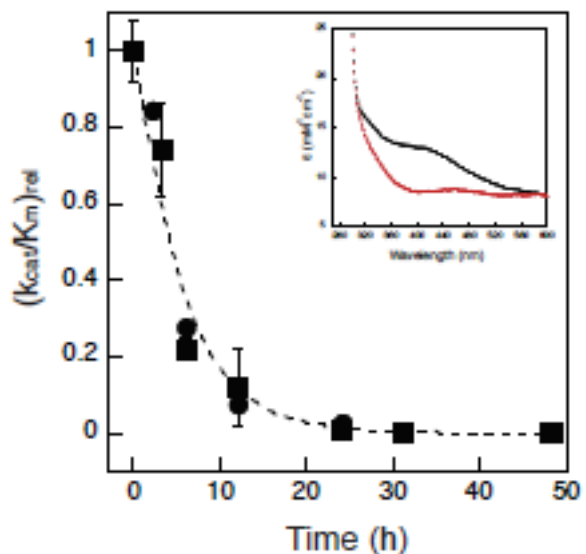
Figure 4.6.7 ITC binding curve for APS binding to wild-type (A) or His252Ala MtAPR (B), and AMP binding to wild-type (C) or His252Ala MtAPR (D).

Representative plots from ITC experiments are illustrated with raw data in the upper panel and fitting curves in the lower panel. The dissociation constant, K_d values calculated by curve fitting (eq 10) are: 0.6 µM (A), 42 µM (B), 7.5 µM (C), and 67 µM (D).
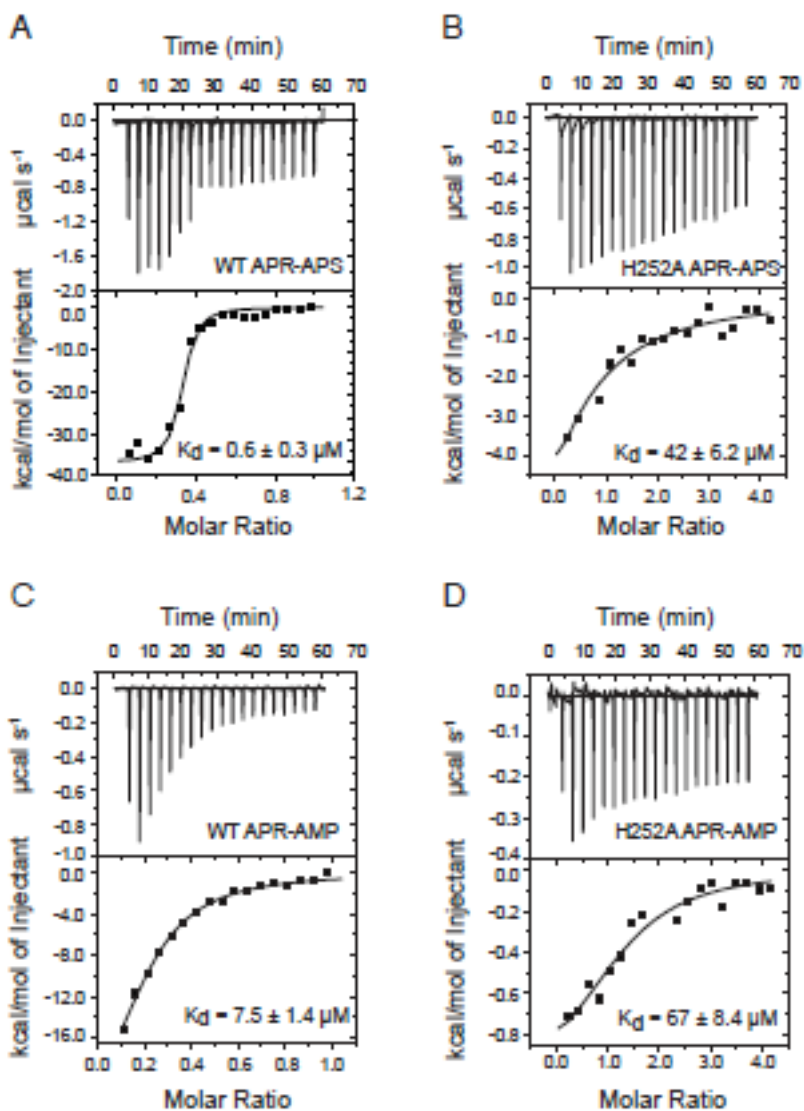
Acknowledgements

99

4.7 Reference

1.   Bhave, D. P., Muse, W. B., 3rd, and Carroll, K. S. (2007) Drug targets in mycobacterial sulfur metabolism, *Infect. Disord. Drug Targets 7*, 140-158.

2.   Schnell, R., and Schneider, G. (2010) Structural enzymology of sulphur metabolism in *Mycobacterium tuberculosis*, *Biochem. Biophys. Res. Commun. 396*, 33-38.

3.   Mdluli, K., and Spigelman, M. (2006) Novel targets for tuberculosis drug discovery, *Curr. Opin. Pharmacol. 6*, 459-467.

4.   Senaratne, R. H., De Silva, A. D., Williams, S. J., Mougous, J. D., Reader, J. R., Zhang, T., Chan, S., Sidders, B., Lee, D. H., Chan, J., Bertozzi, C. R., and Riley, L. W. (2006) 5'-Adenosinephosphosulphate reductase (CysH) protects *Mycobacterium tuberculosis* against free radicals during chronic infection phase in mice, *Mol. Microbiol. 59*, 1744-1753.

5.   Kopriva, S., Buchert, T., Fritz, G., Suter, M., Benda, R., Schunemann, V., Koprivova, A., Schurmann, P., Trautwein, A. X., Kroneck, P. M., and Brunold, C. (2002) The presence of an iron-sulfur cluster in adenosine 5'-phosphosulfate reductase separates organisms utilizing adenosine 5'-phosphosulfate and phosphoadenosine 5'-phosphosulfate for sulfate assimilation, *J. Biol. Chem. 277*, 21786-21791.

6.   Kopriva, S., Buchert, T., Fritz, G., Suter, M., Weber, M., Benda, R., Schaller, J., Feller, U., Schurmann, P., Schunemann, V., Trautwein, A. X., Kroneck, P. M., and Brunold, C. (2001) Plant adenosine 5'-phosphosulfate reductase is a novel iron-sulfur protein, *J. Biol. Chem. 276*, 42881-42886.

7.   Setya, A., Murillo, M., and Leustek, T. (1996) Sulfate reduction in higher plants: molecular evidence for a novel 5'-adenylylsulfate reductase, *Proc. Natl. Acad. Sci. U S A 93*, 13383-13388.

8.   Hirase, K., and Molin, W. T. (2003) Sulfur assimilation in plants and weed control: Potential targets for novel herbicides and action sites of certain safeners, *Weed Biol. and Manage. 3*, 147-157.

9.   Weber, M., Suter, M., Brunold, C., and Kopriva, S. (2000) Sulfate assimilation in higher plants characterization of a stable intermediate in the adenosine 5'-phosphosulfate reductase reaction, *Eur. J. Biochem. 267*, 3647-3653.

10.   Carroll, K. S., Gao, H., Chen, H., Stout, C. D., Leary, J. A., and Bertozzi, C. R. (2005) A conserved mechanism for sulfonucleotide reduction, *PLoS Biol. 3*, e250.

11.   Kim, S. K., Rahman, A., Mason, J. T., Hirasawa, M., Conover, R. C., Johnson, M. K., Miginiac-Maslow, M., Keryer, E., Knaff, D. B., and Leustek, T. (2005) The interaction of 5'-adenylylsulfate reductase from *Pseudomonas aeruginosa* with its substrates, *Biochim. Biophys. Acta. 1710*, 103-112.

12.   Gao, H., Leary, J., Carroll, K. S., Bertozzi, C. R., and Chen, H. (2007) Noncovalent complexes of APS reductase from *M. tuberculosis*: delineating a

mechanistic model using ESI-FTICR MS, *J. Am. Soc. Mass. Spectrom. 18*, 167-178.

13. Berndt, C., Lillig, C. H., Wollenberg, M., Bill, E., Mansilla, M. C., de Mendoza, D., Seidler, A., and Schwenn, J. D. (2004) Characterization and reconstitution of a 4Fe-4S adenylyl sulfate/phosphoadenylyl sulfate reductase from *Bacillus subtilis*, *J. Biol. Chem. 279*, 7850-7855.

14. Kim, S. K., Rahman, A., Bick, J. A., Conover, R. C., Johnson, M. K., Mason, J. T., Hirasawa, M., Leustek, T., and Knaff, D. B. (2004) Properties of the cysteine residues and iron-sulfur cluster of the assimilatory 5'-adenylyl sulfate reductase from *Pseudomonas aeruginosa*, *Biochemistry 43*, 13478-13486.

15. Carroll, K. S., Gao, H., Chen, H., Leary, J. A., and Bertozzi, C. R. (2005) Investigation of the iron-sulfur cluster in *Mycobacterium tuberculosis* APS reductase: implications for substrate binding and catalysis, *Biochemistry 44*, 14647-14657.

16. Kopriva, S., Fritzemeier, K., Wiedemann, G., and Reski, R. (2007) The putative moss 3'-phosphoadenosine-5'-phosphosulfate reductase is a novel form of adenosine-5'-phosphosulfate reductase without an iron-sulfur cluster, *J. Biol. Chem. 282*, 22930-22938.

17. Bhave, D. P., Hong, J. A., Lee, M., Jiang, W., Krebs, C., and Carroll, K. S. (2011) Spectroscopic studies on the [4Fe-4S] cluster in adenosine 5'-phosphosulfate reductase from *Mycobacterium tuberculosis*, *J. Biol. Chem. 286*, 1216-1226.

18. Chartron, J., Carroll, K. S., Shiau, C., Gao, H., Leary, J. A., Bertozzi, C. R., and Stout, C. D. (2006) Substrate recognition, protein dynamics, and iron-sulfur cluster in *Pseudomonas aeruginosa* adenosine 5'-phosphosulfate reductase, *J. Mol. Biol. 364*, 152-169.

19. Hong, J. A., Bhave, D. P., and Carroll, K. S. (2009) Identification of critical ligand binding determinants in *Mycobacterium tuberculosis* adenosine-5'-phosphosulfate reductase, *J. Med. Chem. 52*, 5485-5495.

20. Cosconati, S., Hong, J. A., Novellino, E., Carroll, K. S., Goodsell, D. S., and Olson, A. J. (2008) Structure-based virtual screening and biological evaluation of *Mycobacterium tuberculosis* adenosine 5'-phosphosulfate reductase inhibitors, *J. Med. Chem. 51*, 6627-6630.

21. Yu, Z., Lemongello, D., Segel, I. H., and Fisher, A. J. (2008) Crystal structure of *Saccharomyces cerevisiae* 3'-phosphoadenosine-5'-phosphosulfate reductase complexed with adenosine 3',5'-bisphosphate, *Biochemistry 47*, 12777-12786.

22. Savage, H., Montoya, G., Svensson, C., Schwenn, J. D., and Sinning, I. (1997) Crystal structure of phosphoadenylyl sulphate (PAPS) reductase: a new family of adenine nucleotide alpha hydrolases, *Structure 5*, 895-906.

23. Witt, A. C., Lakshminarasimhan, M., Remington, B. C., Hasim, S., Pozharski, E., and Wilson, M. A. (2008) Cysteine pK_a depression by a protonated glutamic acid in human DJ-1, *Biochemistry 47*, 7430-7440.

24. Hutchison, A., Grim, M., and Chen, J. (1989) A Short and Stereoselective Synthesis of (+/-)-Aristeromycin, *J. Heterocyclic. Chem. 26*, 451-452.

25. Sawai, H., and Ohno, M. (1985) Preparation of Cyclic-Amp Derivatives by Intramolecular Phosphodiester Bond Formation Catalyzed by Pb-2+ Ion, *Chem. Pharm. Bull. 33*, 432-435.

26. Carroll, K. S., Gao, H., Chen, H., Stout, C. D., Leary, J. A., and Bertozzi, C. R. (2005) A conserved mechanism for sulfonucleotide reduction, *PLoS Biol. 3*, e250.

27. Hernick, M., and Fierke, C. A. (2006) Catalytic mechanism and molecular recognition of E. coli UDP-3-O-(R-3-hydroxymyristoyl)-N-acetylglucosamine deacetylase probed by mutagenesis, *Biochemistry 45*, 15240-15248.

28. Noda, L. H., Kuby, S. A., and Lardy, H. A. (1953) Properties of Thiolesters - Kinetics of Hydrolysis in Dilute Aqueous Media, *J. Am. Chem. Soc. 75*, 913-917.

29. Polgar, L. (1974) Mercaptide - Imidazolium Ion-Pair - Reactive Nucleophile in Papain Catalysis, *Febs. Lett. 47*, 15-18.

30. Dawson, R. M., C.E., D. C., Elliott, W. H., and Jones, K. M. (1989) *Data for Biochemical Research*, 3 ed., Oxford University press, Oxford.

31. Herold, J. M., Wigle, T. J., Norris, J. L., Lam, R., Korboukh, V. K., Gao, C., Ingerman, L. A., Kireev, D. B., Senisterra, G., Vedadi, M., Tripathy, A., Brown, P. J., Arrowsmith, C. H., Jin, J., Janzen, W. P., and Frye, S. V. (2011) Small-molecule ligands of methyl-lysine binding proteins, *J. Med. Chem. 54*, 2504-2511.

32. Leavitt, S., and Freire, E. (2001) Direct measurement of protein binding energetics by isothermal titration calorimetry, *Curr. Opin. Struc. Biol. 11*, 560-566.

33. Cosconati, S., Hong, J. A., Novellino, E., Carroll, K. S., Goodsell, D. S., and Olson, A. J. (2008) Structure-based virtual screening and biological evaluation of *Mycobacterium tuberculosis* adenosine 5'-phosphosulfate reductase inhibitors, *J. Med. Chem. 51*, 6627-6630.

Chapter 5

Spectroscopic studies on the [4Fe-4S] cluster in adenosine 5'-phosphosulfate reductase from *Mycobacterium tuberculosis*

This work has been published as "Spectroscopic studies on the [4Fe-4S] cluster in adenosine 5'-phosphosulfate reductase from *Mycobacterium tuberculosis*." *J. Biol. Chem.* **2011**, 286, 1216-1226. My contributions to this work include generation of Lys144Ala APR by site-directed mutagenesis and measuring APR kinetic parameters.

5.1 Abstract

Mycobacterium tuberculosis adenosine 5′-phosphosulfate (APS) reductase (MtAPR) is an iron-sulfur protein and a validated target to develop new antitubercular agents, particularly for the treatment of latent infection. The enzyme harbors a $[4Fe\text{-}4S]^{2+}$ cluster that is coordinated by four cysteinyl ligands, two of which are adjacent in the amino acid sequence. The iron-sulfur cluster is essential for catalysis; however, the precise role of the [4Fe-4S] cluster in APR remains unknown. Progress in this area has been hampered by the failure to generate a paramagnetic state of the [4Fe-4S] cluster that can be studied by electron paramagnetic resonance spectroscopy. Herein, we overcome this limitation and report the EPR spectra of MtAPR in the $[4Fe\text{-}4S]^{+}$ state. The EPR signal is rhombic and consists of two overlapping $S = \frac{1}{2}$ species. Substrate binding to MtAPR led to a marked increase in intensity and resolution of the EPR signal, and to minor shifts in principle *g* values that were not observed among a panel of substrate analogs, including adenosine 5′-diphosphate. Using site-directed mutagenesis,

in conjunction with kinetic and EPR studies, we have also identified an essential role for the active site residue, Lys144 whose side chain interacts with both the iron-sulfur cluster and the sulfate group of APS. The implications of these findings are discussed with respect to the role of the iron-sulfur cluster in the catalytic mechanism of APR.

5.2 Introduction

In bacteria and plants, activation of inorganic sulfur is required for *de novo* biosynthesis of cysteine. To this end, the metabolic assimilation of sulfate from the environment proceeds *via* adenosine 5′-phosphosulfate (APS) or 3′-phosphoadenosine-5′-phosphosulfate (PAPS) (1). These intermediates are produced by the action of ATP sulfurylase (EC 2.7.7.4), which condenses sulfate and ATP to form APS (*2, 3*), and by APS kinase (EC 2.7.1.25), which produces PAPS from ATP and APS (*6*).

Scheme 5.1. Reaction catalyzed by sulfonucleotide reductases.

Figure 5.1. Proposed mechanism of sulfonucleotide reduction.
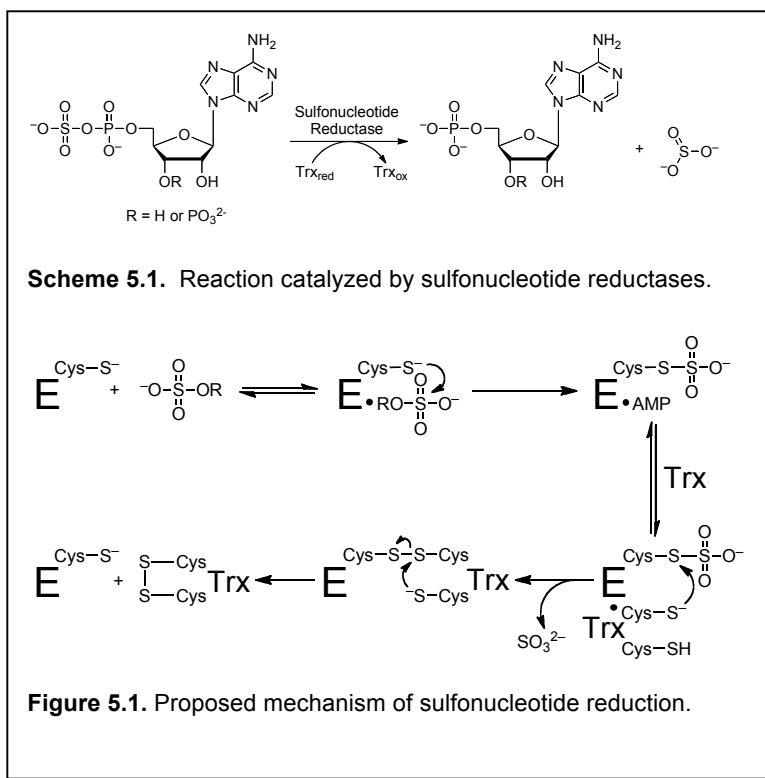
APS and PAPS are reduced by enzymes in the reductive branch of the sulfate assimilation pathway, producing sulfite and adenosine 5′-monophosphate (AMP) or adenosine 3′,5′-diphosphate (PAP) (see Scheme 5.1). These enzymes can be subdivided into two groups

according to their substrate preference, the APS reductases (APR) and the PAPS reductases (PAPR) (EC 1.8.99.4). Functional and structural studies have been used to investigate the chemical reaction mechanism of APR and PAPR enzymes (*1, 7-10*). The mechanism involves nucleophilic attack by the active site cysteine on the sulfur atom of APS or PAPS to form an enzyme *S*-sulfocysteine intermediate (E-Cys-$S\gamma$-SO_3^-), which is cleaved by thiol-disulfide exchange with thioredoxin or glutaredoxin (Figure 5.1). The sulfite product is then reduced to sulfide by sulfite reductase (EC 1.8.7.1) and utilized to synthesize cysteine and other essential sulfur-containing biomolecules (*12*). In the human pathogen *Mycobacterium tuberculosis*, APR is a validated target against the latent phase of infection (*13*).

Only a 3′-phosphate group distinguishes PAPS from APS. Accordingly, APR and PAPR have nearly identical three-dimensional structures (1.6–Å rms deviation of backbone atoms) and share ~20% sequence identity, including the active site motif, ECG and the sulfonucleotide binding pocket (*4, 7, 14*). However, a key difference between the two enzymes is that APR contains two conserved cysteine motifs, CXXC and CC. These four additional cysteine residues coordinate a [4Fe-4S] cluster, which is essential for catalytic activity (*1, 7, 15*). The only known exception is *Physcomitrella patens* sulfonucleotide reductase, PpAPR-B that lacks the cysteine pairs required to bind the cofactor, but can utilize both APS and PAPS as substrates (*16*). However, PpAPR-B has to pay a significant penalty for the absence of the [4Fe-4S] cluster as evidenced by second-order rate constants (k_{cat}/K_m) of 3,520 and 37 $M^{-1}s^{-1}$ with APS and PAPS, respectively.

The 2.7 Å crystal structure of *Pseudomonas aeruginosa* APR (PaAPR) bound to substrate provides valuable insights into the arrangement of active site residues that are conserved among APRs[5] (*7*). The iron-sulfur cluster is coordinated by Cys228 and Cys231, positioned at the tip of a β-loop, along with the tandem pair, Cys139 and Cys140, within an α-helix (Figure 5.2A). Coordination by sequential cysteines is highly unusual for [4Fe-4S] clusters and has been characterized in only one other crystal structure – the NuoB subunit of respiratory complex I (*17*). There are four charged and/or polar NH···S or OH···S hydrogen bonds involving side-chains of absolutely conserved residues (Figure 5.2B and C). In particular, the CysCys motif interacts with a pair of basic residues, Arg143 and Lys144. Other interactions with the iron-sulfur cluster involve Thr87 and Trp246. In the active site the phosphosulfate group of APS is positioned opposite the [4Fe-4S] cluster and, while no atoms intervene, the sulfate moiety is not in direct contact with the [4Fe-4S] cluster.

Given the unusual CysCys dyad coordination and its requirement for catalytic activity, defining the function and properties of the iron-sulfur cluster in APR has generated considerable interest (*1, 7, 9, 18, 19*). Most proteins containing [4Fe-4S] clusters are redox-active (*20-23*), however, the [4Fe-4S]$^{2+}$ cluster in APR does not undergo redox changes during the catalytic cycle (*1*). A purely structural role also appears unlikely, in light of biophysical data obtained on the apo form of APR (*8, 15, 18*) and the fact that APR and PAPR share a common protein fold (*4, 7, 14*). Unfortunately, progress in this area has been hampered by the failure to generate a paramagnetic state of the [4Fe-4S] cluster that can be studied by electron paramagnetic resonance (EPR) spectroscopy and related methods (*18, 19, 24*).

---

[5] Residue numbers in the text correspond to the PaAPR amino acid sequence. The corresponding residue numbers in MtAPR can be identified from the sequence alignment depicted in Appendix 5.7.1.

Herein, we report the EPR spectra of MtAPR in the [4Fe-4S]$^+$ state. The EPR spectrum of MtAPR displays a rhombic signal, but is complex and consists of at least two overlapping $S = \frac{1}{2}$ species. Mössbauer studies of the native and reduced forms confirm the presence of a [4Fe-4S]$^{2+/1+}$ cluster. APS binding to MtAPR is accompanied by marked sharpening of the EPR signal and an increase in intensity, which is not observed among a panel of substrate analogs, including adenosine 5′-diphosphate (ADP). In addition, kinetic and EPR investigation of the Lys144Ala variant of MtAPR demonstrate a key function for this residue in catalysis and as a link
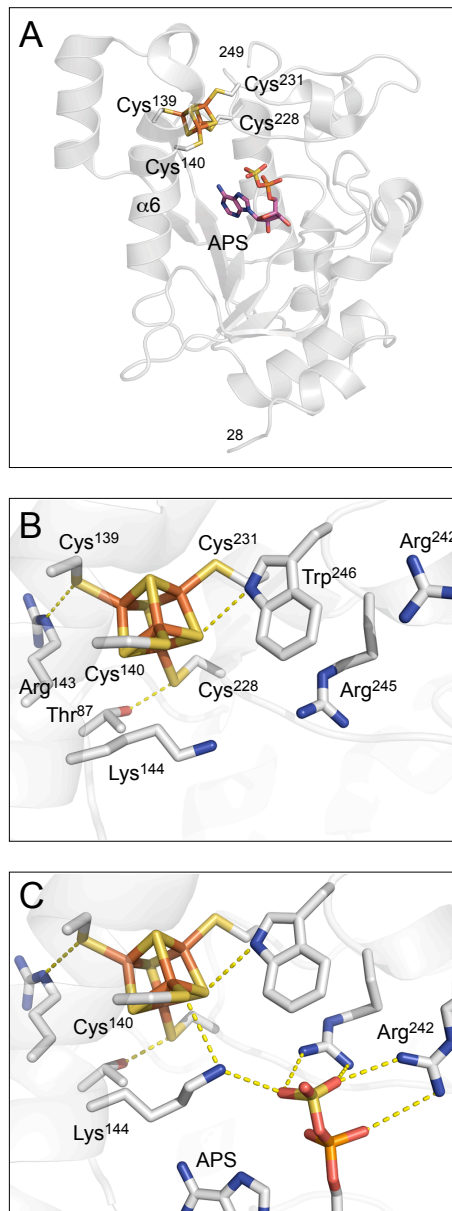
Figure 5.2. The environment of the [4Fe-4S] cluster in PaAPR. *A.* The structure of PaAPR bound to substrate APS. The [4Fe-4S] cluster is ligated by four cysteine residues at positions 139, 140, 228 and 231. PDB code: 2GOY. *B.* Four conserved residues participate in charged or polar NH…S or OH…S hydrogen bonds to inorganic S or cysteine Sγ atoms; Thr87, Arg143, Lys144 and Trp246 (yellow dashes). PDB code: 2GOY, chain A. *C.* Conserved basic residues Lys144, Arg242 and Arg245 in the active site interact with the phosphate and sulfate groups of APS (yellow dashes). Residues that also interact with APS, but are not depicted in this Figure 6.are Arg171 and His259; these residues interact with the α-phosphate group. The shortest distance between a sulfate oxygen atom and a cysteine sulfur atom coordinated to the [4Fe-4S] cluster is 6.0 Å. PDB code: 2GOY, chain B.

between APS and the iron-sulfur cluster. These data, together with known functional and structural information, directly implicate the iron-sulfur cluster in the catalytic mechanism of APS.

5.3. Results

5.3.1 Purification and Spectroscopic Characterization of the [4Fe-4S]$^{2+}$ Cluster in MtAPR.

We have previously reported conditions for the purification of MtAPR (*1*). However, yields from these preparations were low owing to the large quantity of MtAPR present in the insoluble protein fraction. In order to improve the yield and stability of purified MtAPR, we co-expressed the MtAPR gene with the gene products of the *isc* operon required for iron-sulfur cluster biosynthesis in *A. vinelandii* (*25*). Under these conditions the yield of MtAPR was typically 7 mg/L of culture, which represents an improvement over ~1 mg/L obtained when MtAPR is over-expressed in the absence of the *isc* proteins. The specific activity of the purified enzyme was 5 μM min^{-1} mg protein^{-1} with thioredoxin and DTT as reductants. The UV-Vis absorbance spectrum of MtAPR showed a maximum in the visible range at 410 nm that is consistent with the presence of bound Fe (Appendix 5.7.2). Analysis of Fe content by inductively coupled plasma resonance spectrometry for MtAPR indicated that each mole of protein contained 3.5 ± 0.4 mol of Fe, which is indicative of 4 Fe atoms in the cluster. The intensity of the 410 nm peak was unaffected on addition of sodium dithionite (data not shown), but increased slightly on addition of APS (Appendix 5.7.2). These results are analogous to those found for PaAPR (*8*). The minor increase in absorption at 410 nm could reflect substrate-dependent conformational changes within the C-terminal region and a concomitant alteration in cluster environment.

The 4.2-K/53-mT Mössbauer spectrum of MtAPR confirmed the presence of a $[4Fe-4S]^{2+}$ cluster (Figure 5.3). The majority of the Fe (~90%) gives rise to a quadrupole doublet with parameters typical of $[4Fe-4S]^{2+}$ clusters: isomer shift (δ) of 0.45 mm/s and quadrupole splitting parameter (ΔE_Q) of 1.09 mm/s. The appearance of a small peak at ~0.6 mm/s is indicative of a small amount of $[2Fe-2S]^{2+}$ clusters (δ = 0.25 mm/s, ΔE_Q = 0.55 mm/s, ~7% of total intensity). The $[2Fe-2S]^{2+}$ cluster
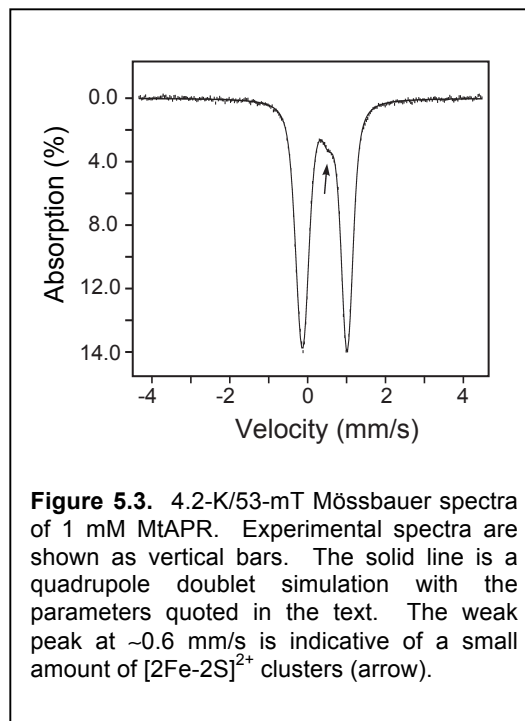
Figure 5.3. 4.2-K/53-mT Mössbauer spectra of 1 mM MtAPR. Experimental spectra are shown as vertical bars. The solid line is a quadrupole doublet simulation with the parameters quoted in the text. The weak peak at ~0.6 mm/s is indicative of a small amount of $[2Fe-2S]^{2+}$ clusters (arrow).

form of MtAPR has also been observed by ESI-FT-ICR MS (*15*) and is most likely caused by aerobic degradation, analogous to other $[4Fe-4S]^{2+}$ proteins. On addition of APS, the Mössbauer spectrum of MtAPR was nearly identical to that in the absence of substrate (Appendix 5.7.3) and can be simulated as a superposition of two quadrupole doublets representing the $[4Fe-4S]^{2+}$ clusters (δ = 0.45 mm/s, ΔE_Q = 1.12 mm/s, 90%) and $[2Fe-2S]^{2+}$ clusters (δ = 0.25 mm/s, ΔE_Q = 0.55 mm/s, 10%).

5.3.2 Photoreduction of the $[4Fe-4S]^{2+}$ cluster in MtAPR.

As-isolated APR from higher plants and *P. aeruginosa* exhibits weak isotropic signals at *g* = 2.01 attributed to a small proportion of $[3Fe-4S]^+$ cluster and at *g* = 4.3 from high-spin Fe(III) (*18, 19, 24*). When MtAPR was prepared according to the previous method (*15*), similar resonances were observed (data not shown). However, such EPR signals were not present in samples of MtAPR produced via the improved co-expression system. Earlier attempts to generate new EPR signals in assimilatory APR from higher plants

and bacteria by titrating the enzyme with dithionite, Ti(III)citrate or photochemical reduction with the deazaflavin/oxalate system have proven unsuccessful (*18, 19, 24*). Similarly, our earlier studies of MtAPR found no evidence for the presence of [4Fe-4S]$^+$ after treatment with dithionite (*15*).

In the present study, we first explored reduction of the cluster in MtAPR using Ti(III)citrate. New EPR signals were observed, however, interpretation of the spectra was confounded by nonspecifically bound Ti(III)citrate that gave rise to an isotropic signal at $g = 1.94$ (data not shown). Next, we tested photoreduction of the [4Fe-4S]$^{2+}$ center in MtAPR in the presence of deazaflavin/oxalate. The resulting EPR spectrum is broad, but shows rhombic symmetry with apparent g-values of 2.04, 1.94 and 1.75 (Figure. 5.4*A*). The EPR signal also gives evidence for a second component with apparent g-values at 2.13
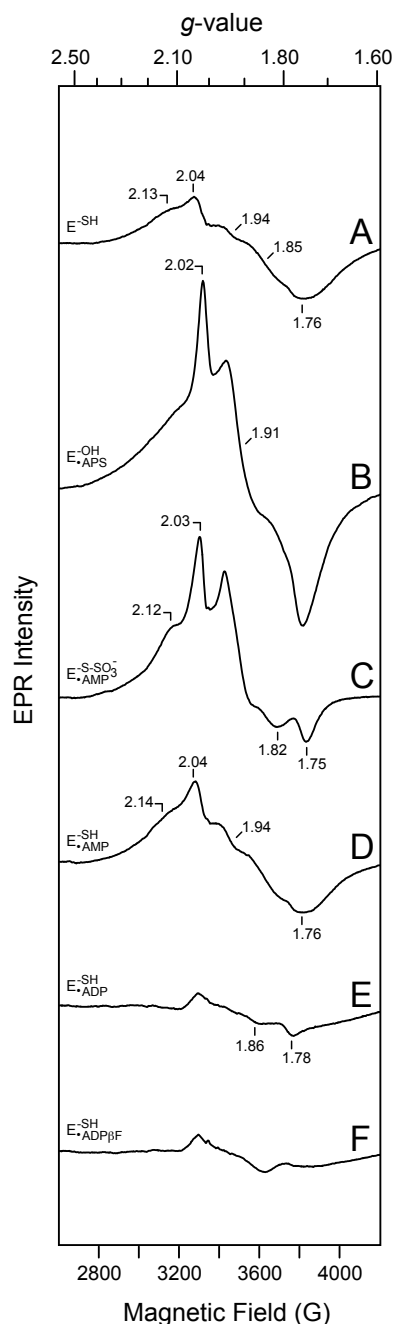
Figure 5.4. Experimental EPR spectra of photoreduced MtAPR. Anaerobic 250 μM MtAPR alone or incubated with 1 mM ligand for 10 min at 25 °C was then photoreduced as described in Experimental Procedures. Samples: *A.* MtAPR alone. *B.* Cys256Ser MtAPR bound to APS. *C.* MtAPR incubated with APS to generate the *S*-sulfocysteine intermediate bound to AMP. *D.* MtAPR bound to AMP. *E.* MtAPR bound to ADP. *F.* MtAPR bound to ADPβF. The EPR spectra were recorded at 10 K and the instrument parameters were: microwave power, 10 mW; receiver gain, 2 x 10^4; modulation amplitude, 10 G; microwave frequency, 9.43 GHz.

and 1.85; however, the broad resonances precluded an accurate simulation of the two paramagnetic species. Spin quantitation of the EPR signals from g = 2.5 to 1.3 indicate 0.3 equiv of spins per mole of enzyme. On the basis of observed g-values, the resonances can be attributed to either an S = ½ $[2Fe-2Fe]^+$ or $[4Fe-4S]^+$ cluster. The temperature dependence of the EPR signal (data not shown) indicated that it was maximal between 8-10 K and was no longer visible at temperatures above 12 K, using a microwave power of 10 mW. This behavior suggests that the paramagnetic signal arises from a $[4Fe-4S]^+$ cluster. By contrast, $[2Fe-2S]^+$ clusters are slow relaxing and observable by EPR at temperatures above 70 K (*26*).

5.3.3 Interaction of the Photoreduced [4Fe-4S]⁺ Cluster with Substrate and Analogs.

The [4Fe-4S] cluster at the active site of APR is required for catalytic activity (1); however, the mechanistic details are unknown and remain a central question for this family of

Figure 5.5. Simulated EPR spectrum of photoreduced wild-type MtAPR after addition of APS. The bottom two spectra show how two separate species might combine to give the observed signal (top spectra, solid line; see also Figure 5.4*C*). The dashed lines denote the simulated EPR spectrum, which is the sum of two components: Component A is a spectral simulation of the narrow component using g = 2.04, 1.94, 1.76, g strain (σ_g) = 0.017, 0.022, 0.020, and a Gaussian line shape. Component B is a spectral simulation of the broad component using g = 2.10, 1.88, 1.75, g strain (σ_g) = 0.038, 0.036, 0.099, and a Gaussian line shape. The ratio of Component A to Component B is 1:1.2. Simulated instrument parameters are as reported in the legend of Figure 5.4.

enzymes. While the iron-sulfur cluster in APR does not undergo redox activity during the catalytic cycle (1), the 1+ state of APR can serve as a useful tool for mechanistic studies analogous to other enzymes that harbor redox-inactive iron-sulfur clusters such as aconitase (27). Therefore, to gain insight into the functional role of the cluster we next investigated whether substrate binding would perturb the EPR spectrum of reduced MtAPR. Two types of protein-ligand complexes were prepared: (i) wild-type MtAPR treated with APS to afford the S-sulfocysteine intermediate form of the enzyme bound to AMP, and (ii) the catalytically inactive variant, Cys256Ser MtAPR bound to APS. Established procedures for complex formation were performed (1, 15) and the resultant samples were then subjected to photoreduction.

Compared to wild-type MtAPR (Figure 5.4A), the EPR spectrum of Cys256Ser MtAPR bound to APS is markedly sharper in appearance with apparent g-values of 2.02, 1.91 and 1.76 (Figure 5.4B). The EPR signal of the enzyme S-sulfocysteine intermediate bound to AMP also exhibits increased resolution with apparent g-values of 2.03, 1.91 and 1.75 (Figure 5.4C). Additionally, both spectra (Figure 5.4B and C) indicate the presence of a second paramagnetic species. Spin quantitation of EPR signals from $g =$ 2.7 to 1.6 indicate a respective 0.45 and 0.4 equiv of spin per mole for the Cys256Ser and wild-type MtAPR complexes. The heterogeneity of these samples was essentially unaffected by the addition of 2.5 M urea, changes in sample pH between the ranges of 7.5 and 9.5, variation in temperature or microwave power levels (data not shown).

Simulation of the signal from wild-type MtAPR treated with APS suggests that it is the sum of at least two $S = \frac{1}{2}$ components (Figure 5.5). One species has narrow lines and g-values at 2.04, 1.94, and 1.76 (component A), whereas the other has broad lines and exhibits principle g-values at 2.10 and 1.88 (component B) with an intensity ratio of 1:1.2.

Although simulated and experimental spectra are in overall agreement, some discrepancies remain, particularly with respect to signal amplitudes. The addition of a third spectral component did not improve the fit quality. However, residual differences between the simulated and experimental spectra may result from weak signal intensity, minor fluctuations in temperature around 10 K, or the large number of variables required to simulate a $[4Fe-4S]^+$ cluster.

Next, we tested whether the observed APS-dependent changes in the EPR spectra of reduced MtAPR were specific to the substrate. To investigate this possibility, we analyzed the spectra of photoreduced MtAPR bound to AMP, ADP and ADPβF. The EPR signal of MtAPR bound to AMP (Figure 5.4D) was similar in shape and intensity to enzyme alone (Figure 5.4A). By contrast, the spectrum in the presence of ADP (Figure 5.4E) showed a significant reduction in signal intensity. To determine whether the observed changes in the EPR spectrum were due to the additional negative charge at a β-phosphate group (*i.e.,* ADP) relative to a β-sulfate group (*i.e.,* APS), we examined fluorine substitution of a β-nonbridging oxygen atom. Interestingly, however, the EPR spectrum of MtAPR bound to ADPβF (Figure 5.4F) was essentially the same as ADP (Figure 5.4E). Spin quantitation of MtAPR bound to ADP or ADPβF indicate less than 0.1 equiv of spins per mole of enzyme in each sample. The marked increase in signal resolution and intensity in the presence of APS, but not upon addition of substrate analogs or product reflects a unique state of the active site and cluster environment, which might be related to catalytic activity.

5.3.4 Characterization of Lys144Ala MtAPR.

The preceding EPR data support the existence of mid-range electrostatic interactions between the cluster and APS. Given that the side chain of Lys144 is positioned between coordinating Cys140 and the β-sulfate group of APS (Figure 5.2C) we reasoned that this residue might help mediate this interaction. To investigate this possibility, we generated the Lys144Ala MtAPR variant and characterized this protein through kinetic and EPR studies. An effect of 63,000-fold on k_{cat}/K_M is observed upon mutation of Lys144 to Ala (Table 1; see also Appendix 5.7.4). Since the chemical step (*i.e.,* *S*-sulfocysteine formation) is rate limiting for the reaction of APS and MtAPR (*5*), this value represents the effect of removal of the Lys residue on the overall binding and chemical transformation. The mutation decreases the value of k_{max} by 270-fold suggesting that the Lys side chain stabilizes the transition state relative to the ground state complex. To further explore the molecular recognition of APS, we measured the K_d value of the substrate for Lys144Ala MtAPR. Relative to wild-type MtAPR, the affinity of APS for Lys144Ala is decreased by 400-fold.

Table 5.1: Effect of Lys144Ala Mutation on APR-Catalyzed Reduction and Binding of APS[a]

	k_{cat}/K_m (M^{-1} s^{-1})[b]	fold reduction	k_{max} (min^{-1})[c]	fold reduction	K_d (µM)	fold reduction
Wild-type	2.5×10^6	(1)	2.7	(1)	0.25[d]	(1)
Lys144Ala	40	6.3×10^4	0.01	270	≥100[e]	≥400

[a]Rate constants for single-turnover reactions were determined at 30 °C in 100 mM bis-tris propane buffer, 5 mM DTT, 10 µM Trx as described in Experimental Procedures. In all cases, the protein was in excess over substrate, with at least 2.5-fold more protein than substrate. [b]In bis-tris propane at pH 7.5. [c]In bis-tris propane at pH 6.5. [d]From Ref. (*5*). [e]The apparent K_d value was determined at 30 °C in 100 mM bis-tris propane pH 7.5 as described in Experimental Procedures.

The UV-Vis absorbance spectrum of Lys144Ala MtAPR showed a maximum in the visible range at 410 nm that is consistent with the presence of bound Fe (data not shown). Analysis of Fe content by inductively coupled plasma resonance spectrometry

for Lys144Ala MtAPR indicated that each mole of protein contained 3.3 ± 0.4 mol of Fe,

which is consistent with 4 Fe atoms in the cluster. Photoreduction of Lys144Ala MtAPR gave rise to a rhombic signal with resonances at g = 2.12, 1.99 and 1.82 (Figure 5.6A and C). However, the signal intensity was decreased relative to wild-type MtAPR and spin quantitation accounted for less than 0.05 equiv of spins per mole of enzyme. In the presence of saturating APS, the feature at g = 1.75 disappears and the remaining signal exhibits g-values at 2.12 and 1.99 (Figure 5.6B and D). A low-field isotropic Fe^{3+} signal accounting for less than 0.01 equiv of spin per mole of enzyme was also observed in the presence of APS, consistent with a small degree of cluster degradation (data not shown). Although the EPR spectra for both samples are relatively broad and weak, a modest reduction in the magnetic heterogeneity of MtAPR can be observed. Together, the kinetic and EPR data indicate a key role for Lys144 in chemistry and substrate
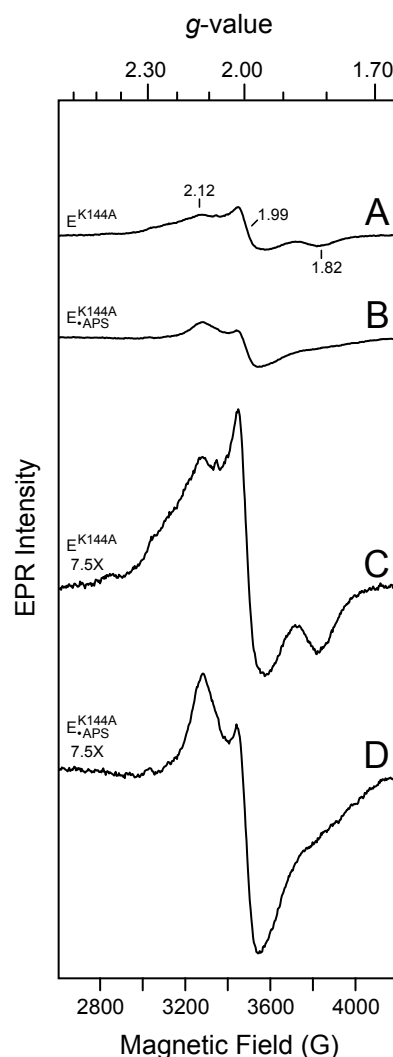
Figure 5.6. Experimental EPR spectra of photoreduced Lys144Ala MtAPR. Anaerobic 250 μM Lys144Ala MtAPR alone (A) and (C) or incubated with 1 mM APS (B) and (D) for 10 min at 25 °C was then photoreduced as described in Experimental Procedures. In (A) and (B) EPR signal intensities have been scaled to match those in Figure 5.4. In (C) and (D) the intensity of the EPR signals has been scaled 7.5-fold. The EPR spectra were recorded at 10 K and the instrument parameters were: microwave power, 10 mW; receiver gain, 2 x 10^{4}; modulation amplitude, 10 G; microwave frequency, 9.43 GHz.

binding, and that this residue helps modulate APS-dependent changes in the iron-sulfur cluster environment.

5.3.5 Cryoreduction of the [4Fe-4S]$^{2+}$ Cluster in MtAPR.

Although the [4Fe-4S]$^+$ cluster serves as a useful spectroscopic tool in the study of MtAPR and variants, we recognize that it is not the native form of the active enzyme. For this reason, we attempted to probe the interaction of substrate with the [4Fe-4S]$^{2+}$ state of MtAPR through cryoreduction-EPR studies. In principle, γ-irradiation of the frozen [4Fe-4S]$^{2+}$ cluster affords the reduced state [4Fe-4S]$^+$ trapped in the geometry of the [4Fe-4S]$^{2+}$ oxidized state (*28, 29*). To this end, the 2+ state of MtAPR was incubated in the presence or absence of APS, frozen in liquid nitrogen and then exposed to high-energy γ-irradiation at 77 K to produce the [4Fe-4S]$^+$ cluster.

The resulting spectrum in the absence of substrate (Appendix 5.7.5) is ill defined and relatively broad. However, the addition of substrate APS was accompanied by a marked increase in signal intensity and resolution with apparent *g*-values at 2.08, 2.04 and 2.02 (Appendix 5.7.5). The observation of substrate-dependent changes in the EPR spectrum is in qualitative agreement with our experimental results from photoreduction. However, we note that the EPR spectra of cryoreduced MtAPR are distinct from those of the photochemically reduced enzyme. These findings may indicate that the substrate interacts differently with the cluster in the +2 and +1 states. An alternative possibility is that the observed EPR signals correspond to a thiyl radical formed by homolytic scission of the *S*-sulfocysteine bond. In support of this proposal, the relatively high *g*-values are consistent with literature data for a sulfur-centered species (*30, 31*).

In addition to the aforementioned g-values, the cryoreduced samples contained an extremely intense signal isotropic signal at g = 2, which could arise from other non-specifically reduced organic radicals present in the sample (Appendix 5.7.5). 4.2-K/53-mT Mössbauer spectra of samples recorded before and after cryoreduction (Appendix 5.7.6) indicate that ~50% of the $[4Fe-4S]^{2+}$ clusters were reduced to the +1 state under these conditions. Thus, Mössbauer analysis confirms the presence of the $[4Fe-4S]^{+}$ cluster in cryoreduced samples; however, the γ-irradiation also appears to have generated extremely intense, new paramagnetic species that are distinct from a simple one-electron reduction of the +2 cluster. Lastly, no significant changes in the Mössbauer spectra from substrate-bound and substrate-free cryoreduced MtAPR were observed (Appendix 5.7.6).

5.3.6 Ferricyanide Oxidation of the $[4Fe-4S]^{2+}$ Cluster in MtAPR.

The $[4Fe-4S]^{2+}$ cluster in PaAPR is partially converted to the $[3Fe-4S]^{+}$ form by treatment with the oxidant potassium ferricyanide (*18*). To assess this possibility for MtAPR, a stoichiometric amount of potassium ferricyanide was added to the enzyme. The resulting EPR signal shows a well-defined EPR resonance at g = 2.03 and a poorly resolved high-field component at g = 1.99 (Appendix 5.7.7). This pattern of EPR signals is very similar to those of S = ½ $[3Fe-4S]^{+}$ clusters in aconitase (*27*) and endonuclease III (*32*). Spin quantitation of the EPR signals from g = 2.1 to 1.8 indicate less than 0.1 equiv of spins per mole of enzyme. The EPR spectrum of oxidized MtAPR also exhibited a signal accounting for less than 0.01 equiv of spins per mole of enzyme at g = 4.3 that is characteristic of high-spin Fe(III). When ferricyanide was added to MtAPR that had been pre-treated with APS, the intensity of the signal at g = 4.3 was increased by 3-fold (data not shown). Attempts to purify the $[3Fe-4S]^{+}$ cluster form of MtAPR were unsuccessful as the cluster rapidly decomposed upon oxidant removal. Nonetheless,

these data are consistent with the existence of a labile Fe site within the $[4Fe-4S]^{2+}$ cluster of MtAPR. Given the constraints of tandem Cys coordination (*7*) and the proximity of Lys144, the Fe coordinated to Cys140 may correspond to the displaced atom.

5.4 Discussion

Iron-sulfur clusters are amazingly versatile cofactors with functions in electron transfer, Lewis acid-assisted enzyme catalysis, radical generation, oxidation of a wide variety of substrates under anaerobic conditions, and protein structure (*33-38*). While numerous studies indicate that the iron-sulfur cluster is essential for APR activity (*1, 7, 9, 15*), the specific role of the iron-sulfur cluster has been elusive. Progress on this front has been limited, in part, by the inability to generate a paramagnetic state of the [4Fe-4S] cluster that can be studied by EPR spectroscopy. The present study is the first reported case in which the $[4Fe-4S]^{2+}$ cluster of APR has been reduced to the $S = \frac{1}{2}$ $[4Fe-4S]^{+}$ form.

Photoreduction in the presence of deazaflavin and oxalate turned out to be the most effective method to generate the paramagnetic 1+ state of MtAPR. By contrast, attempts to photochemically reduce APR from plants and bacteria such as *P. aeruginosa* and *B. subtilis* have not been successful (*15, 24*). Active site residues that interact with the iron-sulfur cluster and/or the substrate (*e.g.,* Thr87, Arg143, Lys144, Arg242, Arg245, Trp246) are highly conserved among APRs and therefore, are unlikely to account for EPR behavioral differences. On the other hand MtAPR is a monomer in solution while APR from other species exists as a homodimer or homotetramer (*1, 19*). Along these lines, the structure of PaAPR shows that the face of the iron-sulfur cluster opposite the active site is buried at the interface between two monomeric subunits (*7*). Studies on the effect of solvent on redox potentials of model clusters indicate that water raises the

118

reduction potential of the $[4Fe-4S]^{2+/+}$ couple (*39, 40*). Hence, increased solvent accessibility to the cluster of monomeric MtAPR may account for the ability to generate the 1+ state.

The EPR signal of reduced MtAPR arises from a mixture of $[4Fe-4S]^+$ clusters with *S* = ½, possibly reflecting the existence of distinct conformational states. Multiple *S* = ½ ground states have been observed for other [4Fe-4S] iron-sulfur enzymes such as the corrinoid protein from *Clostridium thermoaceticum* (*41*), human DNA primase (*42*), and the ribosomal RNA methyltransferase, RumA (*43*). The apparent lack of changes in the EPR spectra between pH 6.5 and 9.5 suggests that the complexity does not result from differences in protonation state of residues near the iron-sulfur cluster. Freezing of samples after photoreduction can also led to multiple signals from the same paramagnetic center – one from aggregated protein molecules and the other from dispersed molecules (*44*). To investigate this possibility, we recorded the EPR spectrum for cryoreduced MtAPR. In these experiments, the EPR signal that arises from the [4Fe-4S]$^+$ form of MtAPR is weak relative to other radical species generated during the γ-irradition process. Nonetheless, magnetic heterogeneity is still apparent in the spectrum (Appendix 5.7.5). Treatment with 1-2.5 M urea has also been reported to convert multiple isomeric states of an [4Fe-4S]$^+$ cluster into a single one (*41*), but this was not the case with MtAPR. This observation may indicate the existence of more subtle differences between cluster forms in MtAPR such as changes in the orientation of a Cys-Sγ-Fe bond or in hydrogen bonding to a sulfur atom.

Regarding possible conformational changes, PaAPR has been fortuitously crystallized with APS bound in two of the four monomeric subunits (*7*). A comparison of bound and

unbound states reveals minor structural changes in residues adjacent to the iron-sulfur cluster (Figure 5.2B and C).   In the absence of substrate, Lys144 is present in an extended conformation such that the distance between the side chain and the Sγ atom of Cys140 is ~5 Å. By contrast, the subunit with APS bound shows that the side chain of Lys144 adopts a bent rotamer conformation, which brings this residue within interaction range (*i.e.,* 3.5 Å) of Cys140 Sγ. In turn, the Cys140 side chain moves slightly upward (*i.e.,* 5° rotation at the β-carbon). It is possible then, that the heterogeneity observed in the EPR spectra may be related to conformational dynamics of Lys144, Cys140 and/or Cys256 within the C-terminus. In support of this hypothesis, a decrease in EPR signal complexity was observed with Lys144Ala MtAPR (Figure 5.6). Structural changes at these key residues may also account for the observation that the iron-sulfur cluster of APR is protected from oxidation on addition of APS (*15*) and that the resonance Raman spectra exhibit changes in Fe-Sγ stretching modes when substrate is bound (*8*).

Previous models for the role of the iron-sulfur cluster in APR catalysis have postulated that one or two non-bridging sulfate oxygen(s) establish a direct interaction with an Fe atom (*i.e.,* monodentate or bidentate coordination of the substrate) (*45*). The interacting Fe atom could facilitate nucleophilic attack at the sulfate sulfur by acting as a Lewis acid, analogous to aconitase (*27*). Since the cluster in APR is ligated to the protein via four cysteine residues the coordination number of the interacting Fe site would increase to 5 or 6. Based on studies of direct interaction between substrate or cofactor and $[4Fe\text{-}4S]^{2+}$ clusters in aconitase (*27*), pyruvate formate-lyase activase (*46*), and biotin synthase (*47*) significant perturbation of the Mössbauer parameters for an interacting Fe site in MtAPR would be expected (*46, 48, 49*). The present work, however, shows no discernable change in the Mössbauer spectrum upon addition of APS to MtAPR (Appendix 5.7.3),

suggesting that the cluster and the substrate do not establish a direct interaction. This proposal is fully consistent with the crystal structure of PaAPR bound to APS, which shows that the sulfate oxygens are 7 Å from the closest Fe atom and 6 Å from the $S\gamma$ atom of Cys140 (Figure 5.2B) (*7*).

On the other hand, substrate binding to MtAPR led to a marked increase in intensity and resolution of the EPR signal, and to minor shifts in principle *g* values that were not observed with closely related substrate analogs, ADP and ADPβF (Figure 5.4). These findings correlate with observed differences in the dissociation constants (K_ds) reported for these ligands (*5*) and can be rationalized on the basis of differences in anionic charges: β-sulfate has a net negative charge of one distributed over three oxygen atoms (*i.e.,* -1/3 charge each; K_d = 0.25 μM), while β-phosphate has a net negative charge of two distributed over three oxygen atoms (*i.e.,* -2/3 charge each; K_d = 5 μM) and β-fluorophosphate has a net negative charge of one distributed over two oxygen atoms (*i.e.,* -1/2 charge each; K_d = 2.5 μM). By contrast, the similarity of EPR spectra obtained in the presence or absence of AMP (Figure 5.4A and D) suggests that the α-phosphate group is too distant from the cluster to exert any significant effect. Taken together, these data are indicative of mid-range electrostatic interactions between the iron-sulfur cluster and the β-functional group of the ligand, which are finely attuned to the electrostatic properties of the sulfate in APS.

In addition to differences in formal anionic charge, the sulfur atom of sulfate is larger, more electronegative and forms shorter bonds with oxygen relative to a phosphorous atom. As a consequence, the oxygen atoms associated with a β-sulfate group are associated with less negative charge density, relative to oxygen atoms attached to

phosphate (*50*).   As compared to APS, the increase in negative charge density associated with β-non-bridging oxygen atoms of ADP and ADPβF might strengthen their interaction with the positively charged Lys144 side chain such that this residue moves away from the Sγ atom of coordinating Cys140. Alternatively, or in addition, considering that the [4Fe-4S(Cys-Sγ)$_4$] cluster has a net charge of -2 (*11*), repulsive electrostatic interactions could arise when ADP or ADPβF are bound in the active site.   Either scenario could account for the observed decrease in analog affinity and hamper the ability of the iron-sulfur cluster in MtAPR to accept an additional electron (*i.e.,* adopt the reduced 1+ state).

In general, spin quantitation of the EPR signals revealed less than 0.5 spin/mol MtAPR. These less than unitary values for the spin integration of the reduced spectra can be attributed to incomplete reduction of the [4Fe-4S]$^{2+}$ cluster that may result from insufficient light intensity or illumination time.   However, changes in these parameters were accompanied by noticeable cluster degradation and were therefore not pursued further.   Despite the modest efficiency of reduction, variations in spin quantitation between substrate-bound (or substrate analog) and substrate-free states of MtAPR were observed.   These differences are likely due to ligand-dependent structural and electrostatic changes in cluster environment, as discussed above.

The positively charged side chain of Lys144 interacts with both APS and coordinating Cys140, forming a link between the substrate and the iron-sulfur cluster. Although strict conservation of Lys144 implies an important role, this study is the first to probe the precise function of this residue. Using site-directed mutagenesis, we demonstrate that Lys144 is necessary for both substrate binding and transition state stabilization (Table 1).

Moreover, the significant decrease in EPR signal intensity for Lys144Ala MtAPR (Figure 5.6) suggests that the proximity of the positively charged side chain of this residue may be an important factor in stabilizing the reduced state of the cluster. Future measurements of midpoint reduction potentials could provide additional support for this proposal.

Comparison of the EPR spectra between wild-type, Cys256Ser (Figure 5.4) and Lys144Ala MtAPR (Figure 5.6) shows that the Lys residue plays an important role in modulating substrate-dependent changes in signal resolution and intensity. However, we note that the EPR spectrum of Lys144Ala still exhibits subtle differences in the presence or absence of APS. In particular, the APS bound state shows small changes in signal intensity at g = 2.12 and 1.99, and a decrease in the spectral feature at g = 1.82. These differences in EPR spectra may be attributable to the intrinsic electrostatic interaction between the iron-sulfur cluster and the substrate.

On the basis of the results reported herein, we propose a catalytic role for the iron-sulfur cluster in the mechanism of APS reduction, specifically in the sequence of events leading up to and through sulfuryl group transfer (Figure 6.7). Prior to APS binding, the $[4Fe-4S(Cys-S\gamma)_4]^{2-}$ cluster may serve to pre-organize the positively charged side chain of Lys144 and possibly Arg245 (Figure 5.2B and C) within the active site, so that the substrate can establish interactions with these residues. Based on the Mössbauer data and structural studies, APS binds to the $[4Fe-4S]^{2+}$ state of APR, but does not appear to come into direct contact with the cluster. Rather, EPR investigation of the $[4Fe-4S]^{+}$ and $[3Fe-4S]^{+}$ states indicate that mid-range electrostatic interactions arise between APS and the iron-sulfur cluster. The charge from and polarization within the $[4Fe-4S(Cys-S\gamma)_4]^{2-}$ cluster could serve to activate the sulfate group of APS, thereby facilitating S-OP

cleavage and S-S bond formation in the reaction. In the absence of an iron-sulfur cluster, PAPR may achieve something similar via repulsion between the extra 3'-phosphate group of PAPS and the sulfate end of the 5'-phosphosulfate. The sulfate group would then be primed for nucleophilic attack by

Figure 5.7. Possible reaction pathway for covalent *S*-sulfocysteine intermediate formation catalyzed by APR. The C-terminal residues 250-267, which carry the catalytically essential Cys256, are disordered in the structure of PaAPR, but can be modeled into the active site using the structure of *S. cerevisiae* PAPR (*4*). In the homology-modeled structure (*5*), Cys256 is proximal to the sulfate group of APS as well as the side-chains of Cys140 and Lys144. Electrostatic destabilization of APS may arise from the juxtaposition of the electron density and partial negative charge that resides on the sulfide and cysteinyl sulfur atoms of the iron-sulfur cluster (see Ref. (*11*) for theoretical treatment of charge distribution in iron-sulfur clusters). Repulsion between APS and the iron-sulfur cluster could be partially relieved in the transition state, thereby enhancing the reaction rate. The charge build-up on the bridging sulfate oxygen could be stabilized by Arg171, Arg242 and His259, which are not indicated in this Figure 5.6.for the sake of simplicity.

Cys256, leading to formation of the *S*-sulfocysteine enzyme intermediate. In support of this proposal, experimental and theoretical studies of sulfuryl group transfer in sulfate esters (*50, 51*) indicate the need for a strong polarizing agent. Regarding Lys144, our analysis demonstrates an essential role for this residue in enzyme catalysis. Although only speculative at present, it is plausible that the active site Lys144 cation may orient the incoming Cys nucleophile with respect to the sulfate moiety and/or act as a "molecular guidewire" during sulfuryl transfer; either possibility could result in transition state stabilization. Analogous functions for Lys and Arg residues in the active site of other enzymes that catalyze sulfuryl transfer have been described (*52, 53*).

In APR from *Bacillus subtilis*, on the basis of its short half-life ($t_{1/2}$ ~12 min) an oxygen-sensing function for has been proposed for the iron-sulfur cluster (*24*). By comparison, the iron-sulfur in MtAPR is significantly more stable with a half-life of about 6 hrs (*15*). Nevertheless, it is important to note that the model we have proposed above does not preclude the possibility that the cluster plays a regulatory role. Rather, the iron-sulfur cluster of APR may function both in a catalytic capacity and, in some organisms, as an oxygen-sensitive switch.

5.5 Conclusion

In summary, the data presented in this work are consistent with a catalytic function for the iron-sulfur cluster in APR. On the basis of these data, we have proposed that the cofactor plays a role in pre-organizing active site residues and in substrate activation. Additional experimental and theoretical tests of these proposals are currently underway and will be reported in due course. Moreover, the finding that MtAPR can be reduced to the $[4Fe-4S]^+$ state opens the door for other forms of spectroscopy such as ENDOR and ESEEM that can provide further insight into the relationship between the substrate and iron-sulfur cluster.

5.6 Experimental procedures

5.6.1 Materials

APS (≥95%) was obtained from Biolog Life Sciences Institute. ADP and AMP were purchased from Sigma Chemical Co. ADPβF was synthesized as previously described (*54*). The structure and purity (≥98%) was confirmed by ^1H and ^{31}P NMR (data not shown). 10-Methyl-3-sulfopropyl-5-deazaisoalloxazine potassium salt (deazaflavin) was a generous gift from Prof. David Ballou (University of Michigan). Titanium(III) citrate was prepared anaerobically from a 15% titanium(III) chloride solution in 1 M HCl with an

equimolar amount of citrate (trisodium salt), and neutralized to pH 7.0 with saturated sodium bicarbonate.

5.6.2 Mutagenesis and Protein Expression

The construction of the expression vector encoding wild-type and Cys256Ser APR from *M. tuberculosis* cloned into the vector pET24b has been previously described (*55*). The Lys144Ala variant was generated from the wild-type MtAPR template using the Quik-change site-directed mutagenesis kit (Stratagene) and the following primer sequence: 5′-GCTGCCGGTTGCGCAAGGTCGTTCCCCTGGG-3′. Plasmids encoding wild-type, Cys256Ser or Lys144Ala MtAPR pET24 and pACYC (containing genes encoding the *isc* operon of six accessory proteins required for Fe–S cluster biosynthesis in *A. vinelandii* under the control of an arabinose-inducible promoter) (25) were co-transformed into *E. coli* BL21(DE3) (Novagen) and plated on L-agar 50 μg/ml kanamycin and 100 μg/ml carbenicillin. A single colony was picked and added to 5 ml of L-broth plus antibiotics and grown overnight with shaking at 37 °C. This culture was used as a 0.5% 1 L of L-broth plus antibiotics and grown with shaking at 37 °C until absorbance at 600 nm reached approximately 0.6. Arabinose and iron citrate were added to final concentrations of 20 mM and 0.8 mM, respectively and the culture grown as above for 1 hr. At this point the flasks were removed from the incubator. IPTG was added to a final concentration of 0.3 mM and the flasks were returned to the incubator and grown overnight at 18 °C with shaking at 200 rpm. Cultures were harvested by centrifugation (4 °C, 4,300*g*). After removal of the supernatant the pellets were stored at -80 °C until required.

All purification steps were carried out at 4 °C. Cell pellets were resuspended in 30 ml Buffer A (20 mM sodium phosphate, 0.5 M NaCl, 10 mM imidazole; pH 7.4) supplemented with 0.1 mM PMSF, 10μg/ml DNase, 5 μg/ml lysozyme and lysed by sonication. Lysates were centrifuged (20,000g, 15 min) and loaded onto a 5 ml HiTrap Chelating column (GE Healthcare, Piscataway, NJ) equilibrated in the same buffer. Unbound material was washed off with 50 ml of Buffer A and bound proteins then eluted with in Buffer B (20 mM phosphate, 0.5 M NaCl, 250 mM imidazole; pH 7.4). Fractions containing wild-type or Lys144Ala were pooled, concentrated by centrifugation (Amicon 10 kDa cutoff, Millipore, Billerica, MA) and loaded onto a 16/60 Superdex 200 size exclusion column previously equilibrated in Buffer C (50 mM Tris-HCl, 150 mM NaCl, 5 mM DTT, 10% glycerol; pH 8.5 at 4 °C). Fractions containing wild-type or Lys144Ala MtAPR were pooled, snap-frozen in liquid nitrogen, and stored at -80 °C. Protein concentrations were determined using the extinction coefficient, ε_{280}=36,815 M^{-1}cm^{-1}, obtained from quantitative amino acid analysis (*1*).

5.6.3 Preparation of MtAPR for EPR and Mössbauer Spectroscopy

Samples of wild-type, Cys256Ser or Lys144Ala MtAPR suitable for Mössbauer or EPR spectroscopy were prepared inside of an anaerobic chamber with O_2 levels ≤ 1 ppm. Purified MtAPR was exchanged into anaerobic buffer containing 50 mM Tris–HCl, 150 mM NaCl (pH 8.5 at 4 °C) and 10% glycerol. To reduce the cluster in MtAPR, reactions contained 250 μM enzyme, 25 mM sodium oxalate, 250 μM deazaflavin in a total volume of 250 μL. When included, substrate or other analogs were added to a final concentration of 1 mM and incubated with MtAPR for 10 min at 25 °C prior to photoreduction. The reaction mixtures were transferred to EPR tubes, chilled in an ice-salt bath (-6 °C) and irradiated with light from a 100 W quartz halogen lamp (Applied

Photophysics, Surrey, UK) for 30 min. After illumination, samples were immediately frozen in liquid nitrogen and analyzed by low-temperature EPR. Mössbauer spectra were recorded on proteins that contained ^{57}Fe in place of natural-abundance iron. ^{57}Fe was incorporated into MtAPR via supplementation of *E. coli* growth media, and samples contained 1 mM protein, and 2 mM APS when appropriate. After 10 min incubation with substrate, samples were transferred to Mössbauer cups and frozen in liquid nitrogen.

5.6.4 EPR Spectroscopy

X-band EPR spectra of photoreduced samples were recorded on a Bruker EMX spectrometer (Billerica, MA) equipped with an Oxford Instruments ITC4 temperature controller, a Hewlett-Packard model 5340 automatic frequency counter and Bruker gaussmeter. Figure legends contain relevant instrumental parameters. The sample buffer was used to record baselines under conditions identical to those in which the sample spectra were obtained. These baselines were subtracted from MtAPR spectra shown in the figures. Spin concentrations in MtAPR samples were determined by double integration of the EPR signal over a range of 2 kgauss and comparison with double integrals of 1 mM $Cu(ClO_4)_2$ in sample buffer. EPR spectra of cryoreduced samples were recorded on a Bruker ER-200DSRC spectrometer equipped with an Oxford Instruments ESR 910 continuous-flow cryostat. Simulations of EPR spectra were performed using Spin Count (ver 2.6.7) created by Professsor M.P. Hendrich at Carnegie Mellon University. Spin Count is available at http://www.chem.cmu.edu/groups/hendrich/.

5.6.5 Mössbauer Spectroscopy

Mössbauer spectra were recorded on a spectrometer from WEB research (Edina, MN) operating in the constant acceleration mode in transmission geometry. Spectra were

recorded with the temperature of the sample maintained at 4.2 K in an externally applied magnetic field of 53 mT oriented parallel to the γ-beam. The quoted isomer shifts were relative to the centroid of the spectrum of a foil of α-Fe metal at room temperature. Data analysis was performed using the program WMOSS from WEB research.

5.6.6 Cryoreduction of MtAPR by Low-Temperature γ-Radiolysis

Samples containing 250 µM MtAPR were loaded into EPR tubes or Mössbauer cups and flash frozen in liquid nitrogen inside the glovebox. When appropriate, APS was added to a final concentration of 1 mM and incubated with protein for 10 min at 25 °C prior to freezing. Samples were γ-irradiated (^{60}Co; total dose of 4 Mrad) at the γ-irradiation facility of the Breazeale nuclear reactor at the Pennsylvania State University. During irradiation, samples were maintained at 77 K by immersion in liquid N_2.

5.6.7 MtAPR Activity Assay

Reactions were carried out at 30 °C. Unless otherwise indicated, the buffer consisted of 100 mM bis-tris propane (pH 7.5) and 100 mM NaCl supplemented with 5 mM DTT and 10 µM *E. coli* thioredoxin. Production of $^{35}SO_3^{2-}$ from ^{35}S-APS was monitored using charcoal-based separation and scintillation counting as previously reported (*5*). The substrate was incubated with excess enzyme to ensure single-turnover conditions (>2.5-fold molar excess of enzyme). The reaction progress curve was plotted as the fraction of product versus time and was fit by a single exponential $F = A[1-e(-k_{obs}t)]$, where F is the fraction product, A is the fraction of substrate converted to product at completion, k_{obs} the observed rate constant, and t time. Reactions were followed for ≥5 half-lives except for very slow reactions. Under single-turnover conditions, it is expected that the concentration dependence of the enzyme will be hyperbolic (eq 1).

$$k_{obs} = \frac{k_{max}[E]}{K_{1/2} + [E]} \quad (1)$$

To determine k_{cat}/K_m, a concentration of enzyme was chosen that was at least 5-fold below the K_m value. Although we refer to the $K_{1/2}$ for maximal activity as K_m, we note that the $K_{1/2}$ for single turnover is not necessarily the same as the K_m for the multiple turnover reaction since the latter can be affected by the rate of product release. For conditions in which $[E] \ll K_m$ the second order rate constant, $k_{cat}/K_m = k_{obs}/[E]$. We note that the reported values of k_{cat}/K_m are for single-turnover conditions, but the measurement is equivalent to steady state k_{cat}/K_m. At a saturating concentration of enzyme, the observed single-turnover rate constant reaches a maximum, k_{max}. To determine k_{max}, the concentration of enzyme was varied by at least 3-fold to establish that the observed rate was independent of the concentration of enzyme, indicating that the enzyme was in excess and at a saturating concentration (*i.e.,* $k_{obs} = k_{max}$). The reported values of k_{cat}/K_m and k_{max} are the average of at least three independent determinations. Unless otherwise indicated, the standard deviation was ≤15% of the value of the mean.

5.6.8 Determination of Substrate Affinity

The apparent dissociation constant (K_d) for ^{35}S-APS from Lys144Ala MtAPR-ligand complexes was measured using an ultrafiltration binding assay reported by Hernick and Fierke (*56*). Because the chemical step (*i.e., S*-sulfocysteine formation) is rate-limiting (*5*) the $K_{1/2}$ is equal to K_d of APS for Lys144Ala MtAPR. In brief, the concentration of substrate was kept low (*i.e.,* below the K_d) and constant, and the concentration of the enzyme was varied (0 to 80 µM). Lys144Ala MtAPR was incubated in 100 mM bis-tris propane, pH 7.5 at 30 °C for 15 min prior to the assay to allow for ligand equilibration.

Assay mixtures were then transferred into ultrafiltration devices (Microcon 30 kDa cutoff, Millipore, Billerica, MA), and the free and bound ligand separated by centrifuging the samples at 3,000 rpm for 2.5 min. Equal volumes of the filtrate and retentate were removed and quantified using scintillation counting. The ratio of EL/L_{total} was determined as a function of $[E]_{total}$, and the K_d value was obtained by fitting eq 2 to these data.

$$\frac{EL}{L_{total}} = \frac{\left(EL/L_{total}\right)_{Endpt}}{\left(1 + \frac{K_d}{E_{total}}\right)} + \left(\frac{EL}{L_{total}}\right)_{Background} \qquad (2)$$

5.7 Appendix

Figure 5.7.1 Structure based sequence alignment of PaAPR and MtAPR.

The ClustalW Multiple Sequence Alignment program was used. The bar graph indicates the degree of conservation per position. Strictly conserved residues are outlined in red, red letters indicate conserved residues and conserved regions are boxed in blue. Alignment pictures were rendered with the server ESPript 2.2 (http://espript.ibcp.fr).
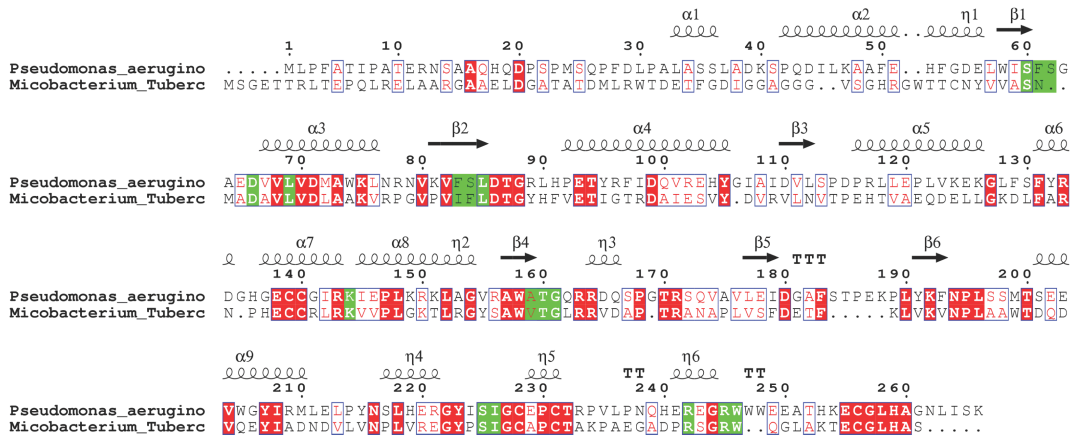
Figure 5.7.2 UV-vis absorption spectra of MtAPR.

UV-vis absorption of 10μM MtAPR in 50 mM Tris–HCl, 150 mM NaCl (pH 8.5 at 4 °C) and 10% glycerol, before (—) and after (••••) the addition of 2-fold stoichiometric excess of APS. Inset shows the corresponding difference spectrum resulting from complex formation between MtAPR and APS. The difference spectrum is the spectrum of the mixture minus spectrum of enzyme alone.
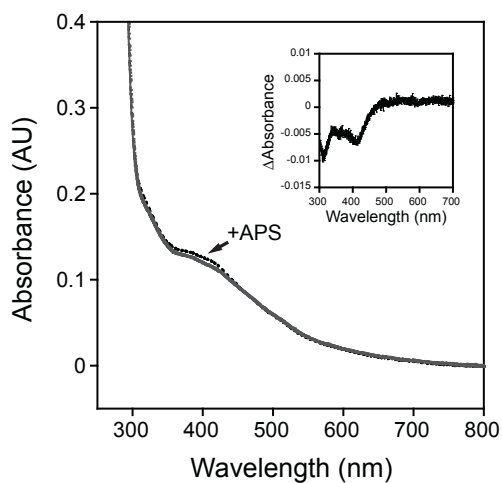
Figure 5.7.3 4.2-K/53-mT Mössbauer spectra of 1 mM MtAPR in the absence (vertical bars) or presence of 2 mM APS (solid line)
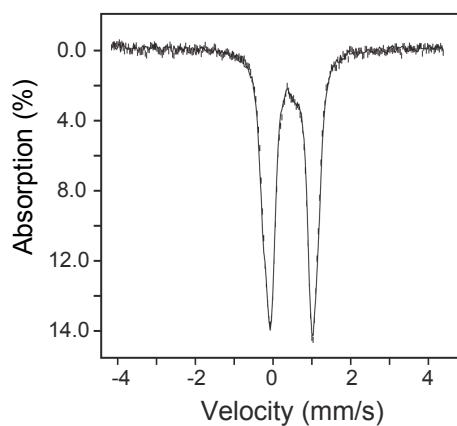
Figure 5.7.4 Rate and equilibrium constants for MtAPR

A. Single-turnover reduction of APS by Lys144Ala MtAPR performed under subsaturating conditions as described in Materials and Methods. Single-turnover reaction to measure k_{cat}/K_m was performed with 5 nM wild-type MtAPR or 20 μM Lys144Ala MtAPR and 0.25 nM APS. *B.* Single-turnover reduction of APS by wild-type (filled circles) and Lys144Ala (filled triangles) MtAPR performed under saturating conditions as described in Materials and Methods. Single-turnover reactions to measure k_{max} were performed with 150 μM enzyme and 50 μM APS. *C.* APS binding to Lys144Ala MtAPR measured by ultrafiltration as described in Materials and Methods.
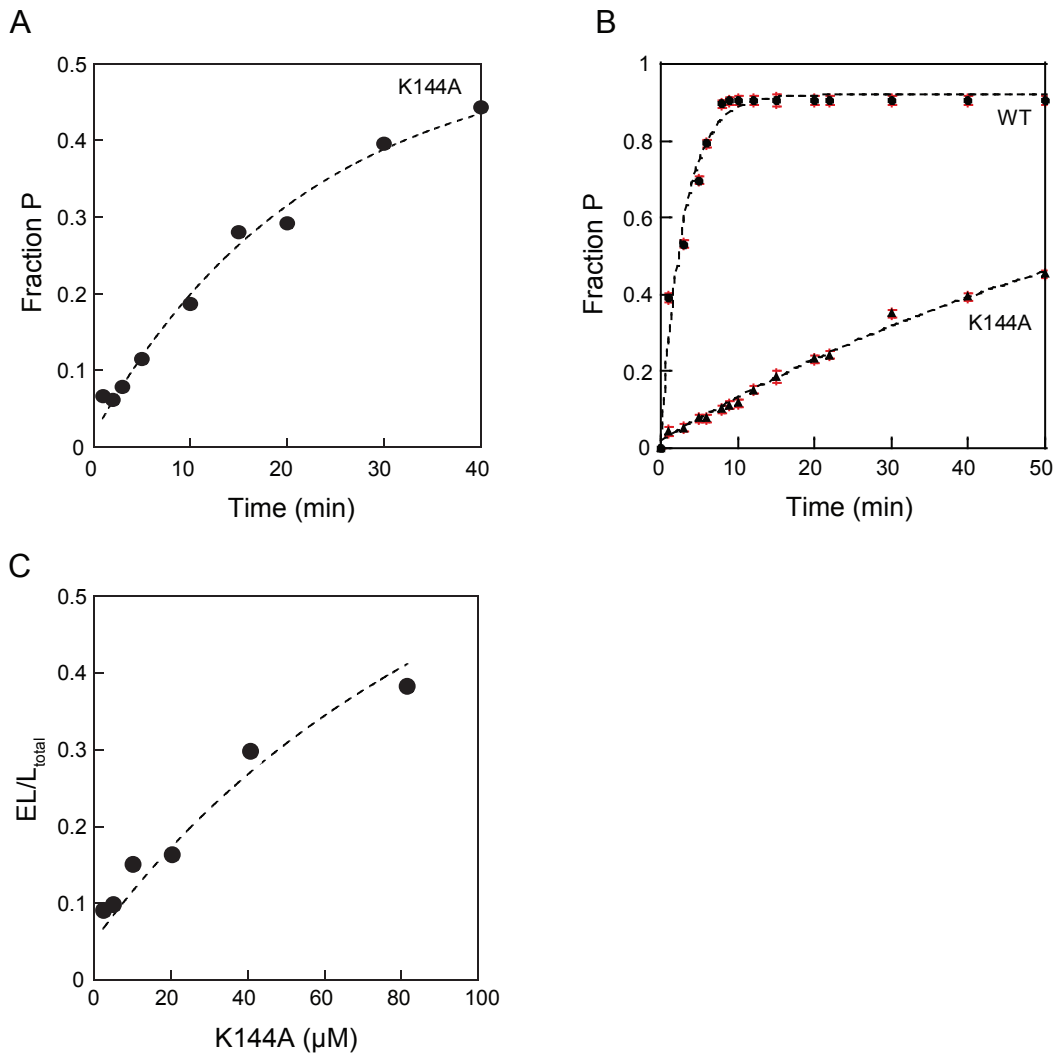
Figure 5.7.5 EPR spectra of radiolytically cryoreduced 250 _μ_M MtAPR in the absence (red) or pre-incubated with 1 mM APS (blue) as described in Materials and Methods.

Conditions: temperature, 77 K; microwave frequency, 9.45 GHz; microwave power, 10 mW; modulation frequency, 100 kHz; modulation amplitude, 10 G; scan time, 167 s; time constant, 167 ms. Asterisks indicate the position of the intense signal at _g_ = 2 emanating from free radicals generated during cryoreduction and the position of the peaks of hydrogen atoms formed during cryoreduction.
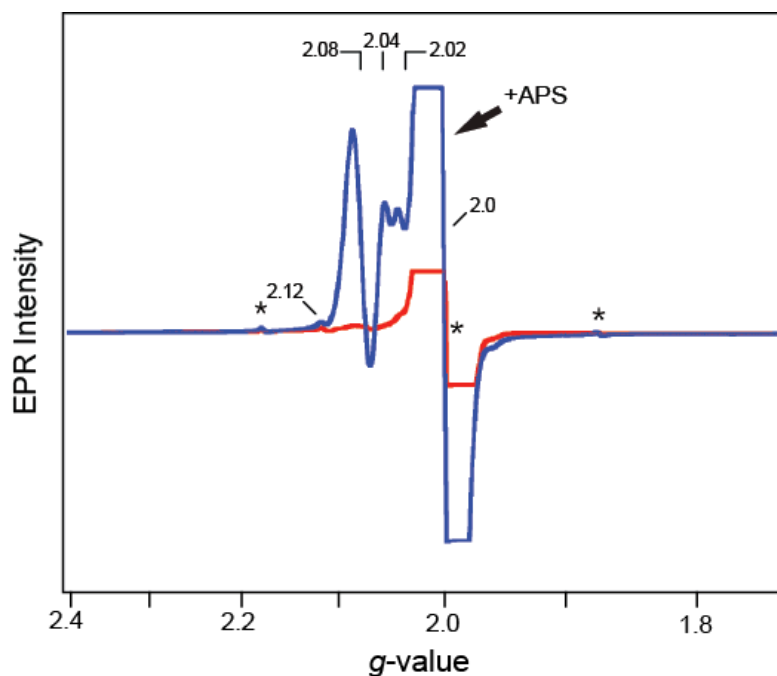
Figure 5.7.6 4.2-K/53-mT Mössbauer spectra of 250 µM MtAPR in the absence (top) or pre-incubated with 1 mM APS (bottom) after γ-irradiation (vertical bars) as described in Materials and Methods.

In these experiments, 50% of the starting material is unchanged (red solid line). Spectral changes that result from different orientations of the externally applied 53-mT magnetic field are highlighted by the black and blue arrows.
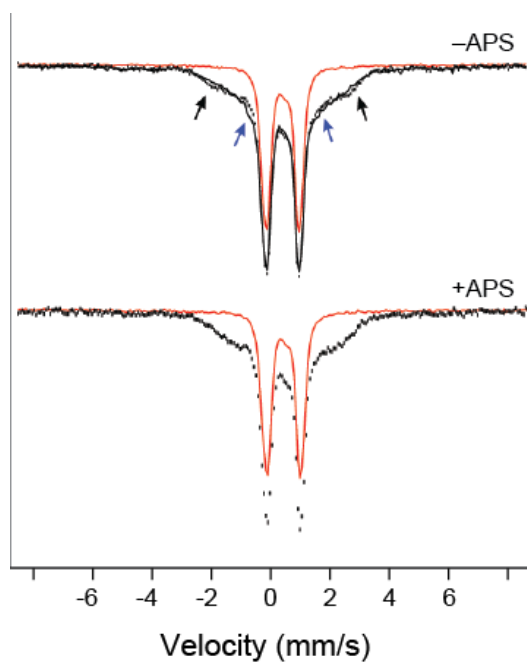
Figure 5.7.7 EPR spectra of oxidized wild-type MtAPR

A. Spectra of 250 μM MtAPR treated with a stoichiometric amount of ferricyanide in buffer containing 50 mM Tris–HCl, 150 mM NaCl (pH 8.5 at 4 °C) and 10% glycerol. *B.* Expanded version of panel *A* around *g* = 2. Prior to freezing, samples with protein were incubated with ferricyanide for 5 min at rt. Unreacted potassium ferricyanide is present in the sample. However, controls reactions carried out in the absence of protein indicate that it does not contribute to features in the spectrum. Conditions: temperature, 10 K; microwave frequency, 9.38 GHz; microwave power, 10 mW.
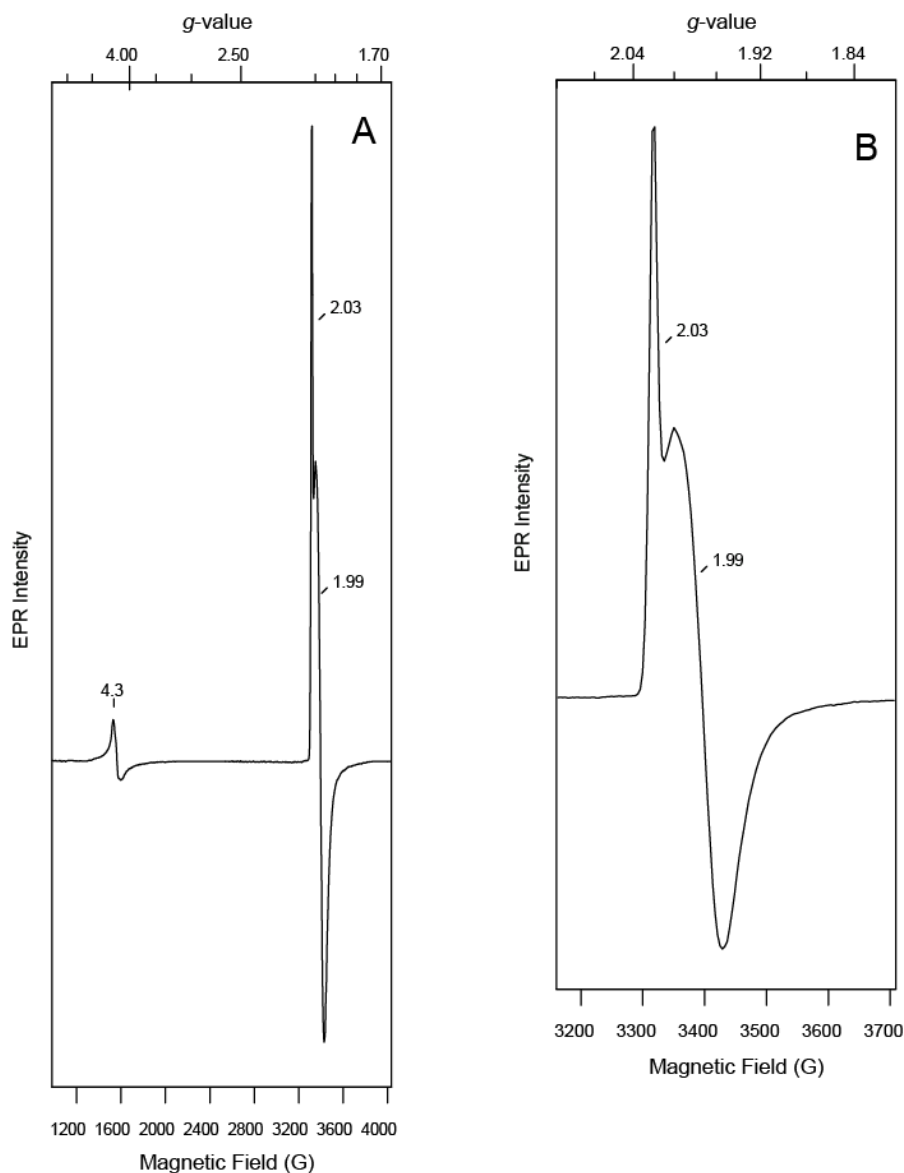
Acknowledgements

5.8 Reference

1. Carroll, K. S., Gao, H., Chen, H., Stout, C. D., Leary, J. A., and Bertozzi, C. R. (2005) A conserved mechanism for sulfonucleotide reduction, *PLoS Biol. 3*, e250.

2. Mougous, J. D., Lee, D. H., Hubbard, S. C., Schelle, M. W., Vocadlo, D. J., Berger, J. M., and Bertozzi, C. R. (2006) Molecular basis for G protein control of the prokaryotic ATP sulfurylase, *Mol. Cell. 21*, 109-122.

3. Leyh, T. S., Taylor, J. C., and Markham, G. D. (1988) The sulfate activation locus of *Escherichia coli* K12: cloning, genetic, and enzymatic characterization, *J. Biol. Chem. 263*, 2409-2416.

4. Yu, Z., Lemongello, D., Segel, I. H., and Fisher, A. J. (2008) Crystal structure of *Saccharomyces cerevisiae* 3'-phosphoadenosine-5'-phosphosulfate reductase complexed with adenosine 3',5'-bisphosphate, *Biochemistry 47*, 12777-12786.

5. Hong, J. A., Bhave, D. P., and Carroll, K. S. (2009) Identification of Critical Ligand Binding Determinants in *Mycobacterium tuberculosis* Adenosine-5'-phosphosulfate Reductase, *J. Med. Chem. 52*, 5485-5495.

6. Renosto, F., Seubert, P. A., and Segel, I. H. (1984) Adenosine 5'-phosphosulfate kinase from *Penicillium chrysogenum*. Purification and kinetic characterization, *J. Biol. Chem. 259*, 2113-2123.

7. Chartron, J., Carroll, K. S., Shiau, C., Gao, H., Leary, J. A., Bertozzi, C. R., and Stout, C. D. (2006) Substrate recognition, protein dynamics, and iron-sulfur cluster in *Pseudomonas aeruginosa* adenosine 5'-phosphosulfate reductase, *J. Mol. Biol. 364*, 152-169.

8. Kim, S. K., Rahman, A., Mason, J. T., Hirasawa, M., Conover, R. C., Johnson, M. K., Miginiac-Maslow, M., Keryer, E., Knaff, D. B., and Leustek, T. (2005) The interaction of 5'-adenylylsulfate reductase from *Pseudomonas aeruginosa* with its substrates, *Biochim. Biophys. Acta. 1710*, 103-112.

9. Kopriva, S., Buchert, T., Fritz, G., Suter, M., Benda, R., Schunemann, V., Koprivova, A., Schurmann, P., Trautwein, A. X., Kroneck, P. M., and Brunold, C. (2002) The presence of an iron-sulfur cluster in adenosine 5'-phosphosulfate reductase separates organisms utilizing adenosine 5'-phosphosulfate and phosphoadenosine 5'-phosphosulfate for sulfate assimilation, *J. Biol. Chem. 277*, 21786-21791.

10. Chartron, J., Shiau, C., Stout, C. D., and Carroll, K. S. (2007) 3'-Phosphoadenosine-5'-phosphosulfate reductase in complex with thioredoxin: a structural snapshot in the catalytic cycle, *Biochemistry 46*, 3942-3951.

11. Torres, R. A., Lovell, T., Noodleman, L., and Case, D. A. (2003) Density functional and reduction potential calculations of Fe4S4 clusters, *J. Am. Chem. Soc. 125*, 1923-1936.

12. Bhave, D. P., Muse, W. B., 3rd, and Carroll, K. S. (2007) Drug targets in mycobacterial sulfur metabolism, *Infect. Disord. Drug Targets 7*, 140-158.

13. Mdluli, K., and Spigelman, M. (2006) Novel targets for tuberculosis drug discovery, *Curr. Opin. Pharmacol. 6*, 459-467.

14. Savage, H., Montoya, G., Svensson, C., Schwenn, J. D., and Sinning, I. (1997) Crystal structure of phosphoadenylyl sulphate (PAPS) reductase: a new family of adenine nucleotide alpha hydrolases, *Structure 5*, 895-906.

15. Carroll, K. S., Gao, H., Chen, H., Leary, J. A., and Bertozzi, C. R. (2005) Investigation of the iron-sulfur cluster in *Mycobacterium tuberculosis* APS reductase: implications for substrate binding and catalysis, *Biochemistry 44*, 14647-14657.

16. Kopriva, S., Fritzemeier, K., Wiedemann, G., and Reski, R. (2007) The putative moss 3'-phosphoadenosine-5'-phosphosulfate reductase is a novel form of adenosine-5'-phosphosulfate reductase without an iron-sulfur cluster, *J. Biol. Chem. 282*, 22930-22938.

17. Sazanov, L. A., and Hinchliffe, P. (2006) Structure of the hydrophilic domain of respiratory complex I from *Thermus thermophilus*, *Science 311*, 1430-1436.

18. Kim, S. K., Rahman, A., Bick, J. A., Conover, R. C., Johnson, M. K., Mason, J. T., Hirasawa, M., Leustek, T., and Knaff, D. B. (2004) Properties of the cysteine residues and iron-sulfur cluster of the assimilatory 5'-adenylyl sulfate reductase from *Pseudomonas aeruginosa*, *Biochemistry 43*, 13478-13486.

19. Kopriva, S., Buchert, T., Fritz, G., Suter, M., Weber, M., Benda, R., Schaller, J., Feller, U., Schurmann, P., Schunemann, V., Trautwein, A. X., Kroneck, P. M., and Brunold, C. (2001) Plant adenosine 5'-phosphosulfate reductase is a novel iron-sulfur protein, *J. Biol. Chem. 276*, 42881-42886.

20. Gillum, W. O., Mortenson, L. E., Chen, J. S., and Holm, R. H. (1977) Quantitative extrusions of the Fe4S4 cores of the active sites of ferredoxins and the hydrogenase of Clostridium pasteurianum, *J. Am .Chem. Soc. 99*, 584-595.

21. Orme-Johnson, W. H., and Holm, R. H. (1978) Identification of iron--sulfur clusters in proteins, *Method Enzymol. 53*, 268-274.

22. Volbeda, A., Charon, M. H., Piras, C., Hatchikian, E. C., Frey, M., and Fontecilla-Camps, J. C. (1995) Crystal structure of the nickel-iron hydrogenase from *Desulfovibrio gigas*, *Nature 373*, 580-587.

23. Noodleman, L., Pique, M., and Roberts, V. (2008) Iron-Sulfur Clusters: Properties and Functions, *WIley Encyclopedia of Chemical Biology* 1-11.

24. Berndt, C., Lillig, C. H., Wollenberg, M., Bill, E., Mansilla, M. C., de Mendoza, D., Seidler, A., and Schwenn, J. D. (2004) Characterization and reconstitution of a 4Fe-4S adenylyl sulfate/phosphoadenylyl sulfate reductase from *Bacillus subtilis*, *J. Biol. Chem. 279*, 7850-7855.

25. Kriek, M., Peters, L., Takahashi, Y., and Roach, P. L. (2003) Effect of iron-sulfur cluster assembly proteins on the expression of *Escherichia coli* lipoic acid synthase, *Protein Expres. Purif. 28*, 241-245.

26. Hagen, W. R. (1992) EPR Spectroscopy of Iron-Sulfur Proteins, *Adv. Inorg. Chem. 38*, 165.

27. Beinert, H., Kennedy, M. C., and Stout, C. D. (1996) Aconitase as Iron-Sulfur Protein, Enzyme, and Iron-Regulatory Protein, *Chem. Rev. 96*, 2335-2374.

28. Walsby, C. J., Hong, W., Broderick, W. E., Cheek, J., Ortillo, D., Broderick, J. B., and Hoffman, B. M. (2002) Electron-nuclear double resonance spectroscopic evidence that S-adenosylmethionine binds in contact with the catalytically active [4Fe-4S](+) cluster of pyruvate formate-lyase activating enzyme, *J. Am. Chem. Soc. 124*, 3143-3151.

29. Davydov, R., Valentine, A. M., Komar-Panicucci, S., Hoffman, B. M., and Lippard, S. J. (1999) An EPR study of the dinuclear iron site in the soluble methane monooxygenase from *Methylococcus capsulatus* (Bath) reduced by one electron at 77 K: the effects of component interactions and the binding of small molecules to the diiron(III) center, *Biochemistry 38*, 4188-4197.

30. Lawrence, C. C., Bennati, M., Obias, H. V., Bar, G., Griffin, R. G., and Stubbe, J. (1999) High-field EPR detection of a disulfide radical anion in the reduction of cytidine 5'-diphosphate by the E441Q R1 mutant of *Escherichia coli* ribonucleotide reductase, *Proc. Natl. Acad. Sci. U S A 96*, 8979-8984.

31. Engstrom, M., Vahtras, O., and Agren, H. (2000) MCSCF and DFT calculation of EPR parameters of sulfur centered radicals, *Chamical Physics Letters 328*, 483-491.

32. Cunningham, R. P., Asahara, H., Bank, J. F., Scholes, C. P., Salerno, J. C., Surerus, K., Munck, E., McCracken, J., Peisach, J., and Emptage, M. H. (1989) Endonuclease III is an iron-sulfur protein, *Biochemistry 28*, 4450-4455.

33. Dos Santos, P. C., and Dean, D. R. (2008) A newly discovered role for iron-sulfur clusters, *Proc. Natl. Acad. Sci. USA 105*, 11589-11590.

34. Fontecave, M. (2006) Iron-sulfur clusters: ever-expanding roles, *Nat. Chem. Biol. 2*, 171-174.

35. Beinert, H., Holm, R. H., and Munck, E. (1997) Iron-sulfur clusters: nature's modular, multipurpose structures, *Science 277*, 653-659.

36. Booker, S. J. (2009) Anaerobic functionalization of unactivated C-H bonds, *Curr. Opin. Chem. Biol. 13*, 58-73.

37. Frey, P. A., Hegeman, A. D., and Ruzicka, F. J. (2008) The Radical SAM Superfamily, *Crit. Rev. Biochem. Mol. Biol. 43*, 63-88.

38. Noodleman, L., Lovell, T., Liu, T., Himo, F., and Torres, R. A. (2002) Insights into properties and energetics of iron-sulfur proteins from simple clusters to nitrogenase, *Curr. Opin. Chem. Biol. 6*, 259-273.

39. Langen, R., Jensen, G. M., Jacob, U., Stephens, P. J., and Warshel, A. (1992) Protein control of iron-sulfur cluster redox potentials, *J. Biol. Chem. 267*, 25625-25627.

40. Jensen, G. M., Warshel, A., and Stephens, P. J. (1994) Calculation of the redox potentials of iron-sulfur proteins: the 2-/3-couple of [Fe4S*4Cys4] clusters in Peptococcus aerogenes ferredoxin, Azotobacter vinelandii ferredoxin I, and Chromatium vinosum high-potential iron protein, *Biochemistry 33*, 10911-10924.

41. Ragsdale, S. W., Lindahl, P. A., and Munck, E. (1987) Mossbauer, EPR, and optical studies of the corrinoid/iron-sulfur protein involved in the synthesis of acetyl coenzyme A by *Clostridium thermoaceticum*, *J. Biol. Chem. 262*, 14289-14297.

42. Weiner, B. E., Huang, H., Dattilo, B. M., Nilges, M. J., Fanning, E., and Chazin, W. J. (2007) An iron-sulfur cluster in the C-terminal domain of the p58 subunit of human DNA primase, *J. Biol. Chem. 282*, 33444-33451.

43. Agarwalla, S., Stroud, R. M., and Gaffney, B. J. (2004) Redox reactions of the iron-sulfur cluster in a ribosomal RNA methyltransferase, RumA: optical and EPR studies, *J. Biol. Chem. 279*, 34123-34129.

44. Antanaitis, B. C., Aisen, P., Lilienthal, H. R., Roberts, R. M., and Bazer, F. W. (1980) The novel "g' = 1.74" EPR spectrum of pink and purple uteroferrin, *J. Biol. Chem. 255*, 11204-11209.

45. Saunders, A. H., Griffiths, A. E., Lee, K. H., Cicchillo, R. M., Tu, L., Stromberg, J. A., Krebs, C., and Booker, S. J. (2008) Characterization of quinolinate synthases from *Escherichia coli, Mycobacterium tuberculosis*, and *Pyrococcus horikoshii* indicates that [4Fe-4S] clusters are common cofactors throughout this class of enzymes, *Biochemistry 47*, 10999-11012.

46. Krebs, C., Broderick, W. E., Henshaw, T. F., Broderick, J. B., and Huynh, B. H. (2002) Coordination of adenosylmethionine to a unique iron site of the [4Fe-4S] of pyruvate formate-lyase activating enzyme: a Mossbauer spectroscopic study, *J. Am. Chem. Soc. 124*, 912-913.

47. Cosper, M. M., Jameson, G. N., Hernandez, H. L., Krebs, C., Huynh, B. H., and Johnson, M. K. (2004) Characterization of the cofactor composition of *Escherichia coli* biotin synthase, *Biochemistry 43*, 2007-2021.

48. Emptage, M. H., Kent, T. A., Kennedy, M. C., Beinert, H., and Munck, E. (1983) Mossbauer and EPR studies of activated aconitase: development of a localized valence state at a subsite of the [4Fe-4S] cluster on binding of citrate, *Proc. Natl. Acad. Sci. U S A 80*, 4674-4678.

49. Lee, K. H., Saleh, L., Anton, B. P., Madinger, C. L., Benner, J. S., Iwig, D. F., Roberts, R. J., Krebs, C., and Booker, S. J. (2009) Characterization of RimO, a new member of the methylthiotransferase subclass of the radical SAM superfamily, *Biochemistry 48*, 10162-10174.

50. Catrina, I., O'Brien, P. J., Purcell, J., Nikolic-Hughes, I., Zalatan, J. G., Hengge, A. C., and Herschlag, D. (2007) Probing the origin of the compromised catalysis of *E. coli* alkaline phosphatase in its promiscuous sulfatase reaction, *J. Am. Chem. Soc. 129*, 5760-5765.

51. Dey, K. R., Wong, B. M., and Hossain, M. A. (2010) Rational design of a macrocyclic-based chemosensor for anions, *Tet. Lett. 51*, 1329-1332.

52. Chapman, E., Bryan, M. C., and Wong, C. H. (2003) Mechanistic studies of beta-arylsulfotransferase IV, *Proc. Natl. Acad. Sci. U S A 100*, 910-915.

53. Cleland, W. W., and Hengge, A. C. (2006) Enzymatic mechanisms of phosphate and sulfate transfer, *Chem. Rev. 106*, 3252-3278.

54. Satishchandran, C., Myers, C. B., and Markham, G. D. (1992) Adenosine-5'-O-(2-fluorodiphosphate) (ADPβF), an analog of adenosine-5'-phosphosulfate, *Bioorg. Chem. 20*, 107-114.

55. Williams, S. J., Senaratne, R. H., Mougous, J. D., Riley, L. W., and Bertozzi, C. R. (2002) 5'-adenosinephosphosulfate lies at a metabolic branch point in mycobacteria, *J. Biol. Chem. 277*, 32606-32615.

56. Hernick, M., and Fierke, C. A. (2006) Catalytic mechanism and molecular recognition of *E. coli* UDP-3-O-(R-3-hydroxymyristoyl)-N-acetylglucosamine deacetylase probed by mutagenesis, *Biochemistry 45*, 15240-15248.

Chapter 6

Iron-sulfur cluster engineering provides insight into the evolution of substrate specificity among the family of sulfonucleotide reductases

This work has been published as "Spectroscopic studies on the [4Fe-4S] cluster in adenosine 5'-phosphosulfate reductase from *Mycobacterium tuberculosis*." ACS Chemical Biology. **2011**, in press. My contributions to this work include generation of p-loop mutants in PaAPR, MtAPR, and EcPAPR by site-directed mutagenesis and performing all kinetic experiments.

6.1 Abstract

Assimilatory sulfate reduction supplies prototrophic organisms with reduced sulfur that is required for the biosynthesis of all sulfur-containing metabolites, including cysteine and methionine. The reduction of sulfate requires its activation *via* an ATP-dependent activation to form adenosine-5'-phosphosulfate (APS). Depending on the species, APS can be reduced directly to sulfite by APS reductase (APR) or undergo a second phosphorylation to yield 3'-phosphoadenosine-5'-phosphosulfate (PAPS), the substrate for PAPS reductase (PAPR). These essential enzymes have no human homolog, rendering them attractive targets for the development of novel antibacterial drugs. APR and PAPR share sequence and structure homology as well as a common catalytic mechanism, but the enzymes are distinguished by two features, namely, the amino acid sequence of the phosphate-binding loop (P-loop) and an iron-sulfur cofactor in APRs. Based on the crystal structures of APR and PAPR, two P-loop residues are proposed to

determine substrate specificity; however, this hypothesis has not been tested. In contrast to this prevailing view, we report here that the P-loop motif has a modest effect on substrate discrimination. Instead, by means of metalloprotein engineering, spectroscopic and kinetic analyses, we demonstrate that the iron-sulfur cluster cofactor enhances APS reduction by nearly 1000-fold, thereby playing a pivotal role in substrate specificity and catalysis. These findings offer new insights into the evolution of this enzyme family, and extend the known functions of protein-bound iron-sulfur clusters.

6.2 Introduction

Assimilatory sulfate reduction supplies prototrophic organisms with reduced sulfur that is required for the biosynthesis of all sulfur-containing metabolites, including the amino acids cysteine and methionine (1, 2). The reduction of sulfate requires its activation by an ATP-dependent activation to form adenosine-5'-phosphosulfate (APS). For incorporation of sulfur into biomolecules, the sulfate in APS must be reduced to sulfite and finally into sulfide. In plants, algae, and many bacteria, APS can be reduced directly to sulfite by APS reductase (APR); alternatively, in fungi, some cyanobacteria, and γ-proteobacteria, this compound requires a second phosphorylation step to yield 3'-
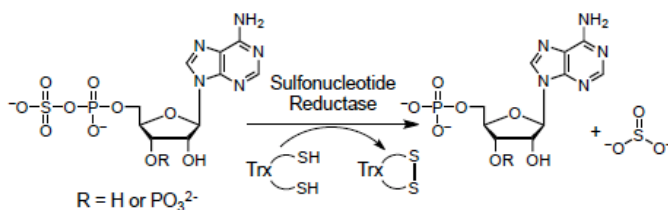
Scheme 6.1. Reaction catalyzed by sulfonucleotide reductases. The reaction is catalyzed by APR when the substrate is APS (R = H) and by PAPR when the substrate is PAPS (R = PO_3^{2-}).
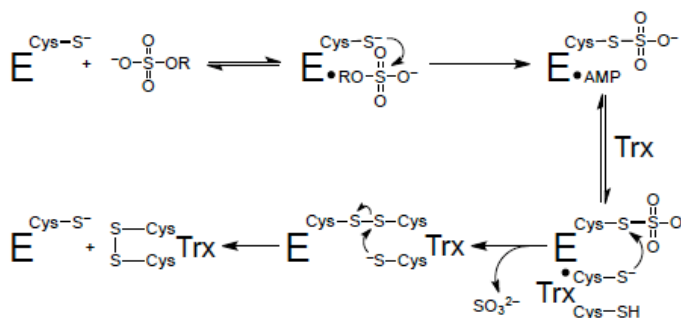
Scheme 6.2. Mechanism of sulfonucleotide reduction.

phosphoadenosine-5'-phosphosulfate (PAPS), the substrate for PAPS reductase (PAPR; Scheme 6.1, Table 6.1 and Figure 6.1). These essential enzymes, collectively known as sulfonucleotide reductases (SRs), have no human homolog, rendering them an attractive target for the development of novel antibacterial drugs and herbicides (*3-6*).

The importance of SR for microbial and plant survival have motivated investigations of their catalytic mechanism and structure (*6-14*). These studies support the mechanism shown in Scheme 6.2, which involves nucleophilic attack by a conserved C-terminal cysteine residue on the substrate leading to the formation of a covalent enzyme *S*-sulfocysteine intermediate. Sulfite is then released by thiol-disulfide exchange with free thioredoxin (Trx) in bacterial and fungal SRs or through the action of a C-terminal Trx-like domain in plants. Therefore, the general features of the thiol reaction chemistry are shared despite the differences in substrate. SRs are homologous in sequence (~25% identity; Appendix 6.7.3), particularly within active site residues that line the active site (~50% identity and 75% similarity; Appendix 6.7.4) and share a common three-dimensional structure (1.2 Å rms deviation; Figure 6.2, panel a) (*8, 15*). The SR monomer adopts a Rossman-like fold and is characterized by four conserved structural elements that define the active site: the LTDG motif, phosphate-binding loop (P-loop), Arg-loop, and C-terminal ECGLH segment with the catalytic cysteine (Appendix 6.7.3).

Upon closer inspection sequence and structure alignments reveal two key differences between APR and PAPR, namely, the amino acid sequence of the P-loop and the presence of the cysteine motif, CC...CXXC, in APR. The P-loop of APR is typically comprised of an SFS–GAED motif while the corresponding sequence in PAPR is SSSFGIQA (Figure 6.1, panels a and b). In contrast to the typical role for the P-loop in binding a 5'-phosphate group, crystal structures show that the P-loop interacts with the

146
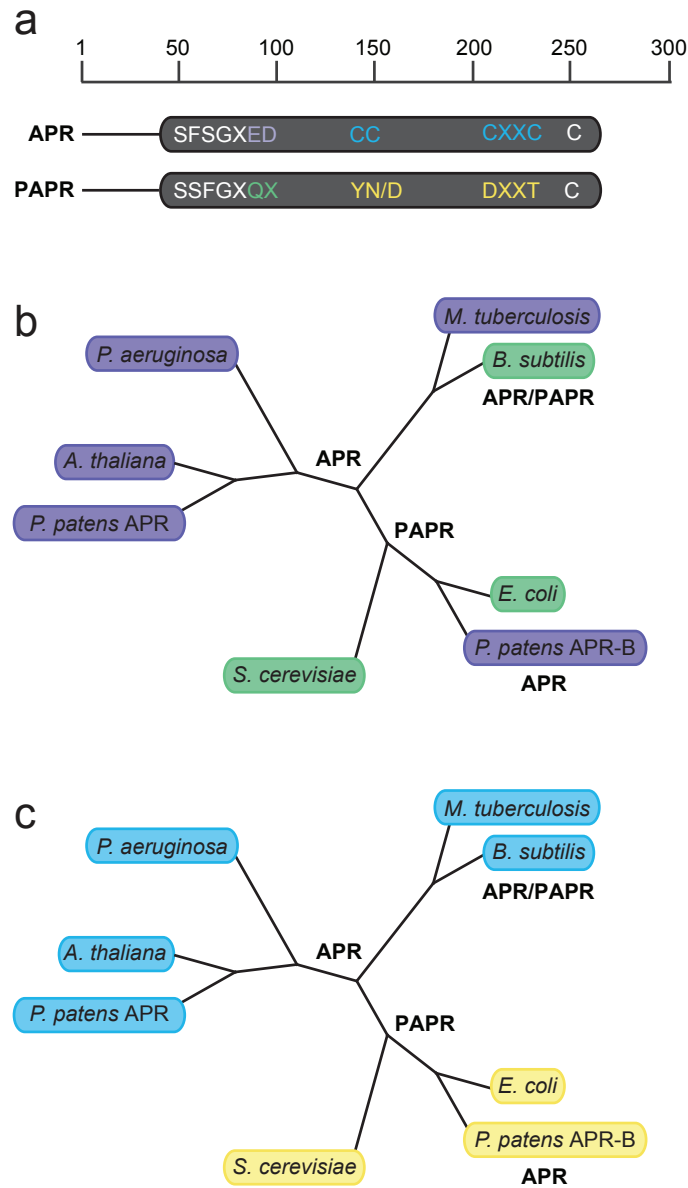
Figure 6.1. Domain organization and phylogenetic classification within the sulfonucleotide reductase family. All SRs have a catalytic cysteine at the end of the C-terminus. a) Bacterial APRs possess the cysteine motif -CC-X~80-CXXC- highlighted in blue that coordinates to a [4Fe-4S] cluster. In PAPRs, conserved residues in yellow replace the cysteine motif. The phosphate–binding loop in APR ends with two negatively charged residues (indicated in purple). These residues preclude binding of the 3'-phosphate moiety of PAPS, which can be accommodated by the P-loop motif of PAPR as it bears residues (in green) with small and neutral side chains instead. b) & c) Dendrograms illustrating the sequence homology between enzymes within the SR family. The sequence alignment was performed using ClustalW (*5*) and the tree was constructed using the Geneious program (*6*). Each of the three subclasses of SRs is clearly delineated: APRs from higher plants with their unique C-terminal domain (*A. thaliana, P. patens*-APR), bacterial APRs (*P. aeruginosa, M. tuberculosis, B. subtilis*) and PAPRs (*E. coli, P. patens-APR-B and S. cerevisiae*). Differentiation in the P-loop region (b) and iron-sulfur cluster coordinating residues (c) of the SRs is indicated by color: purple, reduce APS; green, reduce PAPS; blue, harbor a [4Fe-4S] cluster; yellow, lack the [4Fe-4S] cluster. APR from *B. subtilis* and *P. patens* APR-B are unique and can reduce both APS and PAPS.

APS O3' hydroxyl or the PAPS 3'-phosphate (Figure 6.2, panels b and c). The four additional cysteine residues in APR coordinate an iron-sulfur cluster, whereas the cofactor is replaced by the YN...DXXT motif in PAPR (Figure 6.1, panels a and c and Figure 6.2, panels d and e). Functional analysis indicates that when the [4Fe-4S] cofactor is present, it is required for catalytic activity; however, the cluster is not involved in redox chemistry and does not bind directly to APS (*6, 8, 16*). Two interesting exceptions exist in *Bacillus subtilis*, which harbors the cluster, but can utilize both APS and PAPS as substrates [Bs(P)APR] (*17*), and the moss *Physcomitrella patens*, which lacks the cysteine pairs and associated cofactor, yet can reduce APS (PpAPR-B) (*18*). Notably, these SR variants exhibit 100- to 1000-fold decreases in their second-order rate constants (k_{cat}/K_m) for substrate reduction (Table 6.1). Based on the aforementioned observations, it has been proposed that the P-loop is the principle determinant of substrate specificity in these enzymes (*7-10*), and that the [4Fe-4S] cluster plays a structural and/or regulatory role (*8, 16, 17*).

Table 6.1: Apparent second-order rate constants (k_{cat}/K_m) for assimilatory SRs. Activities were measured with purified recombinant enzymes, as production of sulfite from varying concentrations of [^{35}S]-APS and [^{35}S]-PAPS, in the presence of DTT and recombinant thioredoxin from *E. coli* as the electron donor.

	Iron-sulfur cluster	Substrate	k_{cat}/K_m (M^{-1}min^{-1})	Preference[a]
P. aeruginosa APR[b]	Yes	APS	2.0×10^8	APS
		PAPS	1.6×10^4	
M. tuberculosis APR[b]	Yes	APS	2.5×10^8	APS
		PAPS	6.0×10^4	
B. subtilis APR[c]	Yes	APS	3.1×10^6	None
		PAPS	1.6×10^6	

A. thaliana APR2[d]	Yes	APS	3.8×10^8	APS
		PAPS[d]	1.3×10^4	
P. patens APR[d]	Yes	APS	3.8×10^8	APS
		PAPS[d]	3.8×10^4	
E. coli PAPR[b]	No	APS	7.2×10^2	PAPS
		PAPS	2.3×10^8	
P. patens APR-B[d]	No	APS	2.1×10^5	APS
		PAPS	2.2×10^2	

[a]Defined as difference in substrate utilization of ≥10^2. Values measured at [b]pH 8.0, [c]pH 8.0 *(17)*, [d]pH 9.0 *(18)*. [e]Value estimated as the higher limit from ref. *(18)*.

Much effort has been made to understand substrate specificity in enzymes and several attempts have been made to rationally alter the specificity of an enzyme with sequence and structural information as the blueprint for redesign (*19*). One of the first successful examples was of changing the coenzyme specificity of *Escherichia coli* glutathione reductase from NADP to NAD (*20*). Structurally, NADP and NAD differ by a phosphate group at the 3'-postition of the adenosine 5'-phosphate (AMP) moiety, reminiscent of APS and PAPS. In glutathione reductase, the switch in coenzyme preference was accomplished by changing amino acids within the P-loop. Similarly, protein engineering has been used successfully by Shokat and coworkers to alter the nucleotide specificity of the prototypical tyrosine kinase, Src, to accept non-native nucleotides (*21*). This concept was subsequently extended to redesign kinase active sites to accept unique nucleotide inhibitors to facilitate direct identification of kinase targets (*22*). Overall these studies demonstrate that enzyme redesign is a powerful tool in exploiting substrate recognition elements to elucidate the catalytic mechanism and function of an enzyme.

Although it has been proposed that SR substrate specificity is dictated by the P-loop, this hypothesis has not yet been tested and, moreover, does not address the potential role of the iron-sulfur cluster. To gain insight into the forces driving specificity and catalytic efficiency of SRs we have employed metalloprotein engineering, spectroscopic and kinetic analyses. On the basis of our findings, we propose that the iron-sulfur cluster is a major determinant of specificity in this family of enzymes, specifically by enhancing the efficacy of the chemical step of catalysis. In this way, our findings offer new perspectives on the evolution of SRs, the function of protein-bound iron-sulfur clusters, and hold value for the development of inhibitors for SRs, a validated target for antibacterial therapy, including tuberculosis (*5, 23, 24*).
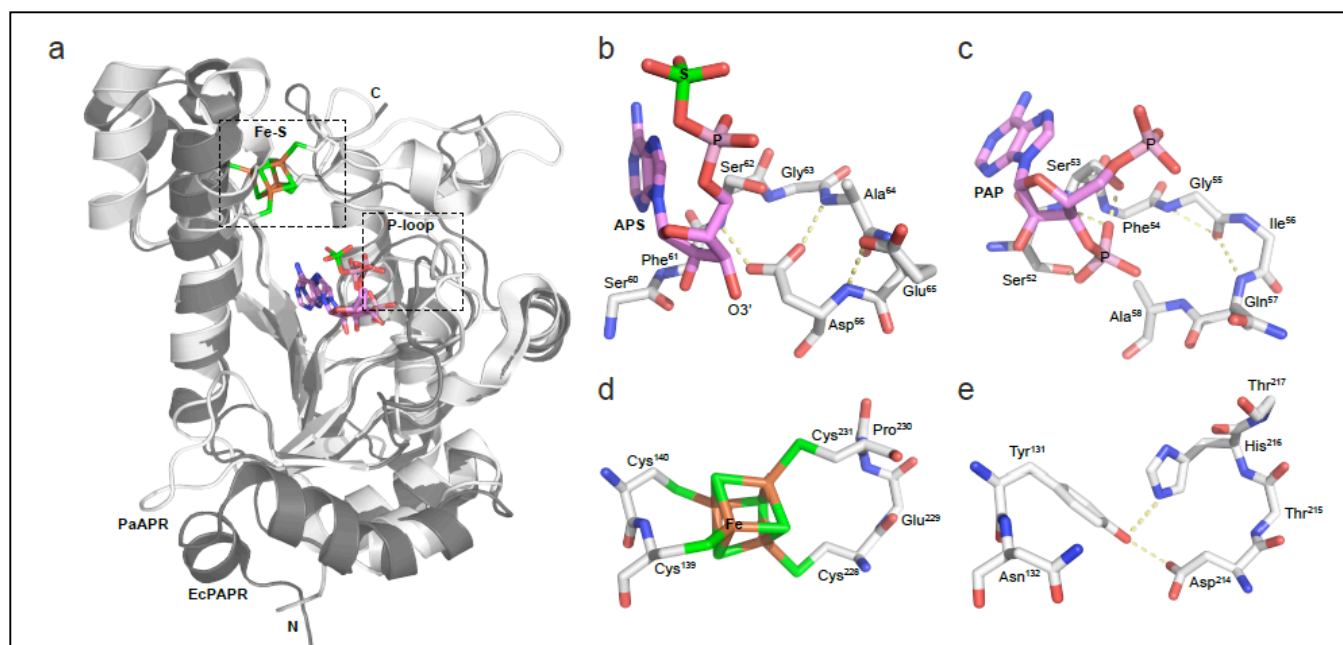
Figure 6.2. Comparison of putative substrate recognition elements in EcPAPR and PaAPR. a) Superposition of the structures of EcPAPR in charcoal (PDB deposition 2O8V) and PaAPR in white (PDB deposition 2GOY) showing the positions of the [4Fe-4S] cluster, the P-loop region and APS bound in PaAPR. The coordinates for PAPS bound to EcPAPR are assumed from ScPAPR (PDB deposition 2OQ2). C and N indicate the carboxyl- and amino- termini of the proteins, respectively. Comparison between the P-loop regions of b) PaAPR bound to APS (PDB deposition 2GOY) and c) EcPAPR bound to PAP (PDB deposition 2O8V, coordinates of PAP assumed from PDB deposition 2OQ2). Hydrogen bonding interactions are indicated by yellow dashes. In EcPAPR neutral Gln57 and Ala58 take the place of negatively charged Glu65 and Asp66 in PaAPR, respectively. These substitutions allow hydrogen-bonding interactions with the 3'-phosphate group of PAP and accommodate the bulkier moiety. In PaAPR, Asp66 compensates for the charge, volume and hydrogen binding potential of the 3'-phosphate group. Comparison between d) the iron-sulfur cluster coordinating region in PaAPR and e) the corresponding conserved residues in EcPAPR. In PaAPR, the [4Fe-4S] cluster ligated by four cysteine residues at positions 139, 140, 228 and 231. In EcPAPR, Tyr131, Asp214 and His216 have cross-linking hydrogen-bonding interactions.

150

6.3 Results

6.3.1 P-loop Residues Have Limited Contribution to Substrate Recognition

The P-loop residues in APRs have the SFS–GAED motif while the corresponding motif in PAPR consists of SSSFGIQA. In APR, the glutamate and aspartate residues interact with three P-loop amide groups and are positioned above the dipole of the α3 helix, as if they were mimicking the interaction of a
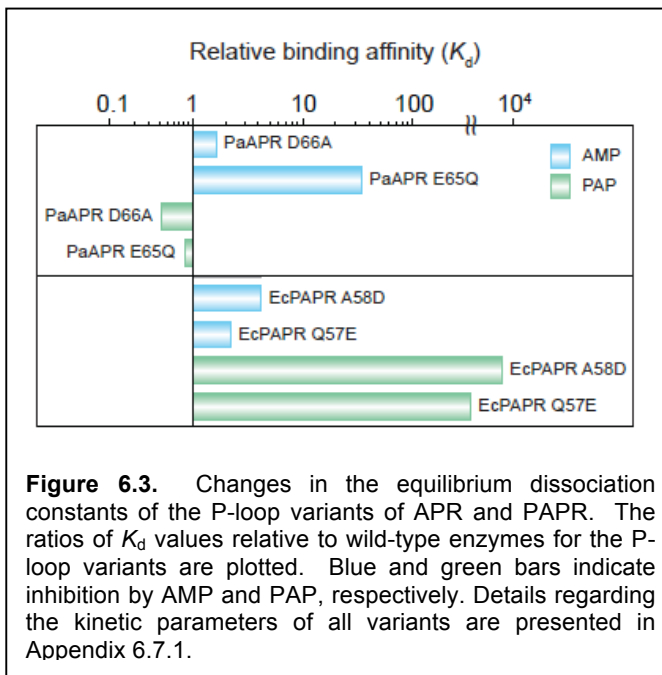
Figure 6.3. Changes in the equilibrium dissociation constants of the P-loop variants of APR and PAPR. The ratios of K_d values relative to wild-type enzymes for the P-loop variants are plotted. Blue and green bars indicate inhibition by AMP and PAP, respectively. Details regarding the kinetic parameters of all variants are presented in Appendix 6.7.1.

negatively charged phosphate (Figure 6.2, panels b and c). Conversely, the replacement of these acidic residues with Gln and Ala in PAPR would facilitate interaction of the amide groups with a 3'-phosphate and accommodate the bulkier moiety. To investigate this proposal, we generated E65Q, D66A and E65Q D66A variants of APR from *Pseudomonas aeruginosa* (PaAPR) as well as Q57E, A58D, and Q57E A58D variants of PAPR from *Escherichia coli* (EcPAPR). Of note, the enzymes from these particular species were chosen on the basis of available structural and functional information. We first tested the activity of the variants with native and non-native substrates. Interestingly, none of these substitutions increased k_{cat}/K_m for the non-native substrate (Appendix 6.7.1). In addition, the D66A and E65Q single substitutions in PaAPR had at most a 10-fold effect on APS reduction, whereas the Q65E and A58D replacements in EcPAPR exhibited a 1000-fold effect on the reduction of PAPS. All double mutants were significantly impaired relative to their wild-type counterparts. To

complement this analysis, we measured the dissociation constants (K_d) for the reaction products AMP and 3'-phosphoadenosine-5'-phosphate (PAP) for the P-loop variants (Figure 6.3). PaAPR variants showed at most a 2.5-fold enhancement in PAP binding, whereas no EcPAPR substitution enhanced association with AMP. Analogous to kinetic studies, the binding of P-loop variants to the native ligand was diminished, relative to the wild-type enzyme. Overall, this analysis shows that modification of the P-loop decreases binding and catalysis for the native ligand; however, the converse does not hold true as amino acid replacements do not correlate with enhancements for the non-cognate substrate or ligand.

6.3.2 EcPAPR4cys Incorporates a [4Fe-4S] Cluster

As the P-loop substitutions did not succeed in altering substrate specificity, a possible contribution of the iron-sulfur cluster was investigated. Based on the similar three-dimensional fold of APR and PAPR, we reasoned that EcPAPR residues (Y131, N132, D214, and T218) might be replaced by cysteine, and enable coordination of an iron-sulfur cluster (Figure 6.2, panels d and e). Thus, site-directed mutagenesis was employed and the resulting protein was co-expressed in bacteria with the pDB1282 plasmid that harbors the *isc* operon for cluster assembly (*25*). This approach afforded 10 mg of protein per liter of culture. The resulting enzyme, termed EcPAPR4cys, eluted as a dimer from the gel filtration column, analogous to wild-type EcPAPR, and the purity was estimated to be greater than 95% (Figure 6.4, panel a, inset). The UV-Vis absorbance spectrum of EcPAPR4cys showed a maximum in the visible range at 410 nm, which is similar to the [4Fe-4S] chromophore of PaAPR (Figure 6.4, panel a) *(16)*. However, ICP analysis of EcPAPR4cys showed that each mole of protein contained only 2.3 mole of iron. The amount of iron could not be increased by reconstitution or anaerobic purification (data not shown).

To identify the types and relative amounts of the Fe/S clusters in EcPAPR4cys, we employed a combination of Mössbauer and EPR spectroscopies and analytical methods. ICP analysis of a sample of EcPAPR4cys enriched in ^{57}Fe for Mössbauer spectroscopy reveals 2.0 Fe per polypeptide. The 4.2-K/53-mT Mössbauer spectrum of this sample (Figure 6.4, panel b) shows that the majority (82%) of the iron associated with EcPAPR gives rise to a quadrupole doublet with parameters typical of [4Fe-4S]$^{2+}$ clusters: isomer shift (δ) of 0.45 mm/s and quadrupole splitting parameter (ΔE_Q) of 1.03 mm/s. The remaining iron (15%) exhibited properties reminiscent of a [2Fe-2S]$^{2+}$ cluster (δ = 0.27 mm/s, ΔE_Q = 0.57 mm/s). The [2Fe-2S]$^{2+}$ form is also observed in plant and bacterial APRs and most likely results from partial degradation of the [4Fe-4S] cluster (*16, 17*). An identical EPR sample does not reveal the spectroscopic signatures of paramagnetic Fe/S clusters with *S* = 1/2 ground state (data not shown). Taken together, Mössbauer and ICP analyses indicate that approximately half of all EcPAPR4cys monomers coordinate a [4Fe-4S] cluster.

Although the iron-sulfur cluster in APR does not undergo redox chemistry during catalysis, the reduced form of the cluster can serve as a useful tool for characterization and mechanistic studies. Along these lines, we have recently characterized the 1+ state of the [4Fe-4S] cluster in APR from *Mycobacterium tuberculosis* (MtAPR) using electron paramagnetic resonance (EPR) spectroscopy *(16)*. Like MtAPR, the EPR signal of the chemically reduced EcPAPR4cys is broad, but shows rhombic symmetry with apparent *g*-values of 2.07, 1.90 and 1.76, which are characteristic of a [4Fe-4S] cluster in the 1+ state (Figure 6.4, panel c). Spin quantitation of the EPR signals from *g* = 2.33 to 1.58 indicate low reduction efficiency (0.04 spins/mol compared to 0.4 spins/mol for MtAPR).

A likely explanation for the lower signal intensity is that the constellation of residues surrounding the EcPAPR4cys cluster differs between from MtAPR, resulting in distinct electronic environments and reduction potentials (Appendix 6.7.3). Nonetheless, the overall similarity of Mössbauer and EPR parameters to those observed for MtAPR provides further support for the coordination of a $[4Fe-4S]^{2+}$ cluster by EcPAPR4cys.

Figure 6.4. Spectroscopic characterization of EcPAPR4cys. a) UV-Vis absorption spectra of EcPAPR and EcPAPR4cys. UV-Vis absorption of 10 μM EcPAPR (O) or EcPAPR4cys (●) in buffer containing 50 mM Tris–HCl, 150 mM NaCl (pH 7.4 at 25 °C) and 10% (v/v) glycerol. *Inset*, denaturing polyacrylamide gel with Coomassie staining displaying purified EcPAPR4cys at an apparent molecular mass of ~28 kDa. b) 4.2-K/53-mT Mössbauer spectra of 1 mM EcPAPR4cys. Experimental spectra are shown as vertical bars. The solid line is a quadrupole doublet simulation with the following parameters: (---) δ1= 0.45 mm/s, ΔEQ1= 1.03 mm/s (82%) and (— —) δ2= 0.27 mm/s, ΔEQ2= 0.57 mm/s (15%). The parameters for the majority species (— —) are consistent with a $[4Fe-4S]^{2+}$ cluster and the parameters for the minor species (---) are consistent with a $[2Fe-2S]^{2+}$ cluster. The remaining area of the spectrum is a broad featureless absorbing species that accounts for approximately 3% of the total area of the spectrum. c) EPR spectrum of photoreduced EcPAPR4cys. Anaerobic EcPAPR4cys (250 μM) was photoreduced as described in Materials and Methods. The EPR spectrum was recorded at 10 K and the instrument parameters were: microwave power, 10 mW; receiver gain, 2 x 10^4; modulation amplitude, 10 G and microwave frequency, 9.43 GHz.

We next evaluated the effect of the [4Fe-4S] cluster in EcPAPR4cys on the ability of EcPAPR to use PAPS or APS as substrates. To this end, we first monitored formation of the *S*-sulfocysteine intermediate, which is stable in plant and bacterial (P)APRs in the absence of Trx (*6, 26*). EcPAPR4cys was incubated in the presence or absence of APS or PAPS and the mass of the intact protein was analyzed by electrospray ionization mass spectrometry (ESI-MS). The deconvoluted *m/z* values obtained from these experiments are listed in Appendix 6.7.2. In the absence of substrate, the mass spectrum of EcPAPR4cys is consistent with the
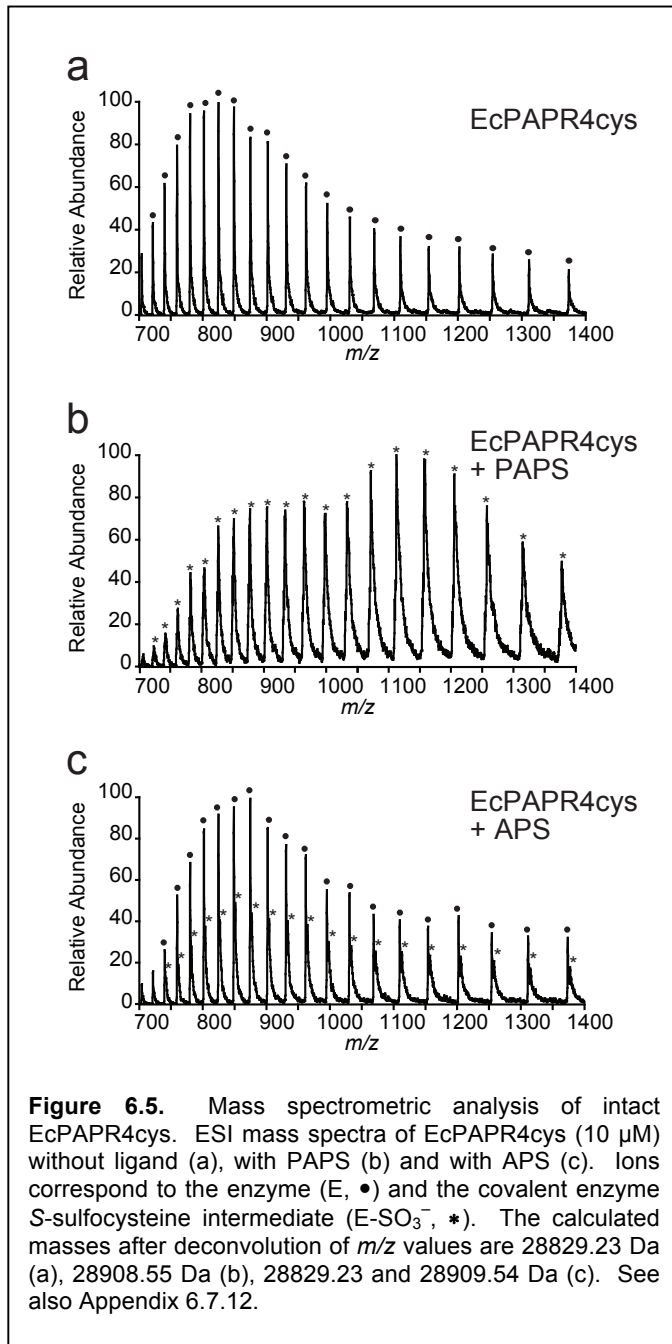
Figure 6.5. Mass spectrometric analysis of intact EcPAPR4cys. ESI mass spectra of EcPAPR4cys (10 µM) without ligand (a), with PAPS (b) and with APS (c). Ions correspond to the enzyme (E, •) and the covalent enzyme *S*-sulfocysteine intermediate (E-SO$_3^-$, ∗). The calculated masses after deconvolution of *m/z* values are 28829.23 Da (a), 28908.55 Da (b), 28829.23 and 28909.54 Da (c). See also Appendix 6.7.12.

molecular weight of the apoenzyme (Figure 6.5, panel a, solid circles). Incubation of EcPAPR4cys with PAPS resulted in formation of a new series of ions with a molecular weight 80 Da higher than enzyme alone, corresponding to the *S*-sulfocysteine adduct (Figure 6.5, panel b, asterisks). In the presence of APS two series of ions were observed corresponding to molecular weight of the apoenzyme (Figure 6.5c, solid

circles) and to the *S*-sulfocysteine intermediate (Figure 6.5, panel c, asterisks). Quantitative adduct formation was likely limited by our finding that not all EcPAPR4cys monomers are associated with a [4Fe-4S] cluster. Control experiments performed with wild-type enzymes and native substrates also showed the expected mass shifts (Appendix 6.7.2). These data show that EcPAPR4cys can generate the adduct with PAPS or APS as a substrate.

6.3.3 EcPAPR4cys can reduce APS as substrate

As reported above, EcPAPR4cys forms an enzyme *S*-sulfocysteine intermediate with APS, which should be competent for reduction by Trx to generate sulfite. To test this possibility, we performed gel-labeling experiments with [^{35}S]-labeled PAPS or APS (Appendix 6.7.5). Incubation of [^{35}S]-PAPS or [^{35}S]-APS with EcPAPR4Cys, and analysis of the reaction by nonreducing SDS-PAGE, showed a radioactive band at the molecular weight of EcPAPR indicating transfer of the [^{35}S]-label to the enzyme. Addition of Trx to this enzyme intermediate resulted in the complete loss of radiolabeling, as expected for reduction of the thio-sulfate bond. Analogous experiments were carried out using wild-type EcPAPR, which demonstrated comparable labeling with [^{35}S]-PAPS; by contrast, only a faint band was seen in reactions that contained [^{35}S]-APS. Taken together, the MS and radiolabeling experiments demonstrate that EcPAPR4cys forms a catalytically competent *S*-sulfocysteine intermediate with PAPS or APS, and that the variant reacts with APS with an enhanced rate compared with wild-type protein.

Having established that the EcPAPR4cys iron-sulfur protein exhibits activity, we proceeded to measure kinetic parameters for this variant. Table 6.2 shows the resultant data and is presented alongside data obtained for wild-type EcPAPR and PaAPR (see also Appendix 6-11). The second-order rate constant also known as the specificity

constant (k_{cat}/K_m; representing the reaction for free enzyme and substrate) demonstrates that EcPAPR4cys catalyzes APS reduction with approximately 600-fold less efficiency relative to PaAPR. Importantly, however, that the rate of APS reduction by the variant protein is nearly 1000-fold increased compared to wild-type EcPAPR. On the other hand, the k_{cat}/K_m for reaction of EcPAPR4cys with PAPS is almost the same as the native enzyme.
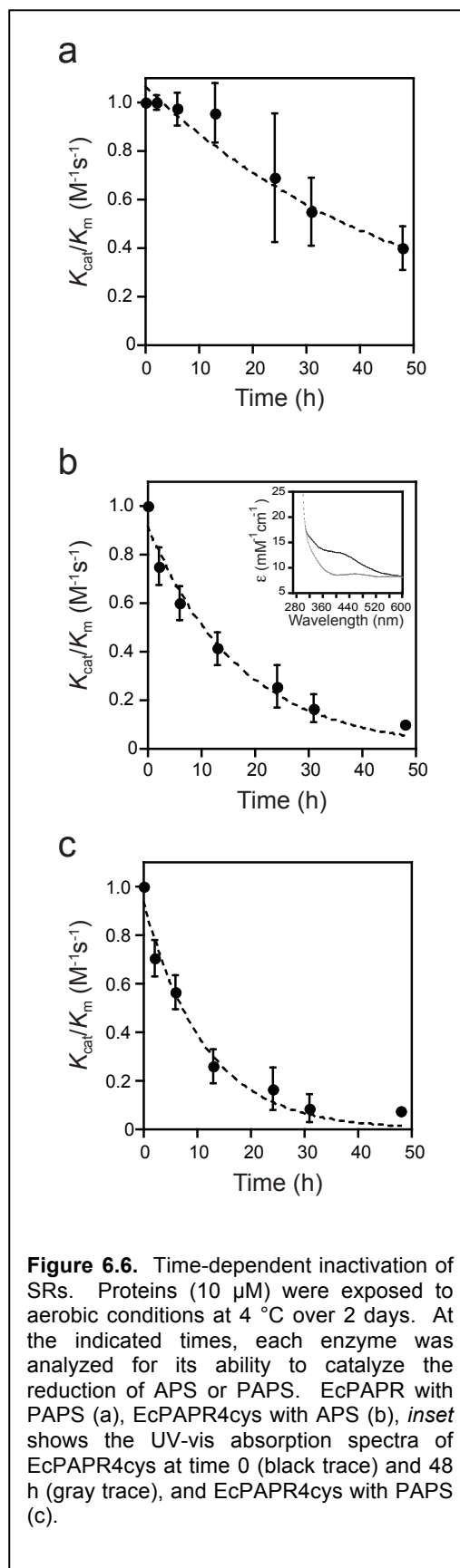
Table 6.2: Single-turnover rate and equilibrium constants for PaAPR, EcPAPR and EcPAPR4cys.[a]

Enzyme	Iron content (mol Fe/mol protein)	k_{cat}/K_m $(M^{-1} min^{-1})$[b]		k_{max} (min^{-1})[c]		$K_{1/2}$ (µM)		K_d^{AMP} (µM)[g]	K_d^{PAP} (µM)[g]
		APS	PAPS	APS	PAPS	APS[d]	PAPS[e]		
PaAPR	3.5	2.2×10^7	1.2×10^3	3.1	$\leq 1 \times 10^{-3}$	0.1	≥ 100[f]	35	8.1×10^3
EcPAPR	≤ 0.1	≤ 40	3.2×10^6	$\leq 1 \times 10^{-3}$	1.6	≥ 100[f]	0.9	3.4×10^3	1.4
EcPAPR 4cys	2.3	3.9×10^4	6.8×10^6	0.1	1.8	≥ 100[f]	0.1	5.6×10^3	4.3

[a]Measurements represent the average of three or more independent determinations and the S. D. was ≤15% of the value in all cases. The concentration of protein was determined by quantitative amino acid analysis and further corrected by the amount of active enzyme present. Unless otherwise stated, reaction conditions were 100 mM Bis-Tris propane, pH 6.5, 5 mM dithiothreitol, and 10 µM thioredoxin at 30 °C (see Materials and Methods). [b]k_{cat}/K_m values were measured as described in Materials and Methods. [c]k_{max} measured with saturating enzyme (see Materials and Methods). [d]10 nM or [e]1 µM thioredoxin was used to measure $K_{1/2}$ values for sulfite production, by varying the concentration of enzyme (see Materials and Methods). [f]At high concentrations of enzyme, the reactions became too fast to measure by hand. [g]K_d measured at pH 7.5

The preceding data indicate that the iron-sulfur cluster in EcPAPR4cys contributes to catalytic efficiency by enhancing substrate affinity and/or stabilizing the catalytic transition state. To gain further insight into the role of the iron-sulfur cluster in these rate enhancements, we evaluated the saturating single-turnover rate constant (k_{max}) and the

$K_{1/2}$ for EcPAPR4cys and wild-type enzymes (Table 6.2). These data reveal that EcPAPR4cys exhibits a 100-fold increase in the value of k_{max} for APS relative to EcPAPR, while the k_{max} for PAPS was the same within error. A 9-fold enhancement in the $K_{1/2}$ of PAPS was observed for EcPAPR4cys compared to wild-type, but differences in the $K_{1/2}$ of APS could not be discerned due to the limitations imparted by the maximum achievable enzyme concentration. As expected, the $K_{1/2}$ values for all enzymes with cognate substrate were 10^2-10^3–fold greater relative to the non-cognate substrate. The binding of AMP and PAP to the aforementioned enzymes was also examined. The resulting K_d values indicate that incorporation of the iron-sulfur cluster in EcPAPR diminishes ligand binding by 1.5 to 3-fold (Table 6.2), suggesting that increased electrostatic repulsion from the negatively charged $[Fe_4S_4(Cys)_4]^{2-}$ center may hamper binding of the 5'-phosphate dianion. Collectively, these results demonstrate that the

Figure 6.6. Time-dependent inactivation of SRs. Proteins (10 µM) were exposed to aerobic conditions at 4 °C over 2 days. At the indicated times, each enzyme was analyzed for its ability to catalyze the reduction of APS or PAPS. EcPAPR with PAPS (a), EcPAPR4cys with APS (b), *inset* shows the UV-vis absorption spectra of EcPAPR4cys at time 0 (black trace) and 48 h (gray trace), and EcPAPR4cys with PAPS (c).

iron-sulfur cluster in EcPAPR enhances substrate binding and APS reduction.

Finally, we evaluated the time-dependent inactivation of EcPAPR and EcPAPR4cys under prolonged exposure to aerobic conditions (Figure 6.6). In the case of EcPAPR4cys, dissociation of the iron-sulfur cluster from the protein scaffold could also be monitored by loss of absorption at 410 nm. Our data show that the half-life of EcPAPR, which lacks the cluster, was ~35 hours (Figure 6.6, panel a). However, inactivation and concomitant cluster decomposition for EcPAPR4cys occurred at an enhanced rate, with a half-life of ~10 hours (Figure 6.6, panels b and c). A strong correlation between an intact iron-sulfur cluster and catalytic activity is consistent with previous data obtained from plant and bacterial APRs (*11, 17, 18, 27*).

6.4 Discussion

Assimilatory sulfonucleotide reductases – APR and PAPR – exhibit similar sequences, structure, and thiol reaction chemistry (*6-9*). Analysis of the phylogenetic distribution of SRs suggests that PAPR evolved from APR through a single horizontal gene transfer event (*28*). The conserved reaction mechanism serves as a template for the divergent evolution of these two subclasses, which catalyze the reduction of substrates that differ by a single 3'-phosphate group. There are over 15 such enzyme families with common reaction mechanisms despite differences in substrate utilization (*29, 30*). In divergent evolution, protein folds and active site structural features are frequently reused amongst different family members and adapted to new catalytic purposes (*31*). Indeed, a closer look at the active sites of PaAPR and EcPAPR reveals that several strictly conserved, positively charged lysine and arginine residues interact with the sulfate moiety or α-phosphate (Figure 6.7 and Appendix 7.6.4). Moreover, the C-terminal peptide segment bearing the ECGH motif, which includes the cysteine nucleophile, is also conserved.

However, two critical features distinguish APR and PAPR active sites: residues in the P-loop region and the presence/absence of an iron-sulfur cluster. These distinctions afford a unique opportunity to explore substrate recognition and identify underlying principles that govern specific features of APR that were targeted for alteration during the specialization of PAPR function.

GTP/ATP-dependent proteins contain a glycine-rich motif with the sequence, GXXGXGKT/S, known as the P-loop (*7, 32, 33*). This structural moiety forms a large anion hole that interacts with phosphates. ATP pyrophosphatases (ATP PPases) harbor a modified P-loop, also known as the PP motif (*34*), with the fingerprint peptide SGGXDS/T. A highly modified version of the PP motif was discovered in EcPAPR (SXG), which is also found in enzymes with homologous protein folds, including ATP sulfurylase and GMP synthetase (*34-36*). Among ATP PPases, the P-loop interacts with the 5'-phosphates of ATP *(36, 37)*. Interestingly, however, structures of APR and PAPR co-crystallized with nucleotides show that the 3'-group on the ribose interacts with residues in the P-loop *(8, 9)*. In SRs, the motif is characterized by the hydrophobic β1-strand and α3-helix that flank the N- and C-terminal sides of the SFS–GAED and SSSFGIQA sequences in PaAPR and EcPAPR, respectively. Differences in the P-loop motif have also been observed in ATP synthases, wherein the sequence alterations have been suggested to imply diversity in nucleotide recognition and/or catalytic mechanism *(38)*. Since SRs share a common catalytic mechanism the change in P-loop sequences, particularly the acidic residues in APR, could be implicated in substrate discrimination.
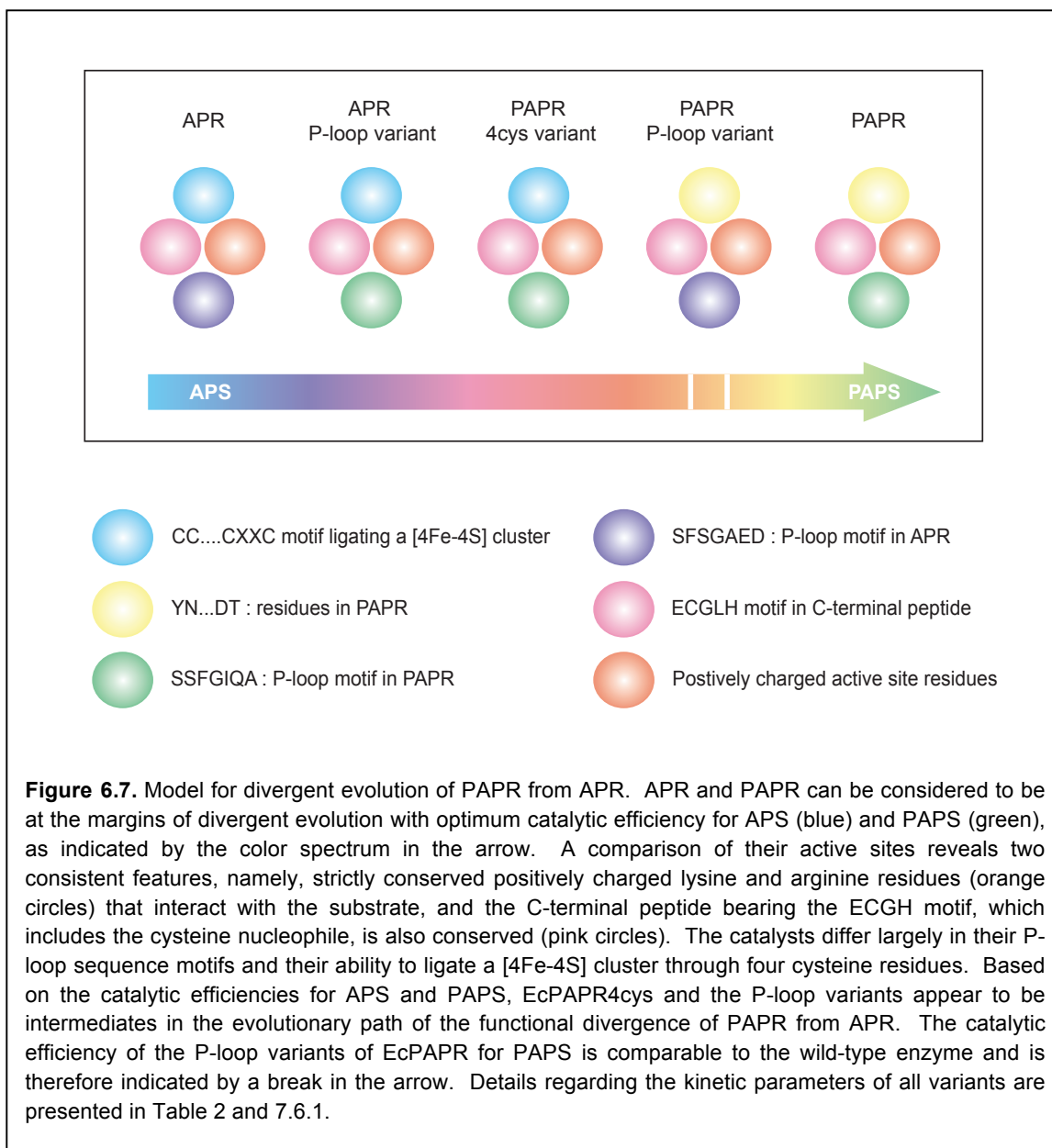
In this study, site-directed mutagenesis of the P-loop entailed the replacement of negatively charged E65 and D66 PaAPR residues with corresponding neutral glutamine and alanine residues found in EcPAPR and *visa versa*. Characterization of the resulting variants has led to two significant observations. First, any change in P-loop residues had an adverse effect on catalytic efficiency, underscoring the essential nature of these highly conserved motifs in the two subclasses of catalysts. Second, variants of APR exhibited only a modest enhancement in PAP binding. This finding indicates that while neutral P-loop residues contribute somewhat to accommodating the 3'-phosphate group, they cannot account entirely for substrate specificity. Moreover, P-loop variants of PAPR did not enhance binding to AMP, showing that the mere presence of a negatively charged residue in the P-loop sequence was insufficient. Along these lines, it is possible that additional P-loop modifications are required to enhance the binding of PAPS. For instance, EcPAPR S52 and S53 (of the **SS**FGIQA sequence) establish hydrogen bonds with the 3'-phosphate group of PAPS, whereas the corresponding residues in PaAPR (of the **SF**SGAED sequence) do not make any contact with the APS 3'-hydroxyl group. Future experiments will be required to delineate this and other possibilities.

The second distinguishing feature among SRs is that APR contains the conserved cysteine sequence, CC…CXXC, which ligates an essential [4Fe-4S] cluster. In place of this cofactor, PAPR possesses the semi-conserved motif, YN…DXXT that links the α7-helix and C-terminal β-turn by hydrogen bond interactions. In the course of our study, we attempted to substitute the cysteine pairs in PaAPR with the YN…DT motif; however, this variant failed to express in *E. coli* (data not shown). As an alternative approach to investigate the role of this region, we engineered an iron-sulfur cluster into EcPAPR. Based on the high degree of sequence and structural homology between SRs an empirical approach was adopted to generate the new metal-binding site. This strategy

has been employed to design novel metalloproteins, including the creation of a Mn(II)-binding site in cytochrome *c* peroxidase based on structural homology with manganese peroxidase *(39, 40)*. Favorable protein folds such as the Trx scaffold have also been exploited to introduce a cofactor and alter enzyme function (*41*). Assembly of a [2Fe-2S] cluster through directed evolution served to bridge two monomeric Trx subunits and enabled the resulting dimer to catalyze oxygen-dependent sulfhydryl oxidation (*42, 43*). In another instance, the second cysteine residue of the native CXXXCXXXC motif in the catalytic subunit of dimethyl-sulfoxide reductase (DmsA) was replaced leading to the assembly of a paramagnetic [3Fe-4S] cluster (*44*).

In the case of EcPAPR, our goal was to introduce a [4Fe-4S] cluster in order to probe the role of the metallocenter in sulfonucleotide reduction. Spectroscopy (UV-vis, Mössbauer, EPR, mass) and single turnover kinetic analysis were employed to characterize the resulting variant, termed EcPAPR4cys. Though we did not identify conditions that permitted quantitative cluster incorporation into each protein monomer, our spectroscopic data provides strong support for the assignment of a $[Fe_4S_4(Cys)_4]^{2-}$ center and compares favorably with studies of MtAPR *(16)*. Comparison of k_{cat}/K_m between EcPAPR4cys with wild-type PaAPR and EcPAPR showed that the installation of an iron-sulfur cluster dramatically improved the ability to turnover the APS ($\sim 10^3$-fold). Further studies revealed a minor role in substrate binding, with the majority of the rate enhancement stemming from the improvement in k_{max}, which reports on the rate of the chemical step. Furthermore, time-dependent inactivation studies also showed that the cluster was required for catalytic activity.

Previously, we have observed mid-range electrostatic interactions between the iron-sulfur cluster and the ligand present within the APR active site (*16*). These findings are

Figure 6.7. Model for divergent evolution of PAPR from APR. APR and PAPR can be considered to be at the margins of divergent evolution with optimum catalytic efficiency for APS (blue) and PAPS (green), as indicated by the color spectrum in the arrow. A comparison of their active sites reveals two consistent features, namely, strictly conserved positively charged lysine and arginine residues (orange circles) that interact with the substrate, and the C-terminal peptide bearing the ECGH motif, which includes the cysteine nucleophile, is also conserved (pink circles). The catalysts differ largely in their P-loop sequence motifs and their ability to ligate a [4Fe-4S] cluster through four cysteine residues. Based on the catalytic efficiencies for APS and PAPS, EcPAPR4cys and the P-loop variants appear to be intermediates in the evolutionary path of the functional divergence of PAPR from APR. The catalytic efficiency of the P-loop variants of EcPAPR for PAPS is comparable to the wild-type enzyme and is therefore indicated by a break in the arrow. Details regarding the kinetic parameters of all variants are presented in Table 2 and 7.6.1.

also supported by computational analysis (*45*). Based on these data, we proposed that

the cluster cofactor plays a role in pre-organizing positively charged active site residues

and in substrate activation. Specifically, that the charge from and polarization within the

$[Fe_4S_4(Cys)_4]^{2-}$ cluster could serve to activate the sulfate group of APS, thereby

facilitating S-OP cleavage and S-S bond formation in the reaction. In the absence of an

iron-sulfur cluster, PAPR could achieve something similar *via* repulsion between the

extra 3'-phosphate group of PAPS and the sulfate end of the 5'-phosphosulfate. Our

observation, that insertion of an iron-sulfur cluster in PAPR enhances the rate of APS reduction, is entirely consistent with this model. In this regard, iron-sulfur clusters are extremely versatile cofactors with enzymatic functions in electron transfer, Lewis-acid assisted catalysis, radical generation, and source of sulfur during biosyntheses of cofactors (*46-53*). This present study extends this list of functions to include substrate specificity.

From our study and sequence analysis, it is clear that the natural evolution of PAPR from APR involved several iterations of mutations. These factors are not easily recapitulated, and we note that none of the variants explored in this study resulted in a complete change of substrate specificity. Functional studies of EcPAPR4cys and the P-loop variants suggest that these enzymes may represent intermediates in the evolutionary pathway of SRs (Figure 6.7). This proposal is based on two interesting observations related to the catalytic efficiency and relative stability. First, is the striking similarity between (P)APR from *B. subtilis* and the P-loop variants of PaAPR. These enzymes coordinate an iron-sulfur cluster, but also contain a neutral residue in the position equivalent to residue 66 of PaAPR (or position 58 of EcPAPR). However, these catalysts all exhibit a significant reduction in catalytic efficiency with APS ($\geq 10^2$), compared to wild-type PaAPR (Table 6.1). Second, like APR-B from *P. patens*, the EcPAPR P-loop variants lack the iron-sulfur cluster and also display a decrease in enzyme activity relative to wild-type PaAPR (Table 1). Interestingly, we note that both PpAPR-B and EcPAPR gain in stability by forfeiting the iron-sulfur cluster. EcPAPR retains enzymatic activity over 2 days in contrast to APR, which loses activity within half a day. Similarly, PpAPR-B remains active for 5 days compared to its homolog, PpAPR, which harbors a [4Fe-4S] cluster and is only active for 2 days under aerobic conditions (*18*). Finally, we note that both BsAPR and PpAPR-B have markedly decreased

164

catalytic efficiency relative to other SRs (Table 6.1), indicating that these enzymes are not as specialized for the reductase function as the latter group of catalysts. Taken together, these observations show how characteristics of our experimentally generated variants resemble those of SRs from naturally occurring species, corroborating our proposal that the variants are representative of intermediates in the path of divergent evolution of PAPR from APR (Figure 6.7).

6.5 Conclusion

In conclusion, the cysteine motif that coordinates the [4Fe-4S] cluster within APR can be accommodated by the PAPR scaffold and confers enhanced binding and catalytic activity for the APS substrate. This work provides valuable insight into the contribution of the iron-sulfur cluster to catalysis, and a better understanding of the mechanisms involved in the divergent evolution of PAPR from APR.

6.6 Experimental procedures

6.6.1 Material

APS (≥95%) was obtained from Biolog Life Sciences Institute (Bremen, Germany). PAPS (≥88%) was obtained from Calbiochem (La Jolla, CA). PAP, AMP, iron (III) chloride were purchased from Sigma-Aldrich (St. Louis, MO). Fe-57 metal was purchased from Isoflex USA (San Francisco, CA) and micro bio-spin P30 columns were from Bio-Rad Laboratories (Hercules, CA).

6.6.2 Cloning, Expression and Purification of SRs.

Construction of the expression vectors encoding wild type PAPR from *E.coli* (EcPAPR), wild-type APR from *M. tuberculosis* (MtAPR) and wild-type APR from *P. aeruginosa* (PaAPR) cloned into the vector pET24b (Novagen) has been previously described (*1, 2*).

The EcPAPR4cys variant was generated from the EcPAPR template using the Quik-change site-directed mutagenesis kit (Stratagene, La Jolla, CA) and the following primer sequences sequentially: YN131CC: 5′ CGTTGAAGGCATTGAAAAGTGCTGTGACATCAACAAAGTCGA ACC 3′, D214C: 5' GAAGGATATTTATCGGTGGGCTGCACC CATACAACCCGT AAATGG 3' and T217C: 5' GGTGGGCTGCACCCATTGCACCCGTAAATGGG 3'. Other PaAPR, MtAPR and EcPAPR variants using site-directed mutagenesis with the following primers: 5′ CAGCGGCGCCGAGGCTGTCGTCCTGGTAG 3′ for PaAPR D66A, 5′ CTTCAGCGGCGCCCAGGACGTCGTCCTG 3′ for PaAPR E65Q, 5′ CTTCCAACATGGCTGCGGCGGTGCTGGTGGATC 3′ for MtAPR D69A, 5′ GCTTTGGCATTCAGGATGCGGTGAGCCTGCATC 3′ for EcPAPR A58D, 5′ CTTTCTTCCAGCTTTGGCATTGAAGCGGCGGTGAGCCTGCATCTG 3′ for EcPAPR Q57E. Successful cloning was confirmed by DNA sequencing analysis. Plasmids encoding EcPAPR4cys, MtAPR or PaAPR pET24 and pACYC (containing genes encoding the *isc* operon of six accessory proteins required for Fe–S cluster biosynthesis in *A. vinelandii* under the control of an arabinose-inducible promoter) (*27*) were co-transformed into *E. coli* BL21(DE3) (Novagen, San Diego, CA) and plated on L-agar 50 µg/ml kanamycin and 100 µg/ml carbenicillin. Plasmid encoding EcPAPR, EcPAPR A58D and EcPAPR Q57E pET24 was transformed into *E. coli* BL21(DE3) and plated on L-agar 50 µg/ml kanamycin. A single colony was picked and added to 5 ml of L-broth plus antibiotics and grown overnight with shaking at 37 °C. This culture was used as a 0.5% 1 L of L-broth plus antibiotics and grown with shaking at 37 °C until absorbance at 600 nm reached approximately 0.6. For EcPAPR4cys, MtAPR and PaAPR arabinose and iron citrate were added to final concentrations of 20 mM and 0.8 mM, respectively and the culture grown as above for 1 hr. At this point the flasks were removed from the

166

incubator. IPTG was added to a final concentration of 0.3 mM and the flasks were returned to the incubator and grown overnight at 18 °C with shaking at 200 rpm. For EcPAPR, EcPAPR A58D and EcPAPR Q57E after the culture reached an absorbance of 0.6 at 600 nm, IPTG was added to a final concentration of 0.4 mM, the flasks returned to the incubator and grown for 5 hours at 30°C. Cultures were harvested by centrifugation (4 °C, 4,300 *g*). After removal of the supernatant the pellets were stored at -80 °C until required. All purification steps were carried out at 4 °C. Cell pellets were resuspended in 30 ml Buffer A (20 mM sodium phosphate, 0.5 M NaCl, 10 mM imidazole; pH 7.4) supplemented with 0.1 mM PMSF, 10 μg/ml DNase, 5 μg/ml lysozyme and lysed by sonication. Lysates were centrifuged (20,000*g*, 15 min) and loaded onto a 5 ml HisTrap Chelating column (GE Healthcare, Piscataway, NJ) equilibrated in the same buffer. Unbound material was washed off with 50 ml of Buffer A and bound proteins then eluted with Buffer B (20 mM phosphate, 0.5 M NaCl, 250 mM imidazole; pH 7.4). Fractions containing the desired protein were pooled, concentrated by centrifugation (Amicon 10 kDa cutoff, Millipore, Billerica, MA) and loaded onto a 16/60 Superdex 200 size exclusion column previously equilibrated in Buffer C (50 mM Tris-HCl, 150 mM NaCl, 5 mM DTT, 10% glycerol; pH 7.4 at 25 °C). Fractions containing sulfonucleotide reductase were pooled, snap-frozen in liquid nitrogen, and stored at -80 °C. Protein concentrations were determined by quantitative amino acid analysis (Molecular Structure Facility, UC-Davis, CA and Ref. *(2)* and corrected by the number of active molecules determined by the activity assay for sulfonucleotide reductases described below. Iron content of each protein preparation was determined in duplicate by inductively coupled plasma (ICP) analysis.

6.6.3 Chemical Reconstitution of EcPAPR4cys

Reconstitution experiments were performed in the glove box. EcPAPR4cys desalted into 1.5 mL Buffer C using P30 columns, was successively incubated, with gentle stirring, with 5 mM DTT (30 min), 5 M equivalents of $FeCl_3$ (added dropwise then incubated for 45 min) and $Na_2S.9H_2O$ (added dropwise then incubated for 2 h). Excess ligand was removed from the reconstitution reaction by desalting the mixture using PD10-Sepharose columns, GE Healthcare) into Buffer C.

6.6.4 Gel-labeling of EcPAPR and EcPAPR4cys

In this experiment, 5 µM EcPAPR (lanes 1-4) and EcPAPR4cys, (lanes 5-8) were incubated at room temperature in 50 mM bis-tris propane (pH 7.0), 100 mM NaCl with ^{35}S-PAPS only (lanes 1 and 5); with ^{35}S-APS only (lanes 3 and 7); with ^{35}S-PAPS for 10 min followed by the addition of 10 µM thioredoxin (lanes 2 and 6) or with ^{35}S-APS for 10 min followed by the addition of 10 µM thioredoxin (lanes 4 and 8). SDS-PAGE load dye (without reductant) was added to terminate the reaction. The samples were heated at 60 °C for 3 min and size-fractionated by 12 % non-reducing SDS-PAGE. The incorporation of radioactivity was analyzed with a Phosphorimager.

6.6.5 Determination of active SR

Reactions were carried out at 30 °C in 100 mM bis-tris propane (pH 6.5) buffer. Non-radioactive APS or PAPS was doped with a trace amount of [^{35}S]-APS or [^{35}S]-PAPS respectively, as previously described (*6*). 1 µM of sulfonucleotide reductase was incubated with 2 µM substrate. The reactions were spotted on PEI-cellulose TLC plates, developed in 1M LiCl and analyzed using Typhoon Phosphorimager (GE Healthcare) analysis with Image Quant quantitation software. Under conditions that had quantitatively produced the *S*-sulfocysteine intermediate, a new signal on the TLC plate was observed as a discrete spot that remained at the origin of the TLC plate. For each

enzyme, the reaction endpoint was determined at the point where no further substrate was consumed or intermediate was formed. The number of active molecules was calculated as the fraction A/(A+B), where A and B are signals quantified from the intermediate formed and the unused radioactive substrate, respectively.

6.6.6 Preparation of EcPAPR4cys for EPR and Mössbauer Spectroscopy.

Samples of EcPAPR4cys suitable for EPR spectroscopy were prepared inside of an anaerobic chamber with O_2 levels ≤ 1 ppm. The procedure for photoreduction was carried out as previously described *(16)*. Briefly, purified EcPAPR4cys was exchanged into anaerobic buffer containing 50 mM Tris–HCl, 150 mM NaCl (pH 8.5 at 4 °C) and 10% glycerol. To reduce the cluster in EcPAPR4cys, reactions contained 250 µM enzyme, 25 mM sodium oxalate, and 250 µM deazaflavin in a total volume of 250 µL. The reaction mixtures were transferred to EPR tubes, chilled in an ice-salt bath (-6 °C) and irradiated with light from a 100 W quartz halogen lamp (Applied Photophysics, Surrey, UK) for 30 min. After illumination, samples were immediately frozen in liquid nitrogen and analyzed by low-temperature EPR. Mössbauer spectra were recorded on proteins that contained ^{57}Fe in place of natural-abundance iron. ^{57}Fe was incorporated into EcPAPR4cys by supplementation of *E. coli* growth media, and samples contained 1 mM protein, were transferred to Mössbauer cups and frozen in liquid nitrogen.

6.6.7 EPR Spectroscopy

X-band EPR spectra of photoreduced samples were recorded on a Bruker EMX spectrometer (Billerica, MA) equipped with an Oxford Instruments ITC4 temperature controller, a Hewlett-Packard model 5340 automatic frequency counter and Bruker gaussmeter. Figure 6.legend contains relevant instrumental parameters. The sample buffer was used to record the baseline under conditions identical to those in which the

sample spectra were obtained. The baseline was subtracted from the EcPAPR4cys spectrum shown in the figure. Spin concentration in EcPAPR4cys samples was determined by double integration of the EPR signal over a range of 2 kgauss and comparison with double integrals of 1 mM $Cu(ClO_4)_2$ in sample buffer. Figures were generated using Spin Count (ver 2.6.7) created by Professor M.P. Hendrich at Carnegie Mellon University. Spin Count is available at http://www.chem.cmu.edu/groups/hendrich/.

6.6.8 Mössbauer Spectroscopy

Mössbauer spectra were recorded on a spectrometer from WEB research (Edina, MN) operating in the constant acceleration mode in transmission geometry. Spectra were recorded with the temperature of the sample maintained at 4.2 K in an externally applied magnetic field of 53 mT oriented parallel to the γ-beam. The quoted isomer shifts were relative to the centroid of the spectrum of a foil of α-Fe metal at room temperature. Data analysis was performed using the program WMOSS from WEB research.

6.6.9 Mass Spectrometry

For mass spectrometric analysis, samples were prepared by incubating 10 μM enzyme with 2 mM APS or PAPS, where appropriate, for 40 min at 30 °C to allow for formation of *S*-sulfocysteine intermediate. Subsequently, the samples were exchanged into 0.1% formic acid using Micro Bio-Spin P30 columns (Bio Rad). Intact proteins samples were analyzed on an electrospray linear ion trap mass spectrometer (LTQ-XL, Thermo Scientific) after separation on an Agilent Eclipse XDB-C8 2.1 mm x 15 mm trap with mobile phases A (0.1% formic acid in water) and B (0.1% formic acid in acetonitrile) which was used to trap, desalt and elute proteins onto a Varian 2.1 mm x 50 mm 5 μm PLRP-S C18 column with a gradient of 5% to 100% in 14 min at a flow rate of 200 μL/min.

6.6.10 Kinetic assays

Reactions were carried out at 30 °C. Unless otherwise indicated, the buffer consisted of 100 mM bis-tris propane (pH 6.5) supplemented with 5 mM DTT and 10 μM *E. coli* thioredoxin. Production of $[^{35}S]SO_3^{2-}$ from $[^{35}S]$-APS or $[^{35}S]$-PAPS was monitored using charcoal-based separation and scintillation counting as previously reported *(54)*. The substrate was incubated with excess enzyme to ensure single-turnover conditions (>2.5-fold molar excess of enzyme). The reaction progress curve was plotted as the fraction of product versus time and was fit by a single exponential (eq. 1), where F is the fraction product, A is the fraction of substrate converted to product at completion, and t time. The observed rate constant (k_{obs}) is the product of the enzyme concentration and the apparent second-order rate constant k_{cat}/K_m (eq. 2). Under these conditions, the observed rate constant is linearly dependent upon enzyme concentration, and independent of substrate concentration, which demonstrated that substrate is not saturating. The reported k_{cat}/K_m values are for single-turnover conditions, but are equivalent to steady-state k_{cat}/K_m *(54)*. Kinetic data were measured in at least two independent experiments and the standard error was typically less than 15%.

$$F = A[1-e(-k_{obs}t)] \qquad (1)$$

$$k_{obs} = (k_{cat}/K_m)[E] \qquad (2)$$

The maximal observed rate constant (k_{max}) was determined at a saturating concentration of enzyme ($[E] \gg K_d$) and this was confirmed by the observation of the same rate constant at two different concentrations of enzyme (150 μM and 300 μM). Because the observed rate constant is independent of the concentration of enzyme, this indicates that the observed rate constant is equal to the maximal single-turnover rate constant ($k_{obs} = k_{max}$) and reports on the chemical steps after substrate binding (eq. 1).

Under single-turnover conditions, it is expected that the concentration dependence of the enzyme will be hyperbolic (eq. 3). The $K_{1/2}$ value indicates the protein concentration at which half of the substrate is bound. For $K_{1/2}$ determinations, the APR concentration was varied over a wide range in the presence of Trx.

$$k_{obs} = k_{max}[E]/(K_{1/2} + [E]) \qquad (3)$$

The inhibition constant (K_i) was measured for ligands, AMP and PAP by inhibiting the APR reaction under k_{cat}/K_m conditions at pH 7.5 with varying concentration of inhibitor (I). The data were fit to a simple model for competitive inhibition (eq. 4) and, with subsaturating APR, the K_i is equal to the equilibrium dissociation constant (K_d) of the inhibitor.

$$(k_{cat}/K_m)^{obs} = (k_{cat}/K_m)/(1 + [I]/K_i) \qquad (4)$$

6.7 Appendices

Table 6.7.1 Appendix Table of P-loop variants kinetics

Single-turnover rate and dissociation constants for PaAPR, MtAPR, EcPAPR and the respective P-loop variants.[a]

Enzyme	k_{cat}/K_m (M^{-1}min^{-1})[b]		K_d AMP (µM)	K_d PAP (µM)
	APS	PAPS		
PaAPR	1.8 x 10^8	3.5 x 10^4	35 ± 2	8.1 x 10^3
PaAPR Asp66Ala	2.5 x 10^7	9.6 x 10^3	57 ± 12	3.3 x 10^3
PaAPR Glu65Gln	7.2 x 10^6	3.5 x 10^3	1.2 x 10^3	6.9 x 10^3
PaAPR Glu65Gln, Asp66Ala	5.0 x 10^5	2.5 x 10^3	2.8 x 10^3	9.7 x 10^3
EcPAPR	840	1.2 x 10^8	3.4 x 10^3	1.4 ± 0.6
EcPAPR Ala58Asp	720	1.3 x 10^5	1.4 x 10^4	8.0 x 10^3
EcPAPR Gln57Glu	420	1.7 x 10^5	7.6 x 10^3	1.0 x 10^3
EcPAPR Gln57Glu, Ala58Asp	420	2.6 x 10^4	1.8 x 10^4	2.4 x 10^3

[a]Measurements represent the average of two or more independent determinations and the S.D. was ≤25% of the value in all cases. Unless otherwise stated, reaction conditions were 100 mM Bis-Tris propane, pH 7.5, 5 mM dithiothreitol, and 10 µM thioredoxin at 30 °C (see Materials and Methods). [b]k_{cat}/K_m values were measured as described in Materials and Methods.

Table 6.7.2 Appendix Table of mass measurements

Mass measurements of EcPAPR, EcPAPR4cys and MtAPR and associated enzyme *S*-sulfocysteine complexes.

Enzyme[a]	Measured mass (Da)[b]	Δm[c, d]
EcPAPR	28910.41 (28909.76)	N/A
EcPAPR + APS	28990.84 (28989.76)	80.43
EcPAPR + PAPS	28989.97 (28989.76)	79.56
EcPAPR4cys	28829.23 (28828.84)	N/A
EcPAPR4cys + APS	28909.54 (28908.84)	80.31
EcPAPR4cys + PAPS	28908.55 (28908.84)	79.56
MtAPR	28356.88 (28356.87)	N/A
MtAPR + APS	28437.45 (28436.87)	80.57
MtAPR + PAPS	28436.29 (28436.87)	79.41

[a]In reactions that contained APS or PAPS, the enzyme was incubated with substrate prior to mass analysis, as described in Materials and Methods. [b]The average experimental value of the most abundant isotopic mass over the charge state distribution, calculated by deconvolution. Theoretical values are shown in parenthesis and were calculated based on the amino acid sequence. [c]The mass differences in this table have been calculated with respect to the masses of the corresponding intact protein. [d]With the exception of EcPAPR + PAPS, EcPAPR4cys + PAPS and MtAPR + APS, two series of ions were observed corresponding to the enzyme alone and the enzyme *S*-sulfocysteine adduct. Relative abundance of these species is provided in the text.

Figure 6.7.3 Primary sequence alignment of sulfonucleotide reductases from *P. aeruginosa*, *M. tuberculosis*, *B. subtilis*, *A. thaliana, P. patens* (two isoforms, APR and APR-B), *E. coli*, *S. cerevisiae* and *P. patens*. The ClustalW2 (v2.1) Multiple Sequence Alignment program (*5*) was used to align all the sequences. Strictly conserved residues are outlined in red, red letters indicate conserved residues and conserved regions are boxed in blue. Residues flanking the active site are boxed in green. Positions of cysteine residues that coordinate to the [4Fe-4S] cluster are indicated below the sequence with (●). Alignment pictures were rendered with the server ESPript 2.2 (http://espript.ibcp.fr).
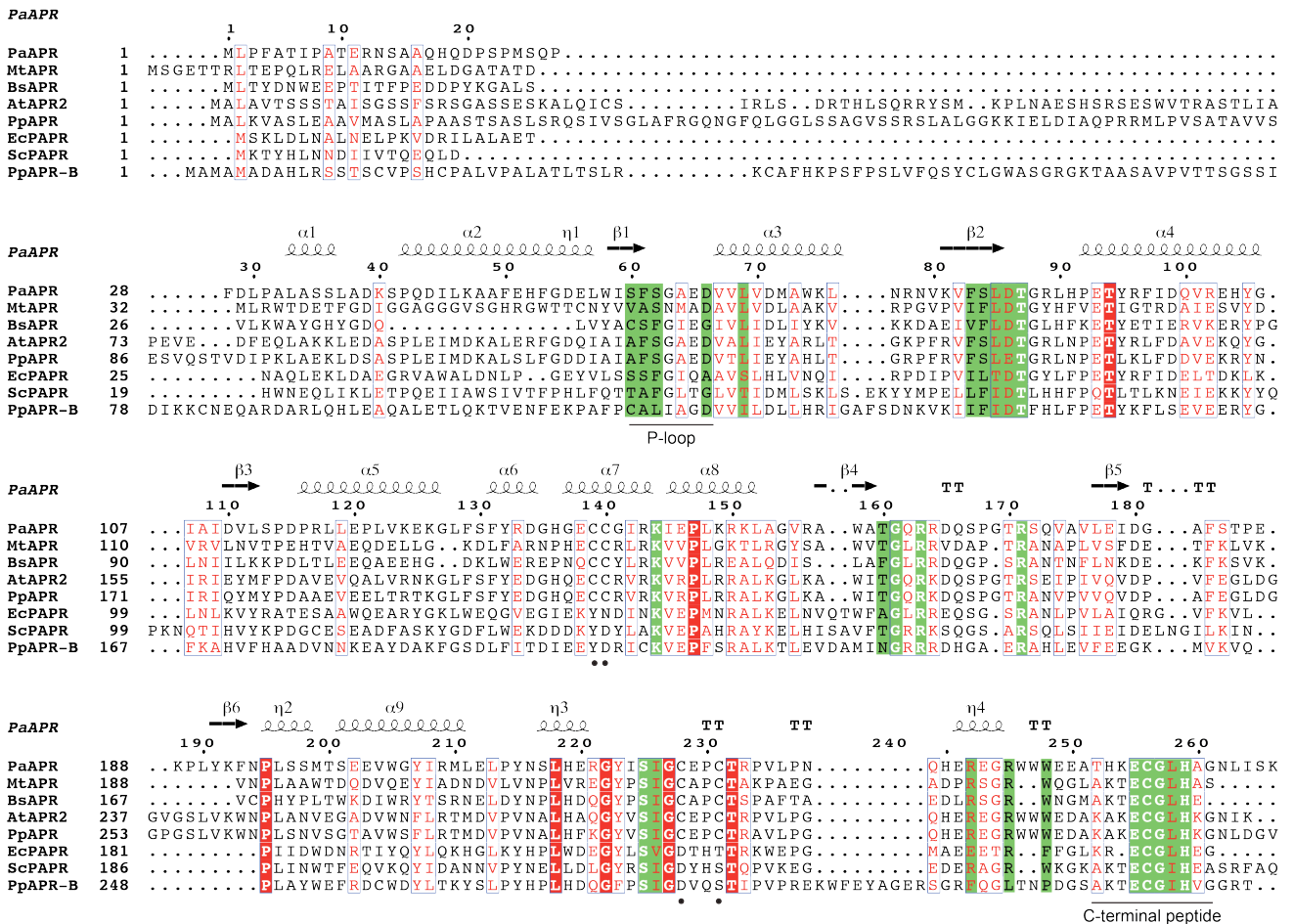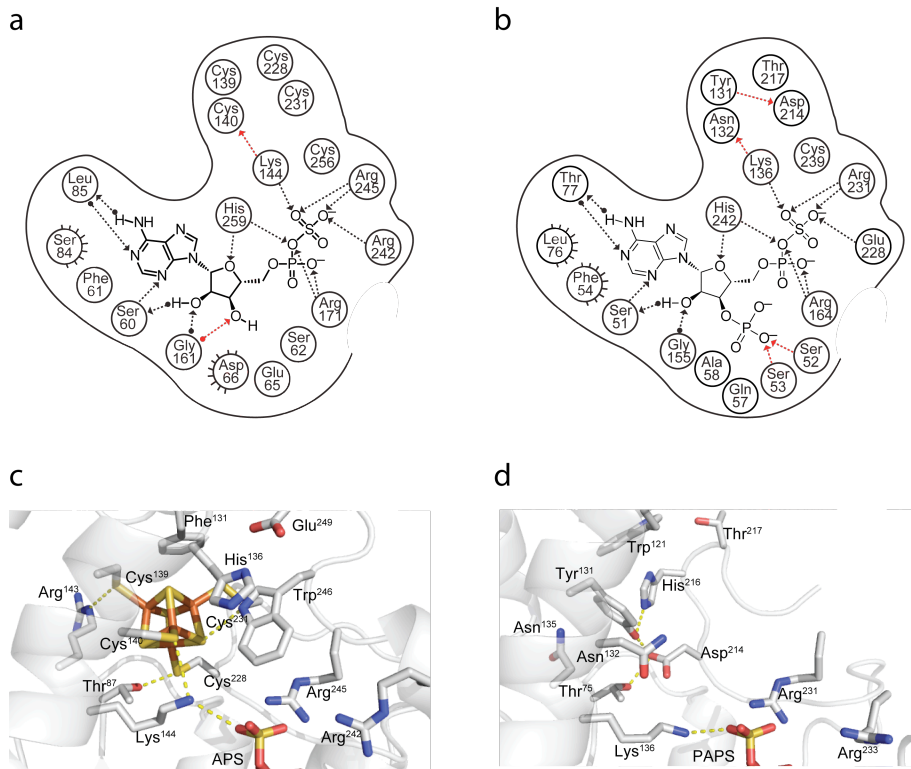

Supplementary Figure 1

Figure 6.7.4 Comparison of key active site regions in PaAPR and EcPAPR

Interactions are based on PaAPR (PDB deposition 2GOY) and EcPAPR (PDB deposition 2O8V), crystal structures, prior functional studies (*6, 7*) and the present study. Contacts of EcPAPR with PAPS have been assumed from the coordinates of PAP (ScPAPR, PDB deposition 2OQ2) and APS (PaAPR, PDB deposition 2GOY). Active site contacts of (a) PaAPR and (b) EcPAPR with APS and PAPS respectively, plotted in two dimensions. Protein residues in proximity of the ligand are shown, with hydrogen bonding interactions indicated as dotted lines with arrows denoting the direction of the bond. Interactions from the substrate or the residue backbones of the enzyme are distinguished from interactions with residue side chains by a solid dot at the end of the interaction line. Interactions highlighted in red are unique between the two active sites. In both structures, P-loop residues reside at the opposite end of the active site cleft with respect to active site lysine and arginine residues that interact with the 5'-sulfate moiety (>7Å away). (c) The environment of the [4Fe-4S] cluster in PaAPR. The [4Fe-4S] cluster is ligated by four cysteine residues at positions 139, 140, 228 and 231. Four conserved residues participate in charged or polar NH…S or OH…S hydrogen bonds to inorganic S or cysteine $S\gamma$ atoms; Thr87, Arg143, Lys144 and Trp246 (yellow dashes). Conserved basic residues Lys144, Arg242 and Arg245 in the active site interact with the phosphate and sulfate groups of APS. (d) Residues surrounding the YN..DXXT motif in EcPAPR. In the absence of the iron-sulfur cluster in EcPAPR, Tyr131 has cross-linking interactions with His216 and Asp214 (yellow dashes). Similar to PaAPR, positively charged Lys136 and Arg231 are poised to interact with the sulfate moiety of PAPS. Arg 231 and Glu228 are missing from the structure of EcPAPR therefore their position is
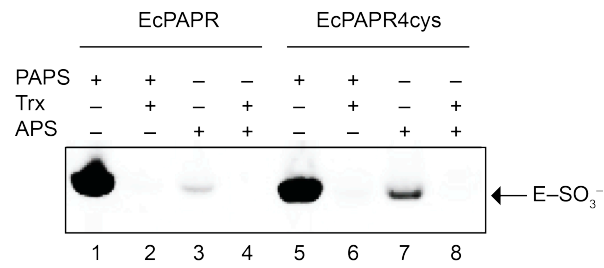
assumed from the coordinates of Arg231 and Arg233 (ScPAPR, PDB deposition 2OQ2).

Supplementary Figure 2

**Figure 6.7.5 Gel labeling of wild type EcPAPR and EcPAPR4cys**

Gel labeling of wild type EcPAPR (lanes 1-4) and EcPAPR4cys (lanes 5-8) with either [^{35}S]-PAPS or [^{35}S]-APS, with or without Trx, was carried out as described in the Materials and Methods.

Supplementary Figure 3

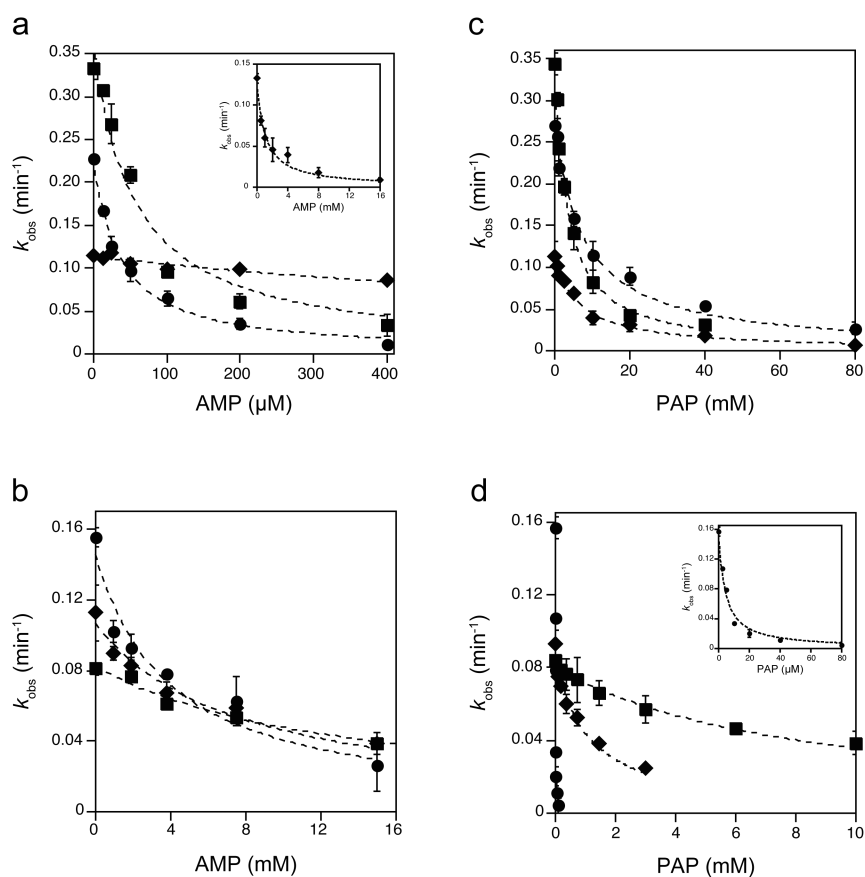**Figure 6.7.6 The reaction progress curve for P-loop variants of PaAPR and EcPAPR**

Under subsaturating concentration of substrate, the reaction is described by the apparent second order rate constant, k_{cat}/K_m. The enzyme concentration was varied as indicated due to the linear relationship between concentration and activity. a) Reduction of APS with PaAPR (2 nM, ●), D66A PaAPR (10 nM, ■) and E65Q PaAPR (20 nM, ◆). b) Reduction of APS with EcPAPR (10 μM, ●), A58D EcPAPR (10 μM, ■) and Q57E EcPAPR (10 μM, ◆). c) Reduction of PAPS with PaAPR (5 μM, ●), D66A PaAPR (10 μM, ■) and E65Q PaAPR (10μM, ◆). d) Reduction of PAPS as substrate with EcPAPR (2.5 nM, ●), A58D EcPAPR (0.5 μM, ■) and Q57E EcPAPR (0.5 μM,◆).
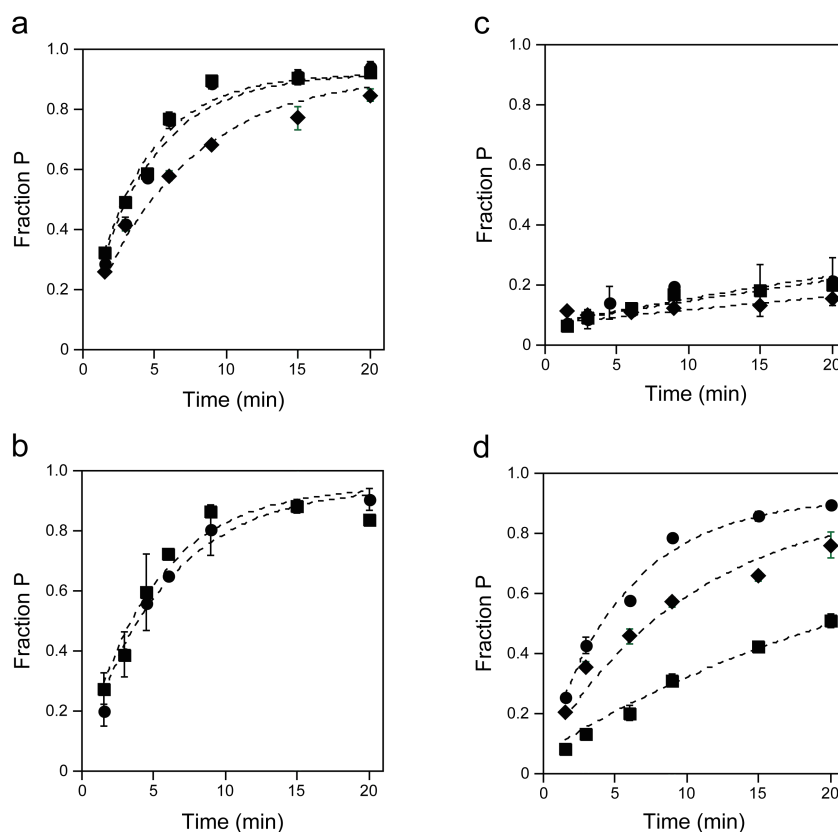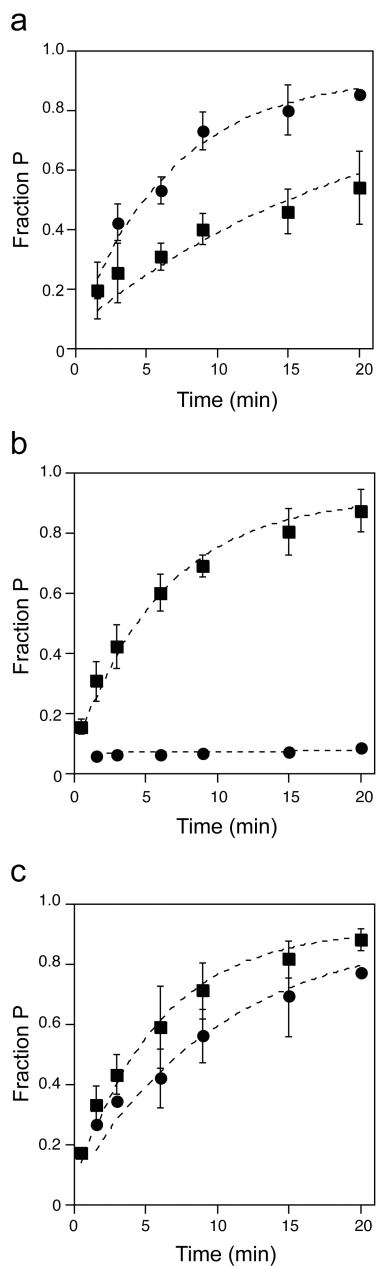

Supplementary Figure 4

179

Figure 6.7.7 Binding of AMP and PAP to P-loop variants of PaAPR and EcPAPR.

Nonlinear-least-squares fit of the data to a model for simple competitive inhibition (eq. 2) gave the dissociation constant K_d. a) K_d^{AMP} of PaAPR (●), D66A PaAPR (■) and E65Q PaAPR (◆); inset, E65Q PaAPR scaled. b) K_d^{AMP} of EcPAPR (●), A58D EcPAPR (■) and Q57E EcPAPR (◆). c) K_d^{PAP} of PaAPR (●), D66A PaAPR (■) and E65Q PaAPR (◆). d) K_d^{PAP} of EcPAPR (●), A58D EcPAPR (■) and Q57E EcPAPR (◆); inset, A58D EcPAPR scaled.
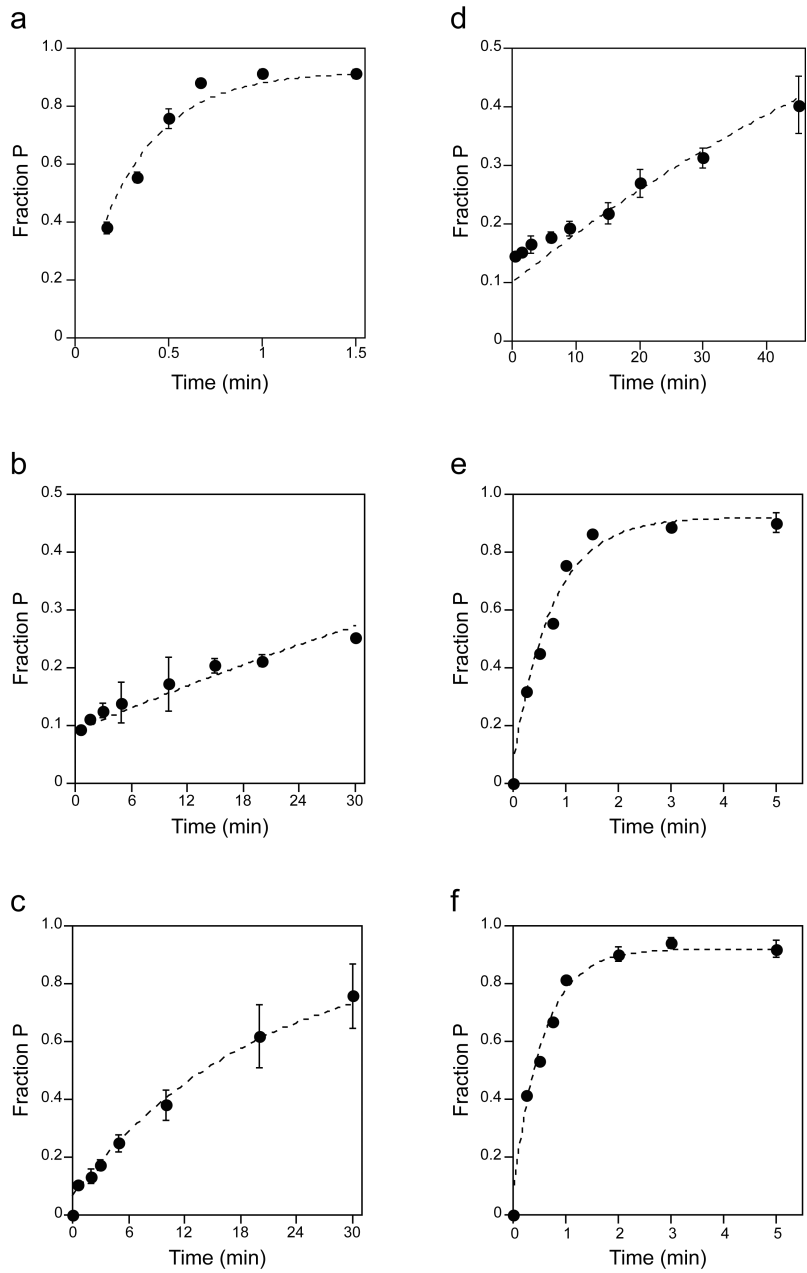

Supplementary Figure 5

180

Figure 6.7.8 Reaction progress curves for PaAPR, EcPAPR and EcPAPR4cys at pH

6.5 Under subsaturating concentration of substrate, the reaction is described by the apparent second-order rate constant, k_{cat}/K_m, for PaAPR (a), EcPAPR (b) and EcPAPR4cys (c) with APS (●) and PAPS (■).

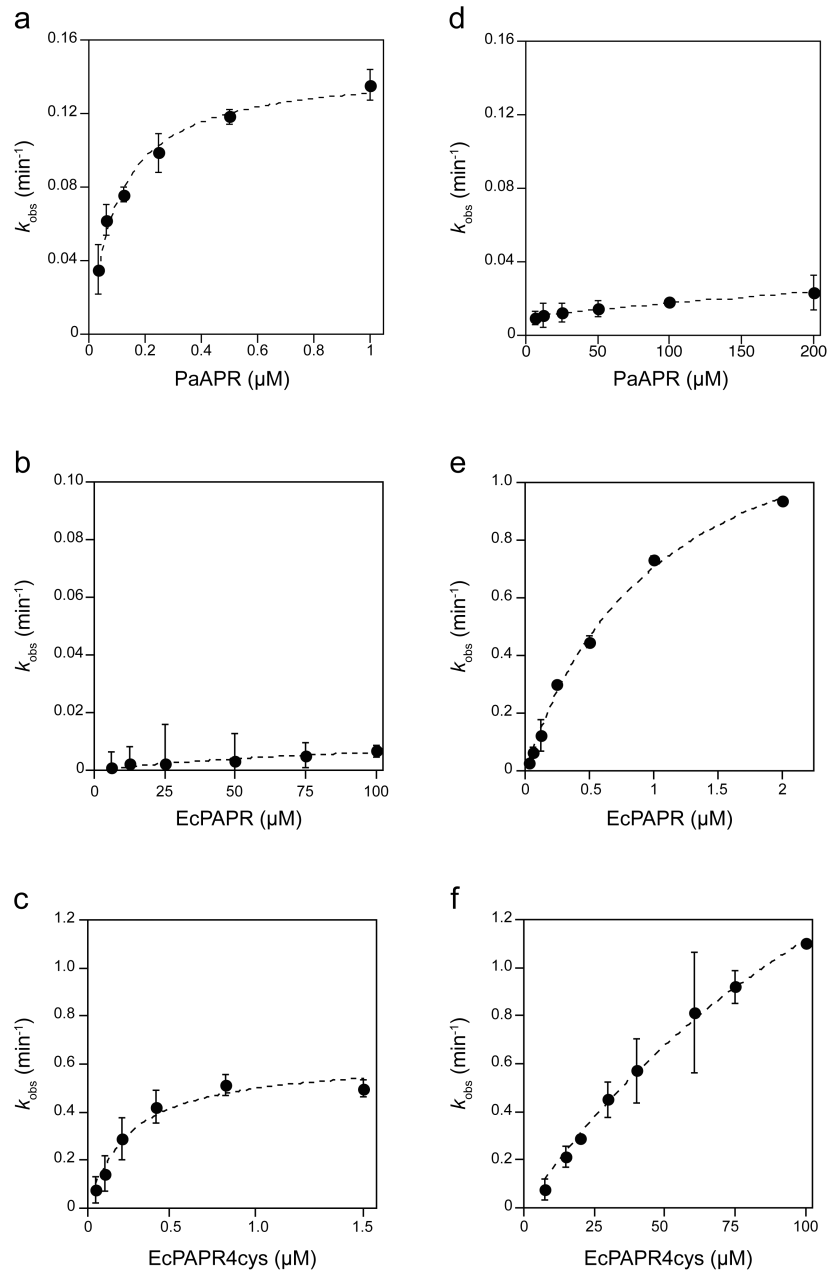Supplementary Figure 6

Figure 6.7.9 Maximal rate constant

k_{max}, measured under single turnover conditions with saturating enzyme at pH 6.5 for PaAPR (a), EcPAPR (b), EcPAPR4cys (c) with APS, and for PaAPR (d), EcPAPR (e), EcPAPR4cys (f) with PAPS.

Supplementary Figure 7

Figure 6.7.10 The apparent affinity

$K_{1/2}$, under single turnover conditions at pH 6.5 for PaAPR (a), EcPAPR (b) and EcPAPR4cys (c) with APS, and for PaAPR (d), EcPAPR (e) and EcPAPR4cys (f) with PAPS.

Supplementary Figure 8

Figure 6.7.11 Binding of AMP and PAP to EcPAPR4cys measured at pH 7.5.

The average of three independent determinations is shown, and the error bars indicate the standard deviations. Nonlinear-least-squares fit of the data to a model for simple competitive inhibition (eq. 4) gave the dissociation constants K_d^{AMP} (a) and K_d^{PAP} (b) for EcPAPR4cys.
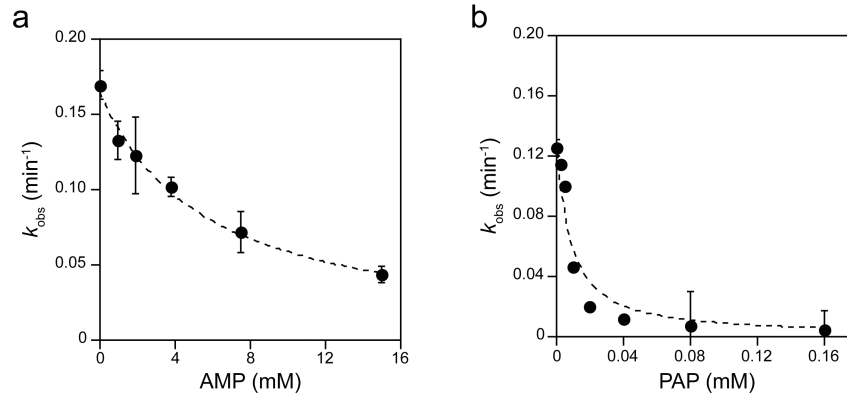
Supplementary Figure 9

184

6.8 References

1.   Schwenn, J. D. (1994) Photosyntheitc sulfate reduction, *Z. Naturforsch 49c*, 531-539.

2.   Kredich, N. M. (1996) *Escherichia coli and Salmonella typhimurium: Cellular and Molecular Biology*, Vol. 1, 2nd ed., ASM Press, Washington, D.C.

3.   Schelle, M. W., and Bertozzi, C. R. (2006) Sulfate metabolism in mycobacteria, *Chembiochem 7*, 1516-1524.

4.   Williams, S. J., Senaratne, R. H., Mougous, J. D., Riley, L. W., and Bertozzi, C. R. (2002) 5'-adenosinephosphosulfate lies at a metabolic branch point in mycobacteria, *J. Biol. Chem. 277*, 32606-32615.

5.   Senaratne, R. H., De Silva, A. D., Williams, S. J., Mougous, J. D., Reader, J. R., Zhang, T., Chan, S., Sidders, B., Lee, D. H., Chan, J., Bertozzi, C. R., and Riley, L. W. (2006) 5'-Adenosinephosphosulphate reductase (CysH) protects *Mycobacterium tuberculosis* against free radicals during chronic infection phase in mice, *Mol. Microbiol. 59*, 1744-1753.

6.   Carroll, K. S., Gao, H., Chen, H., Stout, C. D., Leary, J. A., and Bertozzi, C. R. (2005) A conserved mechanism for sulfonucleotide reduction, *PLoS. Biol. 3*, e250.

7.   Savage, H., Montoya, G., Svensson, C., Schwenn, J. D., and Sinning, I. (1997) Crystal structure of phosphoadenylyl sulphate (PAPS) reductase: a new family of adenine nucleotide alpha hydrolases, *Structure 5*, 895-906.

8.   Chartron, J., Carroll, K. S., Shiau, C., Gao, H., Leary, J. A., Bertozzi, C. R., and Stout, C. D. (2006) Substrate recognition, protein dynamics, and iron-sulfur cluster in *Pseudomonas aeruginosa* adenosine 5'-phosphosulfate reductase, *J. Mol. Biol. 364*, 152-169.

9.   Yu, Z., Lemongello, D., Segel, I. H., and Fisher, A. J. (2008) Crystal structure of *Saccharomyces cerevisiae* 3'-phosphoadenosine-5'-phosphosulfate reductase complexed with adenosine 3',5'-bisphosphate, *Biochemistry 47*, 12777-12786.

10.   Kopriva, S., Buchert, T., Fritz, G., Suter, M., Benda, R., Schunemann, V., Koprivova, A., Schurmann, P., Trautwein, A. X., Kroneck, P. M., and Brunold, C. (2002) The presence of an iron-sulfur cluster in adenosine 5'-phosphosulfate reductase separates organisms utilizing adenosine 5'-phosphosulfate and phosphoadenosine 5'-phosphosulfate for sulfate assimilation, *J. Biol. Chem. 277*, 21786-21791.

11.   Kopriva, S., Buchert, T., Fritz, G., Suter, M., Weber, M., Benda, R., Schaller, J., Feller, U., Schurmann, P., Schunemann, V., Trautwein, A. X., Kroneck, P. M., and Brunold, C. (2001) Plant adenosine 5'-phosphosulfate reductase is a novel iron-sulfur protein, *J. Biol. Chem. 276*, 42881-42886.

12.   Setya, A., Murillo, M., and Leustek, T. (1996) Sulfate reduction in higher plants: molecular evidence for a novel 5'-adenylylsulfate reductase, *Proc. Natl. Acad. Sci. U. S. A. 93*, 13383-13388.

13.   Kim, S. K., Rahman, A., Conover, R. C., Johnson, M. K., Mason, J. T., Gomes, V., Hirasawa, M., Moore, M. L., Leustek, T., and Knaff, D. B. (2006) Properties of

the cysteine residues and the iron-sulfur cluster of the assimilatory 5'-adenylyl sulfate reductase from Enteromorpha intestinalis, *Biochemistry 45*, 5010-5018.

14.   Kim, S. K., Gomes, V., Gao, Y., Chandramouli, K., Johnson, M. K., Knaff, D. B., and Leustek, T. (2007) The two-domain structure of 5'-adenylylsulfate (APS) reductase from Enteromorpha intestinalis is a requirement for efficient APS reductase activity, *Biochemistry 46*, 591-601.

15.   Chartron, J., Shiau, C., Stout, C. D., and Carroll, K. S. (2007) 3'-Phosphoadenosine-5'-phosphosulfate reductase in complex with thioredoxin: a structural snapshot in the catalytic cycle, *Biochemistry 46*, 3942-3951.

16.   Bhave, D. P., Hong, J. A., Lee, M., Jiang, W., Krebs, C., and Carroll, K. S. (2011) Spectroscopic studies on the [4Fe-4S] cluster in adenosine 5'-phosphosulfate reductase from *Mycobacterium tuberculosis*, *J. Biol. Chem. 286*, 1216-1226.

17.   Berndt, C., Lillig, C. H., Wollenberg, M., Bill, E., Mansilla, M. C., de Mendoza, D., Seidler, A., and Schwenn, J. D. (2004) Characterization and reconstitution of a 4Fe-4S adenylyl sulfate/phosphoadenylyl sulfate reductase from *Bacillus subtilis*, *J. Biol. Chem. 279*, 7850-7855.

18.   Kopriva, S., Fritzemeier, K., Wiedemann, G., and Reski, R. (2007) The putative moss 3'-phosphoadenosine-5'-phosphosulfate reductase is a novel form of adenosine-5'-phosphosulfate reductase without an iron-sulfur cluster, *J. Biol. Chem. 282*, 22930-22938.

19.   Penning, T. M., and Jez, J. M. (2001) Enzyme redesign, *Chem. Rev. 101*, 3027-3046.

20.   Scrutton, N. S., Berry, A., and Perham, R. N. (1990) Redesign of the coenzyme specificity of a dehydrogenase by protein engineering, *Nature 343*, 38-43.

21.   Shah, K., Liu, Y., Deirmengian, C., and Shokat, K. M. (1997) Engineering unnatural nucleotide specificity for Rous sarcoma virus tyrosine kinase to uniquely label its direct substrates, *Proc. Natl. Acad. Sci. U. S. A. 94*, 3565-3570.

22.   Bishop, A. C., Ubersax, J. A., Petsch, D. T., Matheos, D. P., Gray, N. S., Blethrow, J., Shimizu, E., Tsien, J. Z., Schultz, P. G., Rose, M. D., Wood, J. L., Morgan, D. O., and Shokat, K. M. (2000) A chemical switch for inhibitor-sensitive alleles of any protein kinase, *Nature 407*, 395-401.

23.   Bhave, D. P., Muse, W. B., 3rd, and Carroll, K. S. (2007) Drug targets in mycobacterial sulfur metabolism, *Infect. Disord. Drug Targets 7*, 140-158.

24.   Mdluli, K., and Spigelman, M. (2006) Novel targets for tuberculosis drug discovery, *Curr. Opin. Pharmacol. 6*, 459-467.

25.   Johnson, D. C., Unciuleac, M. C., and Dean, D. R. (2006) Controlled expression and functional analysis of iron-sulfur cluster biosynthetic components within Azotobacter vinelandii, *J. Bacteriol. 188*, 7551-7561.

26.   Weber, M., Suter, M., Brunold, C., and Kopriva, S. (2000) Sulfate assimilation in higher plants characterization of a stable intermediate in the adenosine 5'-phosphosulfate reductase reaction, *Eur. J. Biochem. 267*, 3647-3653.

27.   Carroll, K. S., Gao, H., Chen, H., Leary, J. A., and Bertozzi, C. R. (2005) Investigation of the iron-sulfur cluster in *Mycobacterium tuberculosis* APS

reductase: implications for substrate binding and catalysis, *Biochemistry 44*, 14647-14657.

28.   Kopriva, S., Buchert, T., Fritz, G., Suter, M., Benda, R., Schunemann, V., Koprivova, A., Schurmann, P., Trautwein, A. X., Kroneck, P. M., and Brunold, C. (2002) The presence of an iron-sulfur cluster in adenosine 5'-phosphosulfate reductase separates organisms utilizing adenosine 5'-phosphosulfate and phosphoadenosine 5'-phosphosulfate for sulfate assimilation, *J. Biol. Chem. 277*, 21786-21791.

29.   Todd, A. E., Orengo, C. A., and Thornton, J. M. (1999) Evolution of protein function from a structural perspective, *Curr. Opin. Chem. Biol. 3*, 548-556.

30.   Babbitt, P. C., Hasson, M. S., Wedekind, J. E., Palmer, D. R., Barrett, W. C., Reed, G. H., Rayment, I., Ringe, D., Kenyon, G. L., and Gerlt, J. A. (1996) The enolase superfamily: a general strategy for enzyme-catalyzed abstraction of the alpha-protons of carboxylic acids, *Biochemistry 35*, 16489-16501.

31.   Wise, E. L., and Rayment, I. (2004) Understanding the importance of protein structure to nature's routes for divergent evolution in TIM barrel enzymes, *Acc. Chem. Res. 37*, 149-158.

32.   Dreusicke, D., and Schulz, G. E. (1986) The glycine-rich loop of adenylate kinase forms a giant anion hole, *FEBS Lett. 208*, 301-304.

33.   Saraste, M., Sibbald, P. R., and Wittinghofer, A. (1990) The P-loop--a common motif in ATP- and GTP-binding proteins, *Trends Biochem. Sci. 15*, 430-434.

34.   Bork, P., and Koonin, E. V. (1994) A P-loop-like motif in a widespread ATP pyrophosphatase domain: implications for the evolution of sequence motifs and enzyme activity, *Proteins 20*, 347-355.

35.   Mougous, J. D., Lee, D. H., Hubbard, S. C., Schelle, M. W., Vocadlo, D. J., Berger, J. M., and Bertozzi, C. R. (2006) Molecular basis for G protein control of the prokaryotic ATP sulfurylase, *Mol. Cell 21*, 109-122.

36.   Tesmer, J. J., Klem, T. J., Deras, M. L., Davisson, V. J., and Smith, J. L. (1996) The crystal structure of GMP synthetase reveals a novel catalytic triad and is a structural paradigm for two enzyme families, *Nat. Struct. Biol. 3*, 74-86.

37.   Smith, C. A., and Rayment, I. (1996) Active site comparisons highlight structural similarities between myosin and other P-loop proteins, *Biophys. J. 70*, 1590-1602.

38.   Kumar, A., Manimekalai, M. S., Balakrishna, A. M., Jeyakanthan, J., and Gruber, G. Nucleotide binding states of subunit A of the A-ATP synthase and the implication of P-loop switch in evolution, *J. Mol. Biol. 396*, 301-320.

39.   Yeung, B. K., Wang, X., Sigman, J. A., Petillo, P. A., and Lu, Y. (1997) Construction and characterization of a manganese-binding site in cytochrome c peroxidase: towards a novel manganese peroxidase, *Chem. Biol. 4*, 215-221.

40.   Wilcox, S. K., Putnam, C. D., Sastry, M., Blankenship, J., Chazin, W. J., McRee, D. E., and Goodin, D. B. (1998) Rational design of a functional metalloenzyme: introduction of a site for manganese binding and oxidation into a heme peroxidase, *Biochemistry 37*, 16853-16862.

41.	Coldren, C. D., Hellinga, H. W., and Caradonna, J. P. (1997) The rational design and construction of a cuboidal iron-sulfur protein, *Proc. Natl. Acad. Sci. U. S. A. 94*, 6635-6640.

42.	Masip, L., Pan, J. L., Haldar, S., Penner-Hahn, J. E., DeLisa, M. P., Georgiou, G., Bardwell, J. C., and Collet, J. F. (2004) An engineered pathway for the formation of protein disulfide bonds, *Science 303*, 1185-1189.

43.	Collet, J. F., Peisach, D., Bardwell, J. C., and Xu, Z. (2005) The crystal structure of TrxA(CACA): Insights into the formation of a [2Fe-2S] iron-sulfur cluster in an *Escherichia coli* thioredoxin mutant, *Protein. Sci. 14*, 1863-1869.

44.	Trieber, C. A., Rothery, R. A., and Weiner, J. H. (1996) Engineering a novel iron-sulfur cluster into the catalytic subunit of *Escherichia coli* dimethyl-sulfoxide reductase, *J. Biol. Chem. 271*, 4620-4626.

45.	Bhave, D. P., Han, W. G., Pazicni, S., Penner-Hahn, J. E., Carroll, K. S., and Noodleman, L. (2011) Geometric and Electrostatic Study of the [4Fe-4S] Cluster of Adenosine-5'-Phosphosulfate Reductase from Broken Symmetry Density Functional Calculations and Extended X-ray Absorption Fine Structure Spectroscopy, *Inorg. Chem. 50*, 6610-6625.

46.	Booker, S. J. (2009) Anaerobic functionalization of unactivated C-H bonds, *Curr. Opin. Chem. Biol. 13*, 58-73.

47.	Dos Santos, P. C., and Dean, D. R. (2008) A newly discovered role for iron-sulfur clusters, *Proc. Natl. Acad. Sci. U. S. A. 105*, 11589-11590.

48.	Beinert, H., Holm, R. H., and Munck, E. (1997) Iron-sulfur clusters: nature's modular, multipurpose structures, *Science 277*, 653-659.

49.	Beinert, H., Kennedy, M. C., and Stout, C. D. (1996) Aconitase as Ironminus signSulfur Protein, Enzyme, and Iron-Regulatory Protein, *Chem. Rev. 96*, 2335-2374.

50.	Walsby, C. J., Ortillo, D., Yang, J., Nnyepi, M. R., Broderick, W. E., Hoffman, B. M., and Broderick, J. B. (2005) Spectroscopic approaches to elucidating novel iron-sulfur chemistry in the "radical-Sam" protein superfamily, *Inorg. Chem. 44*, 727-741.

51.	Fontecave, M. (2006) Iron-sulfur clusters: ever-expanding roles, *Nat. Chem. Biol. 2*, 171-174.

52.	Frey, P. A., Hegeman, A. D., and Ruzicka, F. J. (2008) The Radical SAM Superfamily, *Crit. Rev. Biochem. Mol. Biol. 43*, 63-88.

53.	Booker, S. J., Cicchillo, R. M., and Grove, T. L. (2007) Self-sacrifice in radical S-adenosylmethionine proteins, *Curr. Opin. Chem. Biol. 11*, 543-552.

54.	Hong, J. A., Bhave, D. P., and Carroll, K. S. (2009) Identification of critical ligand binding determinants in Mycobacterium tuberculosis adenosine-5'-phosphosulfate reductase, *J. Med. Chem. 52*, 5485-5495.

55.	Larkin, M. A., Blackshields, G., Brown, N. P., Chenna, R., McGettigan, P. A., McWilliam, H., Valentin, F., Wallace, I. M., Wilm, A., Lopez, R., Thompson, J. D., Gibson, T. J., and Higgins, D. G. (2007) Clustal W and Clustal X version 2.0, *Bioinformatics 23*, 2947-2948.

56.   Drummond, A. J., Ashton, B., Buxton, S., Cheung, M., Cooper, A., Duran, C., Field, M., Heled, J., Kearse, M., Markowitz, S., Moir, R., Stones-Havas, S., Sturrock, S., Thierer, T., and Wilson, A. (2011) Geneious v5.4, Available from http://www.geneious.com.

Chapter 7

Conclusions and future directions

7.1 Abstract

The data presented in the previous chapters illustrate our effort towards elucidating mechanistic details of the APR reaction and identifying small molecule inhibitors. The present Chapter summarizes the key findings and significance of this work. In addition, I discuss future directions to modify the structures of hit compounds and overcome limitations inherent to current therapeutic strategies. I also present an alternative experimental approach to discover APR inhibitors by targeting the [4Fe-4S] cluster of APR, protein-protein interaction interface with thioredoxin, and evaluation of compounds through cell-based assays.

7.2 Conclusions: strategies to develop small molecule inhibitors of APR

Recently, APR has been validated as a promising drug target against the latent phase of the tuberculosis-causing bacteria (*1-3*). The overall aim of this thesis was to investigate the mechanism of APR and exploit this information in the design and discovery of small molecule inhibitors. In Chapter 1, I first discussed the current TB epidemic and limitations of the current treatments. APR, which catalyzes the first committed step in bacterial sulfate reduction, has been identified as drug target against latent TB infection. I illustrated briefly the overall drug discovery pipeline and introduced our strategies to discover APR inhibitors through VLS and rational design. Chapter 2 describes VLS of APR using Autodock, followed by biological evaluation of *in silico* hits. VLS successfully

identified the first non-phosphate based inhibitors against APR, which constitutes an essential step toward inhibitor discovery.

The active site of a protein consists of pockets, dynamic regions and conserved motifs. These active site-defined elements are involved in substrate binding, catalysis or both. In Chapter 3, the molecular determinants of the APR active site that underlie binding and specificity are discussed through a series of substrate and product analogs. This study afforded insight into the key interactions between the substrate and APR, thereby providing a pharmacological roadmap for rational inhibitor design. In Chapter 4, biochemical and biophysical data are presented that indicate the essential role of the conserved residue, His252, in substrate binding. In Chapter 5, kinetic and spectroscopic studies were used to identify Lys144 as a molecular bridge between the iron-sulfur cluster and APS. This interaction network stabilizes the catalytic transition state and indicates a role for the iron-sulfur cluster in APS reduction. Finally, in Chapter 6, we focused on substrate discrimination in the SR family was explored. Using site-directed mutagenesis and metalloprotein engineering, we generated P-loop mutations in SRs and installed a [4Fe-4S] cluster in PAPR. Kinetic and spectroscopic characterization of the variants provided insight into the switch in molecular recognition between APR and PAPR, and permitted a better understanding of evolution in this family of enzymes.

7.3 Future directions

7.3.1 Computational drug design

VLS is a valuable tool to identify inhibitors that target APR (*4*). We used the APR pharmacophore model, generated in Chapter 2, as a template to select promising candidates from the larger and more chemically comprehensive Maybridge database, consisting of 56,000 compounds. We chose this database for its drug-like properties

(*e.g.*, bioavailability and stability). Thus, we expected that optimized compounds from this library would retain these properties and have activity in cell-based systems. The

VLS was conducted using the same method as in the previous NCI screen and 51 compounds, corresponding to 0.1% of the Maybridge
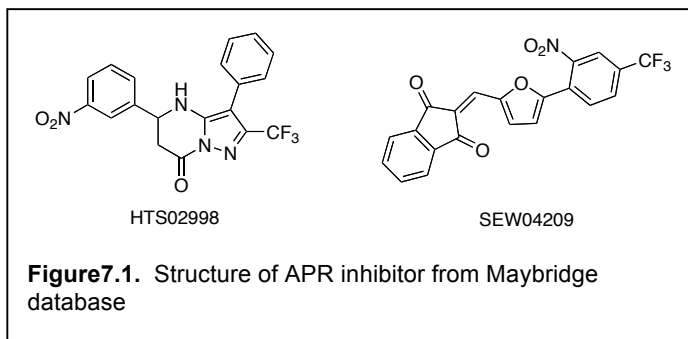

Figure7.1. Structure of APR inhibitor from Maybridge database

database, were selected for further biological evaluation. Surprisingly, only two compounds were identified to have 50% inhibition against APR with dissociation constants of 44 μM (HTS02996) and 101 μM (SEW04209) (Figure 7.1). The failure to identify any potent inhibitors from this library may be an indicator that the *P. aeruginosa* crystal structure used in these studies does not sufficiently model interactions with *M. tuberculosis* APR.

7.3.1.1 Structure activity relationship of current leads
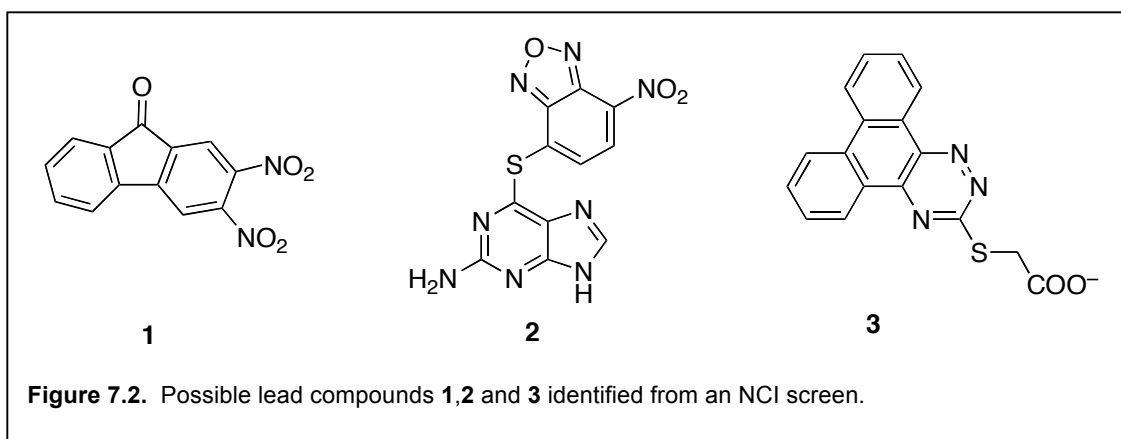

Figure 7.2. Possible lead compounds **1**,**2** and **3** identified from an NCI screen.

Through a combination of VLS and experimental testing, several chemical scaffolds from the NCI library emerged as possible leads, including **1**, **2** and **3** (Figure 7.2). We are planning to investigate SARs for these compounds and possible to synthesize a focused sub-library. In initial studies, we analyzed a series of 9-fluorenone analogs of compound

1. In these studies, 2,3-nitro and/or fluoro disubstituted 9-fluorenones were all effective inhibitors. Since compound **1** has electron-withdrawing groups at the 2 and 3 positions, we must investigate the importance of the ketone moiety and determine whether the carbonyl undergoes nucleophilic attack by cysteine. Compound **2** is composed of a purine and benzooxadiazole moiety joined by a thioether bond. The oxadiazole and 6-nitro functional groups in compound **2** were essential for inhibitor potency; however, the purine could be replaced by other aromatic groups with potential for hydrogen bonding. Compound **3** exhibited the most drug-like properties in our series of inhibitors owing to the absence of nitro or benzooxadiazole functionalities. Hydrogen bonding interactions between the thiocarbonate and critical active site residues such as Lys234, Arg242 or Arg245 are predicted to be required for binding. To investigate the potential of this scaffold, we analyzed a related series of commercially available compounds in which the thiocarbonate was replaced by an aromatic thio group or thioamide (Figure 7.3A). In parallel with these experiments, we also explored variations in the polycyclic moiety of the parent compounds such as 1,2,4-triazino[5,6-B]indole (Figure 7.3B). However, none of these compounds exhibited more than 50% inhibition against APR by biological assay, whereas the free energy of binding calculated from docking studies (ΔG_{AD4}) remained the same. Although SAR of **1**, **2** and **3** with commercially available compounds was not

Figure 7.3. Commercially available compounds that identified by similarity search based on compound 3. (A) modification of thiocarbonate (B) modification of polycyclic ring
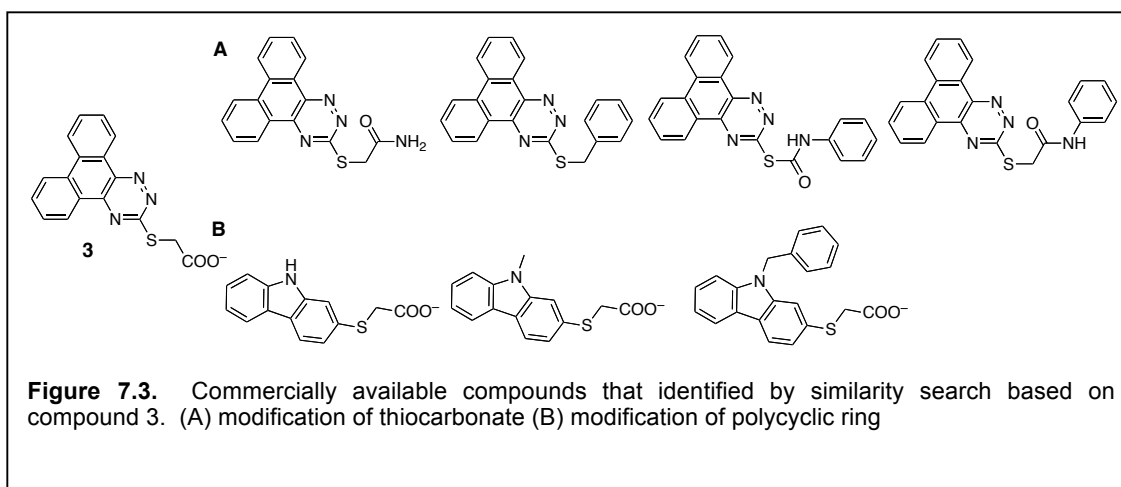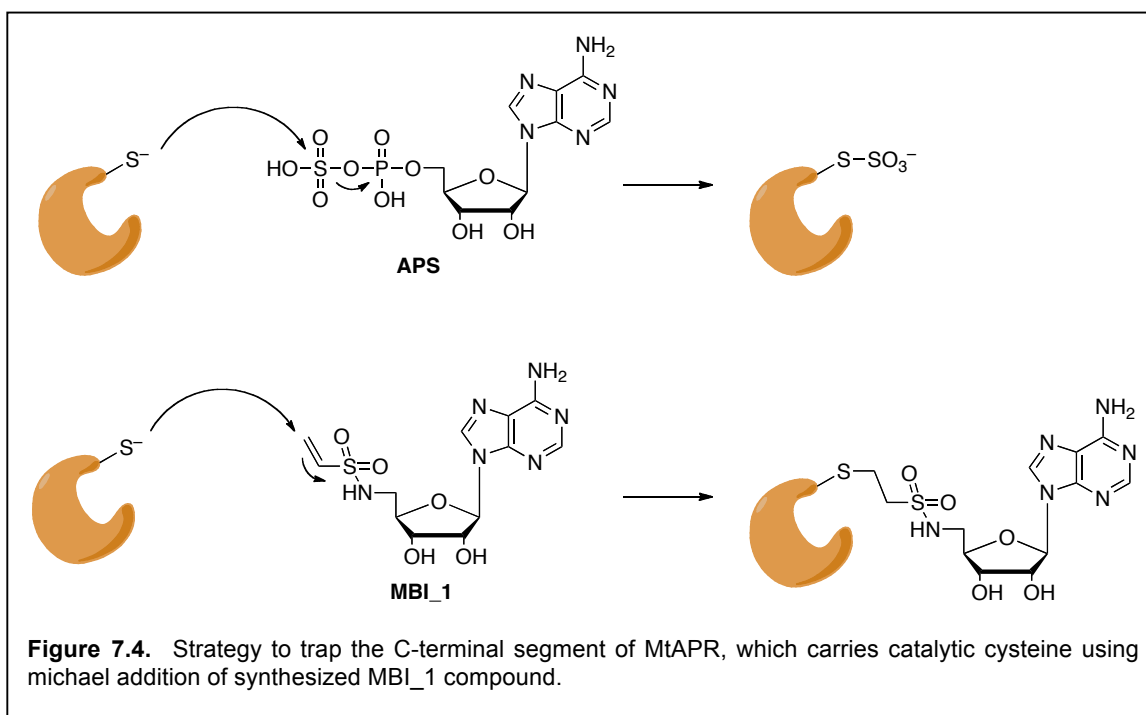
successful identifying compounds with improved potency, these preliminary data should inform the direction of future studies.

7.3.1.2 Solve the X-ray structure of MtAPR in the 'open' and 'closed' states

Once VLS appeared as a tool on the drug discovery market, people predicted that HTS would be replaced by VLS due to its fast and cost effective approach. In addition, the docking program predicts the binding mode of the ligand to the receptor as opposed to a random screen. However, VLS requires knowledge about the spatial and energetic relationships between the receptor and ligand (*5*). Most importantly, VLS heavily relies on the crystal structure of the receptor to predict binding (*6, 7*). An HIV protease inhibitor is a successful example of using VLS for anti-AIDS drug design. Behind this success, there were more than 130 crystal structures of HIV protease available through internet access databases (*8*). In contrast, we have only one APR structure from *P. aeruginosa* species, which is also missing the final 15 residues including the catalytic cysteine. Clearly, an essential step forward in this research area will be to obtain the structure of *M. tuberculosis* APR in different conformational states.

Toward this end, we note precedent in this area for protein kinases, which transfer a phosphoryl group from ATP to the peptide substrate. In recent studies, a covalently linked bisubstrate inhibitor of the insulin receptor tyrosine kinase was synthesized by linking ATPγS to a peptide substrate analog. This mechanism-based inhibitor helped to determine the crystal structure complex with inhibitor (PDB 1GAG) and is also a promising candidate for therapeutic intervention (*9*). Along these lines, a mechanism-based inhibitor of APR, which irreversibly modifies the catalytic cysteine, could be used to trap the C-terminal tail in the active site of APR and facilitate structural studies. A mechanism-based inhibitor was designed by taking a potent binding scaffold and

194

attaching a reactive warhead (*10, 11*). The substrate analog, adenosine 5'-monophosphate (AMP) binds to APR with a moderate K_d value of 5.4 µM. Thus, AMP was used as a binding element in the APR active site pocket (*3*). We conceived of a vinylsulfonamide as an acyladenylate surrogate that contains a Michael acceptor to covalently modify the catalytic cysteine. The vinylsulfonamide was chosen as it is the least reactive member in the series of Michael acceptor to minimize off-target reactions (*12*). Previously, Aldrich and co-workers had evaluated β-ketosulfonamide adenylation inhibitors against alicyl-AMP ligase as potential antitubercular agents (*13, 14*). Similarly, we synthesized 5'-deoxy-5'-*N*-{[(ethenyl)sulfonyl]amino}adenosine (appendix 7.5.1) as an irreversible inhibitor of APR (Figure 7.4) (*13-16*). Mass spectrometry (appendix 7.5.2), biochemical and kinetic analyses (not shown) demonstrate covalent modification of the catalytic cysteine, Cys249 of MtAPR. Currently, we are focusing on crystallization of MtAPR using this first generation mechanism-based inhibitor in collaboration with Dr. Gunter Schneider and Dr. Ömer Poyraz at the Karolinska Institute. If we surmount the formidable obstacle of crystallization, it would significantly facilitate inhibitor discovery.


Figure 7.4. Strategy to trap the C-terminal segment of MtAPR, which carries catalytic cysteine using michael addition of synthesized MBI_1 compound.

7.3.2 Rational design

In Chapters 2-6, we established the various interactions between SR and the substrate. Ligand binding involves many factors, including changes of interactions between the ligand, solvent and target protein, as well as conformational changes in the ligand or receptor (*17*). Rational design of APR inhibitors was initiated from a spatial arrangement of atoms or functional groups of small molecule inhibitors believed to be responsible for interactions with the enzyme. The crystal structure of PaAPR (PDB 2GOY) was solved in an open conformation and revealed the presence of a [4Fe-4S] cluster that has been shown to be essential for catalytic activity (*18*). Subsequently, we reported the EcPAPR-Trx structure (PDB 2O8V) in an open conformation depicting two distinct interaction interfaces (*19*). It is important to emphasize that the closed conformation represents the bioactive conformation wherein the catalytic cysteine can commence nucleophillic attack. Based on these studies, inhibitors that stabilized a closed conformation, interacted with the [4Fe-4S] cluster or these protein-protein interfaces could represent important new strategies in inhibitor discovery.

**7.3.2.1 Design of inhibitors that target specific APR conformations**

We have focused on active site interactions based on the crystal structure of PaAPR detailed in Chapter 3. However, conformational changes were observed upon substrate binding in the active site by a dynamic motif, as described in Chapter 4. Biochemical data and structural data show that the C-terminal 15 residues and an Arg-rich loop in SRs fold over the active site, establishing the closed conformation (Figure 7.5). Using homology modeling and the structure of yeast PAPR in the closed conformation (from Chapter 3 and 4), one could rationally design inhibitors that target different conformational states of MtAPR. This strategy to discover specific inhibitors intended for

different enzyme conformations has proven fruitful with kinases (*20, 21*). I envision that an APR inhibitor designed to stabilize the closed conformation would establish important interactions with the C-terminal tail. As outlined above, this general strategy could also facilitate

Figure 7.5. 'Closed' and 'open' conformation by an arginine-rich loop and C-terminal tail
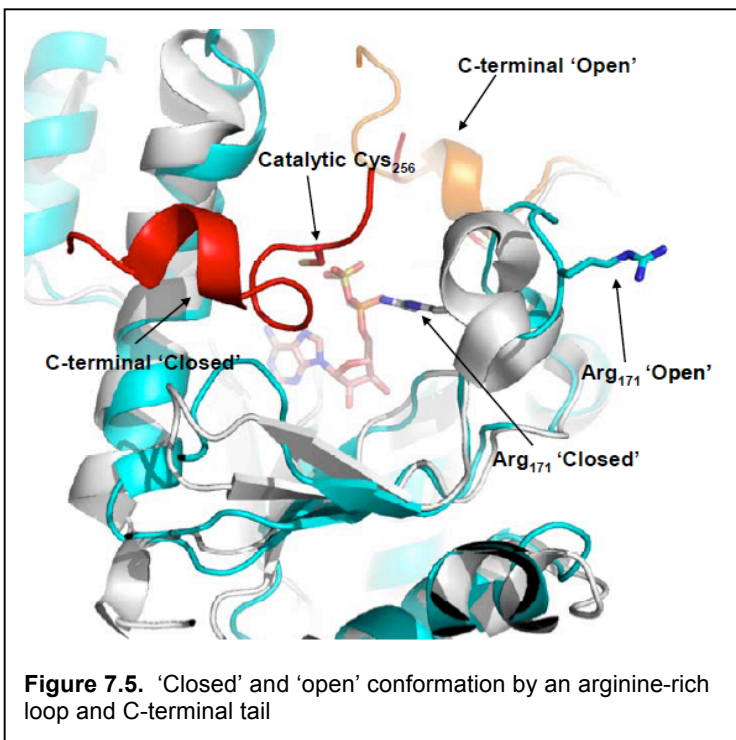
stabilization of the MtAPR enzyme for crystallography.

7.3.2.2 Iron-sulfur cluster targeted APR inhibitors

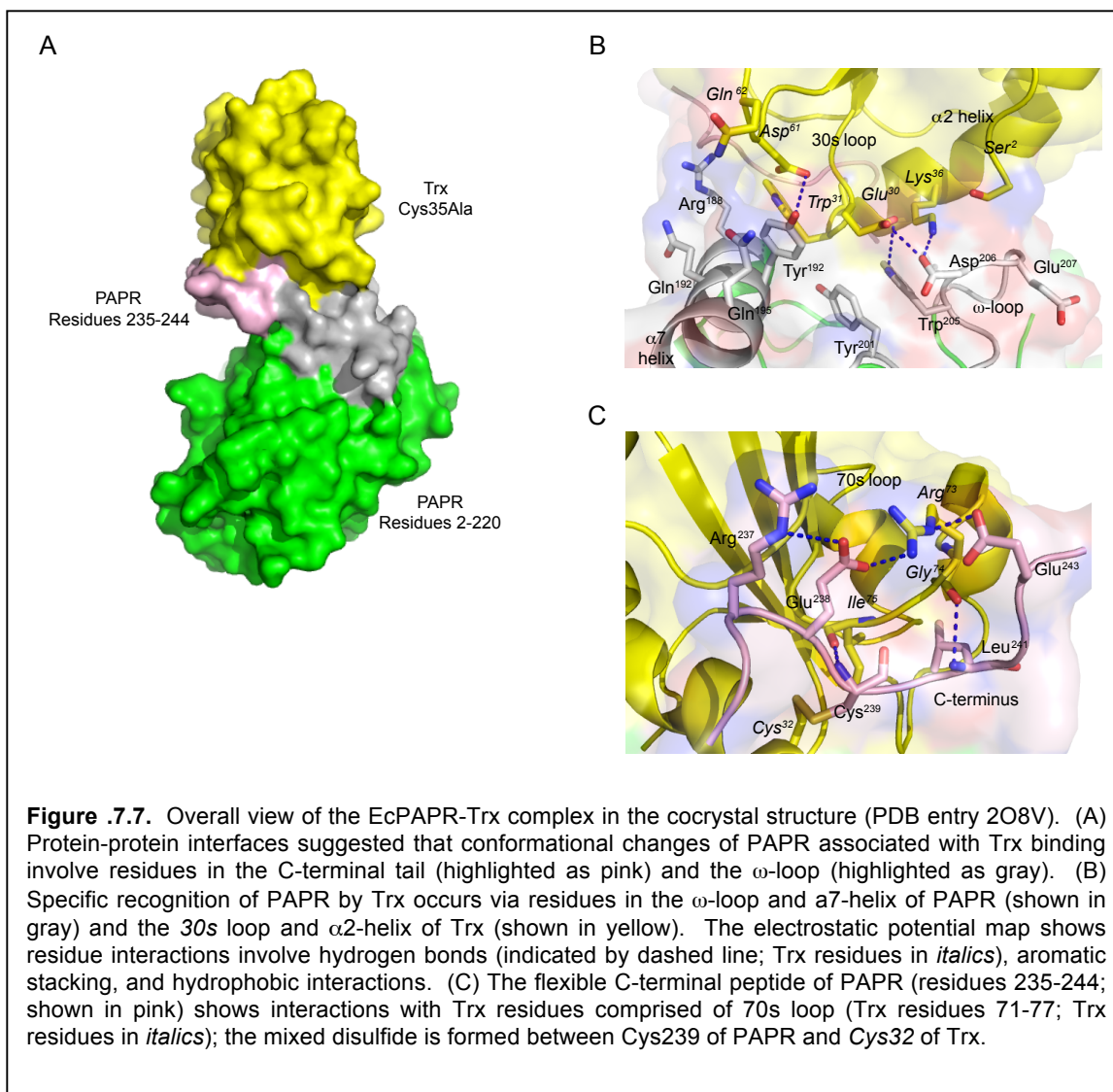**Figure 7.6.** Potential APR inhibitors with Fe-chelating groups (**R**).
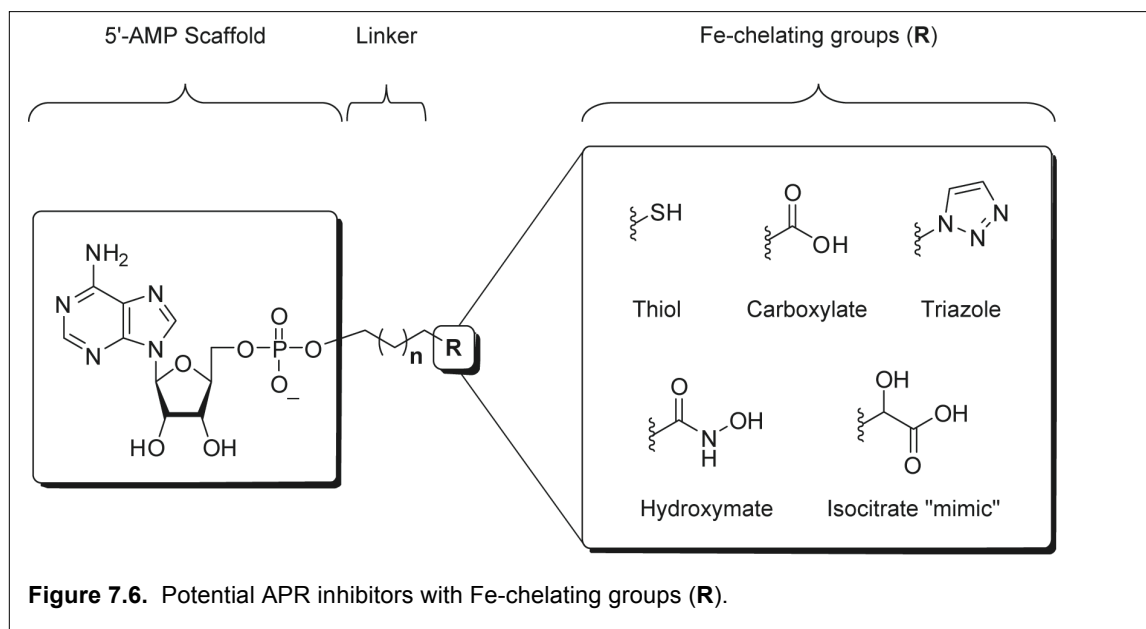
As discussed in Chapter 5 and 6, the [4Fe-4S] cluster plays an essential role in substrate recognition. Functional and structural analyses indicate that the terminal 5'-

sulfate moiety of APS is poised to interact with the [4Fe-4S] cluster. Compounds containing moieties that chelate the catalytic metal ion in APR may have potential as inhibitors. This strategy has proven successful in the development of HDAC inhibitors. In our lab, we have devised a strategy to design bifunctional inhibitors that would interact with the [4Fe-4S] cluster as well as make contacts with the adenosine-binding pocket in the active site (Figure 7.6). We are using combinatorial chemistry to synthesize a library of inhibitors from a solid supported adenosine scaffold. We will then screen for inhibitors from this library using our established APR assay (see Chapter 2).

7.3.2.3 Evaluating SR-Trx interaction interfaces

Recently, the crystal structure of the EcPAPR-Trx complex (PDB 2O8V) revealed two interaction interfaces of ~800 Å each (Figure 7.7A) (*19*). The first interface is established in the vicinity of the mixed protein disulfide between Cys32 in Trx and Cys 239 in EcPAPR (Figure 7.7C). Interaction of the C-terminus of PAPR and the 70s loop of Trx involves electrostatic and hydrophobic interactions (Figure 7.7C). The second recognition interface involves the ω-loop of PAPR and the 30s loop of Trx (Figure 7.7B). Previously, Knaff and colleagues used NMR to investigate the interface interactions on PaAPR and Trx and successfully mapped the important plausible contacts of Trx residues around Cys 32 to PaAPR (*22*). Surprisingly, however, alanine scanning of this region revealed no hotspot Trx residues that significantly reduced binding to PaAPR. Therefore we will investigate interface residues within EcPAPR for their potential contribution to Trx binding based on our crystal structure (*19*). The elucidation of the protein-protein interactions will provide insights into the catalytic mechanism as well as assist in the design of inhibitors to block this interaction.

7.3.2.4 Evaluate inhibitors in a secondary cell-based assay

Figure .7.7. Overall view of the EcPAPR-Trx complex in the cocrystal structure (PDB entry 2O8V). (A) Protein-protein interfaces suggested that conformational changes of PAPR associated with Trx binding involve residues in the C-terminal tail (highlighted as pink) and the ω-loop (highlighted as gray). (B) Specific recognition of PAPR by Trx occurs via residues in the ω-loop and a7-helix of PAPR (shown in gray) and the *30s* loop and α2-helix of Trx (shown in yellow). The electrostatic potential map shows residue interactions involve hydrogen bonds (indicated by dashed line; Trx residues in *italics*), aromatic stacking, and hydrophobic interactions. (C) The flexible C-terminal peptide of PAPR (residues 235-244; shown in pink) shows interactions with Trx residues comprised of 70s loop (Trx residues 71-77; Trx residues in *italics*); the mixed disulfide is formed between Cys239 of PAPR and *Cys32* of Trx.

Jumping over the gap between experiments within recombinant enzymes- to live cells- is important for inhibitor discovery. Unlike radioactivity-based assays with recombinant enzyme, cell-based assays afford additional information on biological activity, toxicity, and off-target interactions. We will employ *M. smegmatis* for these studies because it is a close genetic relative of *M. tuberculosis*. Briefly, *M. smegmatis* cultures will be incubated with the compounds and their growth in minimal media with sulfate as the sole sulfur source will be monitored by turbidity. The specificity of compounds for APR will be confirmed by control experiments in which growth is restored by methionine supplementation (*23, 24*).

7.4 Concluding remarks

TB remains a prominent health threat due to the shortcomings of the current treatment regimes. Since pharmaceutical companies are driven by profit, our efforts in academic institutions will serve as the foundation to identify novel targets and hit compounds. Herein, I have described strategies to discover inhibitors against a newly validated TB target, APR. Thorough studies of enzyme and ligand interactions not only help to identify inhibitors, but also promote an understanding of enzyme mechanism and biological function. The aforementioned computational docking, biochemical and biophysical studies have led to many important new insights into the APR reaction mechanism and should accelerate inhibitor discovery for this medically important enzyme.

7.5 Appendix

Figure 7.5.1 Synthesis of 5'-Deoxy-5'-*N*-{[(ethenyl)sulfonyl]amino}adenosine (*13,14*)
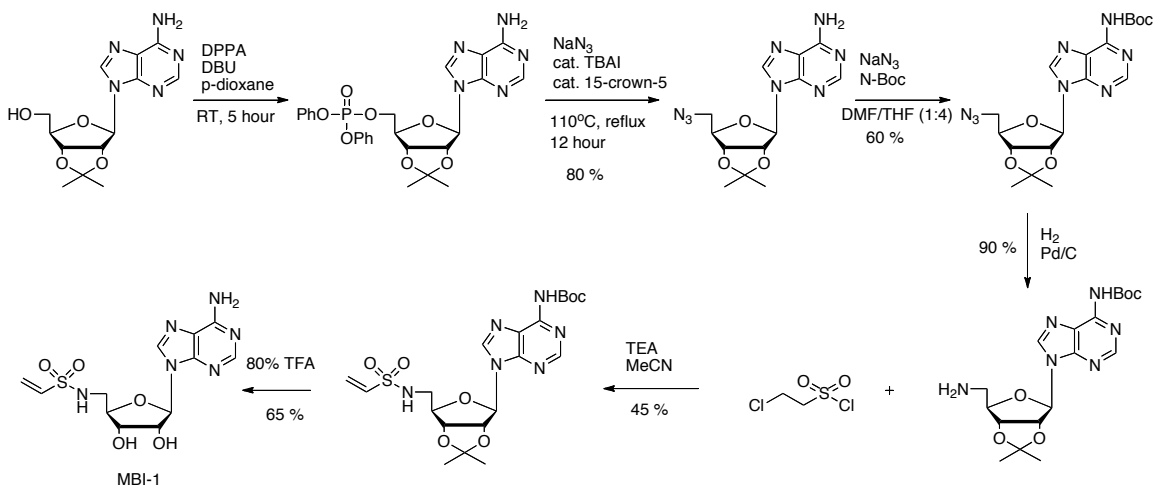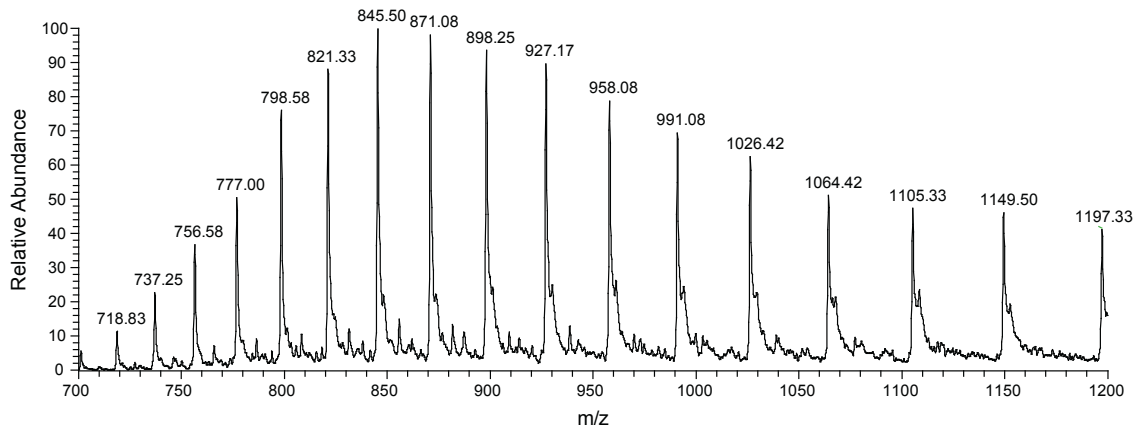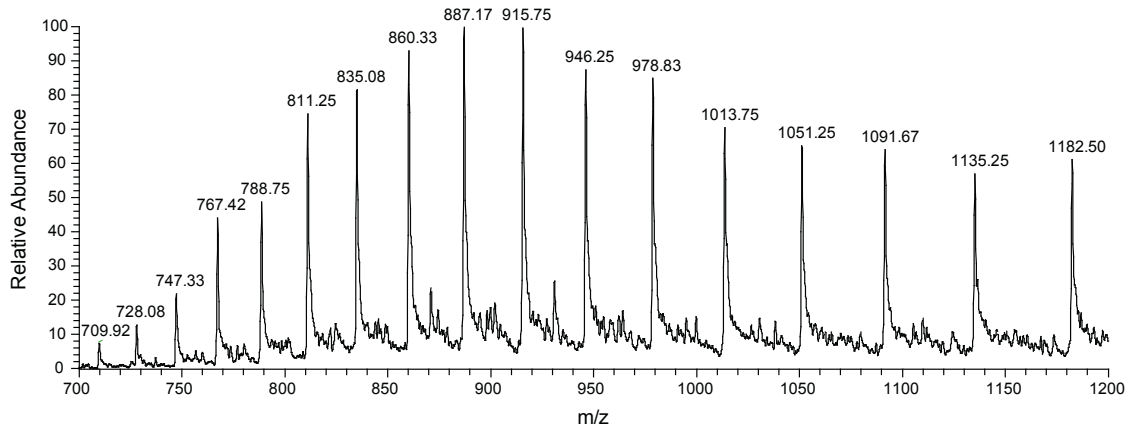
Figure 7.5.2. Mass spectrometric analysis of intact MtAPR complex with MBI

ESI mass spectra of MtAPR (10 µM) without ligand (a), with MBI (b). Ions correspond to the enzyme (E, a) or the covalent enzyme-MBI intermediate (E-MBI, b). The calculated masses after deconvolution of *m/z* values are 28357.0 ± 0.25 Da (a), 28711.9 ± 0.63 Da (b)

7.6 References

1.   Bhave, D. P., Muse, W. B., 3rd, and Carroll, K. S. (2007) Drug targets in mycobacterial sulfur metabolism, *Infect. Disord. Drug Targets 7*, 140-158.

2.   Mdluli, K., and Spigelman, M. (2006) Novel targets for tuberculosis drug discovery, *Curr. Opin. Pharmacol. 6*, 459-467.

3.   Hong, J. A., Bhave, D. P., and Carroll, K. S. (2009) Identification of critical ligand binding determinants in *Mycobacterium tuberculosis* adenosine-5'-phosphosulfate reductase, *J. Med. Chem. 52*, 5485-5495.

4.   Cosconati, S., Hong, J. A., Novellino, E., Carroll, K. S., Goodsell, D. S., and Olson, A. J. (2008) Structure-based virtual screening and biological evaluation of *Mycobacterium tuberculosis* adenosine 5'-phosphosulfate reductase inhibitors, *J. Med. Chem. 51*, 6627-6630.

5.   Klebe, G. (2006) Virtual ligand screening: strategies, perspectives and limitations, π*Drug Discov. Today 11*, 580-594.

6.   Pellecchia, M., Bertini, I., Cowburn, D., Dalvit, C., Giralt, E., Jahnke, W., James, T. L., Homans, S. W., Kessler, H., Luchinat, C., Meyer, B., Oschkinat, H., Peng, J., Schwalbe, H., and Siegal, G. (2008) Perspectives on NMR in drug discovery: a technique comes of age, *Nat. Rev. Drug Discov. 7*, 738-745.

7.   Chen, Y., and Shoichet, B. K. (2009) Molecular docking and ligand specificity in fragment-based inhibitor discovery, *Nat. Chem. Biol. 5*, 358-364.

8.   Wlodawer, A., and Vondrasek, J. (1998) Inhibitors of HIV-1 protease: a major success of structure-assisted drug design, *Annu. Rev. Biophys .Biomol. Struct. 27*, 249-284.

9.   Parang, K., Till, J. H., Ablooglu, A. J., Kohanski, R. A., Hubbard, S. R., and Cole, P. A. (2001) Mechanism-based design of a protein kinase inhibitor, *Nat. Struct. Biol. 8*, 37-41.

10.   Powers, J. C., Asgian, J. L., Ekici, O. D., and James, K. E. (2002) Irreversible inhibitors of serine, cysteine, and threonine proteases, *Chem. Rev. 102*, 4639-4750.

11.   Maly, D. J., Allen, J. A., and Shokat, K. M. (2004) A mechanism-based cross-linker for the identification of kinase-substrate pairs, *J. Am. Chem. Soc. 126*, 9160-9161.

12.   Reddick, J. J., Cheng, J., and Roush, W. R. (2003) Relative rates of Michael reactions of 2'-(phenethyl)thiol with vinyl sulfones, vinyl sulfonate esters, and vinyl sulfonamides relevant to vinyl sulfonyl cysteine protease inhibitors, *Org. Lett. 5*, 1967-1970.

13.   Qiao, C., Wilson, D. J., Bennett, E. M., and Aldrich, C. C. (2007) A mechanism-based aryl carrier protein/thiolation domain affinity probe, *J. Am. Chem. Soc. 129*, 6350-6351.

14.   Somu, R. V., Boshoff, H., Qiao, C., Bennett, E. M., Barry, C. E., 3rd, and Aldrich, C. C. (2006) Rationally designed nucleoside antibiotics that inhibit siderophore biosynthesis of *Mycobacterium tuberculosis*, *J. Med. Chem. 49*, 31-34.

15.   Liu, F., and Austin, D. J. (2001) A general synthesis of 5'-azido-5'-deoxy-2',3'-O-isopropylidene nucleosides, *J. Org. Chem. 66*, 8643-8645.

16. Vannada, J., Bennett, E. M., Wilson, D. J., Boshoff, H. I., Barry, C. E., 3rd, and Aldrich, C. C. (2006) Design, synthesis, and biological evaluation of beta-ketosulfonamide adenylation inhibitors as potential antitubercular agents, *Org. Lett. 8*, 4707-4710.

17. Salemme, F. R., Spurlino, J., and Bone, R. (1997) Serendipity meets precision: the integration of structure-based drug design and combinatorial chemistry for efficient drug discovery, *Structure 5*, 319-324.

18. Chartron, J., Carroll, K. S., Shiau, C., Gao, H., Leary, J. A., Bertozzi, C. R., and Stout, C. D. (2006) Substrate recognition, protein dynamics, and iron-sulfur cluster in *Pseudomonas aeruginosa* adenosine 5'-phosphosulfate reductase, *J. Mol. Biol. 364*, 152-169.

19. Chartron, J., Shiau, C., Stout, C. D., and Carroll, K. S. (2007) 3'-Phosphoadenosine-5'-phosphosulfate reductase in complex with thioredoxin: a structural snapshot in the catalytic cycle, *Biochemistry 46*, 3942-3951.

20. Liu, Y., and Gray, N. S. (2006) Rational design of inhibitors that bind to inactive kinase conformations, *Nat. Chem. Biol. 2*, 358-364.

21. Andersen, C. B., Wan, Y., Chang, J. W., Riggs, B., Lee, C., Liu, Y., Sessa, F., Villa, F., Kwiatkowski, N., Suzuki, M., Nallan, L., Heald, R., Musacchio, A., and Gray, N. S. (2008) Discovery of selective aminothiazole aurora kinase inhibitors, *ACS Chem. Biol. 3*, 180-192.

22. Chung, J. S., Noguera-Mazon, V., Lancelin, J. M., Kim, S. K., Hirasawa, M., Hologne, M., Leustek, T., and Knaff, D. B. (2009) Interaction domain on thioredoxin for *Pseudomonas aeruginosa* 5'-adenylylsulfate reductase, *J. Biol. Chem. 284*, 31181-31189.

23. Barker, L. P., Lien, B. A., Brun, O. S., Schaak, D. D., McDonough, K. A., and Chang, L. C. (2007) A *Mycobacterium marinum* zone of inhibition assay as a method for screening potential antimycobacterial compounds from marine extracts, *Planta. Med. 73*, 559-563.

24. Stamm, L. M., and Brown, E. J. (2004) *Mycobacterium marinum*: the generalization and specialization of a pathogenic mycobacterium, *Microbes Infect. 6*, 1418-1428.